Magmatic fluids in seafloor hydrothermal systems: An in-depth mineralogical, trace element and isotopic study of sulfide chimneys from Brothers volcano, Kermadec arc

by

Heidi Alaine Berkenbosch

B. Sc. Oceanography

University of Washington

Submitted in fulfilment of the requirements for the degree of

Doctor of Philosophy

July, 2017

UNIVERSITY
OF TASMANIA

CODES, ARC Centre of Excellence in Ore Deposits at the University of Tasmania

CODES

Declaration

This thesis contains no material which has been accepted for a degree or diploma by the University or any other institution and, to the best of my knowledge and belief, no material previously published or written by another person except where due acknowledgement is made in the text of the thesis.

Heidi A. Berkenbosch

Date: 5 July, 2017

Authority of access

The publishers of the papers comprising Chapters 2 and 4 (Economic Geology and Mineralium Deposita, respectively) hold the copyright for that content and access to the material should be sought from the respective journals. The remaining non-published content of the thesis may be made available for loan and limited copying and communication in accordance with the Copyright Act 1968.

Heidi A. Berkenbosch

Date: 5 July, 2017

Statement of Co-Authorship

The following people and institutions contributed to the publication of work undertaken as part of this thesis:

Heidi Berkenbosch	School of Earth Science	**Candidate**
Cornel de Ronde	GNS Science	**Author 1**
Bruce Gemmell	School of Earth Science	**Author 2**
Andrew McNeill	Mineral Resources Tasmania	**Author 3**
Chris Ryan	CSIRO Mineral Resources	**Author 4**
Daryl Howard	Australian Synchrotron	**Author 5**
Bence Paul	University of Melbourne	**Author 6**

Author details and their roles:

Chapter 2: Mineralogy and formation of black smoker chimneys from Brothers submarine volcano, Kermadec arc

Published in Economic Geology, 2011, Volume 107, no. 8, pp 1613- 1633

Candidate was the primary author and contributed 85% to the planning, execution and preparation of the research project and subsequent paper.
Author 1 contributed to the conception and design of the project and contributed to the interpretation of the work by critically revising the paper.
Author 2 contributed to the conception and design of the project and contributed to the preparation of the paper.
Authors 3 contributed to the execution of the project and preparation of the paper.

Chapter 3: Trace element mapping of copper- and zinc-rich black smoker chimneys from Brothers volcano, Kermadec arc, using synchrotron radiation XRF and LA-ICPMS

Accepted by Economic Geology for publication pending corrections

Candidate was the primary author and contributed 85% to the planning, execution and preparation of the research project and subsequent paper.
Author 1 contributed to the conception and design of the project and contributed to the interpretation of the work by critically revising the paper.
Author 2 contributed to the conception and design of the project.
Author 3 contributed to the conception, design and execution of the project.
Author 4 contributed to the execution of the project.
Author 5 contributed to the execution of the project.

Chapter 4: Characteristics of copper isotopes from chalcopyrite-rich black smoker chimneys at Brothers volcano, Kermadec arc and Niuatahi volcano, Lau Basin

Published in Mineralium Deposita, 2015, Volume 50, no. 7, pp 811- 824

Candidate was the primary author and contributed 85% to the planning, execution and preparation of the research project and subsequent paper.
Author I contributed to the conception and design of the project and contributed to the interpretation of the work by critically revising the paper.
Author 2 contributed to the conception and design of the project.
Author 6 contributed to the execution of the project.

We the undersigned agree with the above stated "proportion of work undertaken" for each of the above published (or submitted) peer-reviewed manuscripts contributing to this thesis:

J. Bruce Gemmell
Supervisor
CODES, ARC Centre of
Excellence in Ore Deposits
University of Tasmania

7/7/14
Date:

Leonid Danyushevsky
Head of Discipline
Earth Sciences

University of Tasmania

7/7/14
Date:

Abstract

Brothers submarine caldera volcano is one of 30 large volcanic centres that comprise the Kermadec arc, which stretches for ~1300 km NE of New Zealand. The NW Caldera vent field at Brothers straddles the caldera wall and hosts numerous, active, high-temperature (up to 302°C) black smoker chimneys and a greater number of inactive, sulfide-rich spires. The addition of magmatic fluids to the hydrothermal system is indicated by high ^{3}He, $CO_{2(g)}$, and $H_2S_{(g)}$ concentrations, low pH, and negative $\delta^{15}N$ and δD_{H_2O} values for the vent fluids, in concert with local advanced argillic alteration assemblages in the host rocks. This study examines the mineralogy, trace element composition and Cu isotopes of the sulfide chimneys to test the hypothesis that magmatic fluids significantly affect the composition of mineralization at Brothers NW Caldera vent field.

Petrographic analysis was undertaken to describe chimney mineralogy and formation. Chimney types were identified based on the composition and relative proportion of mineralogical layers. Two are Zn-rich, i.e., sphalerite-chalcopyrite and sphalerite-barite chimneys, and two are Cu-rich, i.e., chalcopyrite-sulfate and chalcopyrite-bornite chimneys. Discovery of small Bi-Au telluride inclusions explains previously enigmatic whole rock Au contents up to 91 ppm. Enriched Bi contents are commensurate with large amounts of sediment being subducted at the Kermadec trench, whereas the Bi-Au association suggests liquid Bi scavenged Au. Both findings are consistent with magmatic contributions to the NW Caldera vent site.

Synchrotron radiation X-ray fluorescence microscopy (XFM) was used to produce high-resolution trace element maps (2 μm beam, covering 84 – 136 mm^2) of Fe, Cu, Zn, As, Se, Sr, Pb ± Ga, Au, Bi and U distribution across the inner chimney walls. In addition, lower resolution (47 μm beam) maps generated by laser ablation inductively coupled plasma mass spectrometry (LA-ICPMS) imaged those same elements, plus Ca, Co, Ni, Mo, Ag, Cd, In, Sn, Sb, Ba, Tl ± V and Te. Elemental zonation and textural features of sphalerite in the two Zn-rich chimneys show a progression of sphalerite replacement by chalcopyrite. The two Cu-rich chimneys show contrasting formation styles based on their massive chalcopyrite linings. The first displays elongate chalcopyrite grains radiating into and infilling the conduit, which merge together some millimetres from the centre. The second style shows deposition of successive laminations (0.25 - 1 mm) of chalcopyrite inside the conduit that progressively narrowed the orifice. Additionally, fine (15 - 40 μm) rings of concentrated trace elements occur within,

and between, the laminations of Co, Ni, Zn, As, Se, Mo, Ag, Cd, Sn, Te, Au, Tl, Pb, Bi and U. The presence of U specifically indicates repeated, brief incursions of seawater into the chimney interior, during which perturbation of the resultant chemical gradients induced abrupt precipitation of these elements. Thus, the rings are a proxy for secular variations in vent fluid composition. Calculated enrichment factors, used to differentiate magmatically-derived elements, are generally consistent between the chimney trace element rings, fumarole condensates from subaerial volcanoes, and a 'pond' of molten (condensed) sulfur atop a submarine volcano. These indicate that Au, Te, Bi, Se, Ag and Cu in Brothers chimneys have a magmatic source.

Isotopic analysis of primary chalcopyrite was utilized to investigate high-temperature hydrothermal Cu isotope fractionation at Brothers. The majority of the samples range between δ^{65}Cu = ~0.00 and 0.50‰, which is representative of a mantle source for the Cu. A few higher δ^{65}Cu values (>0.90‰) occur randomly distributed through chalcopyrite of the same age (<1 yr) in two chimneys. This suggests the higher δ^{65}Cu values are not related to seawater oxidation, which would decrease δ^{65}Cu values in residual chalcopyrite, but rather could indicate isotopic variation within the vent fluids. Theoretical studies show significant isotopic fractionation can occur between aqueous and vaporous complexing species. Thus, given the evidence for magmatic volatiles at Brothers, vapour transport of Cu could account for the observed isotopic fractionation, again consistent with a magmatic origin.

In summary, the application of techniques ranging from petrography to element mapping to Cu isotopes, shows that Au, Te, Bi, Se, Ag and Cu in this high-temperature, seafloor hydrothermal system are derived by magmatic fluids, where Bi-melts concentrated Au effectively and Cu may be transported by vapour.

Acknowledgements

At the end of each chapter I acknowledge the people that helped in the collection and interpretation of data for that chapter. I reserve this section for those who contributed beyond any individual research component. Firstly, I thank the institutions that made this dissertation possible, CODES at the University of Tasmania, and GNS Science. CODES accepted me with only an undergraduate in Oceanography and my final-year project as proof of my ability. They gave me both personal and research scholarships and access to the personnel, administrative and technical resources needed to begin this research. Likewise, GNS gave me access to its spectacular chimney collection, took me on a research cruise to the Kermadecs, and provided office support and an intellectually rich environment for many years. I also thank Drs. Jan Peter and John Jamieson for their thoughtful and thorough thesis reviews which helped to improve the text.

For a student with little prior expertise in geology, I certainly needed some help along the way. To begin, I would like to thank my secondary advisor, Dr. Andrew McNeill, who taught me how to identify minerals under a microscope, assisted with using the SEM and EMP, provided general guidance, help in writing and especially assisted with understanding the link between active seafloor hydrothermal systems and ancient VMS systems. Thank you Andrew. Likewise, my other co-authors each patiently walked me through the science and procedures of what were invariably brand new techniques for me, and read various drafts of abstracts and manuscripts. I would like to acknowledge Dr. Bence Paul for his help with the Cu isotope research and Dr. Daryl Howard for assistance with the element mapping data. A special mention is made to Dr. Chris Ryan who fielded umpteen emails about GeoPIXE software and keenly ensured my element maps were the best they could be. Thank you Chris.

I extend my thanks to my primary advisor, Prof. Bruce Gemmell, who took me on unplanned when my initial project fell through. Besides his intellectual help and guidance through thesis planning and execution, Bruce unfailingly supported my candidature through many changes including supervisors, relationships, motherhood, international relocations, and extensions. It's been a long journey. Thank you for not giving up on me Bruce!

My greatest thanks is to, and *for*, Dr. Cornel de Ronde. Where do I begin? When I decided that seafloor chimneys was the research I wanted to pursue for my Ph.D., my colleagues at GNS and

I were coincidently taken on a fieldtrip to White Island. Cornel enthusiastically explained the link between a degassing volcano and chimneys on the seafloor, which previously I had not understood. What an exciting introduction to research on arc hydrothermal systems! He conceived the idea for an interesting Ph.D. project, initiated the conversation with CODES to secure my candidature and supervisors, advocated on my behalf when that project had to change, and then immediately planned a new and equally interesting project. Cornel has been my greatest source of intellectual input and guidance, pushed my writing skills ever forward, encouraged my attendance and presentations at several conferences, and connected me with high-profile researchers and opportunities to pursue my studies. Over and above all that, Cornel has been my emotional rock and financial support through the many years of part-time study and full-time parenting. So from the bottom of my heart, Cornel, thank you so much for everything. I could not have completed this project without you.

A desire to pursue research starts well before a Ph.D. and so I also want to thank my parents, Paul and Jean De Groot, for instilling in me a life-long interest in learning, a belief in the power of hard work, a solid dose of self-esteem and confidence to try new things, and fierce determination to never give up. I needed all of those skills. I believe that curiosity is humankind's greatest trait, and that has been nurtured in me from birth. Thank you Mom and Dad, I love and admire you both.

This list would not be complete without giving thanks to Paul, who supported me through my undergraduate and beginning of my Ph.D., and who shared the fun and challenges of my youth and early adulthood. Thank you Paul.

And to finish.....a story. The story of the moment my interest in oceanography was ignited. It was the summer of 1994 and I was vacationing in the San Juan Islands with my cousins and aunt and uncle. One night we were treated to spectacular phosphorescence in the water and all us kids were out on the dock stirring the water with long sticks and watching the glowing trails. I asked my Uncle John Smit, a Professor of microbiology, how the phosphorescence worked and he explained simply that it was little bugs that glowed when they got excited by movement in the water. Although the concept of glowing bugs was neat, what really struck me was how awesome it was that he could *explain* the ocean's mysteries. And then and there, I decided that I would study the ocean and hoped that one day I might be able to explain my work to others. I pursue that passion to this day. Although it was an ordinary moment for you, Uncle John, it was a turning point for me and I thank you for that special night.

As an epilogue to that story, one night in Wellington there was spectacular phosphorescence in the harbour and my friends and I were stirring the water with long sticks and watching the glowing trails. A woman walked by asked how the phosphorescence worked...and I explained it to her.

Table of Contents

List of Figures

List of Tables

Chapter 1

Introduction

1.1 Intraoceanic arcs and seafloor hydrothermal systems

Owing to their intriguing, dynamic and commonly spectacular ecosystems, seafloor hydrothermal systems have garnered significant attention since their first discovery in 1977 (Corliss et al., 1979). These systems are closely linked in space and time to tectonic plate boundaries where magmatic heat drives seawater circulation through the oceanic crust, leading to the eventual expulsion of a modified hydrothermal fluid at the seafloor and, in some cases, the deposition of massive sulfides. The majority of these systems occur along mid-ocean ridges (MORs) – in part because there has been considerably more exploration done there – where differences in spreading rate, magmatic composition, and sedimentation affect the composition and morphology of any associated mineralized mounds and chimneys (e.g., Hannington et al., 2005; 2011). Despite their abundance, seafloor massive sulfide deposits formed along MORs are not considered the best modern analogues of ancient volcanogenic massive sulfide (VMS) deposits on land, and which similarly formed in a submarine environment. Rather, seafloor massive sulfide mineralization formed at present-day convergent plate boundaries more commonly hosts the polymetallic Cu, Zn, Pb, Ag, and particularly Au mineralization that is most similar to ancient VMS mineralisation (e.g., Von Damm, 1990; Rona and Scott, 1993).

Magmas associated with arc volcanism are more oxidized and volatile-rich than those from MORs (e.g., Arculus, 1994). The subducted, hydrated (altered) oceanic crust and associated sediment release water and other volatiles into the overlying mantle wedge, initiating partial melting and enriching arc magmas in elements such as S, K, V, Cu, Zn, As, Rb, Sr, Mo, Ag, Sb, Ba, Au, Pb, and Bi, (e.g., Hedenquist and Lowenstern, 1994; Timm et al., 2012). The range in variables associated with subduction, including composition of the subducting and overlying plates, water depth and heat flux, can result in locally unique hydrothermal fluid compositions and associated mineralization (e.g., Hannington et al., 2005; de Ronde et al., 2007). Moreover, arc magmas can transfer some of their slab- and sediment-derived volatiles, isotope ratios, metals and trace elements into the overlying hydrothermal system through exsolved fluids and gases, which are believed to account for the polymetallic nature of their associated sulfide deposits (e.g., de Ronde, 1995; de Ronde et al., 2005). Although the geologic record indicates that the largest of these subduction-related deposits develop in back-arc basins, arc front caldera

volcanoes also have the propensity to host significant seafloor massive sulfide mineralization (de Ronde et al., 2005; Hannington et al., 2005). For example, ring faults at caldera volcanoes act as primary structural controls focusing high-temperature hydrothermal discharge and concentrating metals. As of 2010, there were 165 confirmed seafloor massive sulfide deposits discovered on the seafloor, of which 13 are located on arc volcanoes from the Izu-Bonin, Mariana, Tonga-Tofua and Kermadec arcs (Hannington et al., 2011). Further sulfide deposits have been confirmed on seven other arc volcanoes on the Izu-Bonin, Tonga-Tofua, and South Sandwich arcs in the years to 2015 (InterRidge Vents database version 3.4; Beaulieu, 2015).

1.2 Kermadec arc setting and Brothers volcano

The Kermadec arc is the southern ~1300 km of the contiguous Tonga-Kermadec arc that stretches ~2500 km between New Zealand and Tonga, and delineates the margin of westward subduction of the Pacific plate beneath the Australian plate (see Fig. 2.1). The Tonga-Kermadec arc is globally recognized as the type example of intraoceanic subduction from which broad insights have been made into subduction processes and the formation of back arc basins (e.g., Smith and Price, 2006). Along the northern Tonga arc the subduction rate is a fast ~24 cm/year, but decreases to ~5 cm/year along the southern Kermadec arc (DeMets et al., 1994). Likewise, the associated back-arc basins have spreading rates that range from 15.8 cm/year in the northern Lau basin to ≤1 cm/year in the Havre Trough (Schellart and Spakman, 2012). Southward from the arc, subduction of the Pacific plate continues under continental New Zealand, where the associated magmatism is expressed on the Earth's surface as the Taupo Volcanic Zone. In addition, the Hikurangi Plateau, a 25-km-thick Cretaceous large igneous province with ≤500 m of overlying terrigenous sediment, is subducting beneath the southern Kermadec arc and the northern part of the New Zealand continental crust. Fragments of the Plateau and overlying sediment are thought to rise into the mantle wedge via cold diapirism and, along with slab-derived fluids, create a geochemically heterogeneous sub-arc mantle in the southern Kermadec arc (Timm et al., 2016).

The active Kermadec arc front hosts 30 volcanic centres, incorporating either single, large volcanoes or groups of smaller cones, many of which are venting hydrothermal fluids (de Ronde et al., 2003). The volcanoes range from basalt to rhyodacite in composition, and are emplaced west of the Kermadec ridge along most of the arc except for a central section (~29 - 32°S) where they merge with the ridge itself (see Fig. 2.1). Volcanic centres in the southern Kermadec arc include those from the edge of the continental margin of New Zealand to the projected northern edge of the subducted Hikurangi plateau (i.e., the extension of the Rapuhia scarp, or Clark through Kibblewhite volcanoes), with hydrothermal venting occurring on 8 of the 12 volcanoes (67%; de Ronde et al., 2007). The volcanic centres of the mid-Kermadec arc (i.e., from Havre to the northernmost subaerial volcano, Raoul) have a higher incidence of venting (10 of 12 centres, 83%), but lower overall intensity as indicated by plume size and concentration of dissolved gases and ionic species. By contrast, volcanic centres of the northern Kermadec arc (i.e., from Volcano O to Monowai) are all hydrothermally active (C.E.J. de Ronde, pers. comm., 2017). The

difference in intensity between the southern and mid-Kermadec arc vent systems is attributed to the subducting Hikurangi Plateau releasing more fluids into the mantle wedge during slab melting as a consequence of its greater crustal thickness (de Ronde et al., 2007). The resultant extensive partial melting thus provides a greater source of heat and fluids to stimulate the hydrothermal systems of the southern Kermadec arc.

The four Kermadec volcanoes known to host hydrothermal mineralization are Monowai, situated in the northern Kermadec arc, and Rumble II West, Clark and Brothers, all located in the southern Kermadec arc. Three of the volcanoes are calderas with resurgent cones, with Clark representing a special case in which the post-collapse flows and volcaniclastic deposits have entirely infilled the caldera such that it presents today as a cone volcano (de Ronde et al., 2014). Mineralization at Monowai occurs as hydrothermally altered rocks with disseminated sulfides including pyrite, marcasite, and trace chalcopyrite; the maximum measured vent fluid temperature recorded was 57°C (Leybourne et al., 2012b). Rumble II West today is host to inactive chimneys and diffuse, low-temperature venting although chimney breccias that contain chalcopyrite (up to 20 modal %), pyrite, sphalerite and trace galena – indicating venting temperatures between 250 and 300°C – have also been recovered (Leybourne et al., 2012a). Clark volcano has active, sulfate-dominated chimneys up to 7 m tall that are venting fluids up to 185°C at their top (and 221°C at the base), and contain pyrite and marcasite with minor sphalerite and galena. High-temperature, Cu-rich mineralization has been inferred to exist subseafloor, together with the buried caldera, because of the volcano's two-stage growth history (de Ronde et al., 2014).

Brothers is the only known volcano along the Kermadec arc that is today expelling high-temperature (>300°C) fluids, and as such is considered to host the most hydrothermally active vent fields known for any arc volcano, given that hydrothermal plumes occupy ~700 m of the water column (de Ronde et al., 2005). The volcano has a caldera 3 x 3.4 km in size, with walls that rise from the caldera floor at maximum water depth of 1879 m up to the caldera rim that lies between ~1420 and 1520 m (i.e., ~350 - 450 m high). A 1.5 - 2 km diameter, post-collapse cone shoals to 1196 m in the southern portion of the caldera, and has an older, more degraded cone merging with its northeast flank that shoals to a depth of 1330 m. With respect to other Kermadec lavas, Brothers dacites are enriched in chalcophile and siderophile elements such as Mo, Ag, Sn, Sb, Pb, Bi, and Th that are thought to originate from the subducting slab and sediments via hydrous sediment melts and/or supercritical fluids (Timm et al., 2012). Brothers hosts four active vent sites (i.e., NW Caldera, West Caldera, Upper and Lower Cone sites) and a fifth extinct site (the SE Caldera); with several sulfide samples recovered from the NW Caldera site (de Ronde et al., 2011). Both active and inactive sulfide chimneys are abundant along the NW Caldera wall, and are either Cu- or Zn-rich. The chimneys have up to 91 ppm Au as well as elevated Ga, Ge, Se, Mo, Cd, and In content above other seafloor sulfide deposits; the Bi content of these chimneys is particularly enriched, up to 1100 ppm higher than any other seafloor sulfide sample (Monecke et al., 2016). Regional structures control the location of this site, which lies atop intersecting basement ridge lineaments and caldera ring faults (Embley et al., 2012). Data collected during deployment of hydrophones on the caldera floor indicates that a shallow magma body occurs ~2.5 km

beneath the caldera floor, beneath the post-collapse Upper Cone, which provides a source of exsolved fluids and gases and heat to drive the hydrothermal systems at Brothers (Dziak et al., 2008; de Ronde et al., 2011).

Brothers is arguably the best-studied submarine volcano in the world, having been visited during 13 expeditions between 1994 and 2011 to measure (sub)seafloor seismicity, magnetics, gravity and bathymetry, and which recovered rocks, sulfides, animals, microbes, fluids, gases and plumes (e.g. Stoffers et al., 1999; de Ronde et al., 2005 and references therein; 2011; Dziak et al., 2008; Takai et al., 2009; Baker et al., 2012; Caratori Tontini et al., 2012). Additional research cruises have recently been undertaken (e.g., Leg SO235 on the R/V *Sonne* in January, 2017, http://geschichten.ptj.de/so253#74871) or are planned for later in 2017 (*Jason II* ROV cruise with the R/V *Roger Revelle*), with two drilling expeditions scheduled; one in 2018 by the Integrated Ocean Drilling Program (IODP; http://iodp.tamu.edu/scienceops/expeditions/brothers_arc_flux.html) and another (yet to be scheduled) that will deploy the drill rig "*Meeresbodeon-Bohrgerät*" (MeBo).

Evidence for magmatic contributions to the venting at Brothers is most notably found in samples collected from the two (Upper and Lower) Cone sites, and to a lesser degree, in samples recovered from the NW Caldera site (de Ronde et al., 2011). The vent fluids from both the Cone and NW Caldera sites contain high concentrations of CO_2 (maximum 206.0 and 39.9 mM/kg from the Lower Cone and NW Caldera, respectively), H_2S (maximum 13.9 and 7.1 mM/kg) and ^3He (R/R_A values of 6.9 - 7.4 at both sites where $R= {}^3He/{}^4He_{sample}$ and R_A= the same ratio in air), and low pH (down to 1.9 and 2.8 at the Upper Cone and NW Caldera). Magmatic effects influencing mineralogy are noted in the advanced argillic alteration of the flows at the Cone site (i.e., the dissociation of SO_2 forming sulfuric acid, elemental S and sulfate), and enargite-bearing stockwork veins at the NW Caldera site. The various results have been summarized in a comprehensive model of the Brothers hydrothermal system by de Ronde et al. (2011). These workers suggest that fluid pathways between the underlying magma body and the Cone site are relatively 'direct', resulting in the high concentrations of volatiles expelled there; by contrast, pathways to the NW Caldera site are thought to be more convoluted, ensuring greater degrees of water/rock interaction. Today, the NW Caldera site is dominated by modified seawater with inferred periodic pulses of magmatic fluids. My study compliments and expands on previous works by specifically examining the mineralogy, trace element composition and Cu isotope ratios of the sulfide chimneys to test the hypothesis that *magmatic fluids significantly affect the composition of mineralization at Brothers NW Caldera vent field.*

1.3 Thesis organization

To begin, Chapter 2 details petrographic analysis used to form the mineralogical framework for this study. The chimneys are classified as either Cu-rich (chalcopyrite-dominated) or Zn-rich (sphalerite-dominated), and are further subdivided into 2 categories each. Chalcopyrite-sulfate and chalcopyrite-bornite chimneys are characterized by the relative proportion of two mineralogical layers: a chalcopyrite-rich centre surrounded by an exterior of sulfates and disseminated sulfides. Furthermore, chalcopyrite-bornite chimneys have a thin layer of

other Cu-sulfides and Fe-oxides at the boundary between the core and exterior layers. Sphalerite-chalcopyrite and sphalerite-barite chimney types are distinguished by the presence or absence of minor chalcopyrite lining internal channels, respectively. Intricate textural features include plumose sphalerite, framboidal pyrite and complex colloform banding, indicative of rapid and episodic mineral deposition.

Chapter 3 focuses on the detailed distribution of trace elements within the chimneys, using synchrotron radiation X-ray fluorescence microscopy (SXFM) to generate high-resolution trace element maps of sections through the chimney walls. These data show how physicochemical conditions changed dramatically across the chimney walls, which were in contact with hot, acidic, reducing, metal-rich vent fluids near their interior and cold, oxidizing seawater near their exterior. Trace element precipitation may be sensitive to small variations in fluid conditions and thus provide more information about the circumstances under which the various mineral phases formed, than do major elements alone. Furthermore, certain trace elements, or suites of trace elements, are diagnostic of a fluid source, be that seawater, hydrothermal, or magmatic fluid. To sufficiently capture the broad range and fine scale of physicochemical gradients across chimney walls, the high resolution (2 μm beam) SXFM maps covered 84 – 136 mm^2 and detail the distribution of major chimney elements Fe, Cu and Zn, and trace elements As, Se, Sr, Pb ± Ga, Au, Bi and U. In addition, lower resolution maps (47 μm beam) generated with laser ablation inductively coupled plasma mass spectrometry (LA-ICPMS) imaged the above elements together with Ca, Co, Ni, Mo, Ag, Cd, In, Sn, Sb, Ba, Tl ± V and Te. This is a significant increase in mapped area and range of elements studied from previous chimney mapping studies, which investigated up to 8 trace elements across zones up to 13 mm^2 (Ryan, 2001; Bogdanov et al., 2008; Li et al., 2010; Yeats et al., 2010; de Ronde et al., 2011; 2014; Ryan et al., 2015; Wohlgemuth-Ueberwasser et al., 2015; Dekov et al., 2016).

Chapter 4 further examines evidence for magmatic Cu in the mineralization at Brothers through isotopic analysis of primary chalcopyrite contained within the chimneys, and marks the first Cu isotope study of a submarine intraoceanic arc hydrothermal system. The majority of the measured $\delta^{65}Cu$ values are between ~0 to 0.5‰ and represent a mantle source, although there are a few higher (>0.90‰) $\delta^{65}Cu$ values.

This detailed study of mineralization at one volcano along the ~6900 km of submarine convergent margin (de Ronde and Stucker, 2015) advances our understanding of the nature and setting of these modern, potentially economic polymetallic seafloor massive sulfides, and provides insight into their formation to aid in the exploration for their ancient analogue VMS deposits.

Chapter 2

Mineralogy and formation of black smoker chimneys from Brothers submarine volcano, Kermadec arc

Published in Economic Geology, 2011, Volume 107, no. 8, pp 1613- 1633.

2.1 Abstract

Brothers caldera volcano is a submarine volcano of dacitic composition, located on the Kermadec arc, New Zealand. It hosts the NW Caldera vent field perched on the steep slope of the caldera walls, and includes numerous, active, high-temperature (max 302°C) chimneys and a greater amount of dead, sulfide-rich spires. Petrographic studies of these chimneys show that three main zones can occur within the chimneys: a chalcopyrite-rich core, surrounded by a sulfate-dominated zone that is in turn mantled by an external rind of Fe-oxides, calcite and silicates. Four chimney types are identified based on the relative proportions of the chalcopyrite and sulfate layers, and the presence or absence of anhydrite. Two are Cu-rich, i.e., chalcopyrite-sulfate and chalcopyrite-bornite chimneys, and two are Zn-rich, i.e., sphalerite-barite and sphalerite-chalcopyrite.

Chimney growth begins with the formation of a sulfate wall upon which sulfides precipitate. Later, zone refining results in a chalcopyrite-rich core with pyrite/marcasite and sphalerite occurring predominantly near the outer margins. In chalcopyrite-bornite chimneys, the chalcopyrite core rapidly loses permeability and limits the thickness of the surrounding sulfate layer. In these chimneys, bornite, chalcocite, and covellite form along the outer margin of the chalcopyrite zone as a result of oxidation by seawater. Zinc-rich chimneys display a more vertical zonation and their growth involves an upward advancing barite cap followed by chalcopyrite deposition (if present) nearer the base. The vertical zonation and lack of anhydrite in these chimneys also implies that larger chalcopyrite and anhydrite deposits may exist sub-seafloor. The different chimney types are related to sub-seafloor permeability, the amount of fluid mixing that occurs prior to venting, and heterogeneous fluid compositions.

The occurrence of specular hematite and Bi- or Au-tellurides associated with chalcopyrite are consistent with magmatic contributions to the NW Caldera vent site. These tellurides are the first Au-bearing phase to be identified in these chimneys, and the Bi-Au association suggests that Au-enrichment up to 91 ppm is due to scavenging by liquid Bi. The presence of tellurides in Brothers chimneys have implications for other telluride-bearing deposits, such those in the Urals. Likewise, other aspects of the mineralogy (i.e. textures) and zonation, including the implied sub-seafloor deposition, presented here from an active, undeformed environment can aid in understanding

ancient VMS deposits that have undergone various degrees of metamorphism.

2.2 Introduction

Submarine hydrothermal vent fluids and their associated massive sulfide deposits offer a natural laboratory for active ore depositional processes. These diverse systems provide insight into the nature of magmatic degassing, crustal fluid flow, water-rock interaction, metal sources and transport in fluids, and the eventual deposition of those metals on, or immediately below, the seafloor. Submarine arc volcano hydrothermal systems, in particular, are considered the closest modern analogue to ancient Au-rich VMS deposits, and contain significantly higher amounts of precious metals in their sulfide chimneys than systems found in other tectonic settings (e.g. Von Damm, 1990; Rona and Scott, 1993; de Ronde et al., 2003; Hannington et al., 2005). This elevated precious metal content may be due, in part, to a notable magmatic component that contributes to the hydrothermal fluids at intraoceanic arc volcanoes (de Ronde et al., 2011; Huston et al., 2011).

Brothers submarine volcano is the most hydrothermally active volcano on arguably the most hydrothermally active intraoceanic arc segment in the world, the ~1220 km long Kermadec arc (Fig. 2.1; de Ronde et al., 2003; 2011). It is primarily dacitic in composition and hosts three distinct, active hydrothermal systems: the Cone site, the NW Caldera site and the West Caldera site. In addition, the SE Caldera site is a largely dead vent field (de Ronde et al., 2011; Baker et al., 2012; Caratori Tontini et al., 2012). Several lines of evidence elucidate magmatic fluid contributions to the hydrothermal

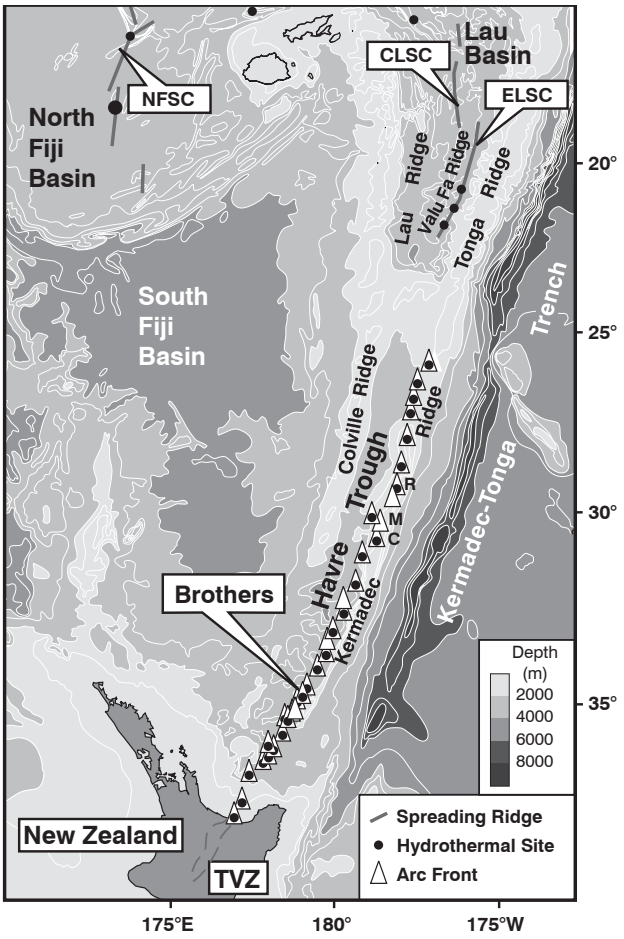

Figure 2.1 Tectonic setting of the Tonga-Kermadec arc-backarc system at the convergence of the Australian and Pacific plates which are situated west and east of the Kermadec-Tonga Trench, respectively. The Kermadec active arc front (≤0.5 Ma) lies within the Havre Trough NE of New Zealand, and merges with the Kermadec Ridge south of the Kermadec islands, Raoul (R), Macauley (M) and Curtis (C). Depth contours are 1000 m with shading every 2000 m. NFSC, North Fiji Spreading Centre; CLSC, Central Lau Spreading Centre; ELSC, Eastern Lau Spreading Centre; TVZ, Taupo Volcanic Zone (from de Ronde et al., 2011).

system at Brothers, particularly at the Cone site. de Ronde et al. (2005; 2011) modelled the Brothers hydrothermal system as being underlain by a magma chamber rising to 2.5 km beneath the volcano, which periodically releases exsolved magmatic fluids. Metal-rich glasses dissolved by magmatic fluids contribute metals to the system, particularly Cu and possibly Au, which are then transported into the

Table 2.1 Sampling method, sample site location, temperature and date of formation for samples used in this chapter.

Cruise	Sampling Method	Sampling Date	Sample	Latitude	Longitude	Depth (mbsl)	Vent Fluid Temp (°C)	Age[1] (years)	Date of formation
TAN 96/03	Dredge	Feb-96	X573/E	?	?	1350- 1640	-	-	-
SO-135	Dredge	Sep-98	SO135-57DR-1	-34 51.651- -34 51.403	179 3.327- 179 3.140	1378- 1491	-	27 ± 6	1971 ± 6 yrs
SWEEPVENTS	Submersible	Oct-04	851-1A	-34 51.769	179 3.493	1665	302	2.05 ± 0.17	Oct, 2002 ± 2 mo
	Shinkai 6500		851-1B "*Leg of Lamb*"	-34 51.769	179 3.493	1665	302	5.50 ± 0.15	Apr, 1999 ± 2 mo
			851-2B	-34 51.766	179 3.492	1658	35	1.12 ± 0.02	Sept, 2003
			851-3A "*Lena*"	-34 51.742	179 3.517	1670	274	2.96 ± 0.38	Oct, 2001 ± 4.5 mo
			851-3[2]	-34 51.742	179 3.517	1670	274	2.82 ± 0.02	Dec, 2001
			852-1A	-34 51.720	179 3.499	1633	inactive	23.0 ± 0.75	Oct, 1981 ± 9 mo
			852-2A	-34 51.720	179 3.481	1627	-	1.71 ± 0.02	Feb, 2003
			852-2B[3]	-34 51.720	179 3.481	1627	292	0.94 ± 0.02	Dec, 2003
NZASRoF	Submersible	Apr-05	PV-626-4min	-34 51.779	179 3.497	1679	inactive	1.62 ± 0.03	Sept, 2003
	Pisces V		PV-628-2min	-34 51.669	179 3.451	1577	inactive	39.7 ± 1.24	Aug, 1965 ± 15 mo
			PV-631-9R	-34 51.657	179 3.422	1572	-	4.58 ± 0.11	Sept, 2000 ± 1.5 mo
			PV-632-11R	-34 51.674	179 3.435	1588	-	1.30 ± 0.02	Jan, 2004

- not measured/calculated. Data from de Ronde et al. (2005, 2011) and Stoffers et al. (1999)

[1] Oldest reported date for the chimney. Sample SO135-57DR-1 was dated using ^{210}Pb as described in de Ronde et al. (2005). The remaining samples were dated using $^{228}Th/^{228}Ra$ and $^{228}Ra/^{226}Ra$ as described in Ditchburn et al. (2012).

[2] Four small fragments from the same chimney structure as 851-3A including 851-3A-a, 851-3A-c, 851-3B-b, 851-3B-

[4] Includes samples 852-2B-a, 852-2B-b, 852-1-a, 852-1-b, all from the same chimney structure

hydrothermal system via magmatic volatiles. The magmatic fluids rise through vertical 'pipes' (~300 m diameter) to the seafloor, mixing with circulating hydrothermal fluid (of seawater origin) along the way. Fluid pathways between the underlying magma body and the Cone site are relatively direct with high concentrations of volatiles being expelled; by contrast, pathways to the NW Caldera site are considered more convoluted, ensuring greater degrees of water/rock interaction. This latter site hosts abundant metal-rich chimneys that can contain up to 91 ppm Au. Today, the NW Caldera site hydrothermal system is dominated by modified seawater with periodic pulses of magmatic fluids, whereas the Cone site is an incipient magmatic-hydrothermal system venting juvenile fluids from depth.

This study concentrates exclusively on chimneys from the NW Caldera vent field, focusing on chimney samples and video and still images obtained during submarine dives and dredging operations over four expeditions (Table 2.1). Our work complements and expands on previous studies of Brothers sulfides by Wright (1998) and de Ronde et al. (2003; 2005; 2011) by providing more detailed descriptions of chimney structure and mineralogy, and through the development of paragenetic and morphological growth models for different chimney types. We also highlight chimney textures of probable biogenic origin. In addition, trace element geochemistry suggests that high contents of gold are associated with chalcopyrite in chimneys from the NW Caldera vent field, yet no free gold or Au-containing phases were found in the previous studies. Here, we report the presence of telluride inclusions in massive chalcopyrite, the first Au-bearing phase identified in NW Caldera chimneys. Our description of the mineralogy and composition of tellurides in an active, undeformed, arc-volcano-hosted system and discussion of their probable magmatic origin lends understanding to the origin and deposition of Cu-associated tellurides found in ancient VMS deposits.

2.3 Brothers volcano

Brothers caldera is the best-studied submarine arc volcano in the world with thirteen expeditions visiting the volcano between 1994 and 2011, including those that deployed manned submersibles (*Shinaki 6500* and *Pisces V*), ROVs (*Kiel 6000*) and AUVs (*ABE* and *Sentry*). These expeditions collected rock, sulfide, biological, and vent and plume fluid samples, recorded video and camera images, high resolution bathymetry, water column (CTD) measurements, seismic profiles, and ship-borne magnetic and gravity data (e.g. Stoffers et al., 1999; de Ronde et al., 2005 and references therein, 2011; Dziak et al., 2008; Takai et al., 2009; Baker et al., 2012; Caratori Tontini et al., 2012).

Brothers forms part of the active Kermadec arc front and sits on a ~35 x 15 km^2 volcanic platform at a depth of 2200 m (Fig. 2.1). The caldera floor averages 1850 m deep, has a diameter of 3 to 3.5 km, and is enclosed by walls 290 to 530 m high (Fig. 2.2). A 1.5 - 2 km diameter post-collapse cone shoals to 1220 m and occupies the southern portion of the caldera, partially coalescing with southern caldera wall. A smaller, older, more degraded cone merges with the northeast flank of the main cone (de Ronde et al., 2005). The volcanic host-rocks are primarily dacitic in composition, although two basaltic samples were dredged from the inner caldera wall (Wright et al., 1998).

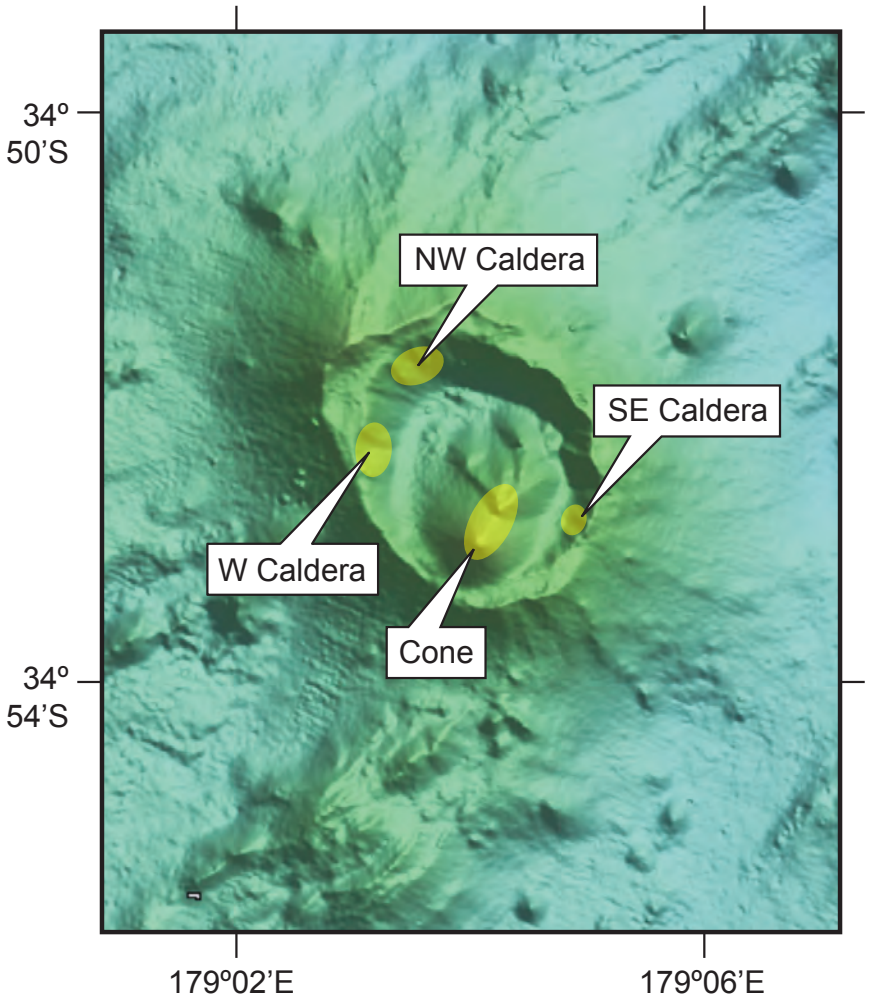

Figure 2.2 Bathymetric map of Brothers volcano derived from EM300 multibeam with a grid cell size of 25 m (illuminated from the N), showing the main hydrothermal vent fields. The regional structural fabric is predominantly NE-SW, with an additional NW-SE lineament through the center of the volcano, parallel to elongation of the caldera. All three Caldera fields (W, NW, SE) are situated where the basement fracture zones intersect caldera ring faults. The NW Caldera field strikes for ~600 m in a SW-NE direction and has a depth range of ~150 m. The W Caldera site is known from water column measurements and magnetic anomalies only. SE Caldera site is largely inactive but hosts sulfide deposits. The Cone site encompasses the summits and upper flanks of both the main and NE cones and is elongate parallel to the NE-SW lineaments. (after de Ronde et al., 2005; Baker et al., 2012; Caratori Tontini et al., 2012).

2.3.1 NW Caldera vent field

Brothers is one of only three submarine volcanoes along the Kermadec arc known to host sulfide chimneys and associated massive sulfide deposits, the others being Rumble II West and Clark (de Ronde et al., 2012; Leybourne et al., 2012a). Regional structures appear to control the location of the two main vent sites at Brothers; the NW Caldera field sits at the intersection of basement ridge lineaments and caldera ring faults, while the cone and its vent site(s) are both elongate parallel to basement morphology (Fig. 2.2; Embley et al., 2012). For additional information on the Cone site, and the locations and characteristics of other hydrothermal sites at Brothers volcano, see de Ronde et al. (2005; 2011); Baker et al. (2012); Caratori Tontini et al. (2012); and Embley et al. (2012).

The northwestern caldera wall comprises many

moderately sloping benches bounded by faults up to 60 m high that range from near vertical to slightly overhanging. The ash-covered slopes have eroded into numerous small box canyons composed of massive, blocky lava flows alternating with scree 'chutes' dominated by hydrothermally altered boulders (de Ronde et al., 2011; Embley et al., 2012). Hexagonal cooling joints occur in some flows, and the slopes appear unstable with large blocks (5 - 6 m), or tall pillars of lava, having broken away from the main caldera wall. The NW Caldera hydrothermal field strikes ~600 m in an overall SW-NE direction and ~150 m vertically, upwards from a depth of ~1700 m. Alteration is unevenly distributed through this terrain and tends to be limited to narrow zones striking orthogonal to the slope (Embley et al., 2012). High degrees of alteration result in bright, white sediment full of finely disseminated pyrite and bacterial mats. The greatest degree and extent of alteration lies between depths of ~1670 and 1600 m (de Ronde et al., 2011). Probes inserted into altered sediment have measured temperatures up to 49°C. Yellow-orange nontronite deposits are widespread throughout the site, ranging from small

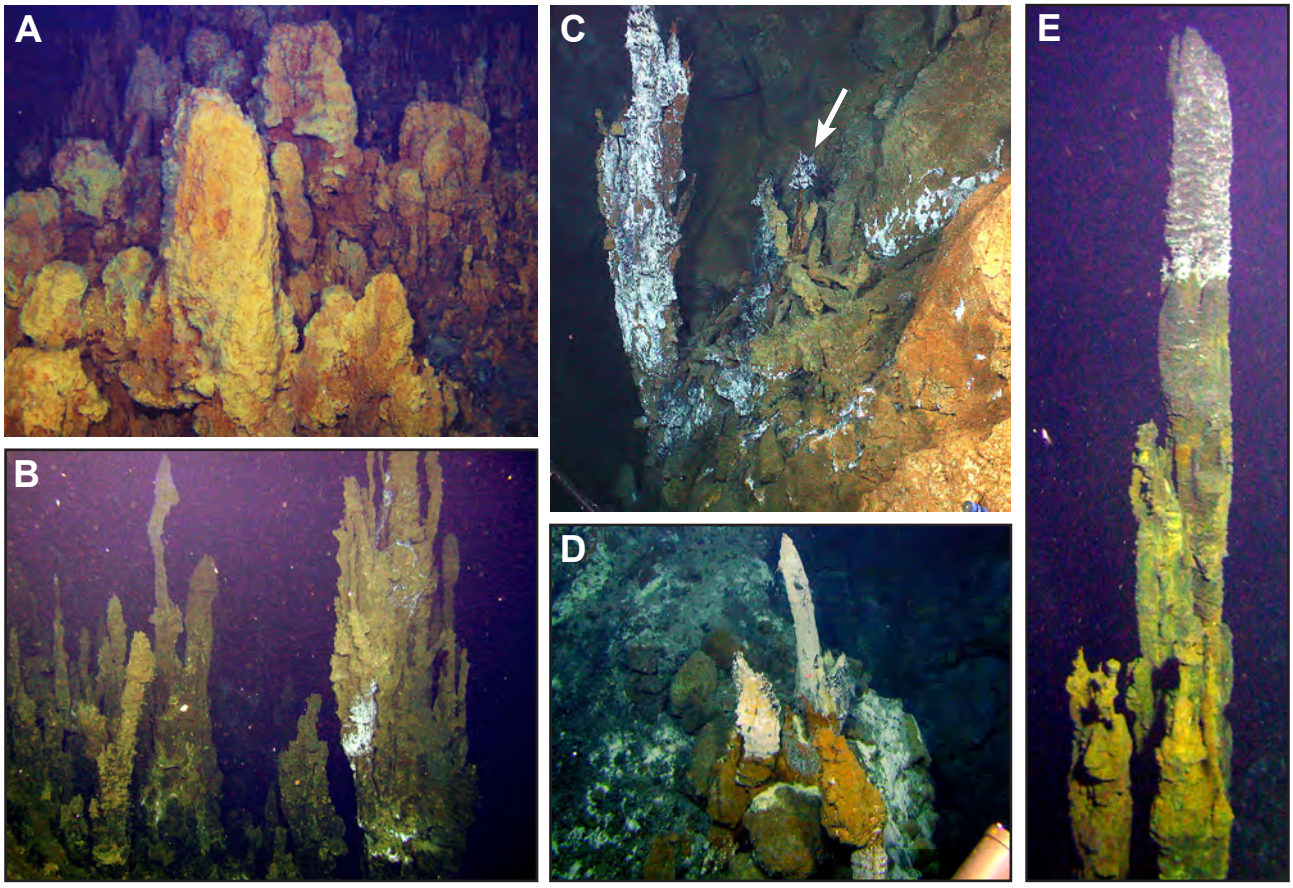

Figure 2.3 Photographs of *in situ* chimneys of the NW Caldera site. (A) A dense cluster of Fe-Si-rich chimneys up to 1 m tall. (B) Narrow, sinewy chimneys with gnarled exteriors typical of the NW Caldera vent field. Several spires have coalesced into a larger chimney super-structure on the right side (~2.5 m tall in frame). (C) A ~1 m tall chimney perched on a steep lava wall (left side). Also shown are several small, dead chimneys, piled up like fallen logs (right side) and a single short, narrow, chimney that has a small beehive growing from its top (arrow). (D) ~30 cm tall, inactive, smooth-sided chimney that has tapered to a point at the orifice (centre). To its left is a bacterial covered, gnarled chimney with another orange, Fe-oxide covered chimney in the foreground. (E) A ~4 m tall, smooth-sided chimney with a beehive growing on the top third. Several shorter, thinner, gnarled chimneys form at the base of this complex.

(~10 cm) patches to wide (meters) swaths. Iron-silica chimneys, from ~5 cm 'fingers' to ~1 m tall, occur throughout the NW Caldera site, but especially around its margins (Fig. 2.3a).

2.3.2 NW Caldera sulfide chimneys

Sulfide chimneys at the NW Caldera site tend to cluster in narrow strips (~10 m wide) that strike perpendicular to the slope. Within these strips, chimneys are typically linearly aligned parallel to the strip, with some chimneys growing on sulfide mounds also elongate parallel to the strip. Active chimneys grow immediately adjacent to the more commonly observed dead spires (de Ronde et al., 2011; Embley et al., 2012). Chimneys can perch precariously on blocky, vertical caldera walls or, more commonly, grow out of the sedimented gullies that occur between those walls (Fig. 2.3b, c; see also Fig. 4 in de Ronde et al., 2011 for more images of NW Caldera chimneys). Most chimneys form narrow, sinewy pipes, typically 2 - 3 m tall and <15 cm in diameter, with a gnarled exterior resembling dripping wax. These chimneys commonly branch and may coalesce into larger chimney super-structures up to 7 m tall and ~1 m in diameter (Fig. 2.3b; de Ronde et al., 2011). Other chimneys have a smoother exterior and are commonly capped by a beehive structure when active, or taper to a point when dead. These chimneys range from short, narrow pipes only ~2 cm across, to taller spires up to ~50 cm in diameter (Fig. 2.3c-e). Beehives are bulbous, horizontally ribbed structures composed of extremely friable material and which expel black smoke uniformly from their sides and top. Rarely, large (1 - 3 m), tapering beehives grow on short (~10 cm high), flaring, sulfide bases. Orange Fe-oxides/oxyhydroxides and white bacterial mats commonly coat the chimney exteriors.

2.3.3 Chimney samples

de Ronde et al. (2011) subdivided chimneys of the NW Caldera site into Cu-rich and Zn-rich types. Here, we retain these categories but further divide the Cu-rich chimneys into chalcopyrite-bornite and chalcopyrite-sulfate types, and the Zn-rich chimneys into sphalerite-barite and sphalerite-chalcopyrite types. These divisions are based on the relative proportions of two zones typically found in the

Table 2.2 Chimney types.

	Copper-rich		Zinc-rich	
	Chalcopyrite-Bornite	Chalcopyrite-Sulfate	Sphalerite-Chalcopyrite	Sphalerite-Barite
Chalcopyrite layer	Well defined Up to 3 cm thick cpy + py + tell + bn + cc + cv + hm + goe ± tn	Well defined Up to 3 cm thick cpy + py + tell ± cv, tn	Poorly defined Very thin cpy + py ± tell	None
Sulfate layer	Thin Anhydrite & Barite ba + anh + py/mr + sph + cv + hm + goe	Thick Anhydrite & Barite ba + anh + py/mr + sph + gn ± cpy, cv, tn, op, gd, Pb-ss	Thick Barite only ba + py/mr + sph + gn + cv + tn + op	Thick Barite only ba + py/mr + sph + gn + rg + op ± cpy, po
Weathering Rind	Present	Present	Present	Present

cpy = chalcopyrite, py = pyrite, tell = tellurides and native metals, bn = bornite, cc = chalcocite, cv = covellite, hm = hematite, goe = goethite, tn = tennantite, ba = barite, anh = anhydrite, mr = marcasite, sph = sphalerite, gn = galena, op = opal A, gd = gordaite, Pb-ss = Pb-As sulfosalts including jordanite, rg = realgar, po = pyrrhotite

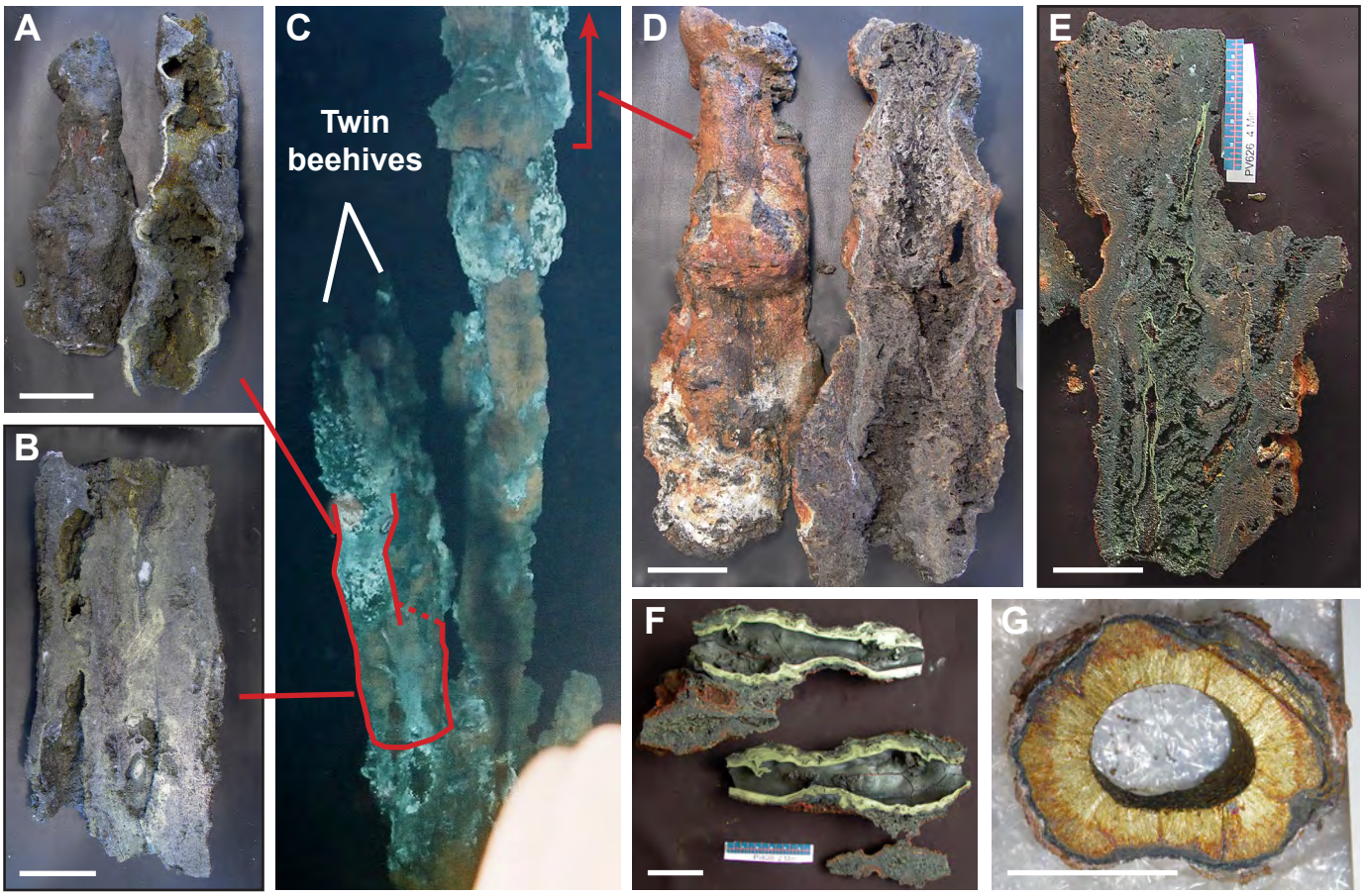

Figure 2.4 Sampled chimneys from the NW Caldera hydrothermal site. Scale bar is 4 cm in all pictures. (A) Chalcopyrite-lined chimney 852-1-a, which is one of the shorter, twin spires shown in C and part of the top of B. (B) Chalcopyrite-sulfate chimney 852-2B with massive chalcopyrite intergrown with other sulfides and sulfates in the interior. This is the base to the sample shown in A and the left spire of the chimney structure shown in C. (C) Still image captured from a dive video of the middle portion of chimney structure 852-2 from which four of the samples used in this study were collected. The larger spire is ~1.5 m tall and continues upwards for ~0.5 m beyond the frame. The structure is also supported by a ~1.5m tall base. (D) Sphalerite-barite chimney 852-2A with porous interior, taken from around the top of the chimney structure shown in C. (E) Sphalerite-chalcopyrite chimney PV-626-4min-a with thin, yellow chalcopyrite lining parts of the interior porous conduit network. This chimney is the basis for the chimney model in Figure 2.9c. (F) Chalcopyrite-bornite chimney PV-628-2min, with massive, yellow chalcopyrite lining the main orifice. This sample was collected from the top of a dead spire. (G) Cross-section of chalcopyrite-bornite chimney 851-1A showing a thick chalcopyrite-lined conduit surrounded by a thin, dark, sulfate-dominated layer. For location, depth, fluid temperatures and ages of these chimney samples, see Table 2.1.

chimneys: an inner chalcopyrite-dominated zone and a sulfate-dominated zone (Table 2.2; Fig. 2.4).

Copper-rich chimneys always contain an inner chalcopyrite zone up to ~3 cm thick that surrounds a smooth, well-defined orifice. This zone is in turn surrounded by a sulfate-dominated zone that is relatively thin (<5 mm) in the chalcopyrite-bornite chimneys, and thicker (cm's) in chalcopyrite-sulfate chimneys (see also Figs. 6 and 7 in de Ronde et al., 2011). Zinc-rich chimneys are always <10 cm in diameter and their interiors ranging from close-packed 'boxwork' textures to those with more distinct conduits. The latter may contain several narrow (<1 cm), anastomosing channels, or a single, wider conduit (Fig. 2.4d). The sphalerite-chalcopyrite subset of Zn-

rich chimneys has thin, friable chalcopyrite lining the porous interior (Fig. 2.4e). These descriptions of the macroscopic features of Cu- and Zn-rich chimneys are consistent with the findings of de Ronde et al. (2011). Many of the Zn-rich chimneys appeared to be inactive upon sampling by submersible, although the diffuse flow emitted from the top of these chimneys could be difficult to detect when viewed from the submersible porthole and/or on the video. For example, chimney PV-626-4min was dated at only 1.62 years old, suggesting it was likely active (Table 2.1). Small diameter chimneys with gnarled exteriors can either be Cu-rich or Zn-rich chimneys, whereas all smooth-sided chimneys collected to date are invariably of the Cu-rich type.

2.4 Mineralogy

Reflected and transmitted light microscopy was used to study forty polished thin sections, several of which were used in previous studies by de Ronde et al. (2005; 2011). Five thin sections were from the central axis of chimney SO-135-57DR-1 (C, E, H, J, K) whose locations within the chimney are given in de Ronde et al. (2005). Similarly, eleven sections came from *Lena* chimney (851-3A) including six from the laminated chalcopyrite conduit. Eight new thin sections were made from chimney samples collected in 2005. Mineral modal percentages were semi-quantitatively estimated, guided by the visual percentage estimation diagrams of M.S. Shvetsov (Terry and Chilingar, 1955). We used an FEI Quanta 600 scanning electron microscope (SEM) fitted with an EDAX Sapphire SUTW Si(Li) energy dispersive spectrometer for backscattered electron imaging and standardless determination of mineral composition to aid with mineral identification and paragenesis. Quantitative mineral analyses were acquired on a Cameca SX100 electron microprobe equipped with wavelength dispersive spectrometers using the Probe For EPMA software package (Probe Software, Inc.) at the University of Tasmania.

2.4.1 Copper-rich chimneys

All Cu-rich chimneys (>5 modal % chalcopyrite, to a maximum of 75.5%, and <5% sphalerite) have a distinct mineral zonation, grading from an interior chalcopyrite-dominated zone, through a zone of disseminated sulfides within a sulfate matrix, and finally to a Fe-oxide/oxyhydroxide and amorphous silicate-dominated exterior (Fig. 2.5a). The chalcopyrite core is commonly laminated, comprising alternating disseminated and massive layers (Fig. 2.5b) that contain minor tellurides (see below). Euhedral to subhedral pyrite grains are scattered throughout the chalcopyrite zone, with subhedral grains increasing in abundance towards the chimney exterior. Near the outer chalcopyrite zone margin, Fe-sulfide can be pyrite, marcasite, or both, and becomes less euhedral, commonly delineating earlier grain boundaries (Fig. 2.5c). Barite and/or anhydrite can be intergrown with chalcopyrite in chimney interiors, although they more typically form outside the chalcopyrite zone, where they comprise the bulk of the sulfate zone. Platy anhydrite up to 5.5 mm long occurs in every Cu-rich chimney with the exception of the dead chimney PV628-2min, and the dredged fragment X573/E. Barite occurs in every chimney, typically forming rosettes. Within the sulfate zone, disseminated chalcopyrite decreases in abundance towards the chimney exterior as both the pyrite/marcasite and sphalerite content increase. The Cu-rich chimneys are subdivided, based on the thickness of the sulfate zone and presence of Cu-sulfides

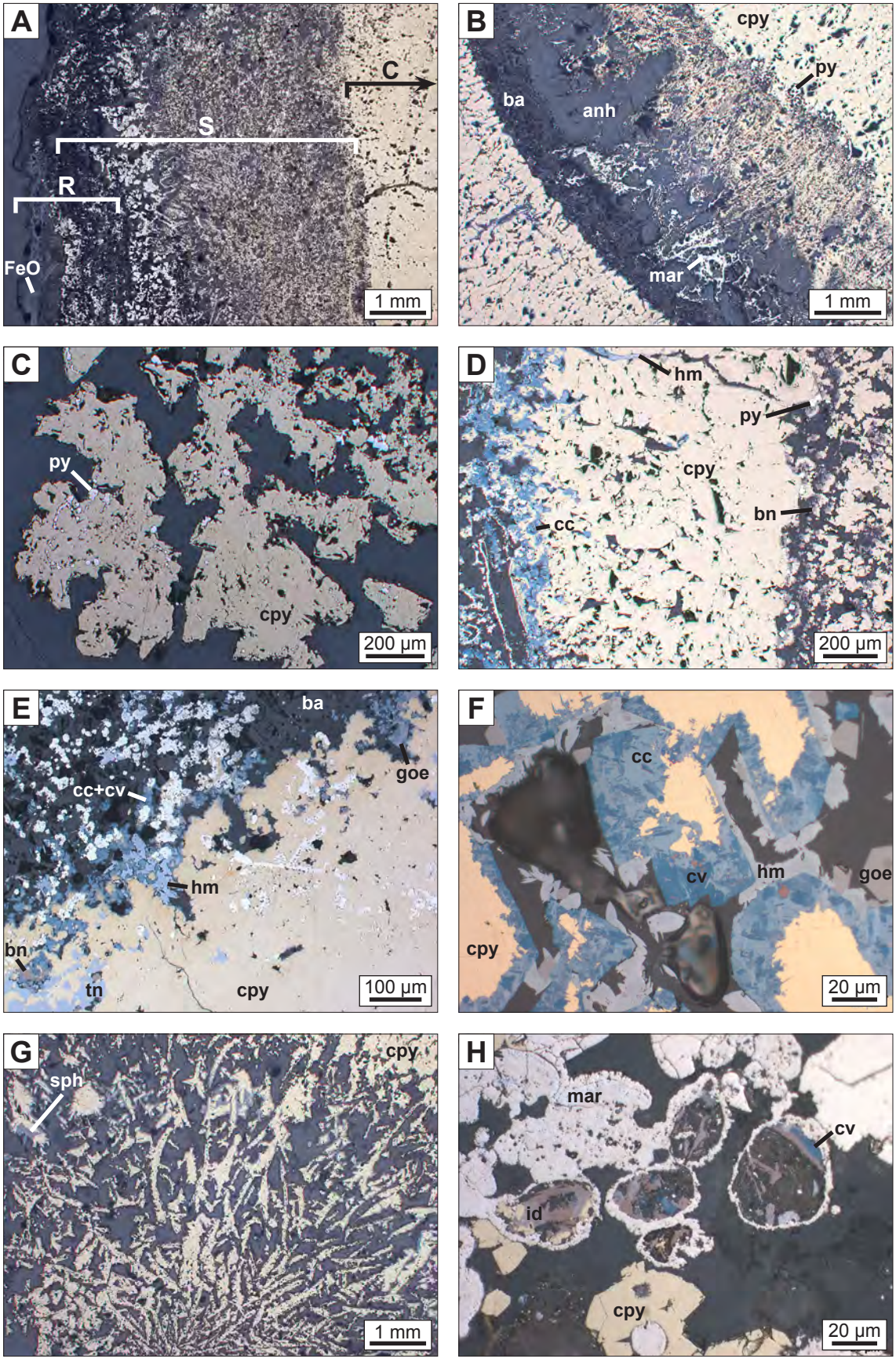
A
C
S
R
FeO
1 mm
B
cpy
py
ba
anh
mar
1 mm
C
py
cpy
200 µm
D
hm
py
cpy
bn
cc
200 µm
E
ba
goe
cc+cv
hm
bn
tn
cpy
100 µm
F
cc
cv
hm
goe
cpy
20 µm
G
cpy
sph
1 mm
H
mar
cv
id
cpy
20 µm

Figure 2.5 (previous page) Photomicrographs, taken in reflected light, of the chalcopyrite layer and Cu-rich mineral phases. (A) Photomicrograph showing the three chimney zones: outer rind [R], sulfates and disseminated sulfides [S] and massive chalcopyrite [C]. Blackish material in the outer rind is amorphous silicates and carbonates; the grey material is amorphous Fe-oxides/oxyhydroxides (FeO). The white mineral is pyrite/marcasite that outlines some sulfate grain boundaries. Sample 851-1B. (B) Two bands of massive chalcopyrite separated by a band of barite (ba), platy anhydrite (anh), disseminated marcasite (mar) and chalcopyrite (cpy) that is faintly altered to brown bornite on the edges. Fe-sulfides towards the right side are pyrite (py). The left side (external) chalcopyrite band is altered to blue chalcocite along cracks. Sample 851-1A. (C) Edge of massive chalcopyrite layer with subhedral pyrite outlining previous grain boundaries. Sample 851-3A. (D) Outer margin of the chalcopyrite core in a chalcopyrite-bornite chimney showing zonation of Cu-sulfides; the exterior of the chimney is to the left. Chalcopyrite alters to brown bornite (bn) in the disseminated band on the right accompanied by euhedral pyrite. Chalcopyrite alters to blue chalcocite (cc) at the transition with the sulfate layer. Light grey hematite (hm) is also present in a crack. Sample 851-1A. (E) Chalcopyrite-bornite chimney showing bornite, chalcocite, covellite (cv), hematite, goethite (goe) and tennantite (tn) in the same zone at the boundary between massive chalcopyrite and the sulfate layer, here dominated by barite. Covellite is difficult to distinguish from chalcocite at this scale (see F). Cu-sulfides replace chalcopyrite and Fe-sulfides, while the Fe-oxides form along chalcopyrite margins and in the disseminated sulfide zone. Sample 628-2min. (F) Close up of chalcopyrite altering to medium-blue chalcocite that in turn is altered to pleochroic indigo to reddish covellite. Euhedral, light grey laths of hematite and darker, euhedral grains of goethite line the inside of void spaces. Sample 851-1A. (G) Interior of massive chalcopyrite 'ring' filled by later, elongate chalcopyrite, probably pseudomorphing barite. Sphalerite mantles the chalcopyrite at a distance from the center. This sample protruded off the side of an active chimney and likely stopped growing after being clogged with chalcopyrite. Late sphalerite (plus galena and realgar, not visible at this scale) precipitated as temperatures dropped when fluid flow was redirected. Sample 851-1B. (H) Pleochroic pinkish grey idaite (id) and indigo covellite laths preserved in marcasite 'rings', with incipient replacement by chalcopyrite in the ring on the left side. Sample 626-4min.

other than chalcopyrite, into chalcopyrite-bornite and chalcopyrite-sulfate types (Table 2.2).

2.4.1.1 Chalcopyrite-bornite chimneys

Chalcopyrite-bornite chimneys display a radially zoned mineral assemblage of bornite, hematite, chalcocite, goethite, and covellite that begins midway through the chalcopyrite core and continues through the sulfate zone (Table 2.3). Bornite and hematite form closest to the interior of the chimney, where bornite replaces chalcopyrite along cracks. Bladed hematite grows up to 250 μm long in several of the same cracks and, more rarely, can be seen in cracks where bornite is absent (Fig. 2.5d). Very rarely, chalcopyrite is seen to mantle bornite. Further outwards, chalcocite is seen both intergrown with bornite and replacing chalcopyrite along cracks, whereas euhedral goethite and hematite partially fill the center of these cracks. The entire mineral assemblage is present at the boundary of the massive chalcopyrite zone with the sulfate zone; here, covellite replaces chalcocite and bornite along grain boundaries (Fig. 2.5e, f). The outer sulfate zone (see section on Zn-rich chimneys below) in chalcopyrite-bornite chimneys is relatively thin (<5 mm). Within this zone, bornite is rare, chalcocite decreases in abundance toward the chimney exterior, and euhedral hematite and goethite, together with covellite, occur through to the chimney rind. The mineral assemblage of dead chimney PV628-2min also includes tennantite replacing chalcopyrite along both the innermost, and especially the outermost, margins of the chalcopyrite core (Fig. 2.5e). The *Leg of Lamb* chimney (851-1B) differs from the other two chalcopyrite-bornite chimneys by having elongate

Table 2.3 Mineral abundances.

			Copper-rich							Zinc-rich						
			Chalcopyrite-bornite			Chalcopyrite-sulfate				Sphalerite-cpy		Sphalerite-barite				
			851-1A	851-1B	628-2M	X573/E	851-3A	851-3	852-2B	626-4M	632-11R	57DR-1	851-2B	852-1A	852-2A	631-9R
Sulfides	Chalcopyrite	$CuFeS_2$	D	D	D	A	A	A	A	C	C	T	M		T	M
	Sphalerite	ZnS	T	M	T	T	M	M	T	C	C	C	A	A	C	C
	Pyrite	FeS_2	M	C	M	C	C	C	M	C	M	C	C	M	M	
	Marcasite	FeS_2	M	M	C		M	C	C	C	A	T	C	C	C	M
	Galena	PbS		T		T	T	T	T	M	T	M	M	M	T	T
	Covellite	CuS	M	T	T		T	T	T	T	T		T			T
	Chalcocite	Cu_2S	M	T	T				T							
	Bornite	Cu_5FeS_4	M	T	T											
	Idaite	Cu_5FeS_6			T				T	T						T
	Tennantite	$(Cu,Ag,Fe,Zn)_{12}As_4S_{13}$			M		T	T	T	T	T		T			T
	Enargite	Cu_3AsS_4			T											
	Realgar	As_4S_4		T							T		T	T	M	T
	Orpiment	As_2S_3								T			T			
	Jordanite	$Pb_{14}(As,Sb)_6S_2$					T	T		T						
	Pb-As sulfosalts						T	T								
	Pyrrhotite	$Fe_{(1-x)}S$						T						M		
Tellurides &	Native tellurium	Te							T							
Native metals*	Native bismuth	Bi			T		T									
	Tellurides			T	T		T	T		T						
Oxides	Hematite	Fe_2O_3	M	T	T		T									
	Goethite	FeO(OH)	T	T	T		T									
	Ilmenite	$FeTiO_3$												T		T
	Rutile	TiO_2					T									

T Trace (0- 1%), M Minor (1- 5%), C Common (5- 25%), A Abundant (25-50%), D Dominant (+50%).

Table 2.3 continued.

			851-1A	851-1B	628-2M	X573/E	851-3A	851-3	852-2B	626-4M	632-11R	57DR-1	851-2B	852-1A	852-2A	631-9R
Sulfates	Barite	$BaSO_4$	M	C	A	D	A	A	C	A	A	C	D	D	D	D
	Anhydrite	$CaSO_4$	C	M			A	C	A							
	Gordaite	$Zn_4Na(OH)_6(SO_4)Cl{\bullet}6H_2O$					T	T	T	T						
Other	Opal A	$SiO_2{\bullet}nH_2O$		T	M		T	T		C	C	A	T	M	T	C
Outer rind*	Calcite/Dolomite	$CaCO_3$	M	T	M			T						T		
	Fe oxides/oxyhydroxides			T	M			T		T			M	M		M
	Amorphous silicates			T						M			T		T	

T Trace (0- 1%), M Minor (1- 5%), C Common (5- 25%), A Abundant (25-50%), D Dominant (+50%). * See Table 2.4 and Figure 2.8 for telluride compositions. Tellurides are likely present in all Cu-rich chimneys, though have only been detected in those examined by SEM. Likewise, not all thin sections included the outer rind, although it is present in all chimneys.

chalcopyrite partially filling the central conduit. Sphalerite and galena mantle the chalcopyrite and grains of euhedral realgar form in pore space (Fig. 2.5g). Chalcopyrite-bornite chimneys PV628-2min and 851-1B do not have the same Cu-sulfide and Fe-oxide mineral assemblage at their base as they do at their tops; the base has a thicker sulfate zone as seen in chalcopyrite-sulfate chimneys (Table 2.2). PV628-2min does, however, contain trace amounts of idaite (Fig. 2.5h) and enargite at its base.

Paragenetic relationships in chalcopyrite-bornite chimneys indicate that sulfates formed first, followed by pyrite/marcasite then trace amounts of early bornite and tellurides (Fig. 2.6). All of these phases are overprinted by massive chalcopyrite in the interior of the chimney. Concurrently, the majority of tellurides and lesser amounts of Fe-sulfides occur as inclusions in several laminated chalcopyrite layers suggesting multiple episodes of deposition. The bornite-hematite-chalcocite-goethite-covellite ± tennantite assemblage occurs late, followed by sphalerite near the outer chimney margins. Amorphous silicates, Fe-oxides/oxyhydroxides, and carbonates mantle all the other phases in the outer rind.

2.4.1.2 Tellurides

Tellurides occur near the margins of, and as inclusions within, the chalcopyrite zone. The vast majority of tellurides are <5 μm in size, although rare prismatic crystals up to 50 μm long and columnar crystals up to 80 μm long are seen. They commonly form in bands, cluster in patches, or occur along internal grain boundaries within chalcopyrite, and also form at the contact between chalcopyrite and pyrite (Fig. 2.7). Tellurides are scattered throughout

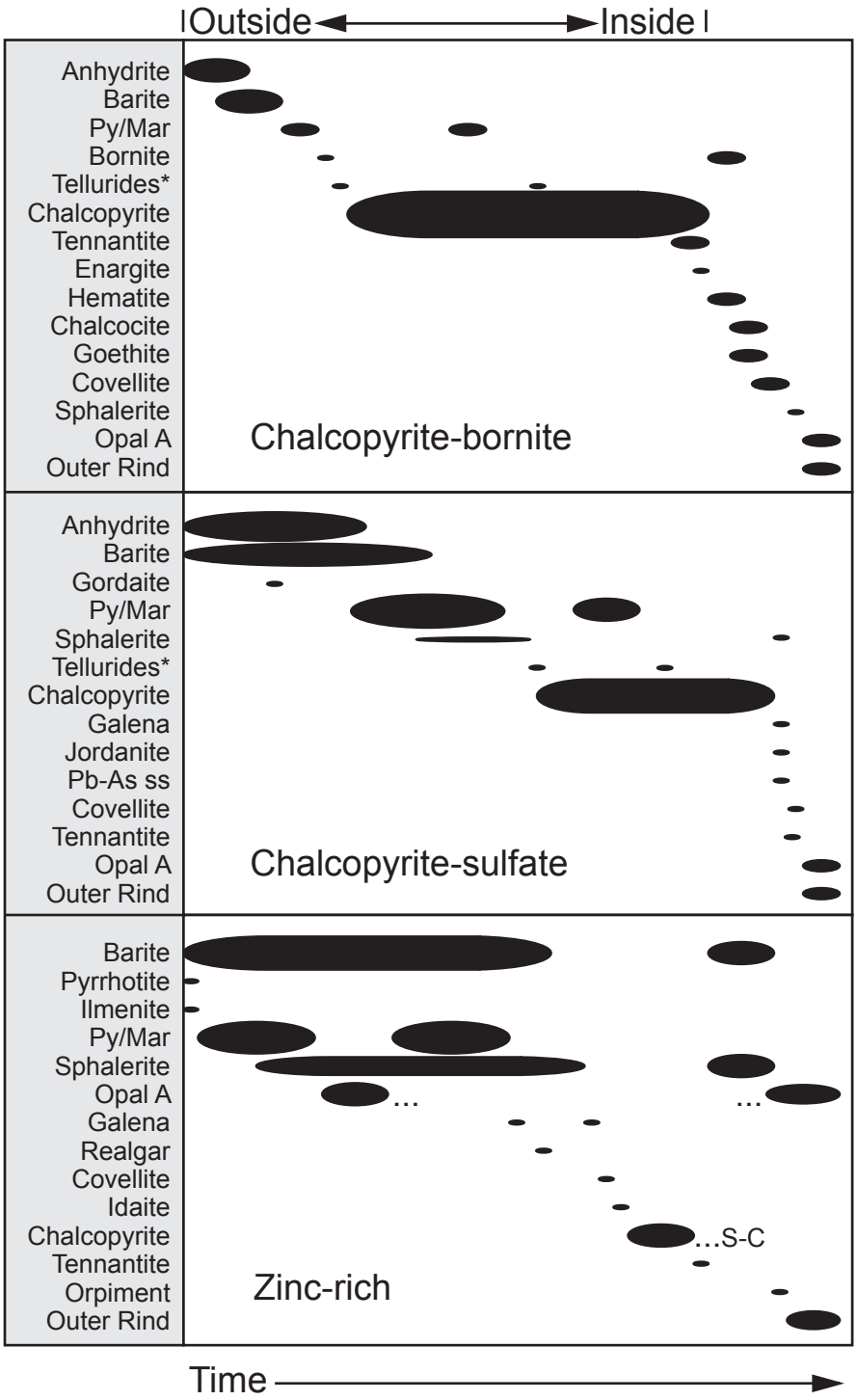

Figure 2.6 Paragenetic tables of the different chimney types as discussed in the text. The area contained by each oval approximates the modal % of the particular mineral phase. Sphalerite-barite and sphalerite-chalcopyrite chimneys are combined in the Zn-rich table. The amount of opal-A can vary significantly between the Zn-rich chimneys, thus in some cases the opal-A ovals would extend further than shown in the figure. The first Cu-sulfides in Zn-rich chimneys are usually covellite and idaite blades in biogenic pyrite/marcasite rings, which can later be replaced by chalcopyrite. The amount of chalcopyrite increases significantly in sphalerite-chalcopyrite chimneys [S-C] and therefore would alter the extent of the oval shown. *, Tellurides includes native Te and Bi; "Outer rind" phases include calcite, Fe-oxides/oxyhydroxides and amorphous silicates; ss, sulfosalts.

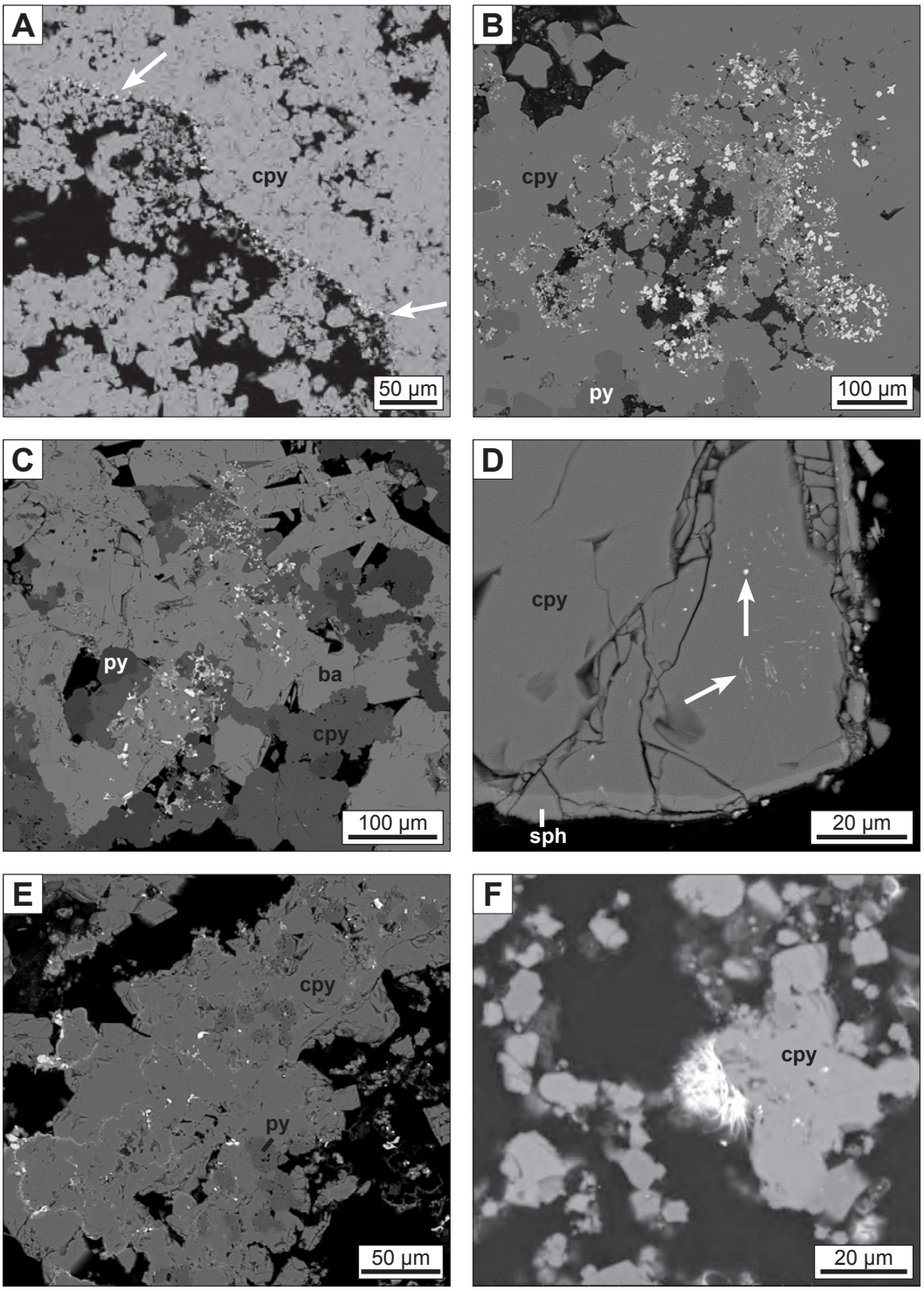

Figure 2.7 SEM backscatter images of tellurides. (A) Aligned trail of very small (<5 µm) Bi- and Au-tellurides at contact between massive and disseminated chalcopyrite layers (arrows). Sample 851-3B-c. (B) Dendritic Bi-Se-tellurides in chalcopyrite and along contact between chalcopyrite and darker pyrite. Sample PV-628-2min. (C) Bi-Se-tellurides (bright flecks) embedded in light grey barite laths and medium grey chalcopyrite, at the contact between the massive chalcopyrite and sulfate layers in a chalcopyrite-bornite chimney. As for image B, the tellurides are located outside of darker pyrite. Sample PV-628-2min. (D) Faint trails of Ag-tellurides (arrows) in massive chalcopyrite, lining a cavity. A thin layer of lighter sphalerite (sph) mantles the chalcopyrite. Sample PV-626-4min-c. (E) Native Te (bright flecks) found along chalcopyrite internal grain boundaries and at the contact between chalcopyrite and darker pyrite. 852-1-a. (F) Wispy, radiating native Bi (center), forming in void space on the margin of a chalcopyrite grain. Sample 851-3A.

both massive and disseminated types of chalcopyrite laminations. More rarely, in the portion of the sulfate zone immediately adjacent to the chalcopyrite core they also occur as inclusions in anhydrite, barite, and pyrite, or can occupy pore space. Chimney 852-2B contains native Te that has a similar distribution to the tellurides within the chalcopyrite layer. Native Bi occurs in two chimneys in a distinctive wispy, radiating form within pore space (Fig. 2.7f). The small size of the tellurides means that they are optically indistinguishable from pyrite. However, their presence was verified in every Cu-rich chimney that was examined using the SEM, and tellurides are likely to be present in all the Cu-rich chimneys.

The compositions of the largest tellurides (i.e., >5 x 5 μm) in several sections were measured by electron microprobe, and clearly divide into Bi-telluride and Au-telluride types (Fig. 2.8; Table 2.4). Two chalcopyrite-bornite chimneys (628-2min and 851-1B) have

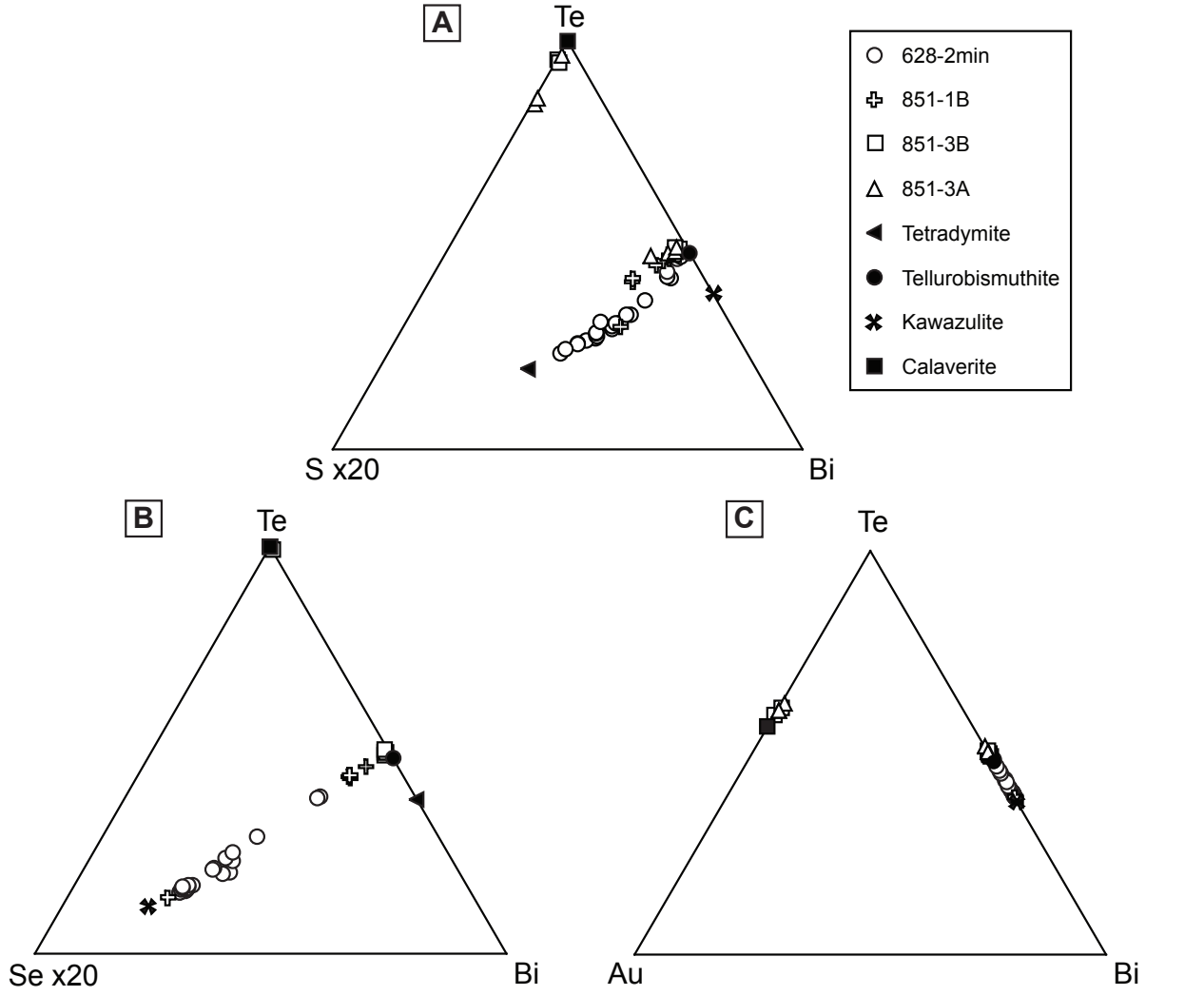

Figure 2.8 Ternary diagrams of telluride compositions reported in Table 2.4. The ideal formulas for tetradymite (Bi_2Te_2S), tellurobismuthite (Bi_2Te_3), kawazulite (Bi_2Te_2Se), and calaverite ($AuTe_2$) are also plotted. Samples 851-3A and 851-3B (chalcopyrite-sulfate chimneys) have bimodal distribution of calaverite and tellurobismuthite, while samples 628-2min and 851-1B (chalcopyrite-bornite chimneys) plot on mixing lines between tellurobismuthite and tetradymite or kawazulite. (A) A Te-Bi-S diagram with Au-tellurides plotting near the Te point and Bi-tellurides plotting along a mixing line. The spread in S content of the Au-tellurides is likely from contamination by surrounding phases that would affect the Bi-tellurides as well. (B) A Te-Bi-Se diagram with Au-tellurides again plotting at the Te point and Bi-tellurides along a mixing line. Selenium was not measured in tellurides from Lena chimney (851-3A). (C) A Te-Bi-Au diagram also clearly distinguishes Au-tellurides from Bi-tellurides, with only 12% of tellurides containing significant amounts of Au.

Table 2.4 Electron microprobe compositions of Bi and Au tellurides.

		wt %								
SAMPLE	Host phase	Te	Bi	S	Fe	Cu	Se	Au	Ag	TOTAL
628-2min-2 T23	chalcopyrite	34.0	55.5	1.76	1.19	1.79	7.03	-	-	101.27
628-2min-2 T9	barite	34.2	54.3	1.69	0.13	0.24	7.37	-	-	97.93
628-2min-2 T10	barite	34.2	54.6	1.94	0.14	0.23	6.88	-	-	97.99
628-2min-2 T5	chalcopyrite	34.5	55.4	1.73	0.66	1.16	6.90	-	-	100.35
628-2min-2 T32	chalcopyrite	34.6	54.6	2.15	0.88	0.78	6.76	-	-	99.77
628-2min-2 T29	chalcopyrite	34.8	55.1	2.17	1.10	1.00	7.00	-	-	101.17
628-2min-2 T28	chalcopyrite	34.9	55.4	1.40	0.71	1.18	7.47	-	-	101.06
628-2min-2 T14	chalcopyrite	35.0	57.5	2.74	0.29	0.41	4.45	-	-	100.39
628-2min-2 T16	chalcopyrite	35.1	55.7	2.52	0.57	1.08	4.70	-	-	99.67
628-2min-2 T22	chalcopyrite	35.4	54.3	1.71	1.15	1.58	6.36	-	-	100.50
628-2min-2 T7	chalcopyrite	35.5	54.6	1.23	1.10	1.55	7.28	-	-	101.26
628-2min-2 T26	chalcopyrite	35.8	54.8	1.71	1.33	1.83	6.71	-	-	102.18
628-2min-2 T30	chalcopyrite	35.8	55.0	1.40	0.92	1.52	6.90	-	-	101.54
628-2min-2 T4	chalcopyrite	36.1	54.6	1.31	0.87	1.53	6.72	-	-	101.13
628-2min-2 T8	barite	36.3	54.0	1.02	0.20	0.26	7.11	-	-	98.89
628-2min-2 T2	chalcopyrite	36.6	53.2	1.07	0.55	0.73	7.01	-	-	99.16
628-2min-2 T19	chalcopyrite	38.9	52.6	1.00	1.07	1.79	5.00	-	-	100.36
628-2min-2 T11	chalcopyrite	39.0	54.0	0.75	0.55	1.01	5.17	-	-	100.48
628-2min-2 T15	chalcopyrite	39.1	54.4	1.58	0.71	1.05	4.21	-	-	101.05
628-2min-2 T13	chalcopyrite	41.5	53.0	0.33	0.60	0.98	4.45	-	-	100.86
628-2min-2 T6	chalcopyrite	41.8	51.7	0.35	1.13	1.66	4.01	-	-	100.65
628-2min-2 T18	chalcopyrite	43.1	51.0	0.32	1.34	2.03	3.02	-	-	100.81
628-2min-2 T17	chalcopyrite	45.2	50.5	0.15	1.23	1.93	1.25	-	-	100.26
628-2min-2 T12	chalcopyrite	45.3	50.5	0.11	0.81	1.27	1.31	-	-	99.30
851-1B-al T12	chalcopyrite	32.8	53.1	1.19	1.56	2.27	8.13	-	-	99.05
851-1B-al T5	chalcopyrite	44.9	49.3	0.79	2.50	3.28	0.63	-	0.06	101.46
851-1B-al T4	vug*	46.1	49.8	0.23	1.20	3.32	0.64	-	0.06	101.35
851-1B-al T8	chalcopyrite	46.1	49.2	0.77	2.29	3.47	0.35	-	-	102.18
851-1B-al T14	vug	46.1	49.7	0.40	0.76	2.84	0.62	-	-	100.42
851-1B-al T15	chalcopyrite	46.3	49.7	0.30	1.47	2.24	0.63	-	0.07	100.71
851-3B-c T1	chalcopyrite	45.8	49.0	0.16	1.72	2.23	0.07	-	-	98.98
851-3B-c T3	chalcopyrite	47.4	49.6	0.14	1.40	2.03	0.06	-	-	100.63
851-3B-c T2	vug*	47.8	50.5	0.08	0.96	1.37	0.05	-	-	100.76
851-3B-c T6a	vug*	47.9	48.9	0.11	0.71	0.91	0.04	-	-	98.57
851-3B-c T5	chalcopyrite	56.8	-	0.12	1.61	2.34	-	40.4	0.47	101.74
851-3B-c T6b	vug*	58.1	0.51	0.12	0.70	1.19	-	37.7	1.87	100.19
851-3A-12 T13	chalcopyrite	47.8	49.7	0.14	0.73	1.06	\	-	-	99.43

Table 2.4 continued.

		wt %								
SAMPLE	Host phase	Te	Bi	S	Fe	Cu	Se	Au	Ag	TOTAL
851-3A-12 T16	anhydrite	48.2	46.5	0.40	0.74	0.58	\	-	-	96.42
851-3A-12 T12	anhydrite	48.6	49.9	0.09	0.46	0.07	\	-	-	99.12
851-3A-12 T11	anhydrite	58.3	0.28	0.08	0.08	0.54	\	39.5	0.74	99.52
851-3A-12 T8	anhydrite*	59.1	0.63	0.46	0.51	2.19	\	36.3	1.38	100.57
851-3A-5 T8	chalcopyrite	56.4	0.43	0.40	1.36	2.78	\	37.8	0.35	99.52
detection limit at 99% confidence		0.07	0.23	0.01	0.02	0.03	0.03	0.13	0.05-0.08	100.22

- below detection limit, \ not measured, * near chalcopyrite. Elements were acquired using analyzing crystals LLIF for Bi Lα, Au Lα, Fe Kα, and Cu Kα, PET for Ag Lα and Te Lα, LPET for S Kα, and TAP for Se Lα. The calibration standards were cuprite for Cu, marcasite for S and Fe, bismuth selenide for Bi and Se, Au metal for Au, Ag metal for Ag, and Te metal for Te. The counting time on peak and background was 20 seconds for Fe, Cu, and Te, 30 seconds for S, Bi, and Au, 40 seconds for Ag, and 60 seconds for Se. The matrix correction was performed using the PAP algorithm and the FFAST set of mass absorption coefficients. The focused beam had an accelerating voltage of 20 keV and a 20 nA beam current.

[1] High totals are assumed to be caused predominantly by contributions of the individual host mineral to the analysis, indicating that concentrations for elements such as Cu, Fe, and S, in the case of chalcopyrite, are lower in the telluride phase than listed.

Bi-tellurides only, whose compositions plot along mixing lines between tellurobismuthite (Bi_2Te_3) and tetradymite (Bi_2Te_2S) or kawazulite (Bi_2Te_2Se; Fig. 2.8). By contrast, *Lena* chimney (851-3A) and fragment 851-3B (both chalcopyrite-sulfate samples from the same chimney structure) contained both Au- and Bi-tellurides, consistent with the composition of calaverite ($AuTe_2$) and tellurobismuthite, respectively.

2.4.1.3 Chalcopyrite-sulfate chimneys

Chalcopyrite-sulfate chimneys typically have one or more well-defined central orifices and smaller, interior vugs lined with a zone of laminated or massive chalcopyrite, similar to that seen in chalcopyrite-bornite chimneys (Fig. 2.4b). The chalcopyrite zone transitions to disseminated sulfides within a relatively thick sulfate zone (Table 2.2; Fig. 2.9a; see section on Zn-rich chimneys below). Anhydrite in *Lena* chimney (Fig. 2.9b) ranges from nearly 90 modal percent near the chimney exterior to 2 modal percent in the center. Similarly, anhydrite ranges from 50 modal percent at the base of the main laminated chalcopyrite conduit to 15 modal percent near the top.

Another sulfate occurred in trace amounts in some chimneys forming acicular, highly striated crystals (Fig. 2.9c). This crystal habit made accurate compositional measurements of this phase difficult, further complicated by rapid destruction of the phase under the electron microprobe beam. However, the composition indicated an unnamed Zn-sulfate chloride hydrate, $Zn_{12}(OH)_{15}(SO_4)_3Cl_{3.5}H_2O$, a phase also found by Brett et al. (1987) in chimneys from the southern Juan de Fuca ridge. However, further studies by Nasdala et al. (1998) determined the mineral described by Brett et al. (1987) was actually gordaite. Thus, we suspect that is the likely mineral found in this study (Table 2.3).

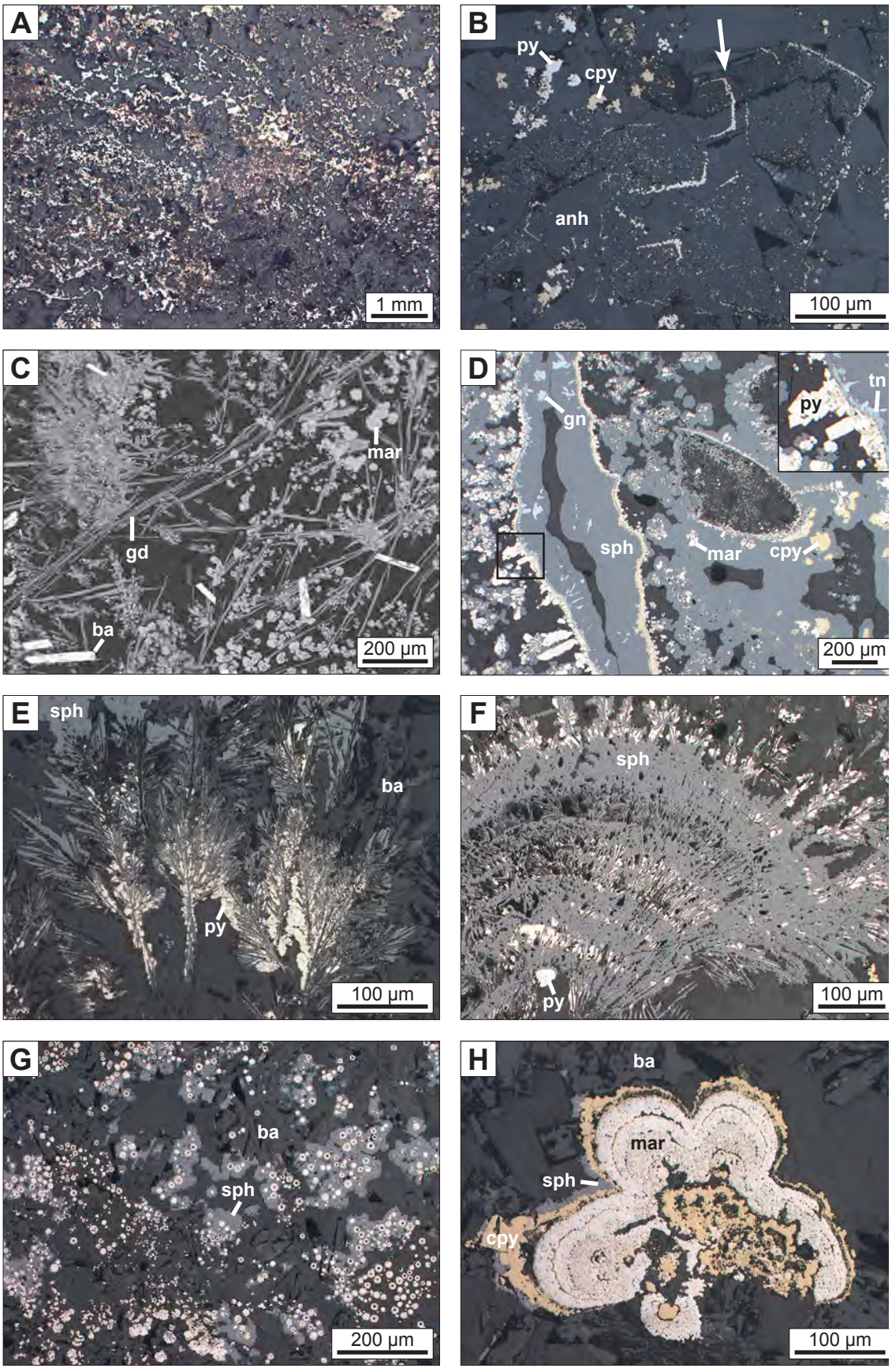
A
1 mm
B
py
cpy
anh
100 µm
C
mar
gd
ba
200 µm
D
gn
py
tn
sph
mar
cpy
200 µm
E
sph
ba
py
100 µm
F
sph
py
100 µm
G
ba
sph
200 µm
H
ba
mar
sph
cpy
100 µm

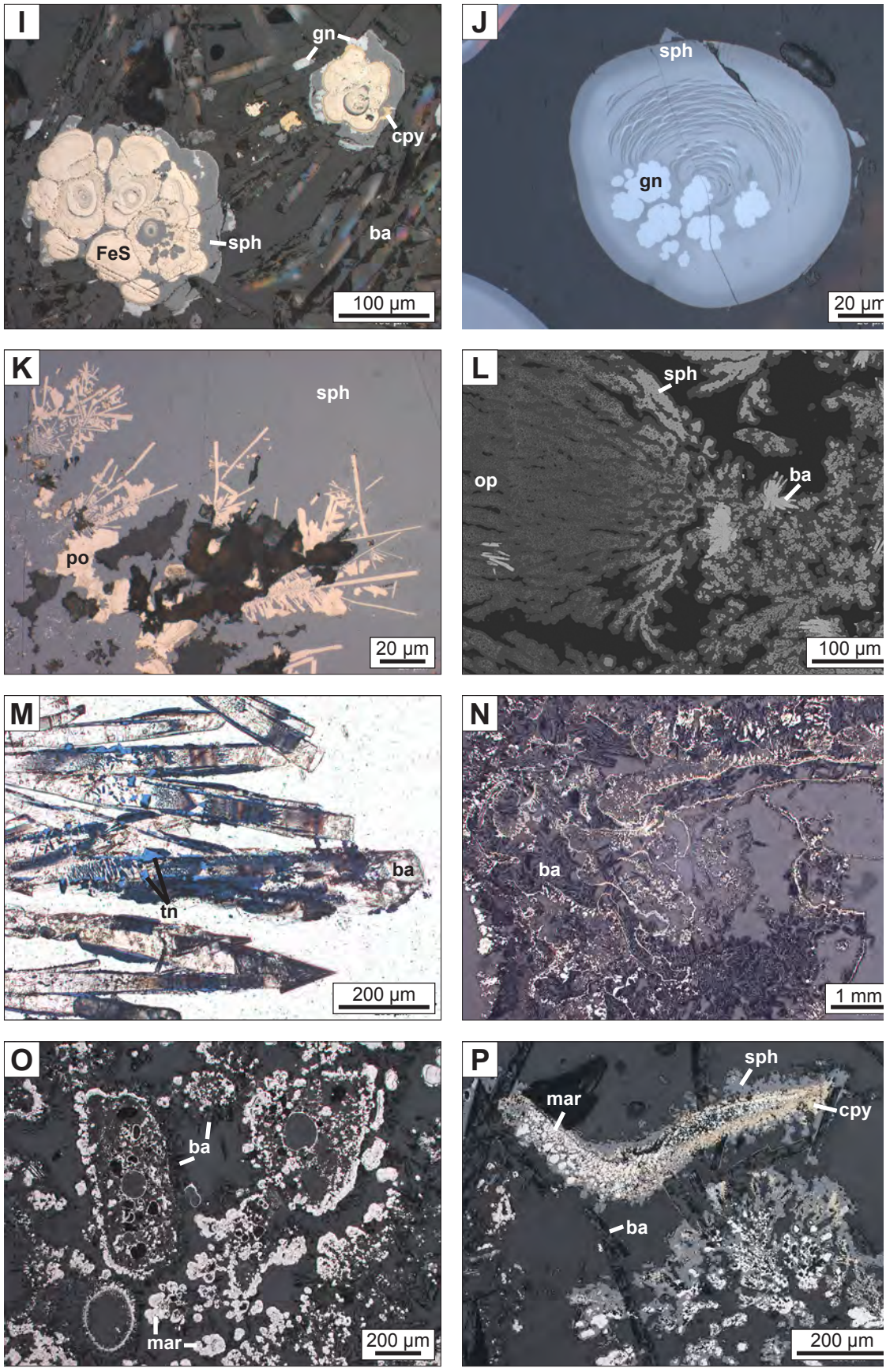
I
gn
cpy
FeS
sph
ba
100 µm
J
sph
gn
20 µm
K
sph
po
20 µm
L
sph
op
ba
100 µm
M
ba
tn
200 µm
N
ba
1 mm
O
ba
mar
200 µm
P
sph
mar
cpy
ba
200 µm

Figure 2.9 (previous pages) Photomicrographs and SEM backscatter images from the sulfate and disseminated sulfide layer of both Cu-rich and Zn-rich chimneys. All photomicrographs taken in reflected light except for O which was taken in transmitted light. (A) Textures typical of the disseminated sulfide zone from a Cu-rich chimney. The high proportion of yellow chalcopyrite to white pyrite/marcasite indicates this region is relatively close to the massive chalcopyrite zone. Anhydrite forms the groundmass (grey). Sample 851-3. (B) Platy anhydrite forming a substrate for disseminated chalcopyrite and pyrite. Small pyrite spheres (arrow) outline previous anhydrite grain boundaries that do not align with the visible boundaries. Sample 851-3A. (C) Backscatter image of gordaite (gd) forming a substrate for disseminated sulfides (greys) of mainly marcasite. Barite laths (bright, i.e. bottom left corner) are scattered throughout the image. Sample 851-3. (D) Ovoid, probable bacterial form and elongate tube replaced by sulfides (cf. figures of biogenic structures in Jones et al., 2008). Euhedral pyrite (recrystallized marcasite) and chalcopyrite grow outwards and light grey tennantite and bright bluish galena (gn) grow inward from the tube wall (see inset); black box shows location of inset. This sphalerite-barite chimney has thick layers of sphalerite (sph) mantling other phases. Sample 851-2B. (E) Plumose barite mantled by intergrown pyrite and sphalerite in a commonly seen texture, particularly near the chimney exterior, and is interpreted to signify rapid precipitation. Sample 851-1B. (F) Massive sphalerite replacing dendritic pyrite that is radiating into a vug. Elongate voids in the sphalerite are likely imprints left by barite laths that have been resorbed. Sample 851-2B. (G) Clusters of white marcasite spheres and barite rosettes mantled by sphalerite, another commonly seen texture in these chimneys. Sample 632-11R. (H) Colloform banding of chalcopyrite, marcasite, and sphalerite with scattered barite laths. This is a rare example of early chalcopyrite mantled by marcasite then a later chalcopyrite phase, signifying pluses of Cu-rich fluids. Sample 851-3A. (I) Intricate colloform banding of pyrite/marcasite (FeS) and sphalerite, indicative of rapid precipitation. This is in turn mantled by a thin layer of chalcopyrite and sphalerite with embedded (white grey) galena. Barite laths are present between the sulfides. Sample 626-4min. (J) Similar texture as I but with sphalerite and bright bluish white galena. Sample 851-2B. (K) Rare, pinkish, dendritic pyrrhotite (po) laths in sphalerite. Sample 852-1A. (L) Backscatter image of a sphalerite and opal-A feature. Darker grey indicates mostly opal-A on the left (op), which transitions to brighter, higher sphalerite content on the right side. Light grey barite rosettes are also mantled in opal-A globules. SO-135-57DR-1. (M) Triangular, bluish tennantite inclusions highlight growth zones in large barite laths that extend into a cavity. Sample 851-3A. (N) Elongate tubes of possible biogenic origin replaced by sulfides, some partially destroyed. Sulfides preferentially deposit outward from tube walls, while the space between and within the tubes is filled with barite laths. Sample 851-3. (O) Rounded, probably biogenic forms replaced by marcasite and filled with several marcasite rings. Colloform marcasite blebs and barite laths grow outward from the forms. Sample 851-3. (P) A presumed bacterial body complexly replaced by marcasite, chalcopyrite and late sphalerite. Sphalerite also mantles barite laths and contains a few bright grains of galena. Sample 851-3.

Anhedral hematite and goethite were observed together filling vugs in the outer margin of the massive chalcopyrite zone in one *Lena* chimney section. Galena largely forms in the center of the disseminated sulfide zone in these chalcopyrite-sulfate chimneys. A few chimneys contain jordanite and/or other Pb-As sulfosalts in addition to, or instead of, galena.

Paragenetic relationships in chalcopyrite-sulfate chimneys mimic those of the chalcopyrite-bornite chimneys, i.e., initial deposition of sulfates is closely followed by deposition of Fe-sulfides (Fig. 2.6). Chalcopyrite overprints earlier precipitated minerals in the centre of the chimney, but forms a zone proportionally much narrower than seen in the chalcopyrite-bornite chimneys. Tellurides have the same paragenetic relationship in both Cu-rich chimney types. Later, Pb(±As)-sulfides form, and rare, small (<20 μm) grains of covellite replace chalcopyrite in the sulfate layer. Calcite, Fe-oxides/oxyhydroxides and amorphous silicates again form an outer rind to these chimneys.

2.4.2 Zinc-rich chimneys

Zinc-rich chimneys are dominated by a zone of sulfate (barite only in this case) and lack a massive chalcopyrite core. Minor chalcopyrite is invariably located near the chimney centers, typically surrounding cavities (Fig. 2.9d). In contrast to Cu-rich chimneys, Zn-rich chimneys generally contain more marcasite than pyrite (Table 2.3). The Zn-rich chimneys can be subdivided, on the basis of relative abundance of chalcopyrite, into sphalerite-barite (>5 modal % sphalerite, to a maximum of 25%, and <5% chalcopyrite) and sphalerite-chalcopyrite types (>5 and <25 modal % sphalerite and chalcopyrite).

2.4.2.1 Sphalerite-barite chimneys

Sphalerite-barite chimneys have textures representative of the sulfate zone seen in both Cu- and Zn-rich chimneys. Sphalerite typically mantles or replaces other sulfide minerals, and also can occur as individual colloform bands, or inclusions in chalcopyrite and/or pyrite and marcasite (Fig. 2.9). Pyrite and marcasite textures in the sulfate zone include small concentric spheres, feathery dendrites and colloform masses, commonly intergrown with other phases (Fig. 2.9e-h). Pyrite both mantles and is mantled by marcasite, which itself can be recrystallized to form euhedral pyrite, particularly in chimney centers. Plumose barite complexly intergrown with pyrite/marcasite and sphalerite is a commonly seen texture, particularly toward chimney exteriors (Fig. 2.9e). Sphalerite also forms intricate, concentric intergrowths with Cu-, Fe- and Pb-sulfides (Fig. 2.9i, j). In this study, we have not distinguished sphalerite from wurztite.

Galena is closely associated with sphalerite, typically occurring as inclusions in the latter, and as isolated grains (Fig. 2.9d, i, j). Euhedral crystals of realgar are scattered throughout the sulfate zone and are also associated with sphalerite (up to 8130 ppm As in the chimneys; de Ronde et al., 2011). Rare laths of pyrrhotite embedded in sphalerite were observed in two samples (Fig. 2.9k). Trace ilmenite and orpiment are only found in Zn- rich chimneys; the former forms euhedral grains and the latter mantles other phases.

Thread-like sphalerite surrounded by aggregates of opal-A microspheres (<5 μm diameter) form a distinct plumose texture, and is common to all four chimneys types, although it is more frequently seen in Zn-rich chimneys (Fig. 2.9l). However, thread-like sphalerite is not always present in the opal-A aggregates. The opal-A microspheres also mantle other phases and can comprise up to ~50 modal percent of a chimney (Table 2.3).

2.4.2.2 Sphalerite-chalcopyrite chimneys

Sphalerite-chalcopyrite chimneys have a thin central zone of chalcopyrite, although it is not as well developed as those in the Cu-rich chimneys. The mineralogy and textures of these chimneys is typically the same as described above for sphalerite-barite chimneys. Relatively thick zones of sphalerite (up to 500 μm) can line cavities in Zn-rich chimneys, but are especially common in sphalerite-chalcopyrite chimneys (Fig. 2.9d). Locally, this massive sphalerite changes in color under the microscope from dark grey to bright blue-white in reflected light (resembling galena), with a corresponding shift from yellow to deep red in transmitted light towards the center of these cavities, reflecting compositional changes.

Tennantite mainly replaces chalcopyrite along grain edges or internal boundaries, and typically forms where chalcopyrite, pyrite, sphalerite ± galena occur together. Tennantite is also associated with vugs, either as a thin zone surrounding the vug, or as inclusions in barite laths that protrude into the cavity (Fig. 2.9d, m). SEM analysis indicated that small inclusions in the thin chalcopyrite zone of chimney PV-626-4min were Ag and Te bearing, but were too small to be confidently identified (Fig. 2.7d).

Paragenetic relationships are similar for both Zn-rich chimneys types, with barite ± pyrrhotite and ilmenite forming first (Fig. 2.6). Barite continued to

precipitate as pyrite/marcasite and sphalerite were deposited. Where abundances of opal-A are high, it appears to have been deposited throughout the life of the chimney, whereas deposition of opal-A may be limited to a later, single pulse in those chimneys where it is a minor or trace component. Galena crystallised both during and after sphalerite deposition. Trace covellite and idaite formed in Fe-sulfide rings in chimneys that also contain at least minor amounts of chalcopyrite in their center (Table 2.3). Chalcopyrite was deposited after Fe- and Zn-sulfides and varies in abundance, depending on whether it is a sphalerite-barite or sphalerite-chalcopyrite chimney. Some vugs are infilled by late laths of barite, or lined by sphalerite. As for Cu-rich chimneys, Fe-oxides/oxyhydroxides, amorphous silica and carbonates form late and are only found on the exterior of the chimneys.

2.4.3 Microbial related textures

A number of textures identified during this study attest to the abundant microbial communities associated with these sulfide chimneys. Bacterial and archaeal communities exist within, and on the surface of, chimneys from Brothers NW Caldera site, with microbial substrates possibly enhancing nucleation and precipitation of opal-A and other minerals (Jones et al., 2008; Takai et al., 2009). Pyrite and/or marcasite replacement of microbial material within chimney walls forms elongate tubes and round vugs that may in turn be replaced, mantled by, or infilled with other sulfides (Fig. 2.9d, n, o). These textures are remarkably similar to those of biogenic origin described by Jones et al. (2008) from Fe-Si chimneys at Giggenbach volcano (located 380 km north of Brothers along the Kermadec arc), although may be up to an order-of-magnitude larger in the Brothers samples. The texture of two-layer microbial walls described from the Giggenbach chimneys (see Fig. 5 in Jones et al., 2008) is also commonly found in the Brothers chimney samples, especially as rings of extremely fine-grained (≤1 μm) sulfides. Rarely, sulfides appear to replace the microbial body itself (Fig. 2.9p).

2.5 Discussion

2.5.1 Paragenesis and chimney growth models

In all the chimney types studied from the NW Caldera site at Brothers, paragenetic relationships show that sulfates form the initial substrate upon which Fe- and then Cu-sulfides are deposited (Fig. 2.6). This is consistent with current models of sulfide chimney development that describe two stages of growth whereby formation of an initial sulfate wall is followed by sulfide deposition on, and in, the pore spaces of that wall (e.g. Goldfarb et al., 1983; Haymon, 1983; Turner and Campbell, 1987; Tivey et al., 1990; Koski et al., 1994). The common texture of plumose barite intergrown with pyrite/marcasite and sphalerite in the Brothers chimneys is indicative of rapid precipitation due to hydrothermal fluid mixing with seawater (de Ronde et al., 2003). As mineral deposition proceeds and porosity decreases, vent fluids are prevented from mixing with ambient seawater permitting precipitation of higher temperature phases (such as chalcopyrite) in the chimney interior. At the same time, minerals that precipitate at relatively cooler temperatures, such as sulfates and sphalerite, dominate the outer parts of the chimneys. To this end, the 'time' spanning sulfate through to chalcopyrite deposition depicted in paragenetic tables also reflects mineralogical

zonation from the exterior to the interior of a chimney (Fig. 2.6). This zone refining reflects radial gradients in temperature, oxidation, sulfidation, pH, and degree of mixing over short distances (mm's to cm's; e.g., Haymon, 1983; Turner and Campbell, 1987; Tivey and McDuff, 1990; Von Damm, 1990).

The composition, temperature, and flow rate of fluids being discharged from a single vent varies over a range of time scales. Recent studies of the NW Caldera vent field show that sub-seafloor phase separation and the addition of magmatic fluid components occurs repeatedly over the lifetime of a chimney (de Ronde et al., 2011). Furthermore, physico-chemical gradients shift within chimney walls with lateral growth and porosity changes. This fluctuating environment causes extensive dissolution, reprecipitation, and overprinting of mineral phases reflected in textural relationships as a mineral's depositional zone contracts or expands within the chimney wall (e.g., Haymon, 1983; Turner and Campbell, 1987; Tivey et al., 1990). The intricate, concentric intergrowths of sphalerite with Cu-, Fe- and Pb-sulfides (Fig. 2.9i, j) can therefore be interpreted as the result of rapid, oscillatory shifts of mineral stability fields within chimney walls. Paragenetic tables cannot adequately portray such complexity; rather, they show the initial order of deposition and highlight major mineral associations. For example, several sulfate-sulfide cycles may occur within a single chimney (e.g., sample 851-1A; Fig. 2.5b) where a second generation of sulfates, pyrite/marcasite, and chalcopyrite are deposited inside an earlier band of chalcopyrite.

Mineralogical and paragenetic work done in this study shows that chalcopyrite-sulfate chimneys at Brothers follow the above model of chimney growth that begins with a wall dominated by anhydrite and ends with chalcopyrite deposited near the interior and sphalerite near the exterior of the chimney (Fig. 2.10a). New minerals precipitate from vent fluids in the center of the chimney and overprint older phases, dissolving and reprecipitating them in the exterior parts of the chimney (see isochrons of *Lena* chimney in Fig. 7d of de Ronde et al., 2011). Massive chalcopyrite overprints earlier phases when vent fluids flow laterally through the chimney wall, whereas laminated chalcopyrite layers precipitate by adiabatic expansion inside the conduit, causing the orifice to narrow (Butler and Nesbitt, 1999).

Isotopic signatures of chimney sulfates show that hydrothermal fluids are the source of Ca and other cations, whereas the SO_4^{2-} is derived from seawater. Hence, sulfates in these chimneys are a proxy for mixing between these two fluids (e.g., Turner and Campbell, 1987; de Ronde, 1995; Seal II et al., 2000). The sulfate zones found within the four chimney types at Brothers differ markedly (Table 2.2), and provide insight into fluid composition, chimney growth, and sub-seafloor processes. For example, chalcopyrite-sulfate chimneys have a thick zone of sulfate that overlaps significantly with the chalcopyrite zone, suggesting that a large degree of mixing occurs within these chimney walls.

By contrast, chalcopyrite-bornite chimneys host a narrow sulfate zone, suggesting that the inner zone of massive chalcopyrite rapidly became impermeable and thereby restricted fluid mixing to the top of the chimney orifice (Fig. 2.10b). Thus, the growth of these chimneys was primarily upwards with limited lateral growth. We believe that chalcopyrite-bornite chimneys form from hot (~300°C), metal-rich fluids that follow more focused

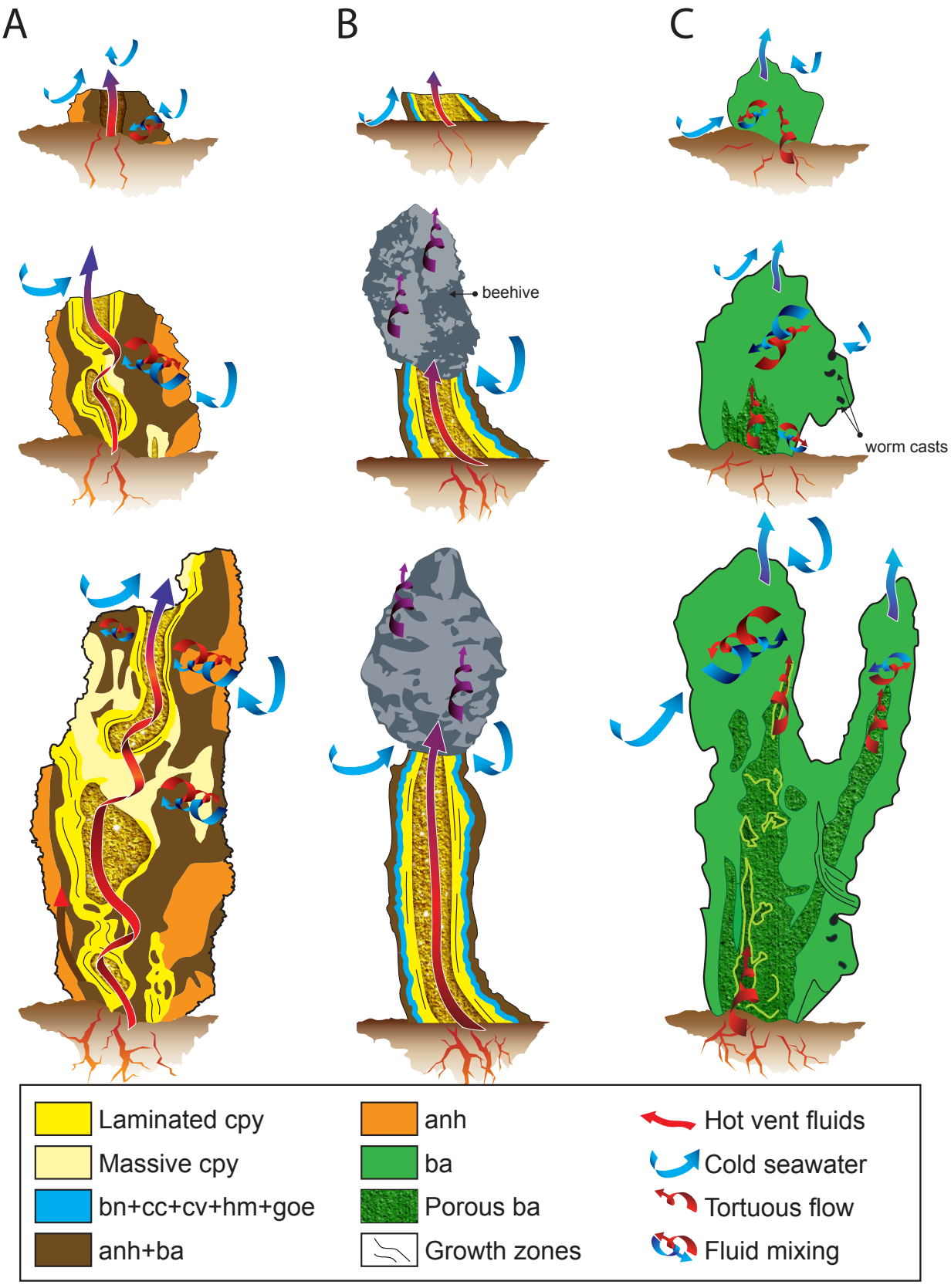
A
B
C
beehive
worm casts
Laminated cpy
Massive cpy
bn+cc+cv+hm+goe
anh+ba
anh
ba
Porous ba
Growth zones
Hot vent fluids
Cold seawater
Tortuous flow
Fluid mixing

Figure 2.10 (previous page) Chimney growth models for the different chimney types seen at the NW Caldera site. Figure not to scale. Time increases towards the bottom of the page. While we do not attempt to constrain the timescale of the models, the top of *Lena* chimney is believed to have grown 66 cm in ~3 years (de Ronde et al., 2011). (A) Chalcopyrite-sulfate chimney type, based on *Lena* chimney (see Figs. 4e and 7 in de Ronde et al., 2011). A sulfate wall builds initially due to mixing between hydrothermal fluid and seawater. As vent fluids are gradually insulated from the seawater, minerals precipitated from relatively hotter fluids (e.g., chalcopyrite) are deposited in the chimney interior. The chimney grows both upwards and outwards as mixing, via tortuous flow, continues to occur within the walls. Fluid flow in the central conduit is focused and laminar. (B) Chalcopyrite-bornite chimney type, based on chimney sample 851-1A that was capped with a beehive structure (see Fig. 4a in de Ronde et al., 2011), although beehives are not exclusive to chalcopyrite-bornite chimneys. The chalcopyrite layer forms early in the growth of the chimney and prevents seawater and hydrothermal fluid from mixing within the walls. Thus, the chimney only grows upwards, with a thin, external sulfate zone. An assemblage of Cu-sulfides and Fe-oxides forms around the chalcopyrite as a result of seawater oxidation. Most mixing is contained within the beehive where the purple arrows indicate unfocused flow of relatively cooler fluids that are eventually expelled out the sides and top of the beehive. (C) Zinc-rich chimney types, based on sample PV626-4min (see Fig. 2.4e). Chimney formation is the same for both the sphalerite-barite and sphalerite-chalcopyrite chimneys, with increased amounts of chalcopyrite in the latter. Initially, massive barite has no distinct conduits and mixing occurs by tortuous flow within a 'mound'. Fluids that form these chimneys are lower temperature than those of the Cu-rich chimneys, represented by the blue arrowhead exiting the top (cf. A and B). The mixing zone moves upwards as the chimney grows, and hotter vent fluids insulated from seawater begin to form porous channels, via dissolution, in the lower parts of the chimney. Some mixing may also occur through the walls at the base of the chimney, allowing for outwards growth. Continued growth sees both the massive barite cap and porous conduits progress upward, via turbulent flow. The hottest fluids in sphalerite-chalcopyrite chimneys are indicated by minor amounts of chalcopyrite lining the main flow channels within the porous interior.

pathways with little sub-seafloor mixing, than those which formed chalcopyrite-sulfate chimneys. This is consistent with vent fluid temperatures; the two active chalcopyrite-bornite chimneys were expelling higher (302°C) temperature fluids than those of *Lena* chimney (274°C), a nearby chalcopyrite-sulfate chimney that occurs at a similar depth (Table 2.1).

The mineralogy of Zn-rich chimneys indicates they form from relatively cooler fluids compared to their Cu-rich counterparts. Zinc-rich chimneys begin with the formation of small, barite-dominated mounds that lack internal conduits, causing fluids to rise tortuously through the interior (Fig. 2.10c). This barite 'cap' marks the main fluid mixing 'front' that advances upward as the chimneys grow, with some concurrent outward growth by lateral flow through the chimney walls. Narrow, internal conduits are formed through barite dissolution in the lower parts of the chimneys, as evidenced by barite-lath-shaped voids in sphalerite that line the conduits (Fig. 2.9f). As these chimneys continue to grow, and the barite 'cap' progresses upwards, chalcopyrite precipitates inside the main fluid conduits, particularly near the base of sphalerite-chalcopyrite chimneys. This growth sequence results in sulfate and chalcopyrite zones that are 'stretched' vertically within the spire, especially compared to the more typical concentric zonation found in Cu-rich chimneys. Given these observations, we believe sub-seafloor chalcopyrite deposition can be expected immediately below sphalerite-chalcopyrite chimneys and indeed, may also indicate areas of deeper Cu-mineralization below sphalerite-barite chimneys.

2.5.1.1 Anhydrite absence in zinc-rich chimneys

Anhydrite absence in Zn-rich chimneys is difficult to reconcile. It may in part be due to fluid temperatures being below ~150°C required for anhydrite precipitation during initiation of chimney growth (e.g., Bischoff and Seyfried, 1978). However, microthermometric data from fluid inclusions in barite from the NW Caldera site indicate formation temperatures between 200 - 290°C (>95% of data; de Ronde et al., 2003). Thus, when combined with the

presence of trace amounts of chalcopyrite in these Zn-rich chimneys, we know the hydrothermal fluids must have been >150°C. Some other Zn-rich chimney growth models assume (or suggest) that anhydrite is still involved in the first stage of chimney growth, despite its absence in the chimneys, and is subsequently dissolved (e.g., Koski et al., 1994; Suzuki et al., 2008). However, we see no mineralogical evidence to support this process having occurred in the Zn-rich chimneys of the NW Caldera site, including anhydrite-shaped voids or anhydrite relicts outlined by sulfides, as seen in the Cu-rich chimneys (cf. Fig. 2.9b). Not a single anhydrite grain was seen in any Zn-rich sample which could be reasonably expected if anhydrite was precipitated, then dissolved.

An alternative explanation is that anhydrite precipitation is limited by SO_4^{2-} availability. The dissolution of barite during conduit development, in combination with trace chalcopyrite consistently appearing in Zn-rich chimneys where the barite zone is 4 cm thick, implies that the walls became impermeable to further seawater influx, allowing relatively hotter fluids to flow in the chimney interior. Therefore, the lack of anhydrite in these chimneys may be due to initially low vent fluid temperatures followed by a lack of seawater sulfate as the chimney grew. That a relatively thin barite layer can be so impermeable may be due to differences in tortuosity (Li and Gregory, 1974) between a barite wall compared to an anhydrite wall. Tortuosity is the degree that fluid must 'twist' and 'bend' to flow through pore spaces, where high tortuosity is analogous to low porosity in that both decrease permeability. In general, tortuosity increases as particle angularity increases (Tivey and McDuff, 1990), thus layers composed of angular barite rosettes are likely to be more tortuous, and thus less permeable, than those composed of tabular anhydrite or subhedral chalcopyrite crystals. Additionally, Zn-rich chimneys tend to have more opal-A mantling other mineral phases, further decreasing permeability (Table 2.3). Thus, by the time vent fluids percolated far enough through the barite layer to mix with seawater, they may have cooled sufficiently to inhibit anhydrite precipitation.

Alternatively, the lack of anhydrite in Zn-rich chimneys may indicate that the Ca content has already been stripped from the hydrothermal fluids due to sub-seafloor mixing with seawater (cf. Cu and chalcopyrite). This is consistent with modelling of the hydrothermal systems at Brothers volcano by Gruen et al. (2012), who show that discrete circulation cells form in areas of higher permeability, with recharge zones located within a few 100 m from outflow areas (vent fields). Mixing of down-flowing seawater with up-flowing hydrothermal fluids could result in large sub-seafloor deposits of anhydrite like those associated with the TAG hydrothermal mound, Suiyo seamount, or Kuroko deposits elsewhere (Humphris et al., 1995; Ogawa et al., 2007; Kawada and Yoshida, 2010). Evidence for sub-seafloor deposits of barite, also a product of mixing, are described for Clark volcano, located ~180 km south of Brothers on the Kermadec arc (Ditchburn et al., 2012). Fluid pathways beneath Zn-rich chimneys may therefore be relatively more permeable and less focused than those below Cu-rich chimneys. With time, these inferred sub-seafloor sulfate deposits may themselves inhibit mixing, leading to conditions ideal for high temperature seafloor venting and the evolution from Zn-rich to Cu-rich vent areas (Kawada and Yoshida, 2010).

2.5.1.2 *Factors controlling chimney type*

Factors controlling chimney type are a complex interplay between fluid compositions, temperature, flow rates, pathways and the permeability of chimneys and sub-seafloor rock. The various fluid end-members described by de Ronde et al. (2011) for the NW Caldera vent field do not correspond to the different Cu-rich chimney types presented here. For example, *Lena* chimney and sample 852-2B, both chalcopyrite-sulfate chimneys, were venting brine (737 mM/kg Cl) and condensed vapour (502 mM/kg Cl) end-member fluids, respectively. However, these compositions represent values at the time of sampling and do not necessarily infer fluid composition throughout the life of the chimney. Indeed, sulfide $\delta^{34}S$ values for *Lena* chimney show that the fluid responsible for the formation of this chimney has almost certainly changed in composition over time (de Ronde et al., 2011).

Chimney complex 852-2 illustrates another scale at which the various factors controlling chimney type can change, with two different chimney types occurring within close proximity to each other. This complex is comprised of multiple spires growing from a ~1.5 m tall massive sulfide base. Chalcopyrite-sulfate chimney 852-2B is one of twin spires, each of which hosted beehives expelling black smoke (Fig. 2.4a, b, c left side). By contrast, sphalerite-barite chimney 852-2A formed the upper portion of a separate, taller spire (Fig. 2.4c right side, d) that was venting clear fluids. Thus, the fluid dynamics and effects of permeability hypothesized to occur sub-seafloor beneath the different chimney types at the NW Caldera site can also occur over a scale of a few meters.

2.5.2 Evidence for magmatic fluid contributions

A wealth of evidence indicates that relatively oxidized fluids of magmatic origin contribute to the hydrothermal systems at Brothers volcano (de Ronde et al., 2011). For example, vent fluids from the NW Caldera and Cone sites have high concentrations of dissolved CO_2 (maximum 39.9 and 206.0 mM/kg, respectively), high $CO_2/^3He$ (9.3×10^9 and 38.8×10^9), low pH (down to 2.8 and 1.9), and negative $\delta^{15}N$ (down to -1.9 and -3.5‰). Furthermore, sulfides and native sulfur have negative $\delta^{34}S$ values as low as -5.7‰ at the NW Caldera site and -10.2‰ at the Cone site. This is supported by the mineralogy associated with the vent fields, especially the occurrence of advanced argillic alteration assemblages (i.e., natroalunite, native sulfur, polymorphs of silica and pyrite) at the Cone site and enargite-bearing veins in rocks at the NW Caldera. The detailed chimney mineralogy presented here provides further evidence for magmatic input, including the presence of enargite together with tennantite in one chalcopyrite-bornite chimney (Table 2.3), as well as specular hematite and Bi-tellurides.

2.5.2.1 *The bornite assemblage*

The bornite assemblage, including chalcocite and covellite, could be considered to result from the proximity of the external chalcopyrite margin to oxidizing seawater in chalcopyrite-bornite chimneys. Mineral assemblages variously including bornite, idaite, chalcocite, digenite, and covellite are also reported from many MOR chimneys, (i.e., Haymon, 1983; Oudin, 1983; Fouquet et al., 1988; Bogdanov et al., 2008). In these studies, these minerals occur at the outer margin of the massive chalcopyrite zone

in thin-walled chimneys, and are also attributed to interaction with seawater through two possible processes: 1) vent fluids mixing with seawater in the outer parts of the chimney walls precipitates zoned, primary bornite through to covellite, or 2) weathering of previously deposited chalcopyrite results in secondary deposition of the enriched Cu-phases in the above-mentioned zonation (i.e., Goldfarb et al., 1983). In Brothers chimneys, the occurrence of these Cu-sulfides similarly distributed near the external margin of the massive chalcopyrite zone, their absence in chimneys with a thick outer sulfate layer, and their corresponding replacement textures together suggest they are secondary in origin (Fig. 2.5b, d, f).

However, we observe *specular* hematite and crystalline goethite along with the Cu-sulfide assemblage in chalcopyrite-bornite chimneys at Brothers, forms not previously reported from other seafloor deposits. Where hematite and goethite have been recorded in sulfide chimneys elsewhere (e.g., East Pacific Rise; Oudin, 1983; Fouquet et al., 1988), they occur as "radiating aggregates" or fine fibers (or otherwise undescribed), and their deposition is attributed to the aforementioned processes. Specular hematite in subaerial geothermal systems have been found to indicate fluid temperatures >240°C (Reyes et al., 2003). Furthermore, at Brothers volcano a combination of high Fe concentrations with high Fe/Mn values for hydrothermal plumes above the Cone site have been interpreted as evidence for a magmatic origin for Fe (Massoth et al., 2003). The mineral assemblage associated with the chalcopyrite-bornite chimneys could indicate more oxidized vent fluids such as those found in high sulfidation environments (Arribas, 1995; Hannington et al., 2005; de Ronde et al., 2011). Therefore, specular hematite and goethite in association with Cu-sulfides, including one occurrence in the interior of the active *Lena* chimney (Table 2.3) – well removed from any oxidizing seawater – could be consistent with a magmatic fluid origin.

2.5.2.2 Tellurium, bismuth and gold

Tellurium, Bi and Au, together with Se, as a suite are considered indicative of a magmatic source (Spooner, 1993). Tellurides are widespread in many types of ore deposits (e.g., skarns, intrusion-related, orogenic, VMS), although those with ore grades of precious metals occurring largely as tellurides tend to be epithermal deposits (Ciobanu et al., 2006, 2009). These epithermal Au-telluride deposits appear to have a genetic link with alkaline/calc-alkaline porphyry intrusions as part of the magmatic-hydrothermal spectrum, with Te sourced from melting of Te-rich sediments in subduction zones (Ciobanu et al., 2006). For example, at the calc-alkaline epithermal deposit at Acupan, Philippines, Cooke and McPhail (2001) suggest magmatic Te is transported in a vapour phase from depth, and that magmatic volatile condensation may be a key ore-forming process in all Te-rich low sulfidation deposits. Telluride precipitation occurs with abrupt changes in fluid parameters, such as decreases in sulfidation and temperature, and increases in oxidation and pH (Cooke and McPhail, 2001; Ciobanu et al., 2006; Vikentyev, 2006). These physicochemical changes are precisely what occur within Brothers chimney walls and likely control telluride distribution at the NW Caldera site. Moreover, recent studies of $^{228}Ra/^{226}Ra$ values for barite from this site suggest an origin also derived from subducted sediments and partial melting in the mantle beneath Brothers volcano (Ditchburn et al., 2012).

Enrichment of Bi in hydrothermal fluids at Brothers could also be attributed to magmatic sources, or leaching of felsic arc rocks, as suggested by Dekov and Savelli (2004) for the occurrence of bismuthinite (Bi_2S_3) in massive sulfides from the Aeolian arc. Bismuth content >2000 ppm in some Brothers chimneys (de Ronde et al., 2011) may in turn explain why Brothers chimneys have the highest known Au contents of any seafloor system. Liquid Bi can incorporate more Au than any other fluid at any temperature, and the low melting point of Bi (271.4°C) means liquid Bi droplets can be transported in hydrothermal fluids (Douglas et al., 2000; Ciobanu et al., 2009). Therefore, liquid Bi may scavenge Au from the hydrothermal fluids resulting in precipitation of Au-rich phases, even in fluids that are undersaturated with respect to Au. The wispy, radiating forms of native Bi seen within Cu-rich chimneys at Brothers (Fig. 2.7f) may represent rapid quenching of these droplets. Bismuth-tellurides have only been reported in one other seafloor system, at the Escanaba trough, where liquid Bi is also thought to scavenge Au (Au to 10.1 ppm; Törmänen and Koski, 2005). Other systems, particularly those with high Au contents that are invariably associated with arcs or backarcs (i.e., East Manus Basin, Valu Fa Ridge), may also host Bi-tellurides that have been missed by conventional microscopy, and the application of other techniques, such as the SEM, may be required to identify them.

2.5.3 Implications for ancient VMS deposits

Active seafloor volcanic systems can aid in understanding ancient, commonly metamorphosed VMS deposits considering various parameters such as depth, geological (and tectonic) environment, age of the chimneys, and fluid temperatures and compositions are known. For example, tube and ovoid structures seen in Brothers chimneys indicate a biogenic component pointing to a submarine environment for the formation of ancient deposits that host similar textures. Furthermore, the very fine textures and inclusions seen in Brothers chimneys would be destroyed during deformation and metamorphism and thus their presence or absence indicates the degree of preservation of the deposit. Telluride inclusions described in this study can be applied to the Silurian-Devonian arc-related VMS ores in the Urals (Russia). Here, the distribution and mineralogy of Au- and Te-phases are poorly understood (Vikentyev, 2006). Tellurides are routinely found in the Uralian Cu and Cu-Zn ores, typically as small inclusions (average 1 - 50 μm, maximum 150 μm) in chalcopyrite, sphalerite, and recrystallized pyrite that are associated with tennantite-tetrahedrite and galena. Any Au-bearing minerals in these ores are thought to relate to the release of solid solution Au from sulfides and/or coarsening of submicroscopic native Au grains during epigenetic hydrothermal alteration (Vikentyev, 2006). However, based on our observations made on Brothers chimneys, we suggest that at least some of the tellurides in the Ural deposits may be primary, particularly where they occur as inclusions in chalcopyrite.

The mineralogical zonation observed in the NW Caldera chimneys and inferred sub-seafloor deposition also has implications for VMS systems. For example, based on the mineralogy of the Zn-rich chimneys, we suggest that chalcopyrite- and anhydrite-rich zones lie structurally beneath sphalerite- and barite-rich zones. This is consistent with the zone refining model for mineralogical

zoning in VMS deposits (e.g., Large, 1992, and references therein). Observations of modern seafloor chimney systems such as those at Brothers and TAG (Humphris et al., 1995), and ancient VMS deposits (Large, 1992), clearly show that zone refining is an important factor in the precipitation and subsequent mineralogical zoning in these types of deposits. Furthermore, the chalcopyrite-rich zones are commonly associated with high Au content, as seen in the Brothers chimneys.

In a recent assessment of geological, geochemical and isotopic data of VMS deposits, Huston et al. (2011) examine a subgroup of VMS deposits that have a dominant magmatic–hydrothermal source of ore fluids and metals. The group is typically characterised by high Cu and Au grades, including deposits such as those in the Neoarchean Doyon-Bousquet-LaRonde (Abitibi, Canada) and Cambrian Mount Lyell districts (Tasmania, Australia). These authors conclude that the sulfur isotopic composition of the ore minerals is one of the most diagnostic characteristics of magmatic fluid. That is, in most instances magmatic-hydrothermal dominated VMS deposits have low values of $\delta^{34}S_{sulfide}$ (with a major population below –3‰), $\delta^{34}S_{sulfate}$ differing from coexisting seawater, and $\Delta^{34}S_{sulfate-sulfide}$ values of ~20 – 30‰. These isotopic signatures are interpreted as a consequence of disproportionation of magmatic SO_2 as the magmatic–hydrothermal fluids ascend and cool. This is in keeping with studies on the Brothers hydrothermal system that show sulfur isotope compositions are strongly influenced by magmatic fluids (de Ronde et al., 2005; 2011). Huston et al. (2011) concluded that magmatic–hydrothermal contributions are favoured in near-arc environments where the melting of metasomatised mantle above subducting slabs produces volatile-rich, oxidised melts to form hydrothermal systems, such as that at Brothers on the Kermadec arc (cf. de Ronde et al., 2007; Ditchburn et al., 2012).

2.6 Conclusions

A variety of chimney types are simultaneously forming at the NW Caldera vent field of Brothers volcano from a range of inferred hydrothermal fluid compositions. The chimneys are categorized as Cu- or Zn-rich varieties, and are dominated by chalcopyrite + barite + anhydrite + pyrite/marcasite, and barite + sphalerite + pyrite/marcasite + opal-A ± chalcopyrite, respectively. Growth models of chimneys at the NW Caldera site involve the initial formation of a sulfate wall by mixing of hydrothermal fluids with seawater. Sulfides are deposited on the wall and are zoned such that chalcopyrite forms in the chimney interior and sphalerite forms near the exterior. This is consistent with chimney growth models developed by other workers. A variation on this model occurs in the Cu-rich, chalcopyrite-bornite chimneys, where the chalcopyrite core rapidly becomes impermeable and thus limits the sulfate wall to a thin, external zone. These chimneys exhibit a radially zoned suite of bornite + chalcocite + covellite on the outer margin of the chalcopyrite core that is not seen in the other chimney types, and is believed to form by seawater oxidation of chalcopyrite. By contrast, Zn-rich chimneys have little (or no) chalcopyrite and are comprised primarily of a sulfate zone. However, because of the 'vertically stretched' mineral zonation observed in some Zn-rich chimneys, we believe Cu-rich mineralization occurs beneath these chimneys. We hypothesize that the main difference in growth between chimney types is related to the degree of permeability represented by sub-seafloor fluid

pathways and hence the amount of fluid mixing (and therefore cooling) that occurs prior to venting.

The chimney mineralogy presented in this study is consistent with magmatic fluids having contributed to the hydrothermal systems at Brothers volcano. Specular hematite and crystalline goethite accompanies enriched Cu-sulfides in chalcopyrite-bornite chimneys, euhedral forms not seen at other seafloor deposits. Furthermore, a magmatic suite of elements, including Te, Bi, Au, and Se occurs together as small Bi(-Se)- or Au-telluride grains that are common in the Cu-rich chimneys. Bismuth-enrichment in Brothers hydrothermal system is considered related to arc magmatism and Bi scavenging of Au leads to very high Au contents in the chimneys. These findings will aid our understanding of ore depositional processes, particularly when applied to modern seafloor and ancient VMS deposits.

2.7 Acknowledgements

This research is supported by an Australian Research Council Centre of Excellence in Ore Deposits research scholarship (University of Tasmania) to H. Berkenbosch, and by New Zealand Foundation for Research Science and Technology (FRST) contracts C05X0207 and C01X0203 to C. de Ronde. We gratefully acknowledge reviews by R. A. Koski, D. L. Huston and an anonymous reviewer, as well as comments from M. I. Leybourne, which helped to improve the manuscript.

Chapter 3

Trace element mapping of copper- and zinc-rich black smoker chimneys from Brothers volcano, Kermadec arc, using synchrotron radiation XRF and LA-ICPMS

Accepted by Economic Geology pending corrections.

3.1 Abstract

High-resolution trace element mapping (2 μm beam) was performed by synchrotron radiation X-ray fluorescence microscopy on Cu- and Zn-rich chimneys from Brothers volcano, Kermadec arc. The maps cover 84 - 136 mm² cross sections of the inner chimney wall and document the distribution of Fe, Cu, Zn, As, Se, Sr, Pb ± Ga, Au, Bi and U. Comparative element maps were generated by LA-ICPMS at a lower resolution (47 μm beam) which additionally measured Co, Ni, Mo, Ag, Cd, In, Sn, Sb, Ba, Au, Tl ± V, Te and Bi. In the two Zn-rich chimneys, Cu distribution ranges from Cu-bearing sphalerite with chalcopyrite-disease to distinct chalcopyrite-lined channels, implying a progression of chalcopyrite replacement of sphalerite. Conversely, the two Cu-rich chimneys have different formation styles of the massive chalcopyrite lining their conduits. The first precipitated elongate chalcopyrite grains that radiate into and infill the conduit, and which merge together some millimetres from the centre. These radial grains may be related to decreased fluid flow during sealing of the chimney at both its top and bottom. The second style involves successive chalcopyrite laminations (0.25 - 1 mm) deposited inside the conduit that progressively narrowed the orifice. Fine (15 - 40 μm), trace element rings are revealed within and between laminations, with variable contents and distributions of Co, Ni, Zn, As, Se, Mo, Ag, Cd, Sn, Te, Au, Tl, Pb, Bi and U. The presence of U specifically indicates seawater ingress into the chimney interior despite it vigorously discharging 274°C fluids at the time of sampling. During these periodic seawater incursions, rapidly changing chemical gradients within the chimney wall induce the instantaneous precipitation of metals from the vent fluid. Thus, the trace element rings are a proxy for the secular evolution of vent fluid compositions. We compared enrichment factors of trace element rings to those of fumarole condensates studied at subaerial arc and rift volcanoes, and molten S pooled atop a submarine back-arc volcano. Our enrichment factors show remarkable consistency with the other volcanoes, and indicate Au, Te, Bi, Se, Cu and Ag are magmatically-derived.

3.2 Introduction

Volcanogenic massive sulfide deposits form from hydrothermal systems on the ocean floor that are driven by the heat of magmas emplaced either above a subducting slab at convergent margins, or below spreading centres at divergent margins. Seawater becomes heated and circulates through

the crust via faults and fractures, interacting with the surrounding host rocks, and evolving into hot, acidic, metal-rich hydrothermal fluid. At subduction zones, water and other volatiles are released from the subducting slab and associated sediments that alter the overlying mantle wedge and lead to the additional input of exsolved magmatic fluids and gases directly into the hydrothermal system (e.g., Hedenquist and Lowenstern, 1994; Timm et al., 2012). These buoyant fluids are expelled at the seafloor, precipitating metals upon contact with cold, ambient seawater, and forming black smoker chimneys and other seafloor massive sulfides. The accumulation of seafloor sulfides over 1,000s to 10,000s of years can form an ore-scale deposit (e.g., de Ronde et al., 2005; Ditchburn et al., 2012; Heinrich and Candela, 2013). Both the magmatic contribution of S, Cl and some metals, and the generally higher oxidation state of arc magmas than those of MOR basalts are believed to cause arc sulfide deposits to contain a greater variety of metals (i.e., Pb-, Zn-, Cu- and Au-rich) compared to those formed at ridges (e.g., Hannington et al., 2011; Henley and Berger, 2013). Thus, subduction-related seafloor massive sulfide deposits are considered closer analogues to ancient VMS deposits preserved in the geological record.

The extent of magmatic contributions in VMS deposits is difficult to ascertain, however, as magmatic input must be isolated from the more prevalent, circulating, modified seawater (e.g., de Ronde, 1995; de Ronde et al., 2011; Huston et al., 2011). The composition and isotopic signature of vent fluids and gases, plume particulates, and seafloor mineralization may indicate a magmatic component; and host rock alteration commonly reflects sustained circulation of low pH fluids related to the dissociation of magmatic gases. In addition, melt and fluid inclusions and unaltered glasses of host rocks provide insight into composition of the evolving, underlying magma and hence the expected composition of magmatic components entrained into the overlying hydrothermal system (e.g., Kamenetsky et al., 2001; Heinrich, 2007). By comparison, porphyry deposits and subaerial volcanic arc hydrothermal systems have minimizal to no seawater input (e.g., De Hoog et al., 2001; Richards, 2003).

In this paper, we focus on elemental compositions and distributions within black smoker chimneys, particularly regarding trace elements. As recognized by Huston et al. (2011), particular trace elements, or suites of trace elements, are diagnostic of a magmatic fluid; although these authors selected the suite of trace elements associated with cassiterite (SnO_2; Sb, Ta, Zr, Sc, Ti, W, and Fe), other researchers identify elements such as Co, Ni, As, Se, Mo, Ag, Cd, In, Te, Au, Hg, Tl, Pb, and Bi as having a strong magmatic affinity (e.g., Yang and Scott, 2002; Grichuk, 2012; Henley and Berger, 2013). Trace element mapping relates bulk geochemistry to mineralogy. For example, the distribution of trace elements may infer subtle changes in depositional conditions that would otherwise be obscured by major element geochemistry and mineralogy alone. Seafloor chimneys are characterised by pronounced physicochemical differences between their internal conduits channelling hot vent fluid and their external contact with ambient seawater, resulting in considerable temperature, pH and oxidation gradients across relatively narrow chimney walls. Concentric mineral zonation in high temperature chimneys reflects these gradients, typically with chalcopyrite dominating the interior, whereas sphalerite, pyrite and sulfates dominate

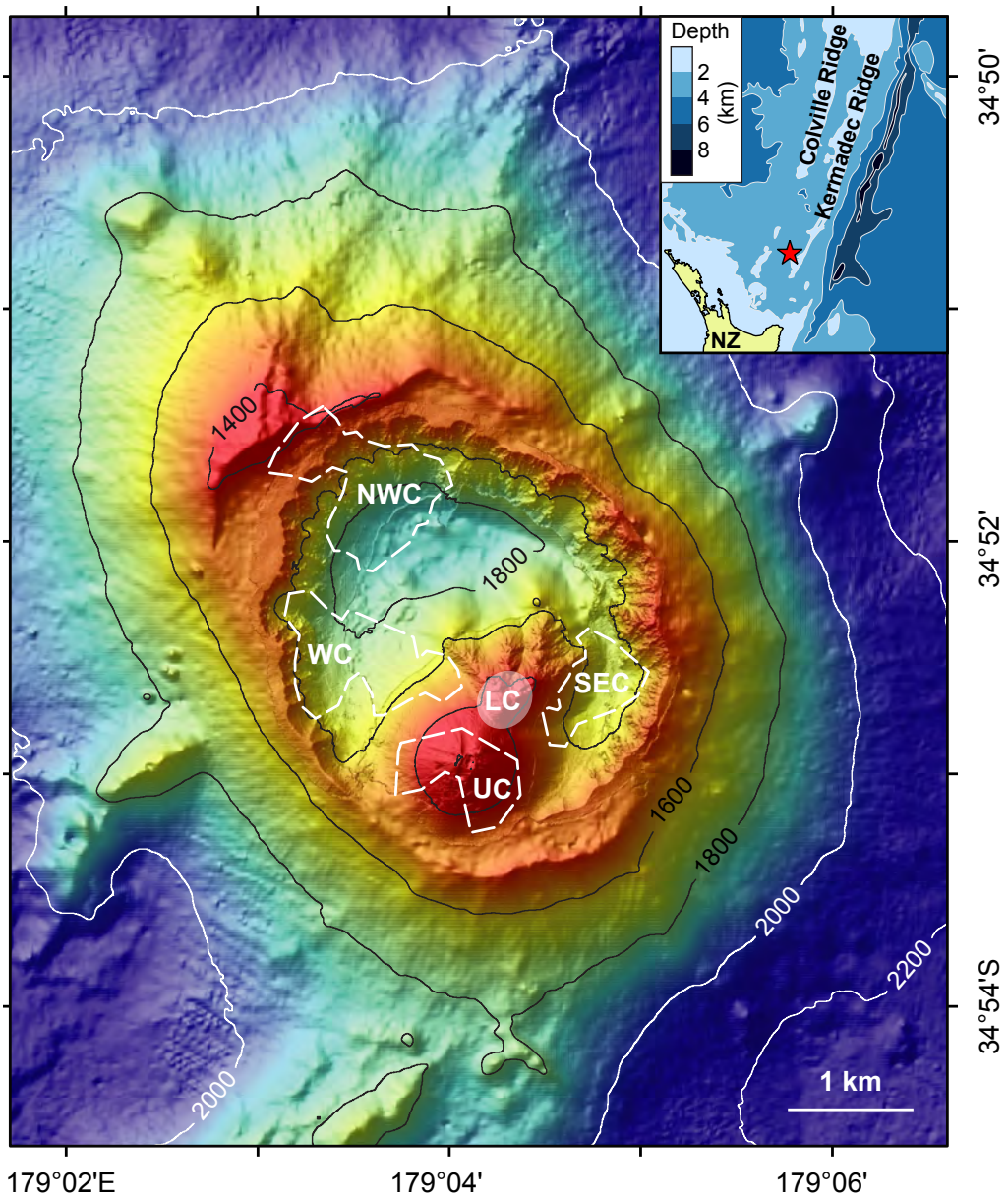

Figure 3.1 Bathymetric map of Brothers volcano. The main hydrothermal sites are outlined by dashed white lines that depict areas of low magnetization, as defined by Caratori Tontini et al. (2012a). These anomalies mark demagnetization of the host rocks from prolonged upflow of hydrothermal fluids. Note the SE Caldera site (SEC) is no longer active, and the Lower Cone site (LC) is another region of diffuse venting (white shading; Baker et al., 2012) that has not been active long enough to demagnetize the host rock. Chimney samples in this study were collected from the narrow neck of the NW Caldera site (NWC), traversing the caldera wall. Inset shows the location of Brothers volcano (★) along the Kermadec arc to the north of New Zealand (NZ). WC, West Caldera site; UC, Upper Cone site. Figure modified from Embley et al. (2012); inset modified from de Ronde et al. (2011).

the exterior. Therefore, trace element mapping of sulfide-rich chimneys is best done at high resolution, orthogonally across a significant portion of the wall to capture areas encompassing both the fine-scale changes and broad range of depositional conditions. Using synchrotron radiation X-ray fluorescence microscopy (SXFM), we mapped parts of chimney cross sections (areas up to 36.5 x 5 mm²) at 2 µm resolution. These are the first chimney samples to be mapped at this scale, resolution, and sensitivity, thus providing detailed images of trace metal distribution across chimney walls.

3.3 Brothers volcano

Brothers dacitic volcano sits on oceanic crust west of the Kermadec Ridge in the southern part of the ~1200 km long Kermadec arc, located between major SW-NE-trending faults (Fig. 3.1; de Ronde et al., 2005; Embley et al., 2012). To its east, at ~35°S, the Pacific Plate – including ~500 m of overlying sediment – is subducting beneath the Australian Plate at ~50 mm/yr (Timm et al., 2012). Brothers rises from an 8 - 13 km diameter base at ~2200 m water depth, to a minimum of 1330 m locally along the caldera wall; two volcanic cones shoal above the caldera rim at 1304 m (Lower Cone) and 1196 m depth (Upper Cone), respectively. The 3 - 3.5 km diameter caldera descends from an average rim depth of ~1470 m to a maximum of 1879 m. Detailed morphology and structure of the volcano are described by Embley et al. (2012). Limited K-Ar dates and aeromagnetic anomalies indicate Brothers is less than 0.78 Ma old (Malahoff et al., 1982; Wright, 1994).

Brothers is host to widespread hydrothermal discharge, with localized, focused, high-temperature (265 - 302°C) venting covering nearly the entire north-western (NW Caldera site) and western (West Caldera site) parts of caldera wall (Fig. 3.1). Additionally, diffuse, lower-temperature (46 - 122°C) venting dominates the fields that sit atop both cones (Upper and Lower Cone sites), and remnant alteration and chimney fragments demarcate an extinct site in the SE Caldera (e.g., de Ronde et al., 2005; 2011; Baker et al., 2012). Fluid, gas and rock/mineral samples collected from the NW Caldera and Cone sites show highly contrasting compositions. For example, in 2004/2005, the maximum total gas content in NW Caldera fluids was 42.6 mM/kg but 221.0 mM/kg at both Cone sites. Maximum Fe and Zn concentrations in NW Caldera fluids were 6.6 mM/kg and 99.2 µM/kg respectively, compared to 1.1 mM/kg and 17.9 µM/kg at the Cone sites, respectively (de Ronde et al., 2011). Furthermore, numerous Cu-, Fe- and Zn-rich chimneys occur at the NW Caldera site whereas the few chimneys present on the Upper Cone are comprised predominately of native S, with only trace amounts of pyrite. Despite these differences, both sites show strong evidence for magmatic contributions, such as high CO_2 (maximum 39.9 and 206.0 mM/kg) and $H_2S_{(g)}$ concentrations (maximum 7.1 and 13.9 mM/kg), and low pH (minimum 2.8 and 1.9) for the NW Caldera and Cone sites, respectively (de Ronde et al., 2011). Together, this indicates direct injection of magmatic CO_2 and the disproportionation of SO_2 from a degassing volcano (e.g., Butterfield et al., 2011). Furthermore, high concentrations of ^3He and R/R_A values of 6.9 - 7.4 at both sites ($R= {}^3He/{}^4He_{sample}$ and $R_A=$ the same ratio in air) are consistent with magmatic gas input (Lupton, 1983; de Ronde et al., 2011). Sub-seafloor phase separation is indicated at both the NW Caldera and Cone sites with Cl concentrations of expelled fluids both greater and less than that of seawater (de Ronde et al., 2011).

Summarizing the above and many other indicators, de Ronde et al. (2011) describes the two vent fields as near end-members of a continuum between water/rock (NW Caldera) and magmatic/hydrothermal (Cones) dominated systems, with distinct and contrasting upflow zones. Magmatic volatiles exsolved from the magma are postulated to rise vertically beneath the Cones, mix with ambient seawater immediately sub-seafloor, and be expelled directly into the water column. By contrast, the greater degree of water-rock interaction indicated at the NW Caldera site suggest either longer and/or

more convoluted conduits lead away from the most recent intrusions beneath the Cones, or a separate, older (cooler) magma body lies below the northern part of the caldera. Fluids at the NW Caldera site are therefore dominated by modified seawater, and vent on the seafloor either as phase-separated brines and/or condensed vapours, forming the metal-rich (Cu-Zn-Au ± Pb) chimneys. Hydrodynamic modelling of Brothers volcano by Gruen et al. (2014) indicates that sub-seafloor phase separation can only occur during injection of saline magmatic fluids into the hydrothermal system at depth. The magmatic vapours emanated rise and vent relatively quickly (within a few years), while the dense magmatic brines accumulate as salt at depth, possibly to be remobilized later ("brine mining").

3.3.1 NW Caldera chimneys

The NW Caldera site hosts over 100 active and inactive chimneys distributed over a strike length of ~600 m between depths of ~1700 - 1550 m along the caldera wall, and has been described in detail by de Ronde et al. (2005; 2011). Chimneys are typically narrow (<0.5 m diameter), 2 - 3 m tall spires, but can coalesce into larger structures up to 7 m tall. They may either be relatively straight and smooth, or bulbous and sinewy, with many capped by beehive structures. Four chimney types were described in detail by Berkenbosch et al. (2012a): two are Cu-rich, i.e., chalcopyrite-sulfate and chalcopyrite-bornite chimneys; and two are Zn-rich, i.e., sphalerite-barite and sphalerite-chalcopyrite chimneys. Both Cu-rich chimney types have a relatively thick, distinct internal chalcopyrite layer surrounded by an external layer of variable thickness that is composed of sulfates (anhydrite and barite) and disseminated sulfides; chalcopyrite-bornite chimneys have an additional intermediate zone of Cu-enriched and Fe-oxide phases (i.e., bornite, chalcocite, covellite, goethite, hematite). By contrast, Zn-rich chimneys are comprised solely of the sulfate (barite only) and disseminated sulfide layer, with only minor or no internal chalcopyrite distinguishing the two types. Brothers chimneys contain high trace element contents, having higher Ga, Ge, Se, Mo, Cd and In compared to chimneys from other arc volcanoes (Monecke et al., 2016). Bismuth is especially enriched reaching contents >2000 ppm – over 1100 ppm higher than in all other seafloor sulfide samples globally.

3.4 Methods

Trace element contents in sulfide chimneys have been measured by electron microprobe (EMP) spot analyses as early as 1987 (Auclair et al.), with other examples of EMP and LA-ICPMS spot/line analyses since (Butler and Nesbitt, 1999; Kristall et al., 2011; Li et al., 2012; Keith et al., 2016). Full element mapping that analyses elemental distributions over an area (cf. a line) has been precluded until recently, mainly due to scanning time limitations of both EMP and LA-ICPMS. Of the few element mapping studies done on chimneys, all map small areas (to a maximum of 1 mm^2) and most measure only major chimney elements (S, Fe, Cu, Zn, Ba, and Pb) plus As and Sb (Bogdanov et al., 2008; de Ronde et al., 2011; de Ronde et al., 2014; Wohlgemuth-Ueberwasser et al., 2015; Dekov et al., 2016). Li et al. (2010a) also mapped the trace elements Se, Ag, Cd, Sn, Sb, Te and Au at 3 - 5 µm resolution but on an area only 40 x 30 $µm^2$. However, since the development of the Maia detector for spectroscopic studies and the Dynamic Analysis (DA) method of data imaging, instrument scanning and data processing times have drastically

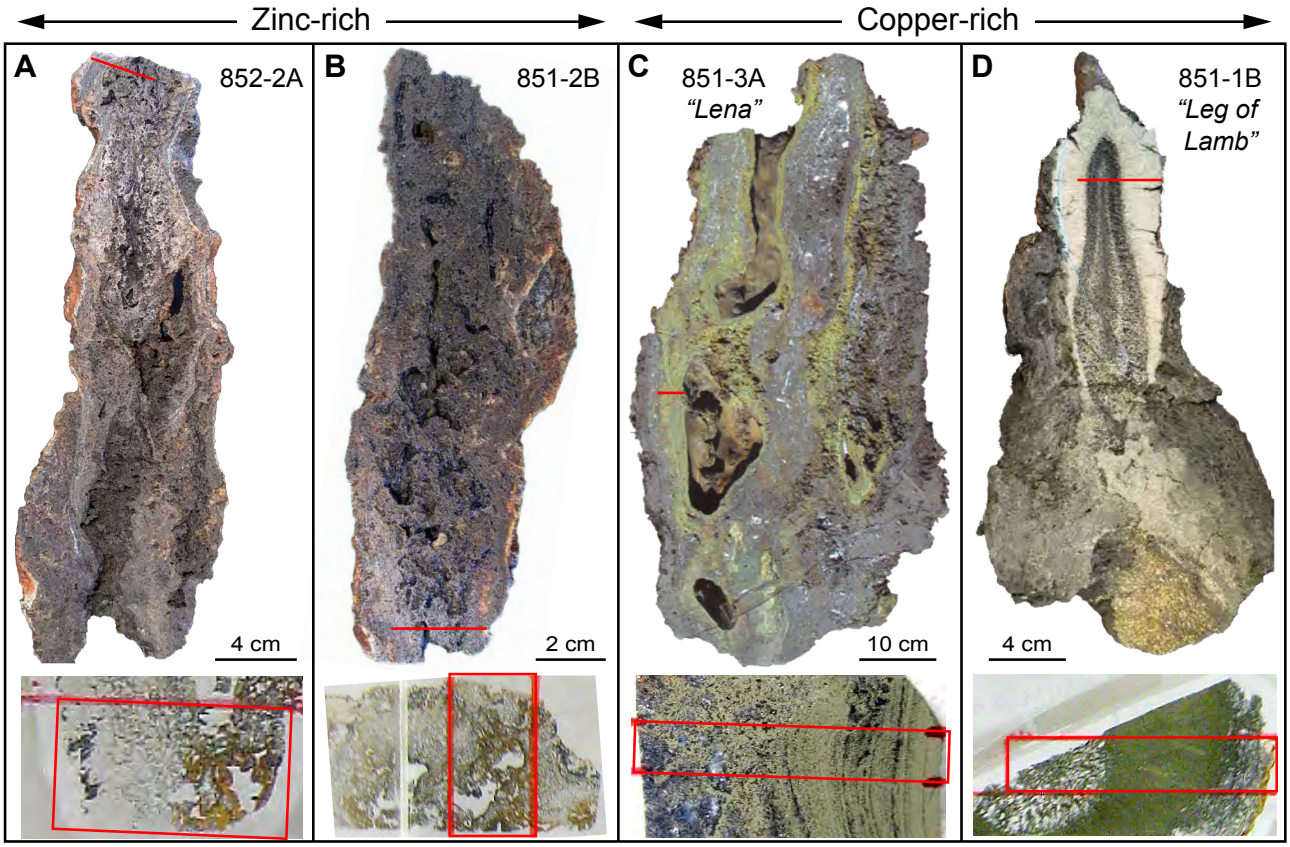

Figure 3.2 Photographs of the chimney samples analysed. The red lines represent the approximate location of the thin section or laser mount. Below each chimney is a photo of the thin section (laser mount for C) showing the area mapped by SXRF or LA-ICPMS.

reduced, thus allowing for non-destructive, large-scale, high-resolution, full-spectral and quantitative element mapping (e.g., Ryan et al., 2005; 2010b; 2015; Yeats et al., 2010; Fisher et al., 2015).

Thin sections from the four chimney types were analysed by SXFM at the Australian Synchrotron (Table 3.1; Fig. 3.2; Paterson et al., 2011). The XFM microprobe end-station uses a Kirkpatrick-Baez mirror pair to focus a 2 µm beam through the sample, and the resulting X-ray fluorescence was detected using a Maia 384A detector array. A beam energy of 18.5 keV was used, allowing detection of elements with atomic numbers 26 - 40 (i.e., Fe through Zr), 60 - 86 (Nd through Rn) and 90 - 94 (Th through Pu). A 160 µm Al filter was used to reduce Fe and Cu count rates, and avoid pile-up interference and dead-time losses. The stage was moved continuously, pixelated into 1 µm pixels, at a rate of 1 µm over a transit time of 0.244 ms and detected X-ray events were logged in order and tagged by XY position. Both Ni and Y foil standards were used to calculate the X-ray flux and monitor drift; the calculated conversion calibration factor (ratio of photon fluence to ion chamber counts) remained at 8.49×10^{-8} for the duration of the experiment.

The resultant full spectral fluorescence event stream was analysed with the GeoPIXE software package, which uses the multiphase DA method for spectral deconvolution to produce elemental images directly from the detected X-ray event data (e.g., Ryan, 2001; Ryan et al., 2005; 2010a; 2015). Whole sample spectra are fitted individually using model X-ray line relative

Table 3.1 Details of samples used in this chapter.

Sample	Chimney type	Mapped area (mm)	Major minerals	Minor minerals	Depth[1] (mbsl)	Vent Fluid[1] Temp (°C)	Age[1] (years)
852-2A-a	sphalerite-barite	14 x 7	ba, py, sph	rg, gn	1627	-	1.29 ± 0.17
851-2B-a	sphalerite-chalcopyrite	16 x 8.5 *16.9 x 2.8*	ba, py, sph	cpy, gn, rg, FeOx	1658	35	1.12 ± 0.02
851-3A-1 "*Lena*"	chalcopyrite-sulfate	33.5 x 2.5 *20.5 x 2.3*	cpy, anh, ba	py, sph	1670	274	1.39 ± 0.07
851-1B-a 1 "*Leg of Lamb*"	chalcopyrite-bornite	26 x 5	cpy	py, ba, sph, bn	1665	302[2]	1.93 ± 0.13

- not measured; anh anhydrite, ba barite, bn bornite, cpy chalcopyrite, FeOx Fe-oxides/oxyhydroxides, gn galena, py pyrite, rg realgar, sph sphalerite; *LA-ICPMS areas in italics*
[1] From Stoffers et al. (1999) and de Ronde et al. (2011)
[2] Venting from an orifice further up the chimney structure

intensities fitted to the observed spectra, although peak overlaps (i.e. low abundances of Au with high abundances of Zn) can make some elements difficult to detect (Fig. 3.3). Overlap resolution was aggravated by the fair energy resolution of the Maia model A (the new model C has greatly improved resolution). GeoPIXE integrates expected yields and X-ray self-absorption effects for the various mineral phases in the sample, resulting in a matrix transformation to project the spectra into element maps. Although processing is normally quantitative, problems with GeoPIXE data calibration caused us to rely on an internal standard approach to set the conversion calibration factor in order to calculate abundances. To do this, we used Fe or Cu abundances from EMP analyses of chalcopyrite as an internal standard to set the conversion factor for three of our samples (Table 3.2). The fourth thin section, 852-2A, had broken into several pieces before we could analyse it on the EMP; for this sample we used the Zn content in sphalerite as measured by SEM prior to the section breaking.

Additionally, we mapped two adjacent samples by LA-ICPMS at lower resolution to complement and compare to the suite of elements imaged by SXFM. The sample mounts were epoxy-reinforced chimney fragments from which the thin sections had been made. A New Wave 213 nm solid-state laser microprobe was used, coupled to an Agilent 4500 quadrupole ICPMS housed at CODES, University of Tasmania. The small volume ablation cell (~2.5 cm^3) has a <1 s response and <2 s washout time. Ablation occurred in pure He and was immediately mixed with Ar upon exiting the ablation cell. The gas and aerosol mixture passed through a pulse homogenizing device prior to direct introduction to the torch.

Laser imaging was done with a 47 μm spot size moving at 100 μm/s; the relatively large beam size maximized the size of the area mapped. Measured elements were: Ca, V, Fe, Co, Ni, Cu, Zn, As, Se, Sr, Mo, Ag, Cd, In, Sn, Sb, Te, Ba, Au, Tl, Pb, Bi and U, as well as La, Ce, Sm, Gd, Yb, Hg, and Th which are not presented here. The acquisition time for most elements was 8 ms, however, Au was 20 ms and Te and Se was 10 ms. Standard STGL2b and blanks were measured at regular intervals to assess background levels and drift (Large et al., 2009; Danyushevsky et al., 2011). Images produced were in counts/s.

The data for section 851-3A-1 were converted to ppm using a central line of data assumed to be pure chalcopyrite, in combination with standard and blank corrections. Twelve EMP spot analyses established an average Fe content of 30.391 weight percent (sd 0.104) in the sample chalcopyrite, and then a python macro was used to calculate the images in ppm. A CODES in-house Microsoft Excel program ("image_auto_min_ID_V3.16", S. Meffre) assigned the mineralogy of each pixel as: chalcopyrite, pyrite, anhydrite, barite, galena, sphalerite, tennantite or blank, accounting for edge effects. The resulting mineralogy was used to apply matrix corrections and modified yields to each pixel, thus correcting elemental abundances. Further correction factors were applied to some elements in the chalcopyrite pixels as detailed in Danyushevsky et al. (2011).

Sample 851-2B was processed in a similar way using EMP analysis, but various issues resulted in a less reliable quantification. Firstly, the Fe content of in sphalerite, intended as an internal standard, varies from 5.01 - 2.43 weight percent (average = 4.163 wt %, sd 0.888, n = 10). Secondly, bleeding at the start of some Zn, As, Sb, Te, Cd, and Pb runs indicates wash-out was incomplete and that there was contamination between ablation runs. Finally, the detector was oversaturated with Pb at times, resulting in no measurement for the remainder of those runs. Therefore, these data are best interpreted by their element distributions and associations and the elemental abundances are not considered accurate.

3.5 Results

3.5.1 Sphalerite-barite, 852-2A

The type and distribution of minerals in Zn-rich chimneys is influenced by proximity to generally narrow (<0.5 mm), anastomosing interior channels

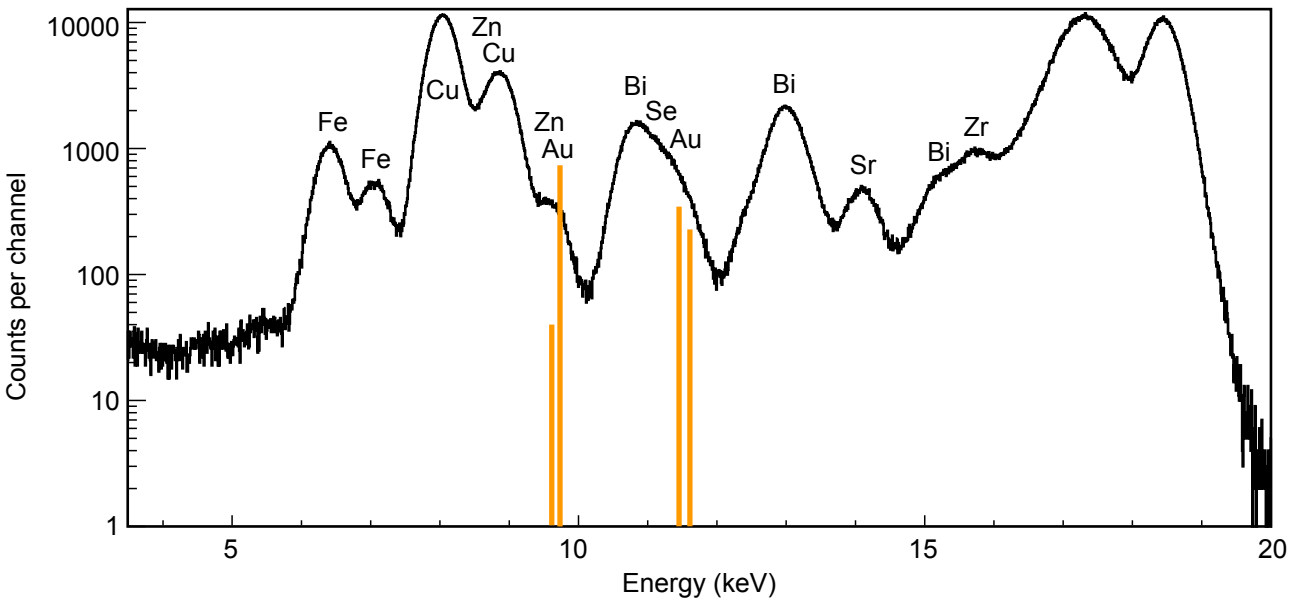

Figure 3.3 Example of a SXFM spectrum for a Bi-inclusion in chalcopyrite from the *Leg of Lamb* chimney (851-1B). As the Bi-inclusion is small (<5 µm), the surrounding chalcopyrite creates the Fe, Cu, and Zn fluorescence peaks (24.60, 27.12 and 1.57 wt %, respectively). Bismuth peaks are distinct (6809 ppm) and the extended right-side shoulder to Zn and Bi peaks (~9.5 and 10.8 keV, respectively), indicate fluorescence contributed by Se (2176 ppm; peaks at 11.2 and 12.5 keV) and Au (1175 ppm; dominant Lα and Lβ peak shown in gold). Gold contents have inflated uncertainty because of the strong overlaps with Zn and Bi. Thus, SXFM spectral processing can produce image artefacts that must be confirmed through other analytical techniques.

Table 3.2 Element abundances used to calibrate SXRF maps (weight %).

Sample	852-2A	851-2B	851-3A	851-1B
Element	Zn	Cu	Cu	Fe
Technique	SEM	EMP	EMP	EMP
	61.09	34.48	34.85	30.26
		34.27	34.89	29.98
		34.29	34.83	30.08
		34.48	34.81	29.99
		34.45	34.81	30.18
			34.97	29.97
			34.81	
			34.85	
			34.95	
			34.96	
			34.85	
			34.82	
Average	**61.09**	**34.39**	**34.87**	**30.08**
s.d.		0.11	0.06	0.12

(here we reserve the term 'conduit' for larger, more well-defined orifices approximately >2 cm diameter). For example, the sphalerite-barite chimney has a thick (~0.4 mm) layer of Ga-bearing sphalerite around the opening on the right half of the sample shown in Figures 3.4 and 3.5 which mantles dendritic pyrite and decreases in thickness towards the interior of the chimney. On the left half of the sample, Sr-bearing barite is dominant, surrounding disseminated pyrite that becomes more massive towards the far left side. A zone of Ga-bearing realgar grains is apparent on the left side of the sample (green – blue), and a zone of As-bearing galena occupies the middle (red – orange; Fig. 3.5b). The sphalerite contains ~2 - 5 weight percent Fe in solid-solution, and displays zonation of trace elements. That is, Pb, As ± Se and Ga dominate the external rims, inward of which is a layer of Se-rich galena inclusions (Fig. 3.6). Even further into the mantling sphalerite, a Cu-bearing layer, both lattice-bound (to ~1500 ppm) and in micro inclusions, is evident and which was not identified in previous studies (Berkenbosch et al., 2012a). Trails of Se-rich galena inclusions are also abundant within the massive sphalerite, adjacent to, or intermingled with dendritic pyrite.

3.5.2 Sphalerite-chalcopyrite, 851-2B

The sphalerite-chalcopyrite chimney is similar to the sphalerite-barite chimney with a layer of Ga-bearing sphalerite, albeit much thinner, concentrated around two prominent channels (Fig. 3.7). In this case, the sphalerite mantles a thin layer of chalcopyrite around the channels, and the smaller-grained, porous pyrite located behind the chalcopyrite, away from the channel, as shown in Figure 3.8a. On the left side, approximately 3 mm from the channels, sphalerite decreases, barite increases, and pyrite is larger grained. As in the other Zn-rich chimney, the sphalerite here displays a similar compositional gradient of decreasing As (and Pb, generally) and increasing Fe, Cu, and Ga progressing inward from the edge of the channel (Table 3.3). There are numerous Pb-As sulfosalt inclusions in the mantling sphalerite (Fig. 3.8b-e), with As ranging from ~1 - 23 weight percent and several inclusions reveal As decreasing away from the channel. Selenium also occurs within these sulfosalts, and is present at low abundances (60 ppm) in the chalcopyrite surrounding the channels (not shown). Some As-free galena also occurs, commonly adjacent to the sphalerite, and is thus "contaminated" by Fe, Zn and excess Pb when analysed (Table 3.3). Lead-free realgar occurs in the pyrite- and barite-rich part of the sample, aligned in a zone of small (<0.5 mm) grains (Fig. 3.8b).

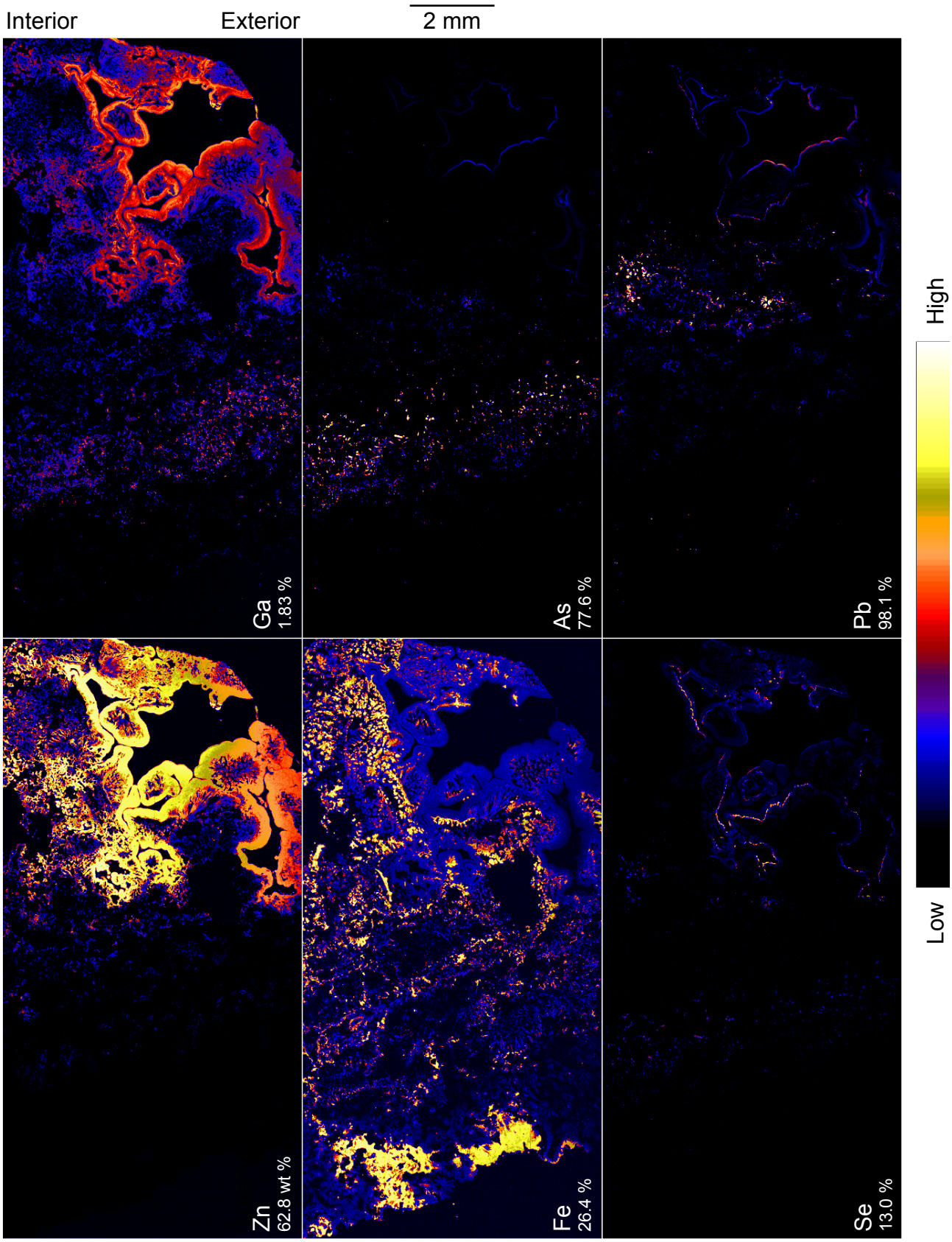
Interior
Exterior
2 mm
Ga 1.83 %
As 77.6 %
Pb 98.1 %
Zn 62.8 wt %
Fe 26.4 %
Se 13.0 %
High
Low

Figure 3.4 (previous page) SXFM element maps of chimney 852-2A (sphalerite-barite) with maximum weight % for each element shown. Area mapped is 14 x 7 mm^2. The linear colour scale has been maximized to show the most detail for each element. Thick, mantling sphalerite occupies the lower right side of the sample containing Fe that generally increases from ~1 - 2 weight % at the channel to 2 - 5 weight % towards the chimney interior. Likewise, Ga is also present throughout the sphalerite at ~1 weight %, although commonly increases in content near the channel, or along internal bands to a maximum of 1.8 weight %.

The LA-ICPMS maps of the sphalerite-chalcopyrite chimney highlight the distribution of other trace elements as shown in Figure 3.9. Strong correlations occur between Sb, Ag, Cd, Au and In, and this suite also correlates with Cu and Zn, showing that these trace elements are distributed between chalcopyrite and sphalerite (Table 3.4). Indium is especially associated with chalcopyrite, whereas Cd more closely associates with sphalerite. The strong correlation between Zn, Fe and Co reflects Co-bearing pyrite included within Fe-rich sphalerite, and is particularly evident on the right side of the images in Figure 3.9. By contrast, the left side is dominated by disseminated pyrite in sulfates (shown by Sr, Ca, and Ba), and sphalerite limited to channel margins. Molybdenum occurs within chalcopyrite in the centre, but is also present in Fe-rich areas marked by disseminated pyrite. Pyrite (Fe) shown in the top-middle of images in Figure 3.9 is unusually enriched in Ni, V and U. Elsewhere, Ni weakly associates with pyrite, and U is generally associated with sulfates (except two spots of higher concentration with high As on the left).

Consistent with the SXRF images, LA-ICPMS data shows sphalerite immediately lining the channels bears As and Pb rims (along with Tl), Se is in a layer further from the channel edge (likely within sulfosalts that are not resolvable), and a Cu-bearing layer (chalcopyrite) is present even further from the edge (Fig. 3.9). The lack of Se shown on the very margin of the mantling sphalerite in Figure 3.9 suggests that the Se within the Pb-As rims on the SXRF map (Fig. 3.8d) is a processing artefact due to an overlap with strong Pb and As fluorescence peaks. Elsewhere in the LA-ICPMS images, scattered As in the sulfate-dominant area (high Ca & Ba) is likely realgar grains, whereas areas with high Pb contents indicate the presence of galena. Beyond the central channel, Tl abundances are high in every phase on the far left of the images in Figure 3.9, and they are associated with pyrite (Fe) on the right. Conversely, Sn does not correlate closely with any element. It occurs both at the margin of the central channel, within surrounding As-Pb-Tl-bearing sphalerite, and with some of the Se-rich chalcopyrite (Cu) to the right of that channel. Otherwise, it is scattered throughout the rest of the sample, which, given its weak correlation with Fe and Mo, may be due to its presence in Sn-bearing pyrite (Table 3.4).

3.5.3 Chalcopyrite-sulfate, 851-3A (*Lena*)

Copper-rich chimneys exhibit systematic zonation from their interior towards their exterior, in contrast to Zn-rich chimneys. *Lena* chimney contains visibly "laminated" chalcopyrite that lines the interior of the main conduit, comprised of alternating disseminated and massive layers that are 0.25 - 1 mm thick. The laminated chalcopyrite grades outwards to a porous chalcopyrite zone with increasing amounts of pyrite and anhydrite (Fig. 3.10). Further outward, the chimney is dominated by a sulfate and disseminated sulfide zone. These three mineralogical zones are evident on a Cu-Sr-Fe image, with Sr content distinguishing barite (brighter green) from anhydrite (duller green; Fig. 3.11a). Lead and As generally correlate with disseminated pyrite

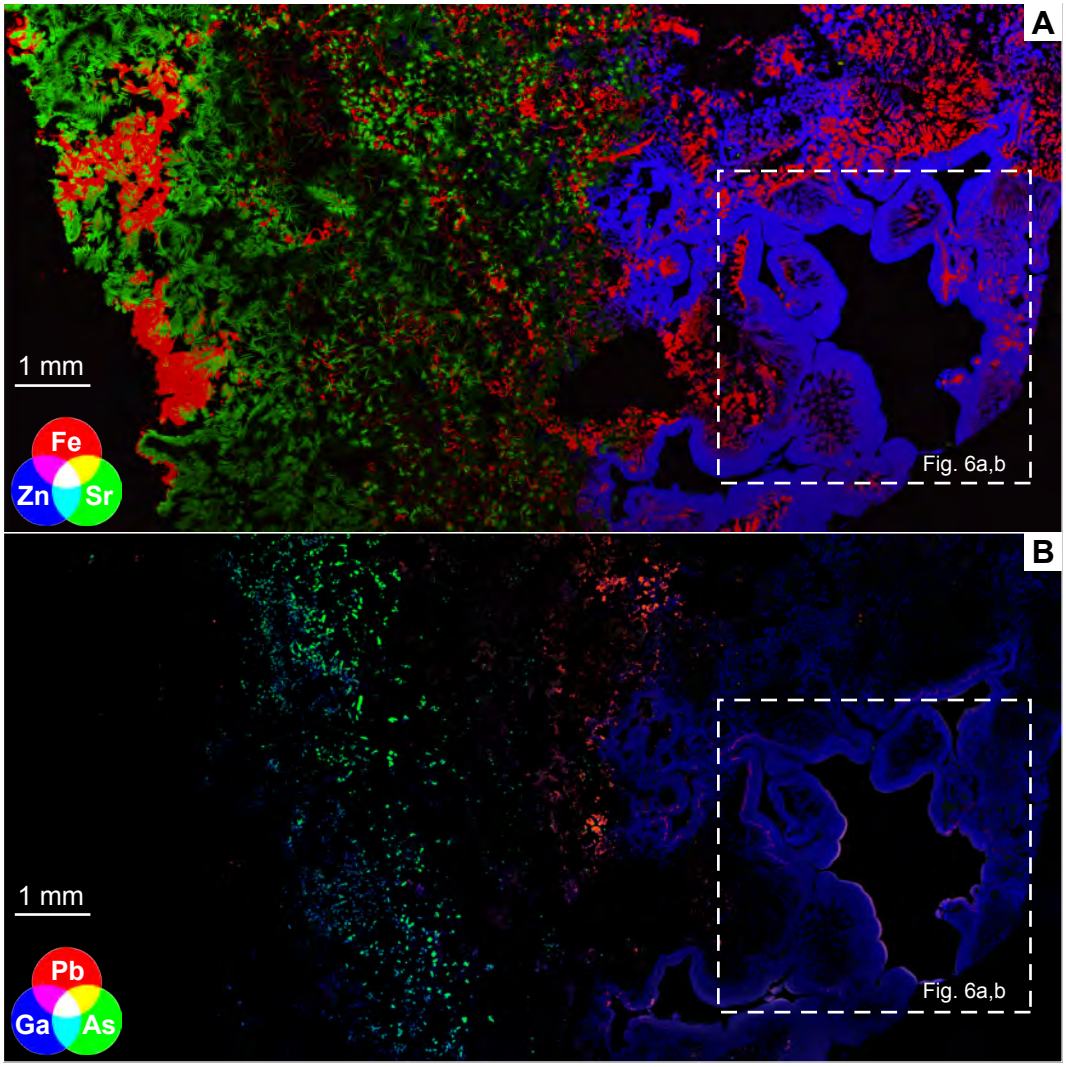

Figure 3.5 RGB images of chimney 852-2A (sphalerite-barite). Brightness indicates content. (A) Depicts the major mineralogy of the sample: pyrite (red), Sr-bearing barite (green) and sphalerite (blue). (B) Depicts the minor mineralogy of the sample: As-bearing galena (red-orange), and Ga-bearing realgar (green-cyan). Gallium-bearing sphalerite (blue) has Pb-rich inclusions and rims (purple), see also Figure 3.6.

in the sulfate-dominated zone (see left half of Fig. 3.10), although the trace Bi, Se and Au apparent here may be artefacts of SXFM processing as they cannot be confirmed on the fluorescence spectrum. Upon magnification, the disseminated pyrite and chalcopyrite show detailed colloform banding of Pb and As (Fig. 3.11b-d).

The most notable feature of *Lena* chimney is the trace element rings within laminated chalcopyrite, appearing as several narrow layers (15 - 40 µm wide) of varying amounts of Bi, Au, As, Se, and U (Fig. 3.12). Selenium appears lattice-bound in the innermost chalcopyrite, showing high abundances outside of the rings, and gradually diminishes away from the conduit. Arsenic occurs within larger, discrete grains instead of being finely distributed within the rings. The rings continues through the innermost chalcopyrite away from the conduit to a distinct, 'wavy' ring marked by especially high trace element abundances (curved line across sample that is particularly high in Bi; Figs. 3.10 and 3.12). Further away from the conduit from this 'wavy' ring, chalcopyrite transitions from laminated layers

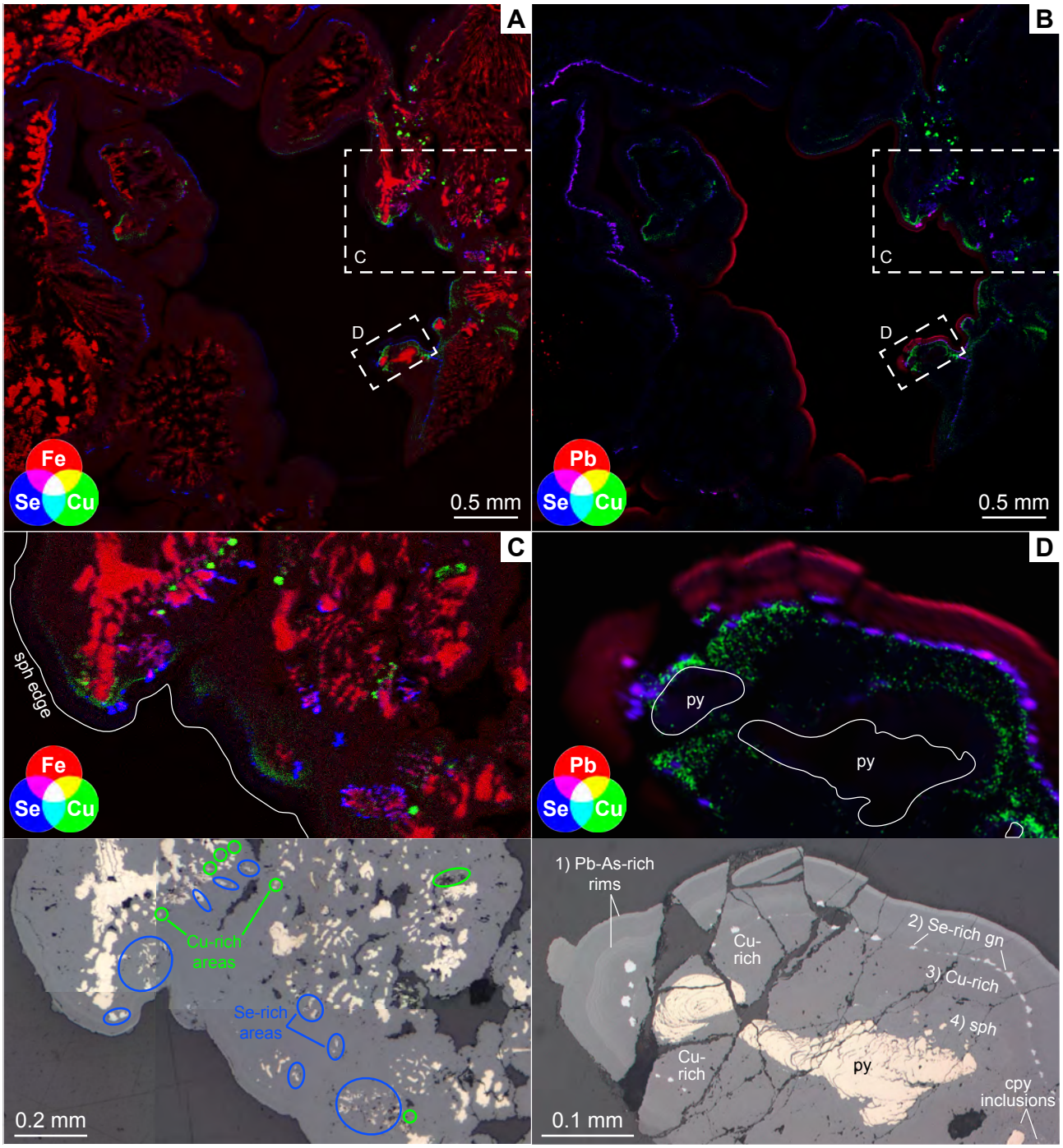

Figure 3.6 RGB images of chimney 852-2A (sphalerite-barite) focused on the sphalerite-rich area of the sample. (A) and (B) Show the same area but with Fe or Pb in red, respectively. Selenium-rich galena inclusions abut dendritic pyrite within the sphalerite, and are particularly visible in the top and left of the images. Copper is generally in solid solution with sphalerite with the exception of some discrete grains in the top right quadrant. (C) Upper half is SXRF image corresponding to lower half photomicrograph. Discrete Cu grains (chalcopyrite) are located in the core of the sphalerite, dispersed amongst internal pyrite, and generally towards the interior of any Se-inclusions or Se-rich pyrite. These Cu- and Se-rich areas are circled in lower part of C, demonstrating their obscurity under reflected-light microscopy. (D) From exterior to interior, the thick sphalerite which mantles pyrite has; 1) Pb-As-(Se)-rich rims then, 2) Se-(As)-rich galena inclusions immediately followed by, 3) a band of Cu-rich sphalerite, faintly visible as chalcopyrite inclusions (cpy-disease) in the lower image and finally, 4) Cu-poor sphalerite. The trace-element zoning within sphalerite is faintly visible on the sample thin section (Fig. 3.2a, lower) as yellow-red colouration from the interior to the exterior.

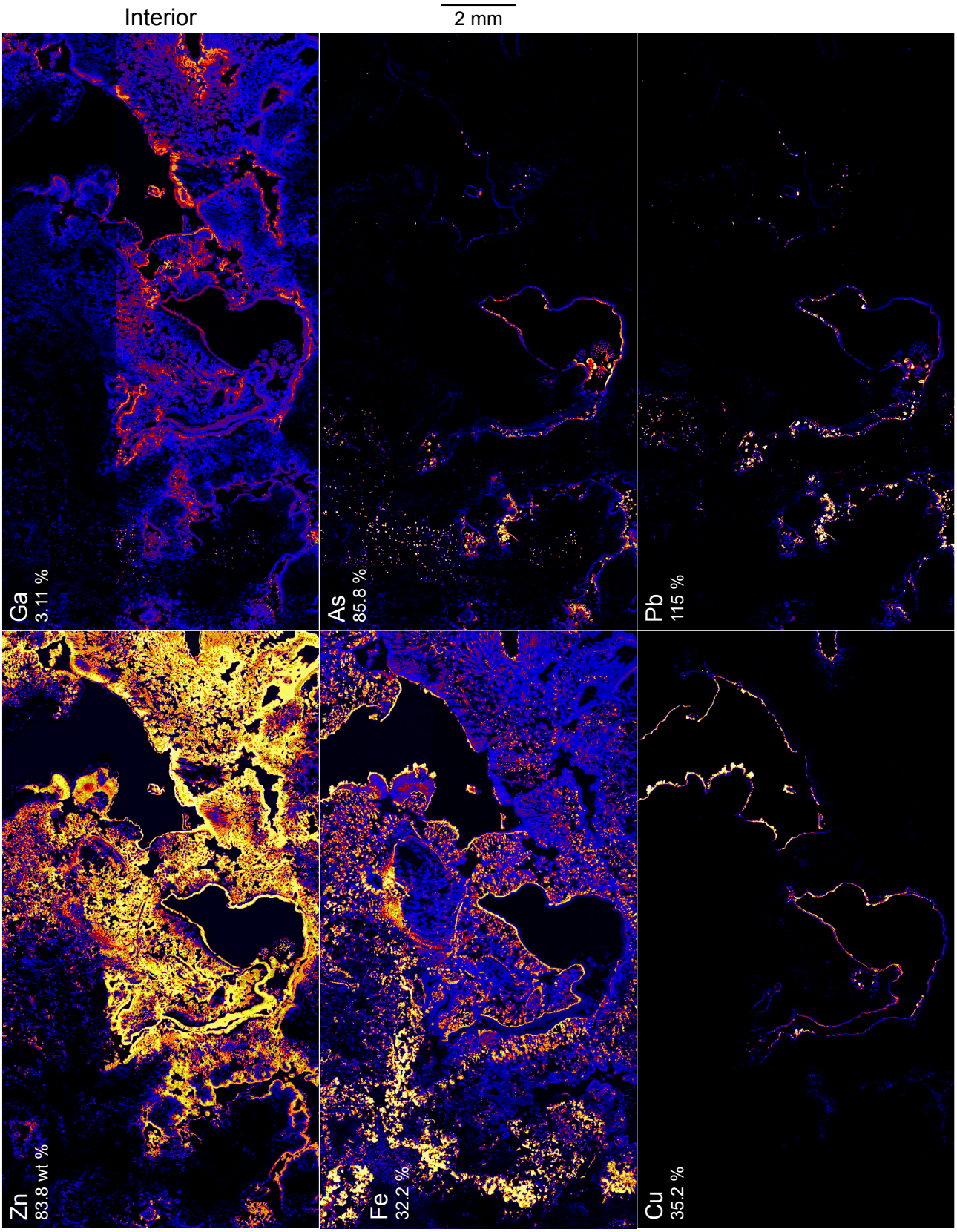

Figure 3.7 SXFM element maps of chimney 851-2B (sphalerite-chalcopyrite) with maximum weight % for each element shown. Area mapped is 16 x 8.5 mm^2. Refer to colour scale in Figure 3.4. Because of its relatively low content, Ga displays an artificial increase in abundance in the lower 2/3rd of the image resulting from a synchrotron incident beam energy boost during mapping. Copper outlines two channels in the middle of the images. Selenium distribution is shown in Figure 3.8d. This section was taken from the middle of the chimney and no exterior margins are shown.

to more randomly oriented grains. A Bi- and Au-bearing phase is present in many of the pore spaces of the non-laminated chalcopyrite, commonly intergrown with pyrite (Table 3.3; Fig. 3.11e), and lattice-bound or micro-inclusions of Bi are also hosted by chalcopyrite and aligned along current and previous (internal) grain boundaries. Both these Bi-phases are likely the Bi-(-Se-Au)-tellurides first described by Berkenbosch et al. (2012a).

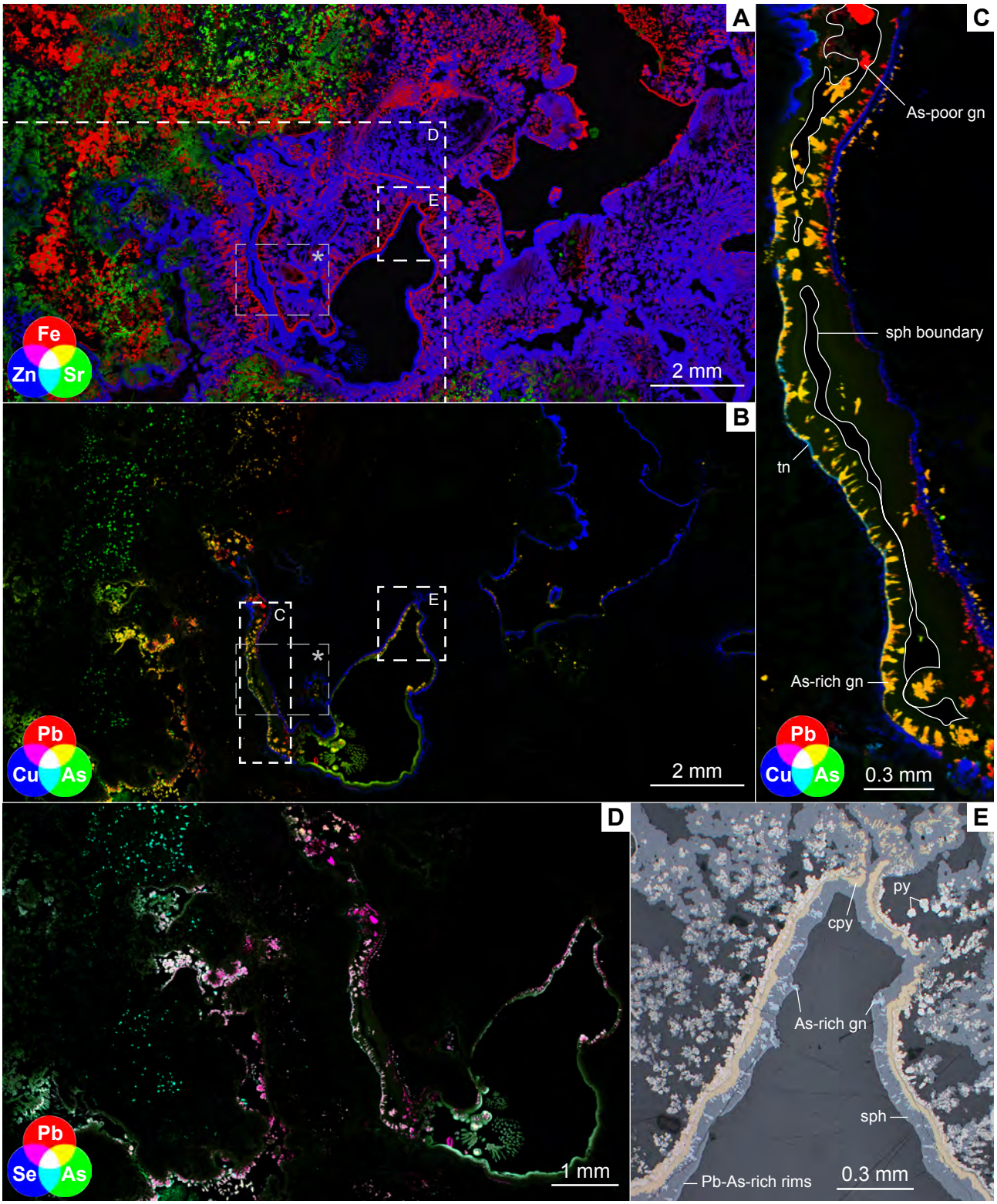

Figure 3.8 (previous page) RGB images of chimney 851-2B (sphalerite-chalcopyrite). (A) Depicts the major mineralogy of the sample: pyrite (red), Sr-bearing barite (green) and sphalerite (blue). * Photomicrograph of this area published as Figure 9d in Berkenbosch et al. (2012a). (B) Pb-As sulfosalts or As-bearing galena (yellow-orange); galena (red); realgar (green, ovoid grains mainly concentrated in a vertical zone on the left); As-(Pb) rims on sphalerite (green to yellow, middle bottom); and chalcopyrite (blue). (C) Close up of B showing the composition of inclusions in sphalerite mantling a narrow channel. Inclusions on the left are Pb-As sulfosalts (yellow), connected by a thin band of tennantite (cyan; $Cu_{12}As_4S_{13}$) inward from the channel. On the right, inclusions are commonly Pb-As rich near channel margin, but transition to Pb-only galena (red). These inclusions are bounded by a band of chalcopyrite (blue), which itself is bordered by smaller, Pb-As-rich inclusions, progressing inward from the channel margin. Sphalerite is faintly yellow, indicating the presence of trace, lattice-bound Pb-As. (D) The lack of any plain blue indicates that all the Se is either with As (tinted blue), Pb (purple); or both (white). Because of fluorescence peak overlaps in areas with high Pb and especially with high As, Se contents may be over estimated or have artefacts (see text for further explanation). (E) Photomicrograph of area shown in A and B showing a typical distribution of the various mineral phases at the margin of a channel.

The LA-ICPMS maps of *Lena* chimney also show fine rings defined by high abundances of certain elements within the laminated chalcopyrite zone (Fig. 3.13). With an expanded range of elements, these rings variously contain: Tl, Ni, U, Cd, Co, Se, Sb, Ag, Au, As, Sn, Pb, Bi, Mo, Te and Zn. Selenium and Sn are in solid solution with the most interior chalcopyrite, decreasing in abundance away from the internal conduit (although retaining broad ring features), whereas In and Ag show the opposite trend. Calcium and Sr are strongly correlated, indicative of their presence in anhydrite. A distinct transition occurs in the chimney from massive, laminated chalcopyrite in the interior (right) half of the images in Figure 3.13 to a sulfate and disseminated sulfide zone in the exterior (left) half.

3.5.4 Chalcopyrite-bornite, 851-1B (*Leg of Lamb*)

The top of the *Leg of Lamb* sample is comprised of an ~8 cm diameter cylinder of massive chalcopyrite in which the central conduit has been filled by elongate laths of chalcopyrite (Figs. 3.2 and 3.14). On the element maps, the exterior of the massive chalcopyrite displays aligned pore spaces suggesting there once were laminations that are now coalesced. Outwards from the massive chalcopyrite is a ~4 mm thick layer of disseminated sulfides in which 'dirty' pyrite includes varying amounts of Pb, As, and Se. A Cu-Sr-Fe image distinguishes the major mineralogy in this chimney (Fig. 3.15a) where the disseminated sulfides are characterised by either Cu-enriched (i.e., bornite, chalcocite, covellite; blue) or Fe-enriched (i.e., pyrite; red) phases. A thin rind of amorphous Fe-oxides/oxyhydroxides mantles the exterior of the chimney (thin, wavy, red line on the far right of Fig. 3.15a). The lack of sulfates in this sample compared to the others is apparent, with only minor Sr-bearing barite occurring amongst the disseminated sulfides on the outside of the chimney and in few pore spaces in the interior of the massive chalcopyrite. In the chimney core, elongate chalcopyrite laths are mantled by a complex mixture of Zn, Pb, and As in sphalerite and galena, or as Pb-As sulfosalts (Table 3.3; Fig. 3.15b-d). Arsenic also occurs as numerous, tiny (few microns) grains bounding the chalcopyrite grains, possibly as realgar.

The most unexpected trace element distribution mapped by SXFM in the *Leg of Lamb* chimney is the lattice-bound Se, present throughout the skeletal and massive chalcopyrite in an intricate, wavy pattern (Fig. 3.14). Lattice-bound Bi is also present in the innermost chalcopyrite, demonstrating a similar, wavy pattern, but decreases sharply in the outer ~80% of the massive chalcopyrite, coincident with an increase in Se (Fig. 3.15d). Numerous, small,

Table 3.3 Selected element abundances for specific regions (ppm).

Region	Fe	Cu	Zn	Pb	As	Se	Bi	Au
Chalcopyrite- Sulfate, 851-3A, Lena								
Band 1	381098	333257	12941	-	bd (<2)	78	699	bd (<5)
	332395	*313327*	*766*	*82*	*100*	*140*	*1179*	*124*
Band 2	379644	330834	14748	-	bd (<3)	bd (<2)	3279	799
	317368	*324107*	*987*	*96*	*32*	*98*	*2609*	*658*
Band 3	278484	223144	29871	-	bd (<3)	bd (<2)	577	bd (<6)
	292259	*262689*	*4658*	*267*	*159*	*72*	*832*	*108*
Band 4	331375	267429	23329	-	bd (<3)	bd (<2)	1984	193
	337666	*287129*	*2221*	*180*	*276*	*75*	*2476*	*286*
Band 5	234866	203481	30322	-	bd (<3)	bd (<2)	5470	2577
	301153	*312759*	*1704*	*204*	*53*	*72*	*3473*	*1291*
Band 6	*186554*	*179788*	*2457*	*122*	*91*	*18*	*1813*	*413*
cpy spots (*n*=12)	**303907**	***348659**	**bd**	**bd**	**bd**			
all cpy (core)	*320573*	*306748*	*1208*	*126*	*126*	*60*	*585*	*96*
Bi- Au in cpy pores 1	363207	196225	15826	3799	3124	bd (<18)	17878	6431
Bi- Au in cpy pores 2	312104	265766	25391	1946	bd (<26)	bd (<18)	10670	2163
Exterior py 1	375912	987	22306	6678	10518	106	bd (<14)	855
Exterior py 2	416923	bd (<107)	6128	8852	16725	204	bd (<14)	1201
Interior py (*n*=10)	**465803**	**9779**	**bd**	**bd**	**1366**			
Chalcopyrite- Bornite, 851-1B, Leg of Lamb								
Massive cpy	293710	305170	12778	bd (<1)	72	2073	67	bd (<2)
massive cpy spots (*n*=6)	***300772**	**343798**	**bd (<300)**	**bd (<600)**	**bd (<200)**	**1791**	**bd (<2200)**	**bd (<1100)**
Bi specks in massive cpy	252604	251505	18015	1427	6793	1627	3281	bd (<5)
Single Bi-Au speck	245970	271225	15701	1440	431	2176	6809	1175
sph mantling skeletal cpy 1	59425	63660	477857	28241	7615	bd (<2)	bd (<4)	bd (<9)
sph mantling skeletal cpy 2	69945	56367	469718	20688	7600	bd (<7)	bd (<11)	bd (<28)
sph mantling skeletal cpy (*n*=5)	**20831**	**3755**	**594496**	**18980**	**6544**	**bd (<200)**	**bd (<2300)**	**bd (<1100)**
gn mantling skeletal cpy 1	bd (<755)	14069	84596	317298	76118	4546	9445	bd (<42)
gn mantling skeletal cpy 2	bd (<474)	bd (<74)	240909	281429	73627	2802	11784	bd (<27)
gn mantling skeletal cpy (*n*=5)	**2534**	**3570**	**21485**	**696563**	**104929**	**bd (<200)**	**bd (<2700)**	**bd (<1300)**
py at outside of chimney 1	272719	bd (<97)	16338	1548	6212	183	bd (<14)	690
py at outside of chimney 2	293688	3161	21185	1376	4829	bd (<7)	bd (<10)	585
Sphalerite- Chalcopyrite, 851-2B								
cpy (*n*=15)	297014	327351	56432	2784	2996	144		
cpy spots (*n*=5)	**296329**	***343905**	**7309**	**bd (<1000)**	**1789**			
Pb-As sulfosalt- high As	38062	bd (<419)	66423	1044561	187605	-		
Pb-As sulfosalt- low As	67524	16010	171781	1093080	41268	-		
Pb-As sulfosalt- mid As (*n*=2)	**920**	**1354**	**36983**	**664719**	**113118**			
"pure" gn	103652	bd (<200)	103078	1154071	bd (<29)	-		
gn (*n*=2)	**317**	**361**	**20687**	**744015**	**853**			
py (*n*=8)	**458465**	**1168**	**17690**	**bd (<1000)**	**977**			
sph Fig. 11c, edge	57413	694	717949	36636	13911	bd (<24)		
sph Fig. 11c, inside	59454	1810	695424	36821	10901	bd (<24)		
sph, high Ga, edge	65639	1203	687635	13017	5468	bd (<24)		
sph, high Ga, inside	75847	6538	720681	3675	bd (<35)	bd (<24)		
sph, Pb-As-rich, edge	38594	bd (<324)	602981	273209	109350	2601		
sph, Pb-As-rich, inside	57513	4833	705919	31627	14500	bd (<31)		
sph, higher Pb-As-Cu (*n*=3)	**14121**	**2571**	**612039**	**23787**	**14149**			
sph, lower Pb-As-Cu (*n*=10)	**41634**	**869**	**619391**	**4543**	**1147**			
Sphalerite- Barite, 852-2A								
sph rim 1 (outside)	21606	bd (<269)	395427	226196	86002	2939		
sph rim 2	45271	5600	485889	39429	16659	1643		
sph rim 3	49969	7762	481942	17403	7330	2150		
sph rim 4 (inside)	52214	7591	477799	14133	5675	1987		
sph (not rim)	57551	3569	594770	8461	3022	1718		
sph average (rim → inside; *n*=14)	50467	5231	515073	35073	12086	2830		
Se inclusion	24044	bd (<0.1%)	355260	730126	9999	182354		
Se inclusion (Fig 15c)	58933	bd (<0.1%)	309326	737906	28622	122842		

SXRF data; **EMP data**; *LA-ICPMS data;* *value used to calibrate SXRF images; blanks not calculated; - not calculated because of strong fluorescence overlaps; bd below detection

Table 3.3 continued.

Region	Ga	U	Ag	Sb	Cd	Sn	Co	Ni	Te
Chalcopyrite- Sulfate, 851-3A, Lena									
Band 1		218							
		2	*19*	*8*	*5*	*503*	*47*	*4*	*2185*
Band 2		204							
		1	*26*	*7*	*6*	*327*	*6*	*2*	*4991*
Band 3		497							
		3	*44*	*19*	*28*	*375*	*67*	*7*	*3143*
Band 4		261							
		2	*103*	*23*	*12*	*250*	*71*	*6*	*6353*
Band 5		508							
		2	*197*	*17*	*12*	*210*	*7*	*2*	*9839*
Band 6		*6*	*69*	*8*	*13*	*88*	*7*	*3*	*3704*
cpy spots (*n*=12)			**bd**	**bd**	**bd**	**184**			
all cpy (core)		*4*	*42*	*18*	*7*	*208*	*16*	*2*	*1478*
Bi- Au in cpy pores 1									
Bi- Au in cpy pores 2									
Exterior py 1									
Exterior py 2									
Interior py (*n*=10)			**bd**	**bd**	**bd**	**bd**			
Chalcopyrite- Bornite, 851-1B, Leg of Lamb									
Massive cpy									
massive cpy spots (*n*=6)			**bd (<200)**	**bd (<200)**	**bd (<300)**	**bd (<200)**	**bd (<200)**	**bd (<200)**	**bd (<200)**
Bi specks in massive cpy									
Single Bi-Au speck									
sph mantling skeletal cpy 1									
sph mantling skeletal cpy 2									
sph mantling skeletal cpy (*n*=5)			**bd (<300)**	**2352**	**6431**	**bd (<200)**	**bd (<100)**	**bd (<200)**	**bd (<200)**
gn mantling skeletal cpy 1									
gn mantling skeletal cpy 2									
gn mantling skeletal cpy (*n*=5)			**576**	**8690**	**bd (<400)**	**bd (<300)**	**bd (<200)**	**bd (<200)**	**bd (<300)**
py at outside of chimney 1									
py at outside of chimney 2									
Sphalerite- Chalcopyrite, 851-2B									
cpy (*n*=15)	3529								
cpy spots (*n*=5)			**2188**	**2976**	**bd (<400)**	**bd (<300)**			
Pb-As sulfosalt- high As	1562								
Pb-As sulfosalt- low As	1918								
Pb-As sulfosalt- mid As (*n*=2)			**3244**	**10366**	**bd (<700)**	**bd (<400)**			
"pure" gn	3577								
gn (*n*=2)			**26152**	**57863**	**bd (<700)**	**bd (<400)**			
py (*n*=8)			**982**	**bd (<300)**	**bd (<300)**	**bd (<200)**			
sph Fig. 11c, edge	10844								
sph Fig. 11c, inside	11691								
sph, high Ga, edge	10395								
sph, high Ga, inside	18510								
sph, Pb-As-rich, edge	13317								
sph, Pb-As-rich, inside	13569								
sph, higher Pb-As-Cu (*n*=3)			**1383**	**2008**	**4584**	**bd (<300)**			
sph, lower Pb-As-Cu (*n*=10)			**2769**	**3120**	**8290**	**bd (<300)**			
Sphalerite- Barite, 852-2A									
sph rim 1 (outside)	14475								
sph rim 2	13090								
sph rim 3	13101								
sph rim 4 (inside)	12448								
sph (not rim)	11551								
sph average (rim → inside; *n*=14)	12566								
Se inclusion	654								
Se inclusion (Fig 15c)	3077								

SXRF data; **EMP data**; *LA-ICPMS data*; blanks not calculated

Table 3.3 continued.

Region	Mo	In	Tl
Chalcopyrite- Sulfate, 851-3A, Lena			
Band 1	*74*	*8*	*3*
Band 2	*126*	*11*	*1*
Band 3	*805*	*10*	*6*
Band 4	*18646*	*11*	*7*
Band 5	*14627*	*13*	*7*
Band 6	*1762*	*11*	*2*
cpy spots (*n*=12)			
all cpy (core)	*1068*	*14*	*2*
Bi- Au in cpy pores 1			
Bi- Au in cpy pores 2			
Exterior py 1			
Exterior py 2			
Interior py (*n*=10)			
Chalcopyrite- Bornite, 851-1B, Leg of Lamb			
Massive cpy			
massive cpy spots (*n*=6)			
Bi specks in massive cpy			
Single Bi-Au speck			
sph mantling skeletal cpy 1			
sph mantling skeletal cpy 2			
sph mantling skeletal cpy (*n*=5)			
gn mantling skeletal cpy 1			
gn mantling skeletal cpy 2			
gn mantling skeletal cpy (*n*=5)			
py at outside of chimney 1			
py at outside of chimney 2			
Sphalerite- Chalcopyrite, 851-2B			
cpy (*n*=15)			
cpy spots (*n*=5)			
Pb-As sulfosalt- high As			
Pb-As sulfosalt- low As			
Pb-As sulfosalt- mid As (*n*=2)			
"pure" gn			
gn (*n*=2)			
py (*n*=8)			
sph Fig. 11c, edge			
sph Fig. 11c, inside			
sph, high Ga, edge			
sph, high Ga, inside			
sph, Pb-As-rich, edge			
sph, Pb-As-rich, inside			
sph, higher Pb-As-Cu (*n*=3)			
sph, lower Pb-As-Cu (*n*=10)			
Sphalerite- Barite, 852-2A			
sph rim 1 (outside)			
sph rim 2			
sph rim 3			
sph rim 4 (inside)			
sph (not rim)			
sph average (rim → inside; *n*=14)			
Se inclusion			
Se inclusion (Fig 15c)			

SXRF data; **EMP data**; *LA-ICPMS data*; blanks not calculated

Bi-bearing minerals are scattered throughout the massive chalcopyrite and probably represent Bi-(Se-Au)-tellurides, as in *Lena* chimney (Fig. 3.14). At the exterior margin of the massive chalcopyrite, a complex distribution of Cu, Fe and Bi occurs with interconnected Bi-, Bi-Fe-, Bi-Cu-, and Bi-Fe-Cu-bearing phases (green, cyan, yellow, and white, respectively in Fig. 3.15e) that are not discernible by optical microscopy (inset).

3.6 Discussion

3.6.1 Depositional processes

3.6.1.1 Zinc-rich chimneys

In this study, Se is one element that shows a varying distribution across the four chimney types and provides insight into the conditions under which the chimneys formed. In the Zn-rich chimneys, it occurs in sphalerite mantling interior channels (Figs. 4 - 9). Element distribution across this mantling sphalerite displays similar patterns in both sphalerite-barite and sphalerite-chalcopyrite chimneys, grading from Pb-As ± Se and Ga-rich rims, through a Se-rich inner zone and into a Cu-rich layer. The Se zone incorporates inclusions of either Se-rich galena or pyrite, while the Cu-rich layer is either distinct chalcopyrite surrounding chimney channels, or micro-inclusions of chalcopyrite embedded in the sphalerite, reminiscent of chalcopyrite-disease. Barton and Bethke (1987) describe chalcopyrite-disease as replacement of sphalerite by chalcopyrite from low-Cu fluids, and a replacement origin is also consistent with textures seen in the Brothers Zn-rich chimneys. For example, microfractures and voids are apparent in the inner, Cu-rich sphalerite of the sphalerite-barite sample inferring a volume loss during replacement, whereas the Pb-As-rich

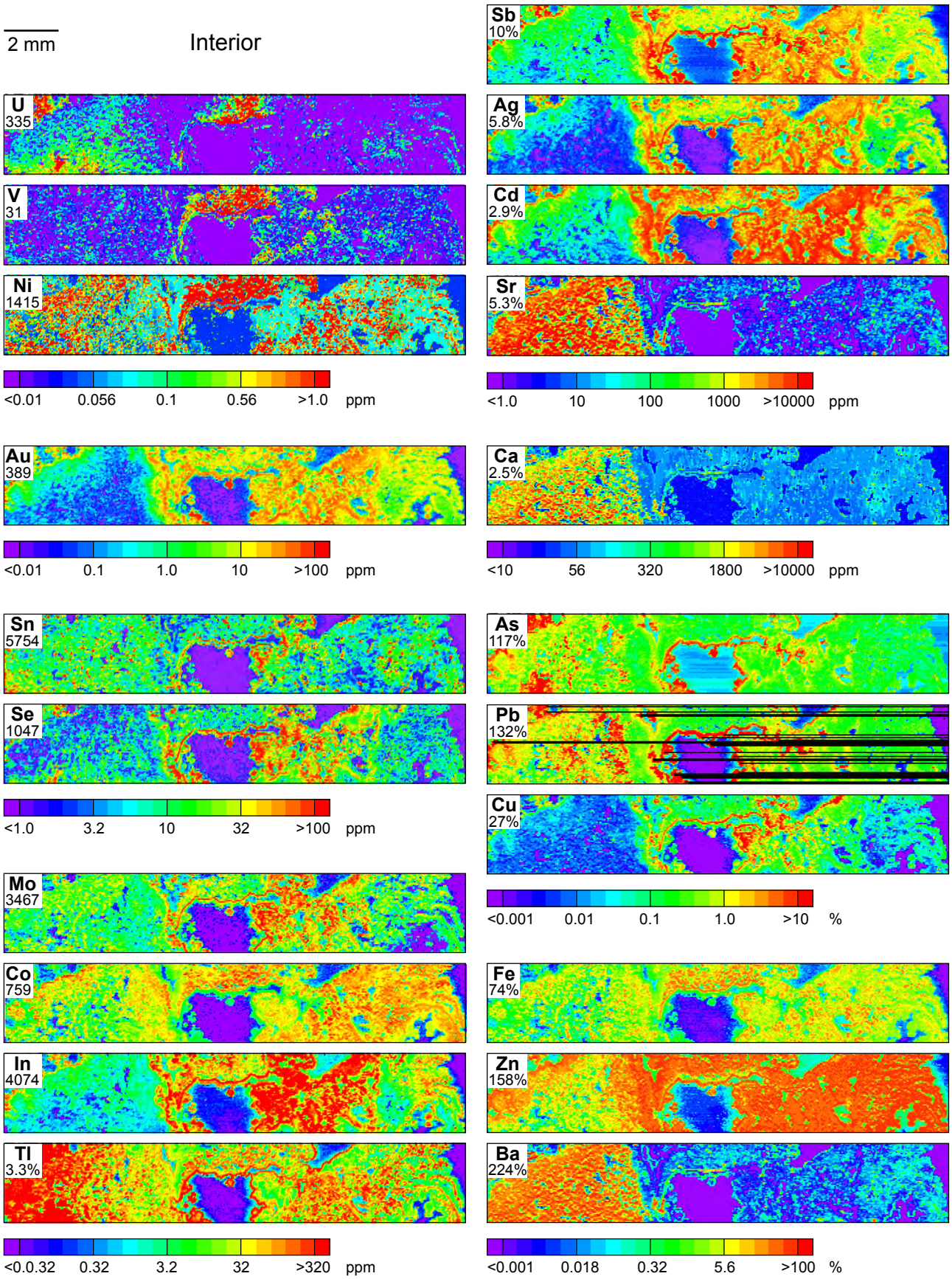
2 mm
Interior
U
335
V
31
Ni
1415
<0.01 0.056 0.1 0.56 >1.0 ppm
Au
389
<0.01 0.1 1.0 10 >100 ppm
Sn
5754
Se
1047
<1.0 3.2 10 32 >100 ppm
Mo
3467
Co
759
In
4074
Tl
3.3%
<0.0.32 0.32 3.2 32 >320 ppm
Sb
10%
Ag
5.8%
Cd
2.9%
Sr
5.3%
<1.0 10 100 1000 >10000 ppm
Ca
2.5%
<10 56 320 1800 >10000 ppm
As
117%
Pb
132%
Cu
27%
<0.001 0.01 0.1 1.0 >10 %
Fe
74%
Zn
158%
Ba
224%
<0.001 0.018 0.32 5.6 >100 %

Figure 3.9 (previous page) LA-ICPMS element maps of chimney 851-2B (sphalerite-chalcopyrite) with maximum content for each element shown (ppm, unless noted as wt. %). Contents in this sample are approximate only, see text for further explanation. Note that the surface of the laser mount is similar to, but not the same as, that shown in Figure 3.7. Also for comparison, the area mapped (16.9 x 2.8 mm^2) and spot size used (47 µm) are narrower and coarser than that for SXFM, respectively. The colour scale shown below each map/group has been maximized to show the most detail for each element, and groups are arranged in increasing content down the left and then right columns. A smearing effect is noted for some elements, particularly at the edges of the central channel (i.e., Au, In, Tl, Sb, Ag, Cd, Pb, Zn). High Pb concentrations also oversaturated the sensor for some lines. Te and Bi maps are not included as their contents were low and dispersed for this Zn-rich chimney (average 5.3 and 0.1 ppm; maximum 310 and 46 ppm, respectively).

rims are a smooth, uniform texture (Fig. 3.6c, d). The sphalerite-chalcopyrite sample suggests a progression of this replacement process where the very porous internal sphalerite indicates significant volume loss (Fig. 3.8a). We suggest the Zn-rich chimneys experienced sphalerite deposition predominantly around interior channels, but periodically discharged hotter, low Cu-bearing fluids wherein chalcopyrite incipiently replaced sphalerite. Selenium partitioned between both chalcopyrite and Pb-As-sulfosalts during this process, possibly by simultaneous co-deposition into chalcopyrite and exsolution from sphalerite (along with Pb and As). The sphalerite-chalcopyrite chimney is thus a progression of the replacement process from sphalerite-barite chimneys, where more Cu-bearing fluids have passed through the inner channels from either thickening (sealing) of chimney walls, or a change in venting conditions. Late, smooth Pb-As-rich sphalerite mantles the chalcopyrite or Cu-rich sphalerite along channel walls that have not undergone chalcopyrite replacement.

3.6.1.2 Copper-rich chimneys

Selenium was also the element of interest in the very first chimney "proto-mapping" study – EMP spot transect analysis – performed by Auclair et al. (1987). These authors measured Se variations across the inner walls of Cu-rich chimneys recovered from the East Pacific Rise, because Se is known to substitute for S in chalcopyrite. They found Se content decreased gradually, though unevenly, through the chalcopyrite conduit lining and dropped off sharply

Table 3.4 Pearson's correlation coefficients [log(10)] for LA-ICPMS data of the sphalerite-chalcopyrite chimney (Fig. 3.12)[1].

	Se	Cu	In	Ag	Sb	Au	Cd	Zn	Fe	Co	Mo	Tl
Cu	0.78											
In	0.74	0.92										
Ag	0.71	0.87	0.92									
Sb	0.77	0.87	0.90	0.95								
Au	0.69	0.85	0.90	0.96	0.94							
Cd	0.65	0.81	0.88	0.94	0.93	0.95						
Zn	0.58	0.71	0.75	0.78	0.83	0.81	0.89					
Fe	0.53	0.68	0.68	0.66	0.71	0.71	0.76	0.90				
Co	0.50	0.62	0.65	0.65	0.69	0.70	0.77	0.92	0.96			
Mo	0.67	0.79	0.73	0.65	0.71	0.67	0.68	0.72	0.79	0.74		
Tl	0.45	0.49	0.42	0.41	0.50	0.46	0.50	0.66	0.67	0.64	0.68	
Sn	0.52	0.55	0.44	0.36	0.45	0.40	0.41	0.56	0.62	0.58	0.65	0.63

[1]Pb coefficients were not calculated because of the blanks in the map

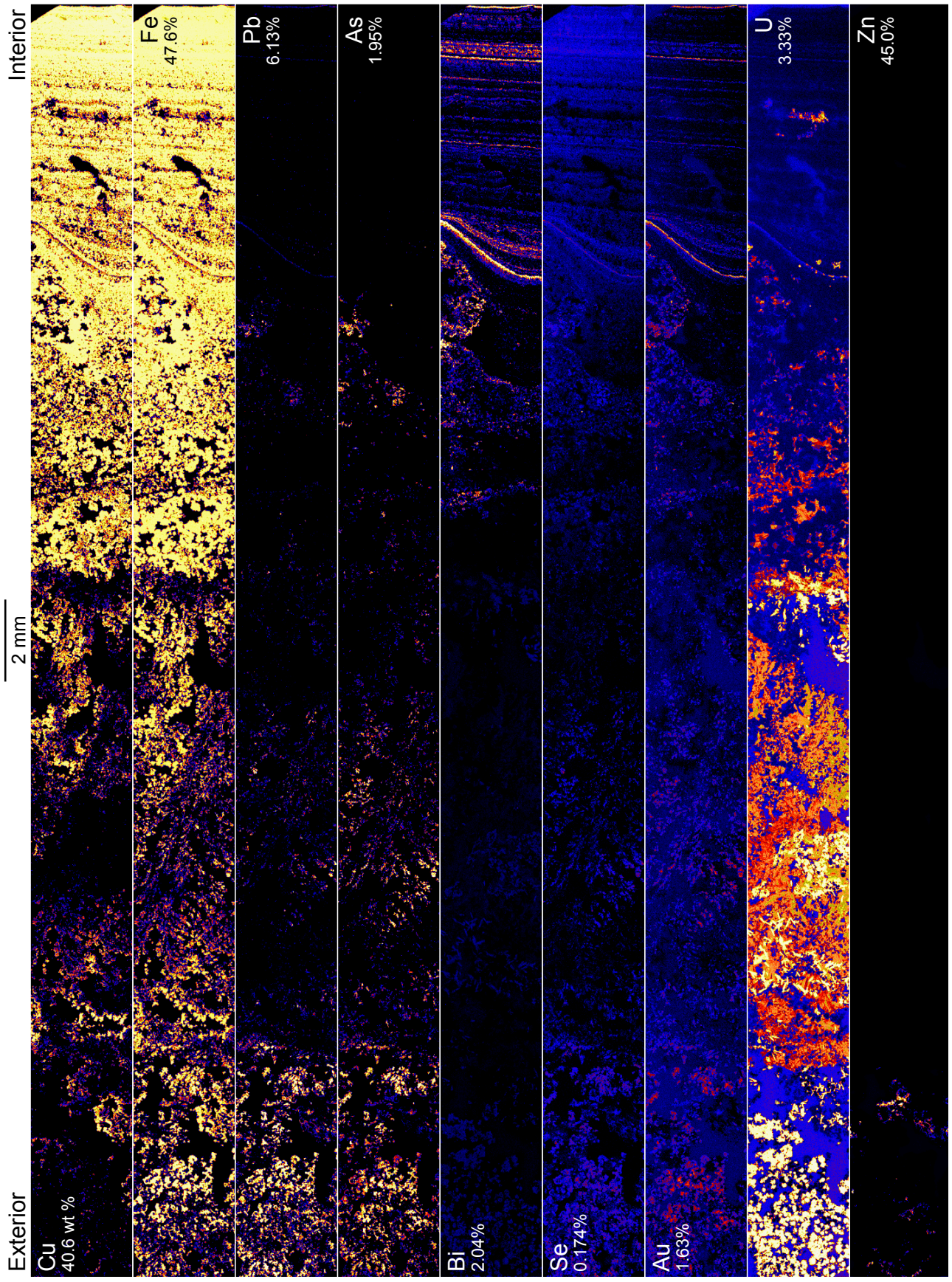
Interior
Exterior
2 mm
Cu
40.6 wt %
Fe
47.6%
Pb
6.13%
As
1.95%
Bi
2.04%
Se
0.174%
Au
1.63%
U
3.33%
Zn
45.0%

Figure 3.10 (previous page) SXFM element maps of *Lena* chimney (851-3A; chalcopyrite-sphalerite) with maximum weight % for each element shown. Area mapped is 33.5 x 2.5 mm^2. Refer to colour scale in Figure 3.4. Glass areas (holes/pores in the chimney) contain minor U and Au and are particularly visible as bright blue on the U map. Uranium otherwise correlates with Sr in the sulfates: barite (bright whites) and anhydrite (oranges-yellows; cf. Fig. 3.11a). Zinc-rich sphalerite is only present at the exterior of the sample.

at the boundary with porous, microcrystalline chalcopyrite seen replacing anhydrite. This boundary represents the approximate location of the initial anhydrite chimney wall that first builds on the seafloor, upon which later sulfides are deposited. The laminated, massive chalcopyrite grew *into* the conduit, while chalcopyrite replacement of anhydrite and further sulfate/sulfide deposition (i.e., sphalerite, pyrite and chalcopyrite) occurred *outwards* from this point (cf. Tivey and McDuff, 1990). As the chimney wall thickened, hydrothermal fluids were progressively insulated from seawater and large variations in pH, fO_2 and fS_2 are not expected near the inner conduit. Furthermore, conductive cooling of hydrothermal fluids is reduced, leading Auclair et al. (1987) to conclude that hotter temperatures were primarily responsible for the Se enrichment in the interior of the chimneys. This finding was consistent with thermodynamic calculations by D'Yachkova and Khodakovskii (1968) and is observed in numerous other modern seafloor and VMS deposits (e.g., Layton-Matthews et al., 2013; Wohlgemuth-Ueberwasser et al., 2015).

This same Se distribution is mapped in the chalcopyrite-sulfate *Lena* chimney (Figs 3.10, 3.12 and 3.13), with fluctuating Se contents in the massive chalcopyrite, but still gradually decreasing away from the chimney interior. At the boundary with anhydrite (Ca) on the left side of the maps shown in Figure 3.13, the Se content drops from an average of 73 ppm to 25 ppm. Tivey and McDuff (1990) modelled mineral precipitation across chimney walls and considered factors such as thermal conductivity, porosity and pressure to calculate physicochemical gradients. While confirming that pH, fO_2 and fS_2 gradients are minor in the inner chimney wall, the modelling did show temperature changes of ~40°C across the zone of massive chalcopyrite. Similarly, we suggest Se distribution through *Lena* chimney indicates a temperature gradient of ~40°C across the anhydrite-free portion of the inner chimney wall (i.e., approximately the right half of the maps shown in Figs. 3.10 and 3.13).

Since Se distribution is predominantly temperature controlled in the chimneys, it guides our understanding of the distribution of the other elements. For example, a similar distribution of Sn suggests it is also mainly temperature controlled (Fig. 3.13), and is likely due to substitution for Fe in chalcopyrite (Maslennikov et al., 2009). By contrast, the distribution of Ag and In throughout *Lena* chimney shows largely the opposite distribution, i.e., a gradual increase in content towards the exterior parts of the chimney. Indium also substitutes for Fe in chalcopyrite (Butler and Nesbitt, 1999), therefore the distribution pattern in this chimney suggests Sn is preferentially incorporated over In into chalcopyrite at higher temperatures. Similarly, Ag may substitute for Cu in chalcopyrite (Butler and Nesbitt, 1999), but may be excluded by previous distortions in the mineral lattice from Se and Sn substitution in the hottest part of the chimney.

The most distinguishing feature of the other element maps for *Lena* chimney is the rings within the zone of massive chalcopyrite (Figs. 3.10, 3.12 and 3.13),

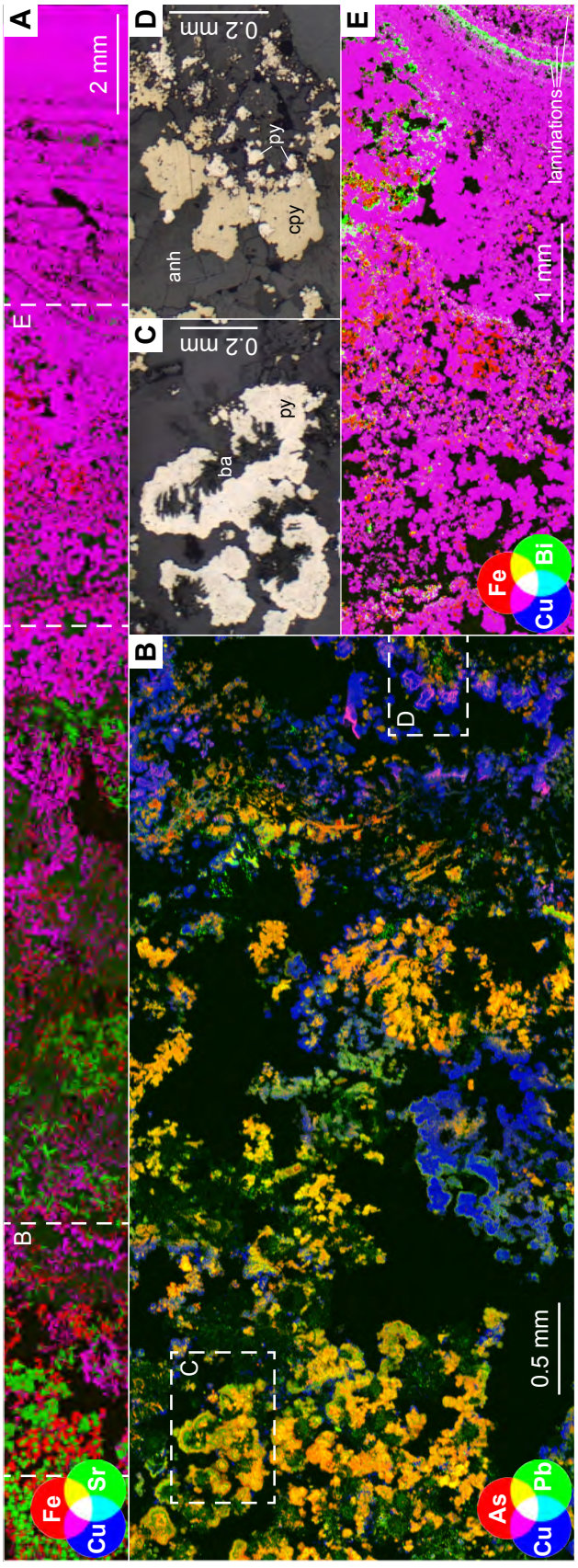

Figure 3.11 RGB images of *Lena* chimney (851-3A; chalcopyrite-sphalerite). (A) Depicts the major mineralogy of the sample: chalcopyrite (purple); pyrite (red); Sr-bearing barite (bright green) and anhydrite (dull green). (B) Towards the exterior of the sample, colloform banding of Pb-rich and As-rich layers within pyrite are displayed by intricate ring patterns (green-yellow; see C), and internal boundaries within chalcopyrite are highlighted by a fine layer of As-bearing tennantite (see D). (C) and (D) Reflected light microphotographs of areas shown in B, in which the trace element detail is not obvious. (E) Micro-inclusions of Bi appear white due to contamination by surrounding chalcopyrite, and are aligned along laminations or internal boundaries. Discrete Bi grains are in one thicker lamination and in pore space just outside of the laminated chalcopyrite, sometimes overlapping with pyrite (yellow). Towards the exterior, outside of this image, Bi is nearly absent.

where each ring contains a different combination and content of elements (Tables 3.3 and 3.5). Ring 3 is clearly different to the others given the presence of anhydrite (Ca), possibly minor barite (Ba), and formation of larger grains particularly visible in the Tl, Cd, Pb and Zn maps shown in Figure 3.13. These elements, along with increased As, suggest sphalerite and galena (or Pb-As sulfosalts) have formed adjacent to the anhydrite, with the whole mineral suite typical of precipitation from relatively lower temperature (~250°C) fluids (e.g., Hannington et al., 2005; Kristall et al., 2011). This is also consistent with the lack of Sn, Au, Bi, Te and Mo in this ring, all of which are typically associated with higher temperature fluids (e.g., Henley and Berger, 2013). Here, temperature once again appears to play a dominant role. The remaining rings mostly correlate with the subtle rings shown by the Se and Sn maps and may similarly be related to temperature. However, if the temperature changes by 40°C across the innermost ~9 mm of the chimney wall, can we reasonably expect a change in temperature of <10°C to account for such dramatic mineral precipitation? Another factor may dominantly control the formation of trace element rings, one that has a pronounced effect on the precipitation of Au, Bi, Te, Ag, Mo, and Tl and especially for rings 4 and 5 (Fig. 3.13).

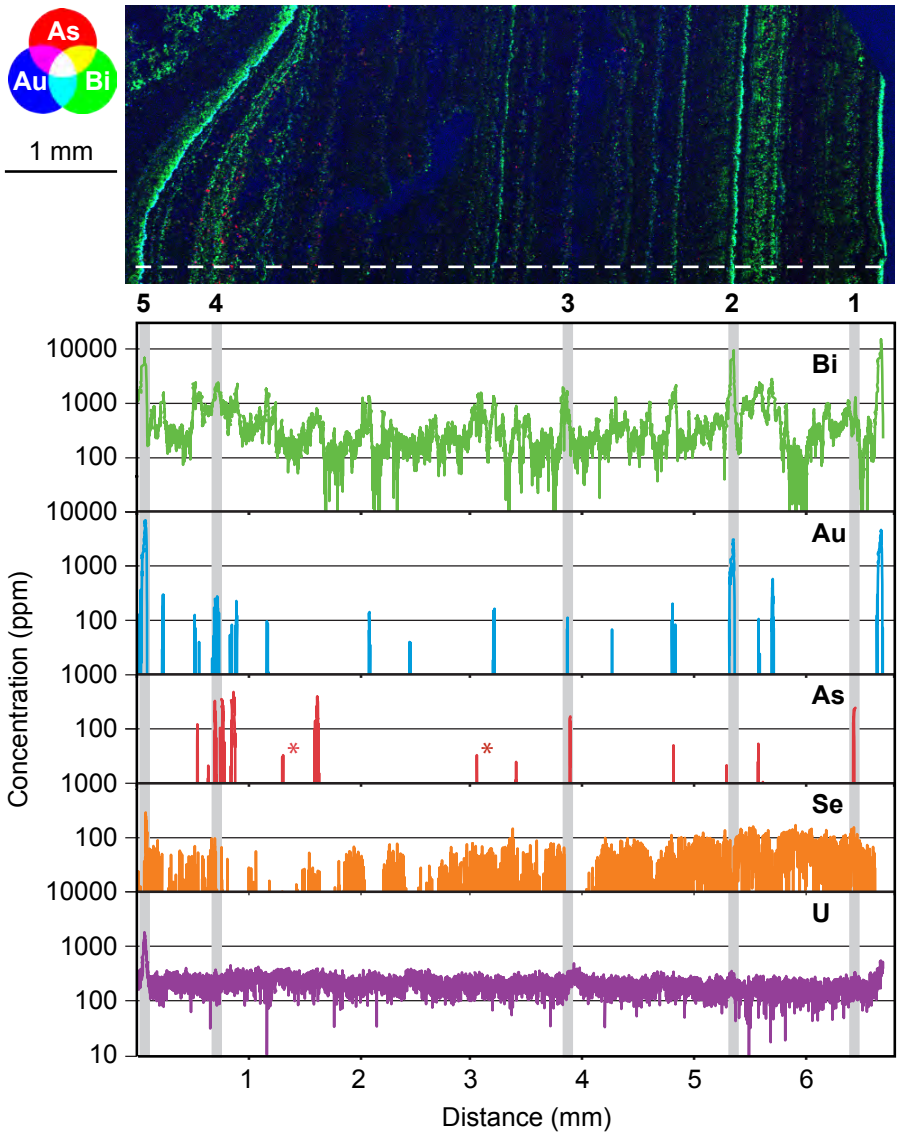

Figure 3.12 RGB image of trace element rings in the interior of *Lena* chimney. Slight variations in green/cyan on the image indicate varying amounts of Au together with Bi. Dull blue in the background is from minor Au-bearing glass showing through holes/pores. The abundance of several elements along a traverse (dashed line) is shown below. Five rings have been highlighted showing a consistent presence of Bi, but variable Au, As, and Se. Arsenic displays more discrete micro-grains (red specks) than uniform distribution through the rings, some of which are displayed along the traverse (*). Lattice-bound Se in the innermost chalcopyrite (far right) gradually diminishes towards the exterior side. Uranium peaks just above background indicate seawater incursion into the chimney (see text).

One of the more diagnostic features of the trace element rings is the presence of U (Figs. 3.12 and 3.13; Table 3.5). Uranium is dominantly sourced from seawater (e.g., Kristall et al., 2011) and thus multiple narrow rings within the chalcopyrite laminations that are high in U content indicate rapid and repetitive advection of seawater into the chimney interior. The resultant changes in chemical properties such as pH, fO_2 and fS_2 may therefore account for precipitation of the other trace elements. The particularly high abundances of Tl, Ag, Au, Bi, Mo, and Te in rings 4 and 5 may indicate that these were the locations of the earliest seawater-hydrothermal mixing 'fronts' that occurred when the chalcopyrite conduit lining was still thin. Molybdenum is particularly enriched in these two rings compared to the rest of the sample. This could be from entrainment of some seawater-derived Mo at these earliest, strongest mixing fronts,

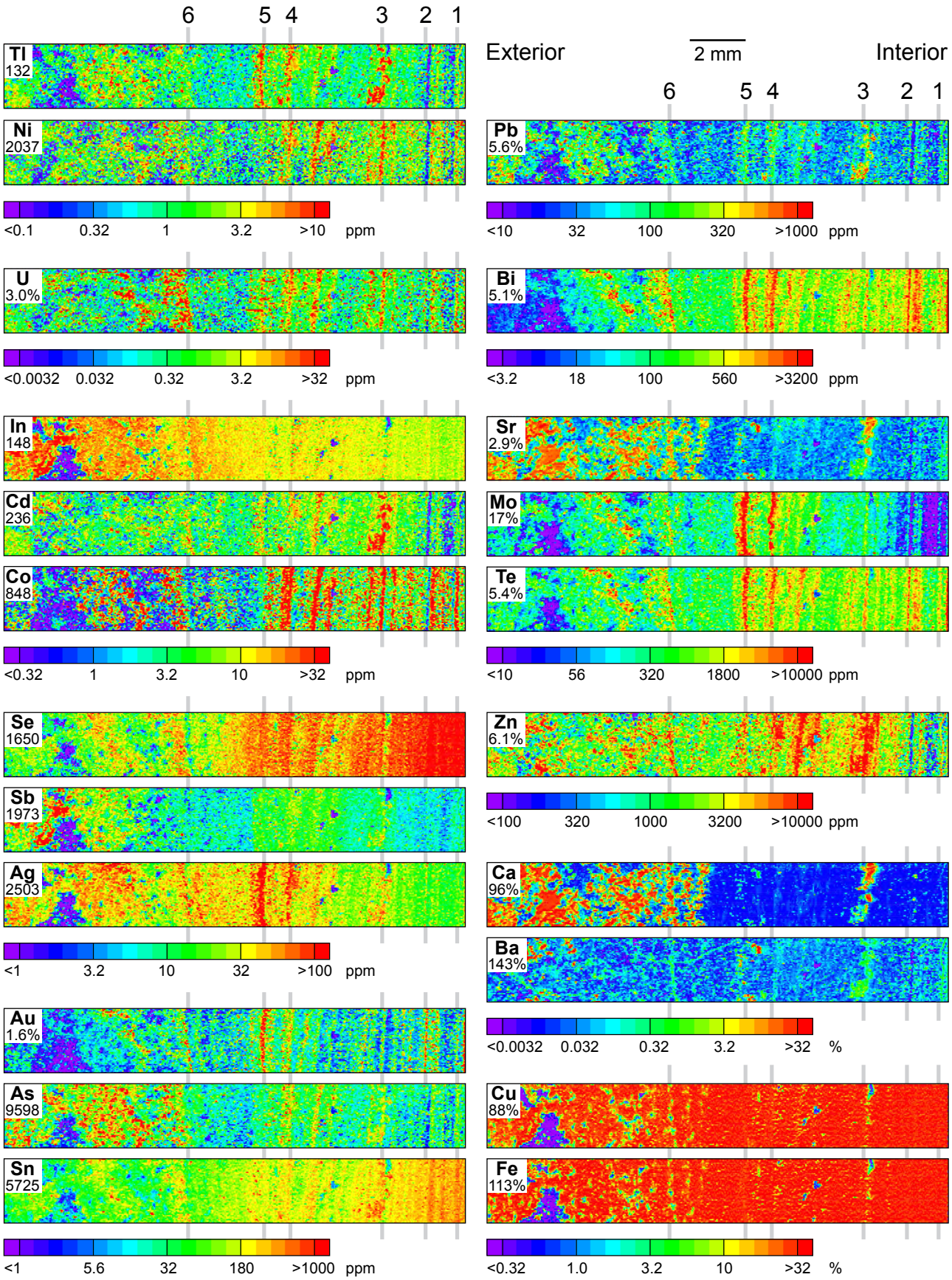
6 5 4 3 2 1
Exterior
2 mm
Interior
Tl 132
Ni 2037
<0.1 0.32 1 3.2 >10 ppm
Pb 5.6%
<10 32 100 320 >1000 ppm
U 3.0%
<0.0032 0.032 0.32 3.2 >32 ppm
Bi 5.1%
<3.2 18 100 560 >3200 ppm
In 148
Cd 236
Co 848
<0.32 1 3.2 10 >32 ppm
Sr 2.9%
Mo 17%
Te 5.4%
<10 56 320 1800 >10000 ppm
Se 1650
Sb 1973
Ag 2503
<1 3.2 10 32 >100 ppm
Zn 6.1%
<100 320 1000 3200 >10000 ppm
Ca 96%
Ba 143%
<0.0032 0.032 0.32 3.2 >32 %
Au 1.6%
As 9598
Sn 5725
<1 5.6 32 180 >1000 ppm
Cu 88%
Fe 113%
<0.32 1.0 3.2 10 >32 %

Figure 3.13 (previous page) LA-ICPMS element maps of *Lena* chimney (851-3A) with maximum abundances for each element shown (ppm, unless noted as wt. %). The calibration of Fe and Ba is obviously incorrect as maximum contents are over 100 weight %. Note that the surface of the laser mount was adjacent to that of the thin section used in SXFM mapping so this image is similar to, but not the same as, that shown in Figure 3.10. Also for comparison, the area mapped (20.5 x 2.3 mm^2) and spot size used (47 μm) are shorter and coarser than that for SXFM, respectively. The colour scale shown below each map/group has been maximized to show the most detail for each element, and groups are arranged in increasing abundances down the left and then right columns. A smearing effect is noted for some elements whereby high abundances in one pixel may bleed into an adjacent pixel; this is most noticeable at the hole in chalcopyrite (purple at left of Cu & Fe images), which is smeared in some images (i.e. Se, Sn, Te). Trace element rings within interior chalcopyrite is apparent in most of the maps, and grey lines in the background highlight six rings discussed in the text and correspond to numbered rings in Figure 3.12.

as seawater contains more Mo than other metals and transition metals (i.e., 110 nmol/kg of Mo compared to 23 nmol/kg of As, 0.06 nmol/kg of Pb, 0.004 μmol/kg of Cu, and .006 μmol/kg of Zn; Metz and Trefry, 2000). Later cycles of inferred seawater advection (e.g., those indicated by rings 2 and 1) may have had a decreased seawater component due to a subsequently thickened chimney wall. Although trace element precipitation does not require these mixing events – as demonstrated by moderate background levels of Te and Bi in the interior chalcopyrite, for example – the periodic seawater influx proves a more *efficient* mechanism for element precipitation.

Which specific chemical factor, or combination thereof, controls trace element precipitation in the Brothers chimneys is difficult to discern. Uranium precipitation is likely controlled by changes in redox conditions, as it has low solubility in reduced (vent) fluids (Kristall et al., 2011); similarly, Au and Te will precipitate from hydrothermal fluids that mix with oxidizing (seawater) fluids (Butler and Nesbitt, 1999; Maslennikov et al., 2009). Silver, by contrast, is highly sensitive to changes in pH, especially above ~4 (Stefánsson and Seward, 2003). However, modelling by Tivey and McDuff (1990) shows inward advection of seawater barely changes the pH, fO_2 and fS_2 gradients in inner chimney walls when compared to a system with strong outward advection of hydrothermal vent fluids. Whether fluids flow inwards or outwards through a chimney wall is a function of the pressure differential exerted between internal hydrothermal fluids and external seawater, and this is largely determined by hydrothermal flow rates. Outward advection of hydrothermal fluids was obviously the dominant process in *Lena* chimney at the time of sampling, considering it was vigorously discharging 274°C hydrothermal fluids. Moreover, Tivey and McDuff (1990) show that bornite forms around the external margin of the chalcopyrite layer during prolonged periods of inward seawater advection; therefore, the lack bornite in *Lena* chimney indicates outward advection of hydrothermal fluids was consistently the dominant process. For inward advection of seawater to occur in a chimney, the flow rate of venting must drop, and the narrowness of the trace element rings (15 - 40 μm) suggest that when it did occur, it was very short-lived. One possible influence on hydrothermal fluid flow rate is sub-seafloor phase separation ("gas explosions"), inferred to be occurring beneath the NW Caldera field, which causes unsteady, turbulent flow and is consistent with temporary, but repetitive cycles of reduced fluid flow (Dziak et al., 2008; de Ronde et al., 2011). Thus, the *equilibrium* pH, fO_2 and fS_2 gradients modelled by Tivey and McDuff (1990) during periods of inwardly advecting seawater are considered not to have been established in *Lena* chimney, but rather it is a combination of *rapidly changing* chemical gradients that induces the

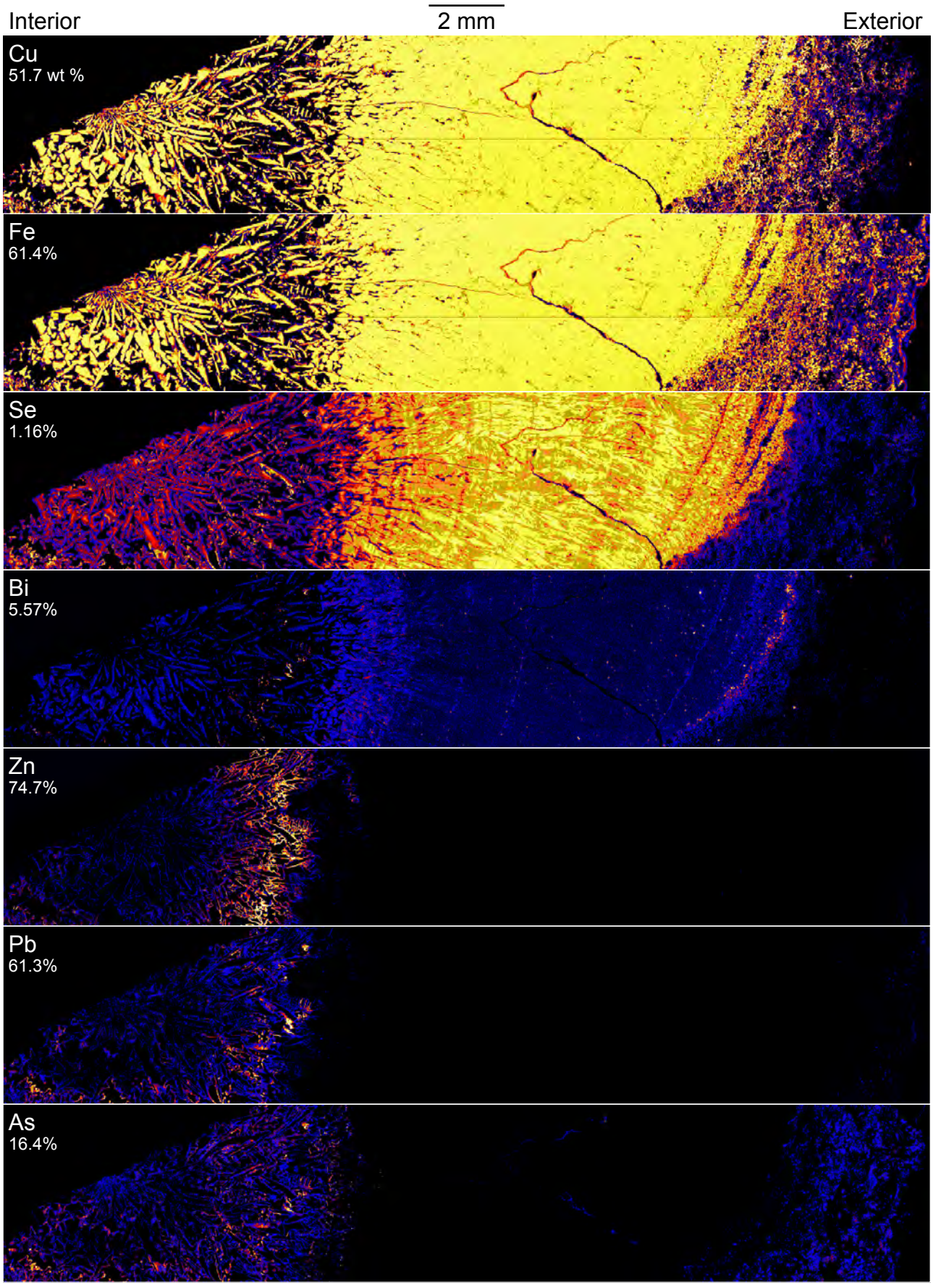
Interior
2 mm
Exterior
Cu
51.7 wt %
Fe
61.4%
Se
1.16%
Bi
5.57%
Zn
74.7%
Pb
61.3%
As
16.4%

Figure 3.14 (previous page) SXFM element maps *Leg of Lamb* chimney (851-1B; chalcopyrite-bornite) with maximum weight % for each element shown. Area mapped is 26 x 5 mm^2. Refer to colour scale in Figure 3.4. Black areas in the top left and far right are glass, while black through the middle of Zn, Pb, and As maps indicate their absence through the massive chalcopyrite. Faint horizontal lines on the Cu and Fe maps are artefacts from image processing.

instantaneous precipitation of the trace element-rich rings. Temperature likely also drops during periods of seawater incursion into the chimney interior and so may be a contributing factor, but the relatively minor decrease of Se and Sn content in response to these mixing events suggests temperature plays a subordinate role. The exception is ring 3, in which decreased hydrothermal fluid flow must have occurred for long enough such that anhydrite, sphalerite, and galena/sulfosalt precipitation occurred within the massive chalcopyrite zone.

A cylinder of massive chalcopyrite dominates the *Leg of Lamb* chimney, and this displays textures that suggest a different style of formation to the chalcopyrite found in *Lena* chimney (Fig. 3.14). That is, the external chalcopyrite margins show relict laminations, whereas the innermost chalcopyrite comprises elongate grains that converge towards the centre of the conduit, and which have coalesced ~6 mm from the central orifice. The distribution of Se is also noteworthy in this chimney as it reflects both of these textures with a fabric that is elongated towards the centre of the chimney, but which also displays internal banding, imparting an overall wavy appearance. In contrast to *Lena* chimney, however, there is no overall variation in Se content through the *Leg of Lamb* chimney wall. Rather, the interior massive chalcopyrite margin, at the transition to elongate grains, grades to a zone where Bi is preferentially incorporated over Se (Fig. 3.15d). A double substitution is required for Bi^{3+} to substitute for Fe^{2+} or Cu^{2+} in chalcopyrite, with Au^{1+} a likely candidate for the substitution partner due to scavenging by liquid Bi (see below). Furthermore, the internal elongate chalcopyrite grains in this chimney contain significantly more Au than the external massive chalcopyrite (i.e., >30.0 versus 20.8 ppm, respectively; de Ronde et al., 2011), and EMP analysis confirms that this difference is not associated with the internal sphalerite or galena (Table 3.3). Unfortunately, spectral interference with Zn did not allow us to resolve the distribution of Au in the centre of the *Leg of Lamb* chimney.

The exact mechanism(s) responsible for the change from Se-bearing to Bi-bearing chalcopyrite are unclear. Two studies have proposed $Bi_2S_2(OH)_2$ as a dominant complex for Bi transport in reduced-S, acidic, hydrothermal fluids at 275 - 350°C. Skirrow and Walshe (2002) supported increasing pH (from an initial value of 5.2) was the dominant trigger to destabilize the complex, whereas Törmänen and Koski (2005) noted this complex is strongly temperature dependant, and could be sensitive to changes of < ~30°C. Given that fluids from the NW Caldera site have a pH of around 3, a shift to over 5 seems unlikely without significant seawater mixing and there is no other evidence for that to have occurred within the massive chalcopyrite. Conversely, mantling of the elongate grains of chalcopyrite by sphalerite and galena signify a shift to relatively lower-temperature fluids late in this chimney's growth. However, the chalcopyrite in *Lena* chimney doesn't show a transition from Se-bearing to Bi-bearing as temperature decreases; that is, the background Bi content in the inferred lower temperature chalcopyrite (left side) of Figure 3.13 does not increase compared to that of the high-temperature, Se-rich (right side) chalcopyrite; rather

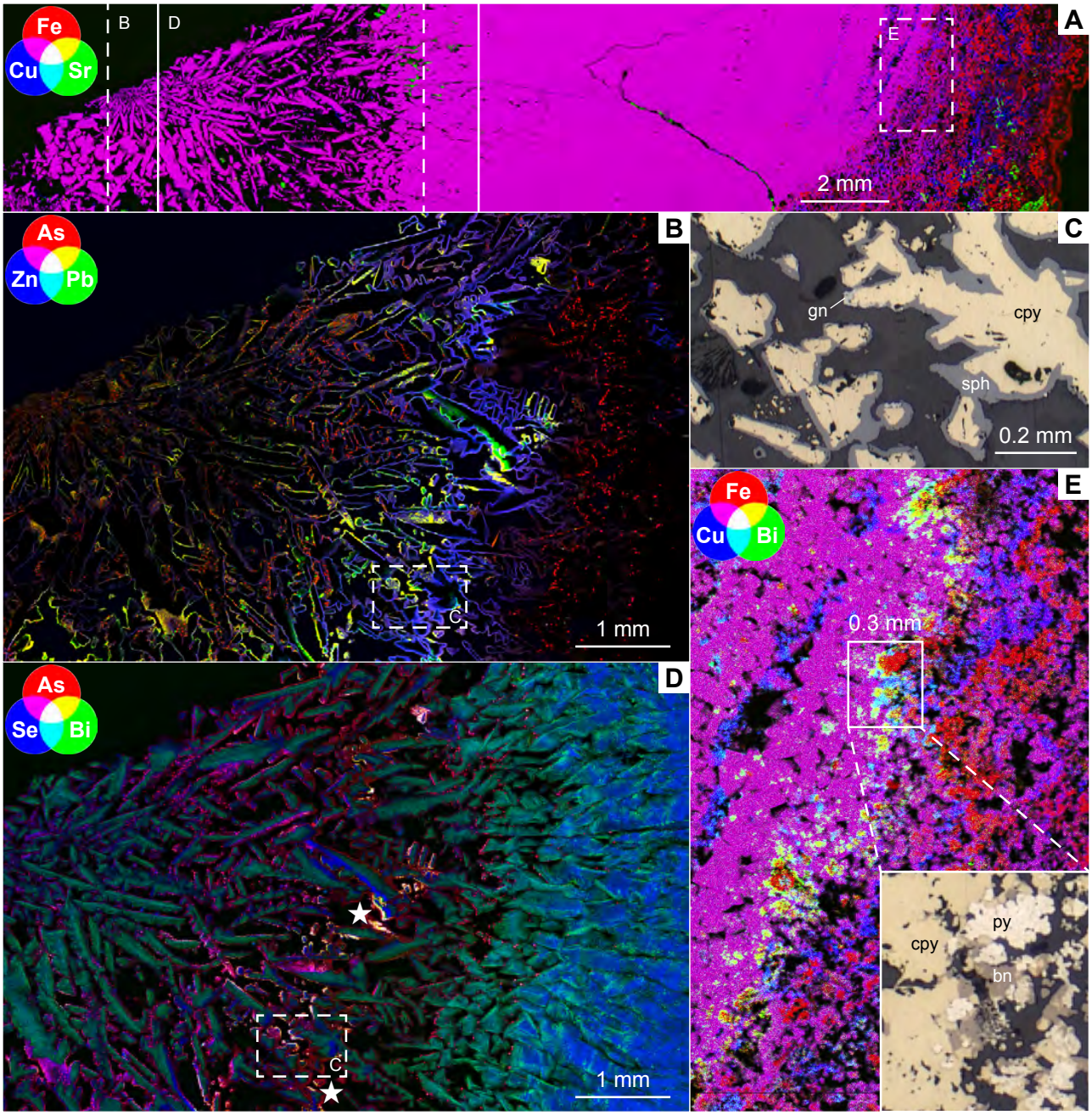

Figure 3.15 RGB images of *Leg of Lamb* chimney (851-1B; chalcopyrite-bornite). (A) Depicts the major mineralogy of the sample: chalcopyrite (purple); Cu-enriched bornite, chalcocite, covellite (blue); Fe-rich pyrite, hematite, goethite, Fe-oxides (red); Sr-bearing barite (green). (B) Sphalerite (Zn) and galena (Pb) mantle the internal, elongate chalcopyrite (see C), with each containing various amounts of As (note the blue to purple and orange to yellow ranges in sphalerite and galena, respectively). Arsenic is also present as discrete, micro-grains lining the outside of the chalcopyrite (compare with D). (C) Reflected light microphotograph of the mantling sphalerite (grey) and minor galena (bright blue) around skeletal chalcopyrite. (D) Lattice-bound Bi highlights the internal, elongate chalcopyrite and displays a similar wavy pattern to, and overlaps with, Se at the internal massive chalcopyrite margin. This image also shows some Bi, Se and As (magentas, yellows and whites) in the mantling sphalerite and galena, which EMP spot analyses (★) contradicts (Table 3.3). Thus, this mantling Bi and Se are likely SXFM artefacts caused by Bi and Se fluorescence escaping from the elongate chalcopyrite. (E) Bismuth displays a complex distribution at the exterior of the massive chalcopyrite: it is either lattice-bound or present as micro-inclusions within chalcopyrite (white); within pyrite (yellow) and bornite (cyan); and as discrete grains (green). Reflected-light microscopy does not show this complexity (inset).

the opposite occurs. Thus, there is no compelling evidence to suggest that either pH or temperature caused the transition from Se- to Bi-bearing chalcopyrite. Auclair et al. (1987) also analysed one chimney sample in which Se distribution did not decrease through the massive chalcopyrite and, like the *Leg of Lamb* chimney, it has a more oxidized suite of Cu-phases in its outer chalcopyrite margins (i.e., bornite, digenite, and covellite). These authors attributed the uniform Se distribution to 'oxidative leaching'. Although we cannot exclude the possibility of redox control on Bi distribution, the lack of other trace element layers at the same transition do not support this theory. Finally, Berkenbosch et al. (2012a) suggested that the elongated, internal chalcopyrite is a pseudomorph after barite, thus it is possible that the chemistry of this replacement reaction influenced Bi precipitation. What is certain, is that this chimney became clogged and eventually sealed at both its top and bottom, during which time a host of physicochemical fluid parameters would have changed (Fig. 3.2d).

Table 3.5 Elemental abundances in *Lena* chimney rings compared to that of the background (see LA-ICPMS maps, Fig. 3.9).

	Element	Background mean (ppm)	*Exterior* 6	5	Band 4	3	2	*Interior* 1
Metals	Sn	251						√
	Au	121	√	√	√		√	
	Bi	775	√	√	√		√	
	Te	1842	√	√	√		√	
	Ag	38		√	√			
	Mo	1327		√	√			
	Tl	2		√	√	√		
	Pb	101		√		√		
	As	67			√	√		
	Ni	3			√	√		
	Co	18			√	√		√
	Cd	8				√		
	Zn	1438				√		
Sulfates	Ca	3634	√			√		
	Sr	147	√	√		√		
	Ba	2980		√				
	U	6	Δ	Δ	Δ	Δ		Δ

√ band mean is >2x that of background
Δ band median is >2x that of background
□ indicates element is in Zn- or Pb-rich sphalerite or galena

3.6.2 Origin of chimney trace elements

One aim of this study was to investigate whether element mapping could elucidate any information about magmatic contributions to Brothers mineralization. In the chimneys studied, the abrupt precipitation of trace element rings in *Lena* chimney is largely not mineralogically controlled. Although depositional conditions are not considered the same for each element (e.g., Ag is especially limited in the inner rings), we suggest the elemental content of each ring (except Mo and U) serves as a first-order proxy for vent fluid composition through time.

A common method to establish magmatically-derived components of a degassing volcano is to determine which elements are enriched above that expected from wall-rock dissolution by calculating the enrichment factor (EF) per element, *i*:

$$EF_i = \frac{(C_i/C_r)_{sample}}{(C_i/C_r)_{rock}}$$

where $(C_i/C_r)_{sample}$ is the concentration of *i* relative to that of a reference element, *r*, in the sample, and $(C_i/C_r)_{rock}$ is the same ratio in the host rock (e.g., Zoller et al., 1974; Lepel et al., 1978). A non-volatile reference element is commonly used, such as Mg or Al (e.g., Taran et al., 1995; Symonds et al., 1996). Elements with EFs close to 1 indicate a host-rock source (i.e,

dissolution) whereas those with higher EFs are enriched in the fluid and indicate a magmatic source. To calculate the EFs for the trace element enriched rings in *Lena* chimney (Table 3.6; Fig. 3.16a), Brothers dacite compositions were averaged from the work of Timm et al. (2012) and Haase et al. (2002). As these published data do not include certain elements, we calculated $(C_i/C_r)_{rock}$ values for Cd and In using the more recent (unpublished) rock data of L. Gubbay-Nemes (pers. comm., 2016; n = 18 samples). Likewise, for Au, Se, and Te values we followed the example of Symonds et al. (1996) and used abundances from geological reference sample GSP-1 (Govindaraju, 1994), a granodiorite from Silver Plume Quarry, CO, that most closely represents the composition of Brothers dacite. In this study, we chose non-volatile Sm (Rubin, 1997) as a reference element since Mg and Al were not analysed. Similar results were obtained using La and Th as reference elements except they calculate to slightly higher enrichment values. Additionally, to ensure Sm was a reliable reference element we calculated EFs using *bulk* chimney Mg values for $(C_r)_{sample}$ (instead of individual values from each band; de Ronde et al., 2011), and although the range is narrower the average values are in good agreement, with the exception of Au, Se and Te (derived from the granodiorite standard; Fig. 3.16a, lower). Since U is sourced mainly from seawater, it was excluded from the analysis.

A plot of the *Lena* enrichment factor curve for Brothers trace elements is shown in Figure 3.16a. Rings 3 and 6 have the lowest enrichment overall, but as noted above, are associated with anhydrite and thus have likely experienced pronounced mixing with seawater, consistent with their EF increase for Sr; the other four rings generally overlap at higher values. Silver is notably enriched in rings 4 and 5, concomitant with less Se and Sn, which we believe reflects a decreasing temperature gradient. Likewise, the strong enrichment of Mo in rings 4 and 5 represents an additional seawater component as described above. For comparison, EFs using whole rock analysis from this chimney plot within the lower range of *Lena* EFs (Fig. 16a; de Ronde et al., 2011), demonstrating that bulk analysis of chalcopyrite-rich, sulfate-poor samples can be used as a first-order proxy of elemental enrichment.

The criteria used to define the EF value that divides host-rock-derived elements from those that are magmatically derived differs between workers. For example, some authors suggest any enrichment over ~10 x that of the host rock/magma is considered to be magmatic (e.g., Taran et al., 1995; Kim et al., 2011). Alternatively, Symonds et al. (1990) attributed those elements with log(EF) <3.2 to be at least partially derived from wall-rock dissolution, solely because elements below that value comprised the flatter parts of their enrichment curves. This criterion may better suit our data, in which even the lowest EF value averages >10. Hence, we adopt the prominent slope increase between Sn and Ag as our divide between magmatic and host-rock sourced elements. Therefore, highly enriched elements in *Lena* chimney Au, Te, Bi, Cu, Se, and Ag indicate input from an exsolved magmatic fluid. Molybdenum is excluded from this list due to the artificial enhancment of its EFs by seawater in rings 4 and 5. Considering the EFs of Mo in rings 3, 2, and 1, it may be only be partially sourced from exsolved magmatic fluids along with Sn, In, Sb, Cd, As, Zn, Pb, and Tl, which together comprise a suite of 'transitional' elements. Iron, Ba, Ni, Sr, and Co, with the lowest EF values, originate solely from dissolution from the host-rock (see below).

Table 3.6 Enrichment factors for *Lena* chimney rings (851-3A-1).

Dacite concentration (ppm)[1]	0.0014	0.023	0.078	31.5	0.069	0.040	2.00	0.076	0.154	0.117	2.82	77.1	7.24	0.48	36232	946	5.68	223	83.0	5.55
Sample	Au^2	Te^2	Bi	Cu	Se^2	Ag	Sn	In^3	Sb	Cd^3	As	Zn	Pb	Tl	Fe	Ba	Ni	Sr	Co	Sm
Band 1	50036711	53839249	1808931	1191741	1146112	55021	30158	13460	6071	5562	4254	1190	1364	704	1098	188	88	25	68	
Band 2	328693405	151784409	4940323	1521582	991869	96645	24184	21486	6595	7902	1700	1891	1958	422	1294	214	41	27	11	
Band 3	2849280	5037680	82999	64999	38332	8528	1462	1074	970	1892	440	470	287	106	63	34	10	44	6	
Band 4	87936774	118693795	2880048	828174	469424	232042	11379	13535	13589	9195	8895	2614	2261	1257	846	71	91	13	77	
Band 5	328724499	152453266	3350614	748080	370956	368997	7912	13047	8506	7705	1421	1663	2120	1160	625	835	32	120	6	
Band 6	34088370	18606799	567252	139439	30912	41762	1072	3697	1346	2677	784	777	412	107	126	45	14	263	2	
Bands average	**138721507**	**83402533**	**2271694**	**749002**	**507934**	**133832**	**12695**	**11050**	**6180**	**5822**	**2916**	**1434**	**1400**	**626**	**675**	**231**	**46**	**82**	**29**	
Bulk analysis[4]	*6659536*		*530415*	*240950*	*60986*	*9656*	*1085*	*3654*	*3245*	*929*	*1438*	*241*	*269*		*153*	*165*	*15*	*92*	*3*	

[1] Averaged (n=5) from Timm et al. (2012) and Haase et al. (2002) except where otherwise noted
[2] Dacite values from sample GSP-1 in Govindaraju (1994) with 26.3 ppm Sm
[3] Dacite values averaged (n=18) from L. Gubbay-Nemes (pers. comm) with 5.63 ppm Sm
[4] *Calculated with data from de Ronde et al. (2011). Blanks were not analysed*

We have compared our results to those of condensates from volcanic fumaroles of active, subaerial, arc volcanoes (i.e., Showa Shinzan, Japan arc; Augustine, Aleutian arc; Kudryavy, Kuril arc; Tolbachik, Kamchatka arc), a rift volcano (Erta Ale, East African Rift), and quenched, molten S from a submarine, backarc volcano (MTJ-1, Lau Basin; Fig. 3.16b). Overall, our EF values are the highest and those from MTJ-1 (also referenced in literature as volcano "O"; Arculus, 2005; and Niuatahi volcano; Embley et al., 2013) are the lowest. Considering that even the lowest of our enrichment factors is above 0, our values may be overestimated by at least half an order of magnitude, possibly because Sm is present in such low abundances in our samples. Thus, we have also plotted a lowered range to account for this effect. Similarly, the use of Zn as the EF reference element for MTJ-1 by Kim et al. (2011) may underestimate those values, as Zn is a moderately volatile element itself. In terms of absolute values, our data compare favourably with those from the subaerial volcanoes, particularly when applying the lowered *Lena* chimney range. Of the magmatic elements, only *Lena*'s Au and Cu enrichments are significantly higher than those seen in subaerial volcano condensates, with Cd, As and Tl enrichment lower in the transitional elements and Fe, Ba, and Sr higher for the rock-derived elements. The EFs for Brothers Mo data compare well to condensates from three of the subaerial volcanoes, supporting the idea that at least some of the Mo content in the trace element rings may be magmatic.

For the volcanoes other than Brothers there is a consistent pattern in the *order* of enrichment, i.e., Bi, Te, or Cd have the highest value and together with Se, Au ± As and Ag are distinctly magmatically derived. A middle group with moderate to high

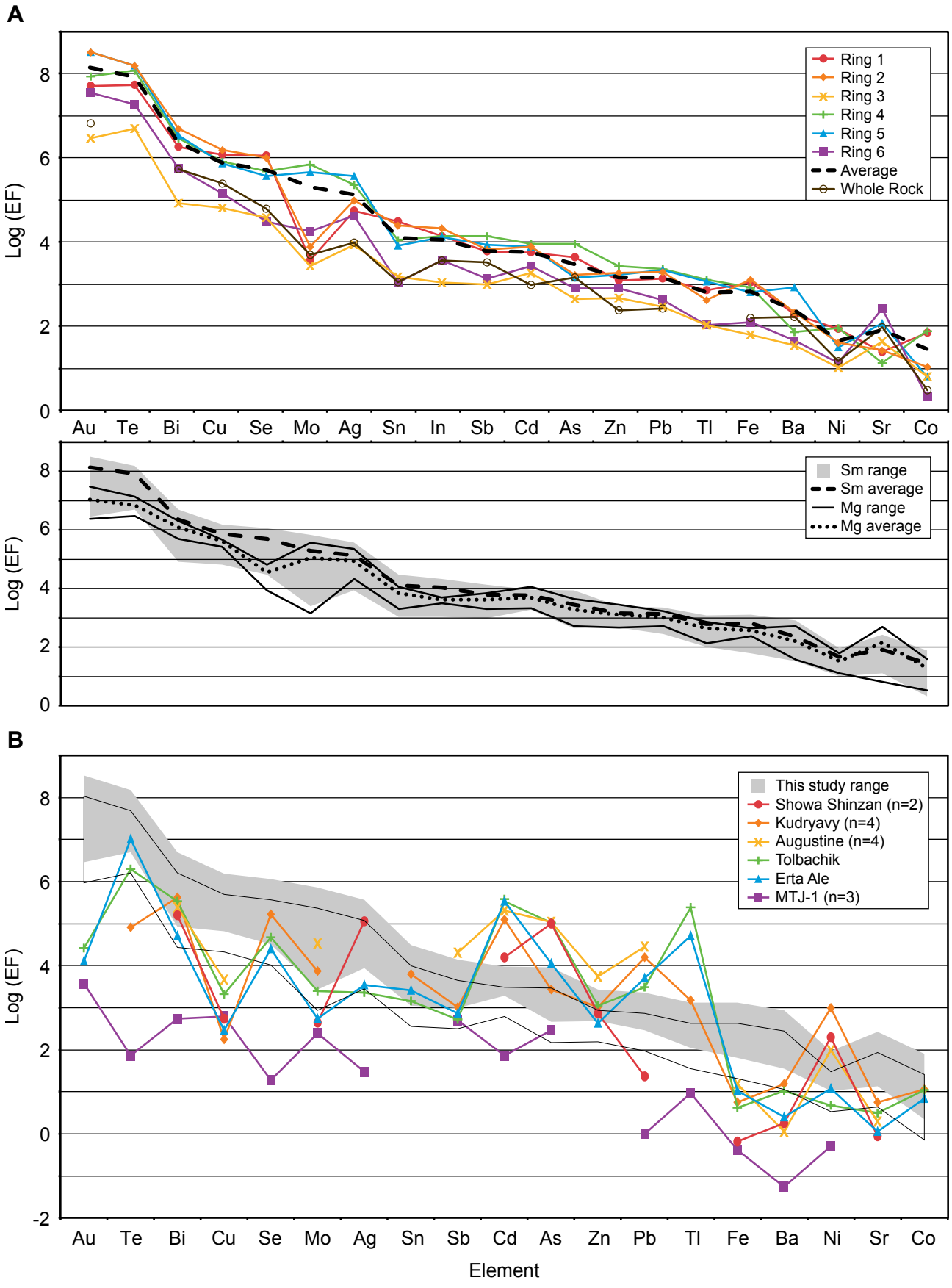
A
Log (EF)
8
6
4
2
0
Au Te Bi Cu Se Mo Ag Sn In Sb Cd As Zn Pb Tl Fe Ba Ni Sr Co
Ring 1
Ring 2
Ring 3
Ring 4
Ring 5
Ring 6
Average
Whole Rock
Log (EF)
Sm range
Sm average
Mg range
Mg average
B
Log (EF)
-2
Au Te Bi Cu Se Mo Ag Sn Sb Cd As Zn Pb Tl Fe Ba Ni Sr Co
Element
This study range
Showa Shinzan (n=2)
Kudryavy (n=4)
Augustine (n=4)
Tolbachik
Erta Ale
MTJ-1 (n=3)

Figure 3.16 (A) Enrichment factors (EFs) for elements within the trace element rings of *Lena* chimney, 851-3A, using Sm as a reference element. The rings correspond to those in Figures 3.12 and 3.13. Ring 3 is generally the least enriched, followed by ring 6. Gold and Mo have the most variable enrichments, spanning over 2 orders of magnitude, although the enrichment of Mo in rings 4 and 5 reflects an additional seawater component (see text). Lower graph shows the range of enrichment factors calculated using bulk chimney Mg content (de Ronde et al. 2011) as the reference element for comparison. The Mg range is narrower and average values are slightly lower but largely agree for most elements except Au, Te and Se (see text for further explanation). (B) Enrichment factors from A compared to those for fumarole condensates from subaerial arc volcanos and a continental rift volcano (Erta Ale), plus quenched, molten S from a submarine, back-arc volcano (MTJ-1). Erta Ale values correlate well with those from the arc volcanoes despite being from a different tectonic setting, and particularly match Tolbachik, which is the only other basaltic volcano. The published literature values use Mg and Al as the reference element, except for MTJ-1, which uses Zn for lack of a better choice. Indium has been removed due to lack of data. We excluded one sample (S4) from MTJ-1 in our average as it was significantly different from the rest. Data from: Augustine, Symonds et al., 1990; Kudryavy, Taran et al., 1995; Showa-shinzan, Symonds et al., 1996; MTJ-1, Kim et al., 2011; Erta Ale, Zelenski et al., 2013; Tolbachuk, Zelenski et al., 2014.

levels of enrichment includes As, Ag, Pb, Mo, Sn ± Zn, whereas lower levels of enrichment are typical of Zn, Sb, Cu and Ni. Barium, Sr, Co, Fe ± Ni are the rock-derived elements (Symonds et al., 1990; 1996; Taran et al., 1995; Zelenski et al., 2013; 2014). Likewise, condensates from subaerial arc volcanoes show no U enrichment (not shown; Symonds et al., 1987; Zelenski et al., 2014), supporting its entrainment in Brothers chimneys from seawater alone. Only Tl does not readily fit into these groups with enrichment factors both very high or in the lower middle range. The order of enrichment factors for *Lena* chimney are largely in agreement with the above pattern, with three significant exceptions that duplicate the discrepancies in absolute values noted above; 1) Au is the most enriched element, 2) Cd is only moderately enriched, and 3) Cu is magmatically derived.

To evaluate whether *Lena* chimney Au and Te EF values are spuriously high due to unrepresentative values from the standard GSP-1, we compared nine Au/Sm values and four Te/Sm values for other reference andesites, rhyolites and granites, as given in Govindaraju (1994). Even using the highest values for these ratios for each element (thus giving the lowest EF), Te and Au still have the 1st and 5th (i.e., between Se and Mo) highest EFs, respectively. However, that *Lena* chimney may be extremely enriched in Au is not surprising, as its bulk analysis of 70 ppm Au is one of the highest contents reported for a seafloor chimney (de Ronde et al., 2011). Berkenbosch et al. (2012a) suggested that the high Au content in *Lena* chimney may be due to scavenging by liquid Bi, consistent with high chimney Bi contents (>2000 ppm), numerous Bi-Au-tellurides and possible quench textures of native Bi in the chimney. The melting point of Bi (271°C) is below that of *Lena*'s venting temperature (302°C), and liquid Bi can concentrate Au from hydrothermal fluids, even in fluids that are Au-undersaturated (Tooth et al., 2008). The high Bi content is also reflected in Brothers dacite (and therefore magma, by extension), which contains more Bi than any other Kermadec arc volcano, likely due to a greater influence from subducted marine sediments (Timm et al., 2012).

The decreased Cd enrichment in *Lena* chimney rings could be a result of mineralogical control. For example, Cd content is highly correlated with sphalerite in the sphalerite-chalcopyrite chimney type (Table 3.4), and sphalerite from all the chimneys has Cd contents >4500 ppm, as opposed to <700 ppm in chalcopyrite, galena, pyrite, and Pb-As sulfosalts (Table 3.3). Similarly, de Ronde et al. (2011) showed a strong correlation between Cd and Zn in an expanded range of Brothers mineralized samples. Thus, Cd enrichment could be limited by sphalerite precipitation in all rings except for ring 3 (Table 3.5).

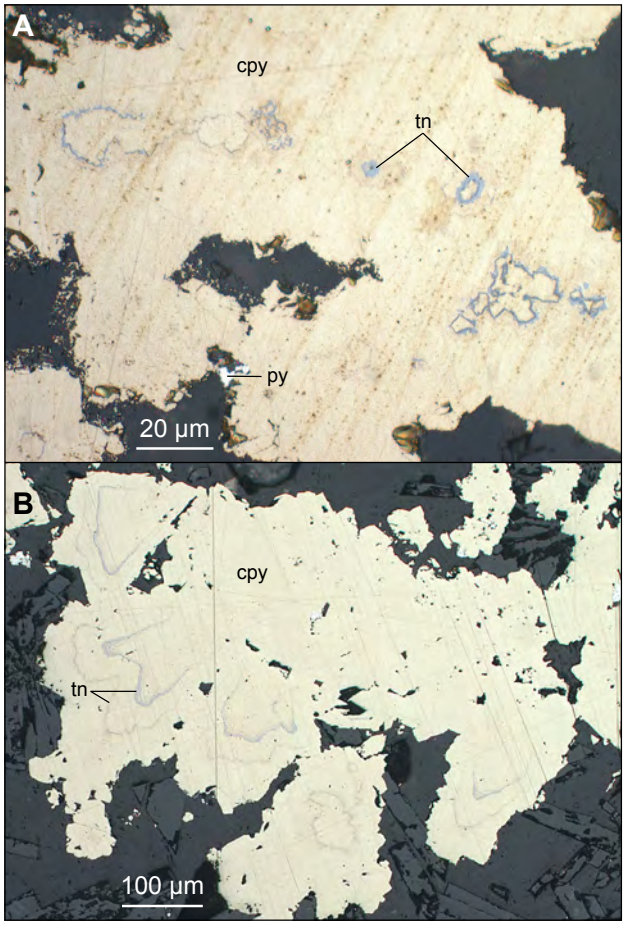

Figure 3.17 Photomicrographs of inclusions in chalcopyrite of *Lena* chimney. (A) Sub-rounded tennantite (light grey) inclusions in chalcopyrite; with dark blue covellite inside? Compare with Figure 3 of Kim et al. (2011) showing Cu-As sulfosalt (tennantite?) and spherical covellite inclusions in quenched, molten submarine S. (B) Tennantite inclusions along internal boundaries in chalcopyrite. These may initially have been more rounded such as those in A and become angular as the chalcopyrite underwent further crystallization.

The suggested magmatically derived Cu in *Lena* chimney is consistent with the findings of other studies. Berkenbosch et al. (2015) measured a range of Cu isotope values for chalcopyrite in the interior of *Lena* chimney, and attributed them to fractionation during vapour transport of Cu in magmatic fluids 'pulsing' out of the system. Melt inclusions in Brothers dacite show that Cu does not partition into the melt as expected and displays a highly variable content (57%), which is consistent with Cu loss to exsolved magmatic fluids through degassing (de Ronde et al., 2011). Finally, Kim et al. (2011) found anhedral and spherical covellite and Cu-As sulfosalt inclusions (tennantite?) within the quenched, molten sulfur that was considered distinctly primary in origin, similar to covellite in sublimates of volcanic vapours (Ramdohr, 1980). Similarly, rare, small (~5 - 15 µm) grains of covellite occur within massive chalcopyrite of *Lena* chimney, as well as misshapen, probable tennantite (and covellite?) inclusions within larger chalcopyrite grains distal from the exterior of the chimney (Fig. 3.17). Other similarities between the enrichment factors from MTJ-1 volcano and Brothers are noteworthy. That is, the molten sulfur collected from the seafloor also has Au as the most enriched element, Cu as the 2nd or 4th most enriched element, and Cd with a lower EF (Kim et al., 2011). Although there is currently only one other arc seafloor example to compare with, these distinct enrichment factor patterns are common to both Brothers and MTJ-1 volcanoes, where the molten S collected from the latter has undoubtedly condensed from magmatically exsolved vapours.

3.6.3 Origin of metals in Brothers magmas

Arc environments are generally regarded as ideally suited for the formation of polymetallic sulfide deposits since the release of water and other volatiles from the downgoing slab initiates partial melting of the mantle wedge and generates a replenishing supply of magma and heat beneath the crust. Furthermore, magmas associated with arc volcanism are oxidized, volatile-rich and contain elevated S, K, V, Cu, Zn, As, Rb, Sr, Mo, Ag, Sb, Ba, Au, Pb, Bi, and U (e.g., Arculus, 1994; Hedenquist and Lowenstern, 1994; Timm et al., 2012). Arc caldera volcanoes in particular host sulfide mineralization where, for example, ring faults act as primary structural

controls to focus high-temperature discharge (de Ronde et al., 2005; Hannington et al., 2005).

Beyond these general processes, large-scale features of the southern Kermadec arc may contribute to the abundant Au-rich sulfide chimneys at Brothers among the Kermadec volcanoes sampled to date; that is, the subduction of the Hikurangi Plateau and the proximity of continental New Zealand (e.g., de Ronde et al., 2007; Timm et al., 2016). The Hikurangi Plateau is a 25-km-thick, Cretaceous large igneous province that is subducting beneath the southern Kermadec arc, and which is overlain by ≤500 m of terrigenous sediment largely derived from New Zealand continental crust. Due to its increased thickness the subducting Hikurangi slab releases more fluids into the mantle wedge during melting with concomitant extensive partial melting of the mantle wedge providing increased heat and fluid flow to the hydrothermal systems of the southern Kermadec arc (de Ronde et al., 2007). In addition, fragments of the Plateau and overlying sediment are thought to rise into the mantle wedge via cold diapirism and, along with slab-derived fluids, this creates a compositionally and geochemically heterogeneous sub-arc mantle in this region (Timm et al., 2016). Compared to other Kermadec arc lavas, Brothers dacites have anomalous element enrichments of Mo, Ag, Sn, Sb, Ba, Tl, Pb, Bi, U, other incompatible elements, and REE (Timm et al., 2012). These enrichments are believed to result from: (1) significant slab input through transport by hydrous fluids from the subducted sediments or altered ocean crust (i.e., V, Cu, Zn, As, Mo, Sb, Au, Tl, Pb, and Bi), or (2) sediment partial melting, bulk mixing between slab and mantle wedge, or (3) solute-rich supercritical fluids (i.e., Ag and Sn). However, Wysoczanski et al. (2012) suggest the degree of partial melting is the primary control on Zn and Cu content in southern Kermadec lavas, and thus modelled the magmatic composition of the lavas as resulting from melting of ambient mantle enriched by a ~1% fluid and sediment melt component. Both Timm et al. (2012) and Wysoczanski et al. (2012) pointed out a mafic ridge located in the vicinity of Brothers, which they interpret to strike beneath the NW Caldera site and which they infer may provide a transient source of heat and magmatic fluids together with a first-order zone of permeability that may contribute to the initiation of this hydrothermal system and its associated mineralization.

3.7 Conclusions

Element mapping has revealed previously unrecognized characteristics of the sulfide chimneys at Brothers volcano. A sphalerite-barite chimney is shown for the first time to contain Cu, which has clarified its relationship with sphalerite-chalcopyrite chimneys as representing two stages of chalcopyrite replacement of sphalerite. An intricate pattern of Se distribution is noted in chalcopyrite within the chalcopyrite-bornite chimney, and Bi distribution in the same chimney highlights its complex growth history. Finally, trace element rings are apparent within the laminated chalcopyrite of a chalcopyrite-sulfate chimney, illustrating alternating cycles of fluid flow within the chimney from outward advection of hydrothermal fluids to inward advection of seawater. Using the trace element rings as a proxy for vent fluid compositions, EFs suggest significant magmatic enrichment of Au, Te, Bi, Se, Ag and Cu in the chimney. Symonds et al. (1992) noted that trace element abundances in volcanic condensates are highly variable, whether at several volcanoes in the

same arc, different fumaroles on a single volcano, or a single fumarole at different times. Despite this variability in absolute abundances, trace element EFs for arc and rift, subaerial and submarine, and basaltic to dacitic volcanoes are remarkably consistent. We suggest the relatively large amount of terrigenous sediment subducted and subsequently melted beneath the southern Kermadec arc is the main source of magmatically-derived Bi, Te, Ag and possibly Se in Brothers chimneys as proposed by Timm et al. (2012), and that Au is strongly enriched through its scavenging into liquid Bi. Thus, Brothers Cu-Bi-Au-rich chimneys result from a combination of high amounts of subducted continental sediments, enriched sub-arc magma and heat generation from the subducting Hikurangi Plateau, the exsolution of volatile-rich magmatic fluids, and the fluid-focusing effect of ring faults at a caldera volcano.

3.8 Acknowledgements

This research is supported by an Australian Research Council Centre of Excellence in Ore Deposits research scholarship (University of Tasmania) to H. Berkenbosch. C. de Ronde was supported by public research funding from the Government of New Zealand. SXFM analysis was undertaken on the X-ray fluorescence microscopy beamline at the Australian Synchrotron, Victoria, Australia, and we thank Dr. David Paterson for his guidance. Additionally, we thank Dr. Karsten Goemann for assistance while at the synchrotron, Susan Merle for help with Figure 1, Nathan Steeves for undertaking some of our EMP analysis, and Leeora Gubbay-Nemes for sharing Brothers dacite compositions with us. Insights from Dr. Christoph Heinrich also improved the interpretation of our results for which we are grateful.

Chapter 4

Characteristics of copper isotopes from chalcopyrite-rich black smoker chimneys at Brothers volcano, Kermadec arc, and Niuatahi volcano, Lau Basin

Published in Mineralium Deposita, 2015, Volume 50, no. 7, pp 811- 824.

4.1 Abstract

We analysed primary chalcopyrite from modern seafloor 'black smoker' chimneys to investigate high-temperature hydrothermal Cu isotope fractionation unaffected by metamorphism. Samples came from nine chimneys collected from Brothers volcano, Kermadec arc, and Niuatahi volcano, Lau backarc basin. This is the first known study of Cu isotopes from submarine intraoceanic arc/backarc volcanoes, with both volcanoes discharging significant amounts of magmatic volatiles. Our results (n = 22) range from δ^{65}Cu = -0.03 to 1.44 ±0.18‰ (2 sd), with the majority of samples between ~0.00 and 0.50‰. We interpret this cluster (n = 17) of lower δ^{65}Cu values as representing a mantle source for the chimney Cu, in agreement with δ^{65}Cu values for mantle rocks. The few higher δ^{65}Cu values (>0.90‰) occur; (1) within the same chimneys as lower values, (2) randomly distributed within the chimneys (i.e., near the top and bottom, interior and exterior), and (3) within chalcopyrite of approximately the same age (<1 yr). This suggests the higher δ^{65}Cu values are not related to oxidation by mixing with ambient seawater, but to isotopic variation within the vent fluids over a relatively short time. Theoretical studies demonstrate significant isotopic fractionation can occur between aqueous and vaporous complexing species. When combined with evidence for periodic release of magmatic volatiles at Brothers, we believe vapour transport of Cu is responsible for the observed isotopic fractionation. When compared to global δ^{65}Cu data for primary chalcopyrite, volcanic arc chimneys are most similar to porphyry copper deposits that also form from magmatic-hydrothermal processes in convergent tectonic settings.

4.2 Introduction

Research on copper isotopes has accelerated over the past 15 years, expanding into disciplines as diverse as medicine, archeology, and geology. Within the latter field, Cu isotopes have been applied to studies of cosmology, environmental science, sedimentology, igneous, metamorphic and sedimentary rocks, and economic geology. The resulting global database of Cu isotope values may, among other things, elucidate differences between various magma, rock, and/or ore deposit types. This study adds to that body of literature by reporting for the first time, Cu isotope measurements from an intraoceanic arc seafloor hydrothermal system, i.e., those from black smokers chimneys hosted by Brothers volcano of the Kermadec arc, as well as from Niuatahi backarc volcano of the Lau basin.

Several hypotheses have been presented on the processes responsible for fractionation of Cu isotopes, such as Cu-complexation, crystallography, and physicochemical parameters such as Eh, pH, and temperature (e.g., Asael et al., 2009; Mathur et al., 2009a; Sherman, 2013). The largest fractionations are observed in low-temperature alteration environments. For example, the range of measured Cu isotopes in nature spans from -17 to 10‰, where both ends of this range occur within secondary ore minerals (Mathur et al., 2009a). Not surprisingly, much attention has therefore been paid to economically important supergene mineral deposits and the oxidation of Cu (e.g., Mathur et al., 2005; 2012; Markl et al., 2006; Haest et al., 2009; Braxton and Mathur, 2011). Oxidation of Cu(I) in minerals (i.e., chalcopyrite) to aqueous Cu(II) in leachate can cause fractionations of up to 2.7‰ at 40°C; the leachate may be removed to precipitate ^{65}Cu-enriched deposits, while the residual minerals are ^{65}Cu-depleted (Ehrlich et al., 2004; Mathur et al., 2005; Kimball et al., 2009). Rayleigh fractionation and multiple episodes of oxidation and reprecipitation are therefore believed to account for the extreme high and low Cu isotope values in low-temperature environments. Since low temperature alteration (seafloor weathering) of active sulfide chimneys is relatively minor and does not form supergene deposits, we have largely disregarded secondary alteration processes in this study, consistent with petrographic studies of the chimneys (Berkenbosch et al., 2012a). Instead, we focus exclusively on δ^{65}Cu values of primary chalcopyrite and address the possible fractionation mechanisms that may occur during high-temperature processes.

To date, the causes of Cu isotope variation in hypogene depositional environments is poorly understood, with some deposits showing an increase in δ^{65}Cu values with successive intrusions (e.g., Grasberg, Indonesia; Graham et al., 2004), while others have limited variation in δ^{65}Cu values over district-wide scales (e.g., the Schwarzwald district, Germany; Markl et al., 2006). Potential non redox-driven fractionation processes examined by other workers include equilibrium (or isotope kinetics), variation in source, physicochemical fluid controls, fluid-mineral fractionation during precipitation, and fluid-vapor fractionation (e.g., Graham et al., 2004; Maher and Larson, 2007; Li et al., 2010b; Maher et al., 2011). Brothers volcano is an ideal site to further examine high-temperature Cu isotope fractionation as it is a hydrothermally active submarine volcano that has been comprehensively studied, and where several unaltered, chalcopyrite-rich chimneys have been sampled. Furthermore, seafloor hydrothermal systems related to intraoceanic arc volcanoes are typically shallower and discharge higher concentrations of magmatic volatiles than their MOR counterparts (de Ronde et al., 2012), where studies of Cu isotopes related to seafloor mineralization have been focused to date (Zhu et al., 2000; Rouxel et al., 2004). The Brothers and Niuatahi chimneys thus provide an alternate, modern tectonic environment to add to, and compare with, the global database, and are particularly suited to examine the effects of magmatic volatiles on isotopic fractionation.

4.3 Geological setting of Brothers volcano

Brothers is one of 30 major submarine volcanoes along the Kermadec arc between New Zealand and Tonga (Fig. 4.1), and one of only three known to host mineralization (de Ronde et al., 2011). The

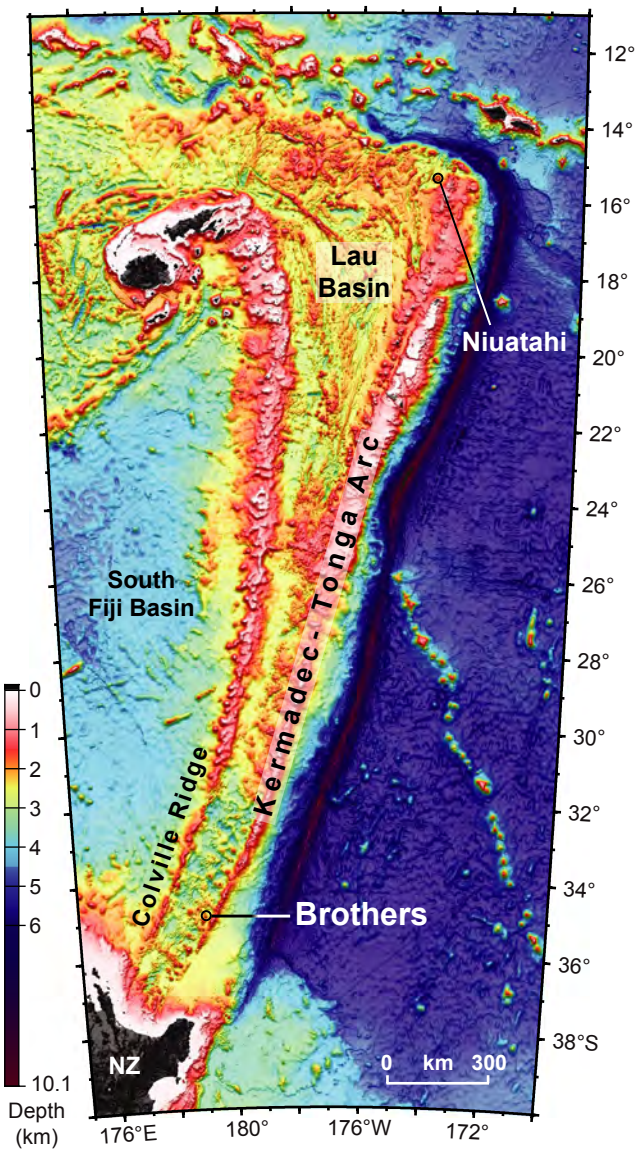

Figure 4.1 Map of the ~2500 km long Kermadec-Tonga arc extending north from New Zealand, showing locations of Brothers and Niuatahi volcanoes. To the east of the arc, at the Kermadec Trench, the Pacific Plate and Louisville seamount chain are subducting westward under the Australian plate.

predominantly dacitic volcano lies to the west of the Kermadec ridge and is situated between major SW-NE-trending faults (Fig. 4.2a). Embley et al. (2012) detail the morphology and structure of the volcano, regional lineaments, and possible collapse mechanisms for the formation of the large central caldera (3.0 x 3.4 km). The base of Brothers volcano lies at a water depth of ~2200 m, with the caldera rim situated between depths of ~1420 and 1520 m (de Ronde et al., 2005). The floor of the caldera has a maximum depth of 1879 m. Two volcanic cones occupy the southern half of the caldera: the older, more degraded Lower Cone shoals to 1304 m, whereas the younger Upper Cone shoals to a depth of 1196 m while merging with the southern caldera rim and the southwestern flank of the Lower Cone (Fig. 4.2a).

Three active vent sites and a fourth extinct one make Brothers the most hydrothermally active volcano along the Kermadec arc (e.g., Baker et al., 2012). From 1996 to 2005, a series of expeditions utilizing dredges, camera and TV grab tows, miniature autonomous plume recorders (MAPRs), Conductivity-Temperature-Depth-Optical (CTDO) tow-yos and casts, and manned submersibles identified and surveyed the gas-rich, diffusely-venting Cone site; the high-temperature, metal-rich NW Caldera site (Fig. 4.2); and the extinct SE Caldera site (e.g., de Ronde et al., 2005; 2011; 2012 and references therein) The similarly high-temperature, metal-rich West Caldera site was only discovered after high-resolution mapping of hydrothermal fluid discharge and magnetic anomalies throughout the caldera by the autonomous underwater vehicles (AUVs) *ABE* in 2007 and *Sentry* in 2011 (Baker et al., 2012; Caratori Tontini et al., 2012). The AUV data further show sparse, high-temperature venting occurring between, and beyond, the boundaries of the main NW and West Caldera sites to cover nearly the entire northern half of the caldera wall, with localized diffuse venting also apparent at the SE Caldera site. Such widespread venting along the caldera walls is primarily controlled by discontinuous ring faults and their intersection with regional lineaments (e.g., de Ronde et al., 2005; Embley et al., 2012). High-resolution magnetic data highlight the longevity

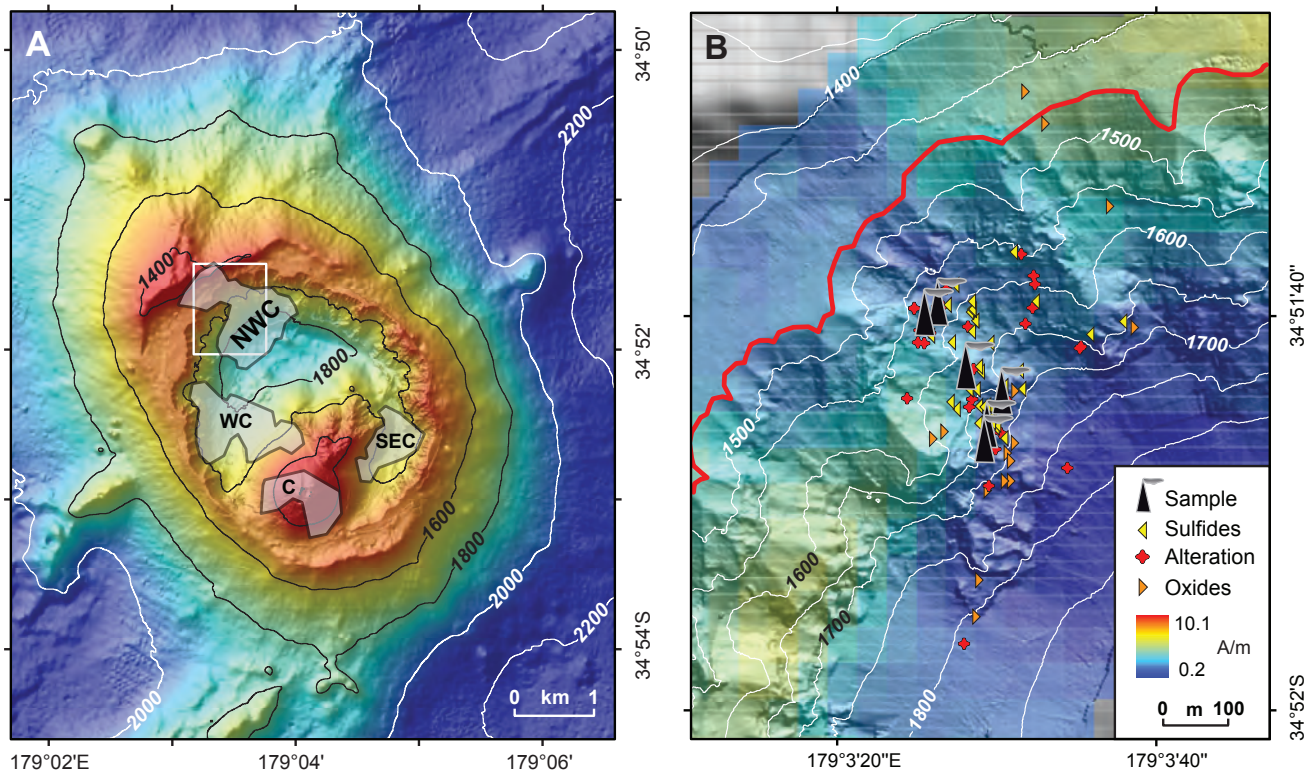

Figure 4.2 (A) Bathymetric map of Brothers volcano showing the relationship between intersecting regional SW-NE and SE-NW (the long axis of the volcano) lineaments. The location of the four hydrothermal sites are outlined by their low magnetization anomalies: NW Caldera, West Caldera, SE Caldera and Cone (C) (from Caratori Tontini et al., 2012). White box shows the area in B. (B) Bathymetric map of the NW Caldera site overlain by values for magnetization in A/m. The caldera rim is outlined in red. Dark purple magnetization values indicate areas of prolonged hydrothermal upflow that destroyed magnetite in the host rock, effectively reducing the magnetization. Submersible observations of hydrothermal manifestations such as sulfide chimneys, oxide crusts, and extensive alteration correspond to the area where the low magnetization anomaly traverses the caldera wall, with sulfides concentrated in the centre of this zone (see symbols). Locations of samples used in this study are also shown. Both A and B modified after Embley et al. (2012).

of the four hydrothermal sites by delimiting four corresponding zones of low magnetization, the result of prolonged demagnetization of host rocks by the upflow of hot, buoyant, hydrothermal fluids (Fig. 4.2a; Caratori Tontini et al., 2012).

Due to the drastic differences in venting style, fluid composition, and corresponding mineralization types between the NW Caldera and Cone sites (i.e., largely rock-dominated vs. magmatic-hydrothermal), de Ronde et al. (2011) and Gruen et al. (2012; 2014) modelled the sites as having distinct and contrasting upflow zones. Recorded regional seismicity and local harmonic tremor indicate that the top of the present-day magma chamber lies approximately 2.5 km and a '2 phase' zone attributed to the collapse of vapor bubbles ~800 m beneath the Cone site, respectively (Dziak et al., 2008; de Ronde et al., 2011). Magmatic volatiles exsolved from the magma are postulated to rise vertically to be expelled directly on the seafloor at the Cone site, with some mixing with ambient seawater immediately sub-seafloor. By contrast, pathways beneath the NW Caldera site are considered to be longer and more convoluted leading away from the most recent intrusions beneath the Cone. This ensures greater degrees of water-rock interaction occur as the fluids migrate to the NW Caldera site, where they are incorporated into a

hydrothermal circulation cell and then expelled on the seafloor at the NW Caldera site, either as phase-separated brines and/or condensed vapors, forming the metal-rich (Cu-Zn-Au ± Pb) chimneys.

4.3.1 Brothers chimneys

This study focuses on samples collected from the NW Caldera vent site (Fig. 4.2b). High temperature venting occurs over a strike length of ~800 m in a SW - NE direction along the caldera walls, between depths of ~1800 to 1550 m; additional diffuse venting occurs on top of the caldera rim at ~1450 m (Baker et al., 2012). Approximately half of the NW Caldera vent field has been surveyed by manned submersibles in 2004 (*Shinkai 6500*) and 2005 (*Pisces V*), and has been described in detail by de Ronde et al. (2005; 2011) and Berkenbosch et al. (2012a). Widespread, white-grey colored hydrothermal alteration of lavas and pyroclastics, and Fe-rich amorphous silica crusts and chimneys, indicate diffuse venting occurs throughout the field. Over 100 active and inactive chimneys have been surveyed, typically as narrow (<0.5 m diameter), 2 - 3 meter tall spires, but also coalescing into larger, wider structures up to 7 m tall. Individual chimneys may either be relatively straight and smooth-sided, or bulbous and sinewy, with many capped by beehive structures. High-temperature vent fluids exiting chimneys in this field typically measured between 265 and 302°C; other chimneys expelled clear, diffuse fluids of ~35°C.

Four types of chimneys at the Brothers NW Caldera field were identified by Berkenbosch et al. (2012a). Two are Cu-rich, i.e., chalcopyrite-sulfate and chalcopyrite-bornite chimneys; and two are Zn-rich, i.e., sphalerite-barite and sphalerite-chalcopyrite chimneys. The four types are based on the presence (or absence) of two concentric zones, their thickness, and composition; 1) an inner chalcopyrite layer, and 2) an outer sulfate and disseminated sulfide layer. Both Cu-rich chimney types have a thick internal chalcopyrite layer and a sulfate layer of variable-thickness composed of anhydrite and barite (Fig. 4.3). In addition, chalcopyrite-bornite chimneys have an intermediate zone of Cu-enriched phases (i.e., bornite, chalcocite, covellite), which Berkenbosch et al. (2012a) have attributed to seawater weathering (oxidation). However, these authors and de Ronde et al. (2011) also suggested that the suite of bornite, chalcocite, and specular hematite could indicate more oxidized vent fluids, like those characteristic of high sulfidation environments. By contrast, Zn-rich chimneys have a barite-only sulfate layer and either no, or trace chalcopyrite.

4.3.2 Niuatahi volcano

We also analyzed samples from *Pui 'O Tafahi* chimney collected in 1998 by Nautilus Minerals Inc. from Niuatahi volcano (previously known as volcano "O" and MTJ-1; Arculus, 2005; Kim et al., 2009; 2011) in the Lau backarc basin (Fig. 4.1). Niuatahi is a large (~10 km diameter), off-axis caldera volcano located ~90 km west of the Tofua arc, or ~45 km E of the NE Lau Spreading Centre. Like Brothers, it is dacitic in composition and has two post-collapse cones located within the caldera, shoaling to ~1300 and ~1500m depth, respectively. Also similar to Brothers, extensive hydrothermal activity is manifest as high-temperature sulfide deposits along caldera ring faults, with a more magmatic hydrothermal system emplaced on the shallower cone (Kim et al., 2011; Embley et al., 2013). *Pui 'O Tafahi* chimney is a very large (~2.5 m long x 1 m diameter), chalcopyrite-sulfate chimney that was recovered from the

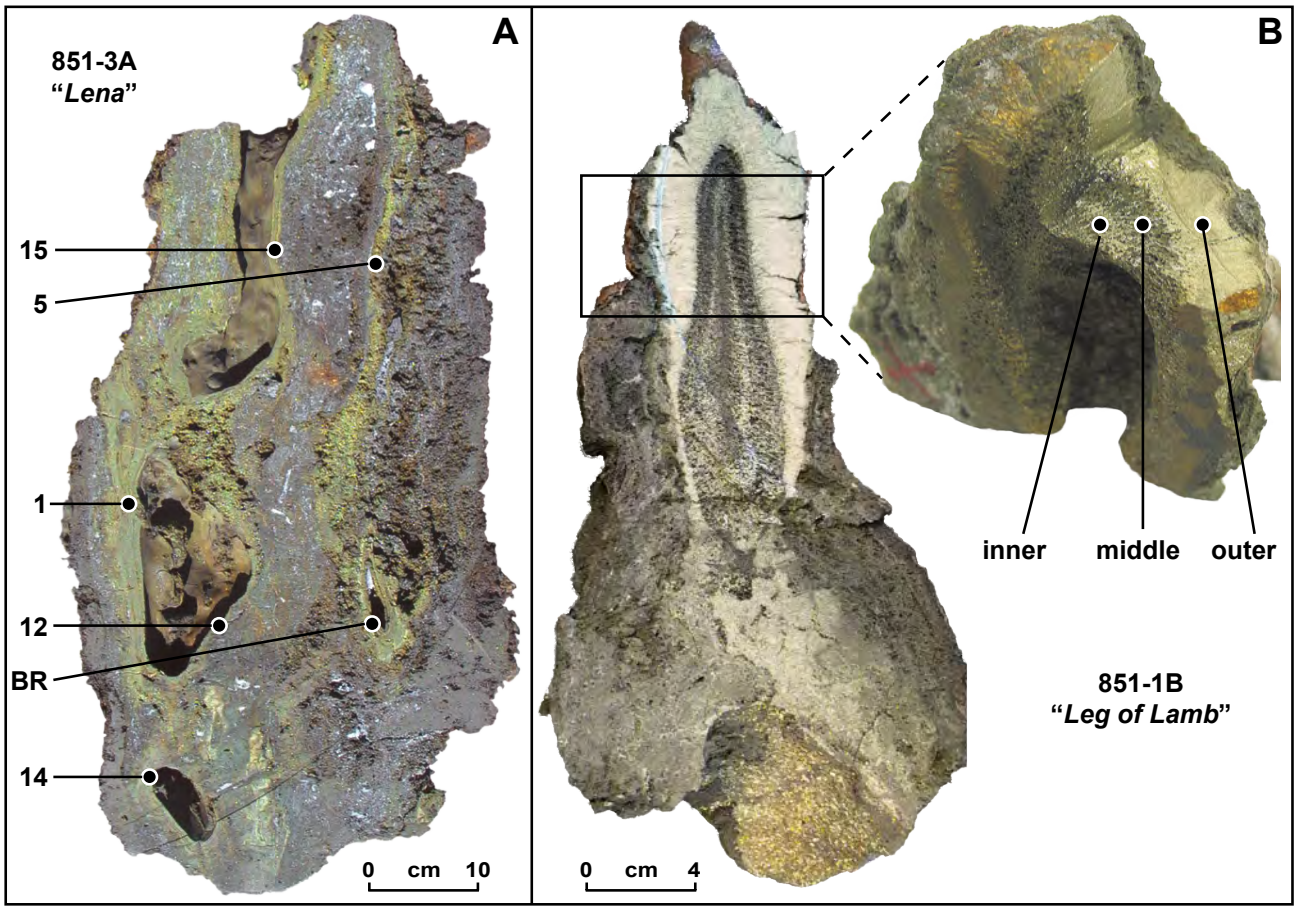

Figure 4.3 Two Brothers chimneys used in this study showing locations of individual samples used in the analysis of Cu isotopes. (A) *Lena* chimney (851-3A) is considered to represent the coalescing of two chimneys (de Ronde et al., 2011). On the left side, laminated bands of pale greenish-yellow chalcopyrite surround a well-defined central orifice, while the poorly defined orifice on the right side is comprised of more massive chalcopyrite. Surrounding grey areas with white flecks are primarily composed of anhydrite, barite, sphalerite and pyrite. The lowest, and only negative δ^{65}Cu value in this study comes from sample #1 (-0.03‰) while the 2nd highest δ^{65}Cu value comes from sample #14 (1.24‰), only ~25 cm below. BR = bottom right. (B) *Leg of Lamb* chimney (851-1B) in which the central orifice was in-filled by late 'box-work' chalcopyrite in possibly two generations, as given by an internal boundary of thicker chalcopyrite. Black box outlines the area from where a smaller sample was sawed off and chalcopyrite analysed in this study (right side). Here, the concentric zonation of the orifice is apparent. Inner sample = thicker box-work; middle sample = thinner box-work; outer sample = massive chalcopyrite. The highest δ^{65}Cu value for this study of 1.44‰ comes from the outer sample while the two box-work samples had much lower values of 0.18 and 0.13‰, respectively.

northern caldera wall. It is primarily comprised of a massive chalcopyrite zone that surrounds a chaotic network of internal orifices, with sphalerite- and sulfate-rich zones dominating the exterior.

4.4 Methods

In this study we analyzed primary chalcopyrite from *Pui 'O Tafahi* and the three Brothers chimney types that have Cu-rich mineralization in their cores. Hand samples were crushed and pure chalcopyrite separated by picking under a binocular microscope, where possible. A total of seventeen samples were processed from eight different Brothers chimneys (Figs. 4.2b and 4.3; Table 4.1), together with five samples from *Pui 'O Tafahi*.

Copper isotope analysis was undertaken at the Isotope and Trace Element Geochemistry laboratory at the University of Melbourne, under standard clean room conditions. All acids were triple distilled

Table 4.1 Sample descriptions and copper isotope results.

Chimney	Depth (mbsl)	Vent Fluid Temp (°C)	Fragment/ Zone	Age (years)	Comments on the chalcopyrite	δ^{65}Cu	Procedural duplicate[a]	Chimney duplicate[b]	Analytical duplicate[c]	Average δ^{65}Cu
Sphalerite- Chalcopyrite										
PV-632-11R	1588	-		0.34	Minor tarnishing, slightly spongy, minor sphalerite?	0.561		0.587		0.574
PV-626-4min	1679	inactive	-a	1.35	Tarnished, spongy, mixed with pyrite and sphalerite.	0.927	0.983			0.955
Chalcopyrite- Bornite										
851-1A	1665	302		2.05	Clean, massive.	1.086	0.994 0.935			1.005
851-1B	1665	302	outer	-	Clean, massive.	1.592	1.386		1.355	1.444
"*Leg of Lamb*"			middle	-	Laths of tarnished chalcopyrite with dirty mineral coating, minor barite?	0.176				0.176
			inner	1.93	Laths of tarnished chalcopyrite with dirty mineral coating.	0.132				0.132
PV-628-2min	1577	inactive		33	Minor tarnishing, minor sphalerite?	0.178				0.178
Chalcopyrite- Sulphate										
X573/E	1350-1640	-		-	Rare tarnishing, massive.	0.054		0.064		0.059
852-2B	1627	292	852-2B-a	0.11	Minor tarnishing, slightly spongy.	0.029				0.029
			852-1-a	-	Minor tarnishing, slightly spongy.	0.171	0.224			0.198
			852-1-b	-	Minor tarnishing, massive.	0.032		0.192		0.112
851-3A	1670	274	1	1.39	Rare tarnishing, slightly spongy.	-0.029				-0.029
"*Lena*"			5	1.93	Rare tarnishing, slightly spongy.	0.118				0.118
			12	1.01	Rare tarnishing, slightly spongy.	0.355				0.355
			14	-	Rare tarnishing, slightly spongy.	1.244				1.244
			15	-	Moderate tarnishing, spongy, minor anhydrite?	0.354			0.450 0.480	0.428
			BR	-	Rare tarnishing, slightly spongy.	0.329	0.114			0.222

Table 4.1 continued.

Chimney	Depth (mbsl)	Vent Fluid Temp (°C)	Fragment/ Zone	Age (years)	Comments on the chalcopyrite	δ^{65}Cu	Procedural duplicate[a]	Chimney duplicate[b]	Analytical duplicate[c]	Average δ^{65}Cu
Niuatahi Volcano										
"Pui 'O Tafahi"[d]	?	-	PT-B-7	-	Rare tarnishing, massive.	0.139				0.139
			PT-B-9	-	Finely crushed mixed sulfides, chalcopyrite not separated, no barite.	0.058				0.058
			PT-B-10	-	Finely crushed mixed sulfides, chalcopyrite not separated, no barite.	-0.002				-0.002
			PT-B-11	-	Finely crushed mixed sulfides, chalcopyrite not separated, no barite.	0.286				0.286
			PT-D-9	-	Finely crushed mixed sulfides, chalcopyrite not separated, no barite.	0.250				0.250

- not measured/analysed, BR= bottom right; depth, vent fluid temperature, and age data from de Ronde et al. (2011)
[a] Dissolution, column separation, and isotope analysis performed on a second aliquot of sample powder.
[b] Chalcopyrite from the same chimney but of a slightly lower quality.
[c] Replicate isotope analysis from the same solution.
[d] Samples come from the centre of the chimney either at the base (PT-B) or ~80cm from the base (PT-D)

in quartz stills, with all sample containers doubly acid-cleaned Teflon Savillex beakers. Approximately 15 mg of each sample was digested in 1 ml inverse aqua regia, dried completely, then dissolved in 5 ml 7 N HCl in preparation for Cu purification by anion-exchange chromatography. The purification method used 2 ml of AG-MP1 resin and followed a procedure modified from Li et al. (2009) by S. Paleri (pers. comm.), as detailed in Table 4.2. The purified Cu was evaporated to dryness, dissolved in ~2 ml concentrated nitric acid, and then re-evaporated. Finally, the residue was dissolved in 2 ml 2% HNO_3 mass spectrometer run solution and further diluted to an approximately 0.3 $\mu g.g^{-1}$ solution in preparation for isotopic analysis.

Samples were analyzed on a Nu-Plasma MC-ICPMS machine, and introduced via an Aridus II desolvating nebulizer. Instrumental mass bias was corrected for by sample - standard bracketing procedures using a solution of NIST SRM 976 copper solution as a reference material. Sample contamination was examined through the analysis of two total procedural blanks (including sample digestion, purification, and mass spectrometry), both of which contributed <0.002 V for ^{63}Cu and ^{65}Cu combined. Reproducibility and accuracy of measurements was estimated through eight analyses of an in-house standard (a homogeneous seafloor hydrothermal sediment) over two sessions that yielded an error of ±0.18‰ (2 sd). Because this uncertainty encompasses the difference in δ^{65}Cu for all of our duplicate measurements (Table 4.1), it is the reproducibility we are reporting for this study. Data were reduced using the Iolite software package (Paton et al., 2011) using an in-house data reduction scheme, and results are expressed in standard δ^{65}Cu notation where:

Table 4.2 Protocol for Cu purification by anion-exchange[1].

Eluant	ml	Purpose
dilute HCl (~1 N)	~25	Clean column
concentrated HCl (~12 N)	~25	Clean column
7 N HCl + 0.001% H_2O_2	9.5	Equilbrate column
7 N HCl + 0.001% H_2O_2	0.5	Sample loading
7 N HCl + 0.001% H_2O_2	9	Elution of the bulk sample matrix
7 N HCl + 0.001% H_2O_2	33	Cu peak, left & right shoulder
dilute HCl (~1 N)	~40	Rinse

[1]Protocal modified from Li et al. (2009) by S. Paleri (pers. comm.)

$$\delta^{65}Cu\ ‰ = \left\{ \frac{\left(^{65}Cu/^{63}Cu\right)_{sample}}{\left(^{65}Cu/^{63}Cu\right)_{NIST\ SRM\ 976}} - 1 \right\} \times 1000.$$

4.5 Results

The total range of δ^{65}Cu values measured in this study is from -0.03 to 1.44 ±0.18‰ (Table 4.1). The majority (n = 17) of the δ^{65}Cu values cluster within 0.5‰ of each other at the low end of this range (<0.5‰), while a smaller group (n = 4) cluster within 0.5‰ of each other at the higher end (>0.9‰; Fig. 4.4). A single measurement of 0.57‰ lies between these two groups. We measured only relatively high δ^{65}Cu values for the sphalerite-chalcopyrite chimneys, whereas chalcopyrite-bornite chimneys have both high and low values, and the chalcopyrite-sulfate chimneys have only one high value.

Two individual chimneys have δ^{65}Cu values in both the groups, i.e., with relatively higher and lower values; the higher values do not correlate with location inside the chimneys. That is, the highest δ^{65}Cu value in the *Leg of Lamb* chimney (851-1B) comes from near the outer margin, at the top, whereas the highest δ^{65}Cu value from *Lena* chimney (#14; 851-3A) comes from the interior conduit, at the base (Fig. 4.3). The difference in δ^{65}Cu values over only ~2 cm in *Leg of Lamb* chimney is 1.31‰, while the variance is similar (1.25‰) in *Lena* chimney, though over ~30 cm. Furthermore, that range of δ^{65}Cu values in *Lena* chimney occurs within the lining of the internal conduit, and thus in chalcopyrite of approximately the same age (de Ronde et al., 2011). By comparison, the five δ^{65}Cu values from Pui O' Tafahi chimney all fall between 0.00 and 0.29‰ despite one sample being located ~80 cm higher in the chimney than the others.

4.6 Discussion

The δ^{65}Cu data for arc-related chimneys is similar to data from active, basalt-hosted MOR chimneys, which range from 0.02 to 1.22‰, excepting a single lower value (-0.35‰) from Lucky Strike (Fig. 4.5). Ultramafic-hosted MOR chimneys also have minimum values near 0‰ but extend to much higher values i.e., to a maximum of 3.22‰. A compilation of δ^{65}Cu values for primary chalcopyrite from other global ore deposits with a known hydrothermal origin shows a dominant peak between -0.50 and 0.75‰, which is entirely consistent with the δ^{65}Cu data presented here (Fig. 4.6). This cluster of δ^{65}Cu values likely reflects a mantle-rock source for Cu in these deposits. For example, published values for whole-rock δ^{65}Cu measurements of basalts are around -0.2‰, while peridotites are between 0.05 and 0.14‰ and granites 0.01 ±0.30‰ (Rouxel et al., 2004; Li et al., 2009; Ikehata and Hirata, 2012). Similarly, chalcopyrite from mantle-derived deposits (e.g. Cornwall, England; Bushveld, South Africa; Stillwater, MT, USA) range between -0.15 and 0.21‰ (Zhu et al., 2000; Maher, 2005; Maher and

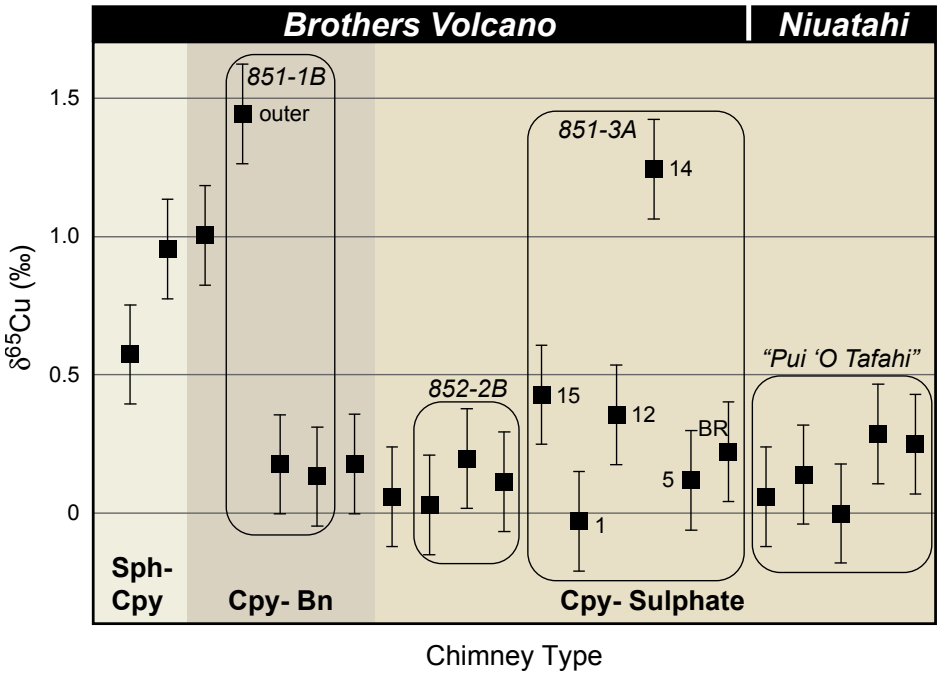

Figure 4.4 Scatter plot of δ^{65}Cu value versus chimney type. Multiple samples from the same chimney are enclosed in boxes, and labels are given to select data points. The chimney on the far right is from Niuatahi. Error bars are ±0.18‰ (2 sd). Isotopic values show no discernible trend between chimney types, as the majority of samples fall in the range ~0.0 to 0.5‰, and the few higher values (to ~1.4‰) are found within the same chimney as the relatively lower values. Although sphalerite-chalcopyrite chimneys have no lower values (<0.5‰), two samples are insufficient to determine any correlation. Sph-Cpy = sphalerite-chalcopyrite; Cpy-Bn = chalcopyrite-bornite; Cpy-Sulfate = chalcopyrite-sulfate.

Larson, 2007), while chalcopyrite from two granite-hosted deposits has values of -0.11 and 0.07‰, respectively (Zhu et al., 2000). The consistency of mantle rock δ^{65}Cu values around -0.2 to 0.2‰ suggests that the mantle and associated igneous rocks are relatively homogenous with respect to Cu isotopes. Furthermore, the surface expression of deep source isotopic compositions is not unexpected, as mass dependent fractionation is minimal when in equilibrium at hydrothermal temperatures ≥300°C (Larson et al., 2003).

When the data for primary chalcopyrite is divided by ore deposit types some apparent trends may be insightful with regards to mineralization (Fig. 4.7). For example, with one exception active chimneys from arcs, backarcs and MORs have minimum δ^{65}Cu values of around 0.0‰, likely reflecting the

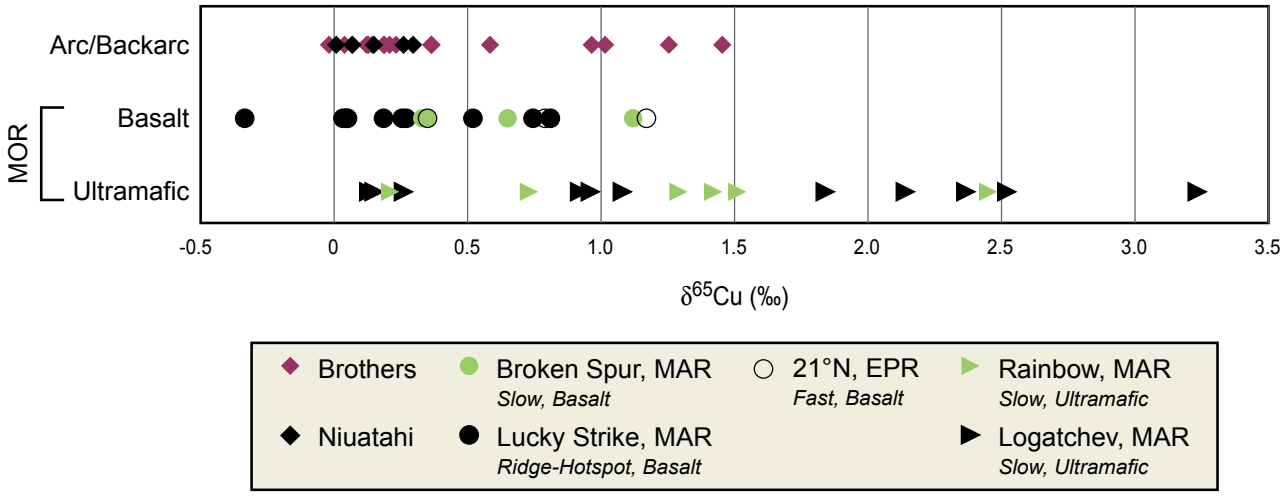

Figure 4.5 δ^{65}Cu values for active chimneys from intraoceanic arc and MOR environments, distinguished by location. Ridge spreading rate and composition are included in the legend for MOR chimneys. Data largely overlap between the two tectonic environments except for chimneys hosted by ultramafic rocks, which extend to heavier values. EPR = East Pacific Rise; MAR = Mid-Atlantic Ridge. MOR data from Zhu et al. (2000); and Rouxel et al. (2004).

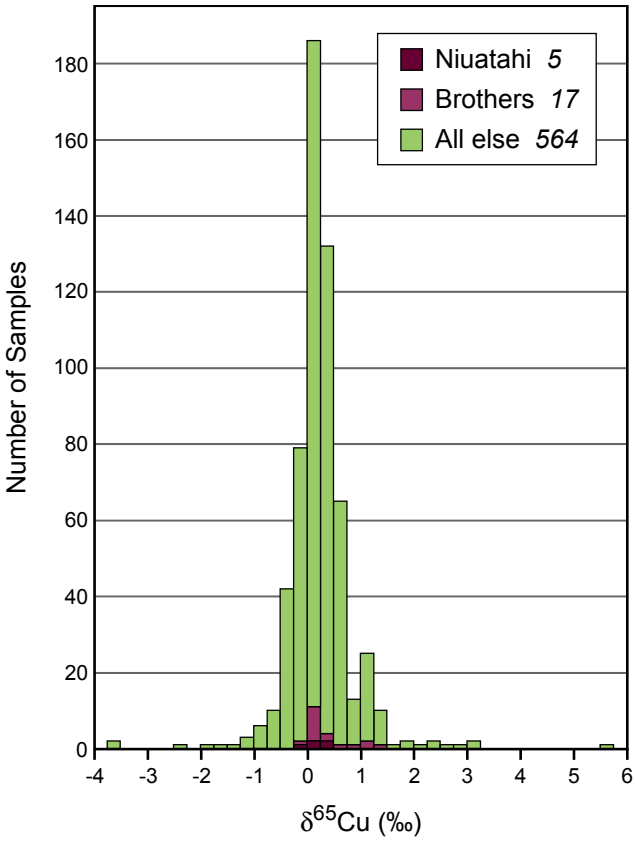

Figure 4.6 Histogram of primary chalcopyrite δ^{65}Cu values from Brothers and Niuatahi volcanoes and those from 73 different deposits over 19 countries and the seafloor of two oceans. Regardless of location, primary chalcopyrite typically has δ^{65}Cu values between -0.50 and 0.75‰, with ~88% of the data points falling within that range. Data from the two arc volcanoes mirrors the general distribution of chalcopyrite δ^{65}Cu values from other worldwide localities, with a consistent peak between 0.00 and 0.25‰, extended slightly to more positive values. The few data points at the ends of the range shown are far from their nearest data point, suggesting that they may not come from primary chalcopyrite, as it can be difficult to distinguish in some deposits. Data from: Maréchal et al. (1999); Zhu et al. (2000); Jiang et al. (2002); Larson et al. (2003); Graham et al. (2004); Rouxel et al. (2004); Maher (2005); Mason et al. (2005); Mathur et al. (2005; 2009a; 2009b; 2012; 2013); Markl et al. (2006); Asael et al. (2007); Maher and Larson (2007); Haest et al. (2009)); Li et al. (2010b); Mirnejad et al. (2010); Braxton and Mathur (2011); Ikehata et al. (2011); and Palacios et al. (2011)). See Appendix for more information on the global data included in this plot, including deposit names and locations.

mantle/igneous source. While most hydrothermal ore deposit types have δ^{65}Cu values approaching a normal distribution, active chimneys in both MOR and arc-related environments are skewed towards higher values, suggesting they have been influenced by a Cu isotope enrichment process. The lack of negative δ^{65}Cu values in active chimneys suggests these deposits are separated from the corresponding isotopically depleted part of the system. Inactive chimneys have distinctly depleted δ^{65}Cu values relative to active chimneys and other ore deposit types, implicating seawater oxidation that results in isotopically light (<0‰), residual chalcopyrite and the dispersing of ^{65}Cu-enriched fluids, which could otherwise form a supergene deposit in a subaerial environment. Values of δ^{65}Cu for ancient seafloor VMS deposits lie intermediate between modern active and inactive chimneys, displaying a narrow isotopic range, and suggesting isotopic homogenization occurs over time for these deposits. Thus, the study of modern seafloor systems may be preferable to ancient massive sulfide deposits with respect to understanding high temperature Cu isotope fractionation processes.

The distribution of Brothers data is almost exactly the same as that of positive δ^{65}Cu values for porphyry copper deposits (i.e., box and upper whisker; Fig. 4.7), which have a relatively well defined, narrow range for a large number of samples (n = 256), and which also form in convergent plate margin settings. In contrast to active black smoker chimneys, the negative δ^{65}Cu values for porphyry copper deposits suggest that they *are* connected to the isotopically depleted part of the system, which extends to the same minimum as inactive chimneys. The near normal distribution of all ore deposit types implies that ancient deposits in general incorporate both the enriched and depleted parts of the Cu isotope system. Skarn deposits have a similar Cu isotope distribution to porphyry copper deposits although extend to a wider range, which is perhaps not surprising considering these deposits utilize similar magmatic-hydrothermal fluids but occur in a greater variety of host rocks.

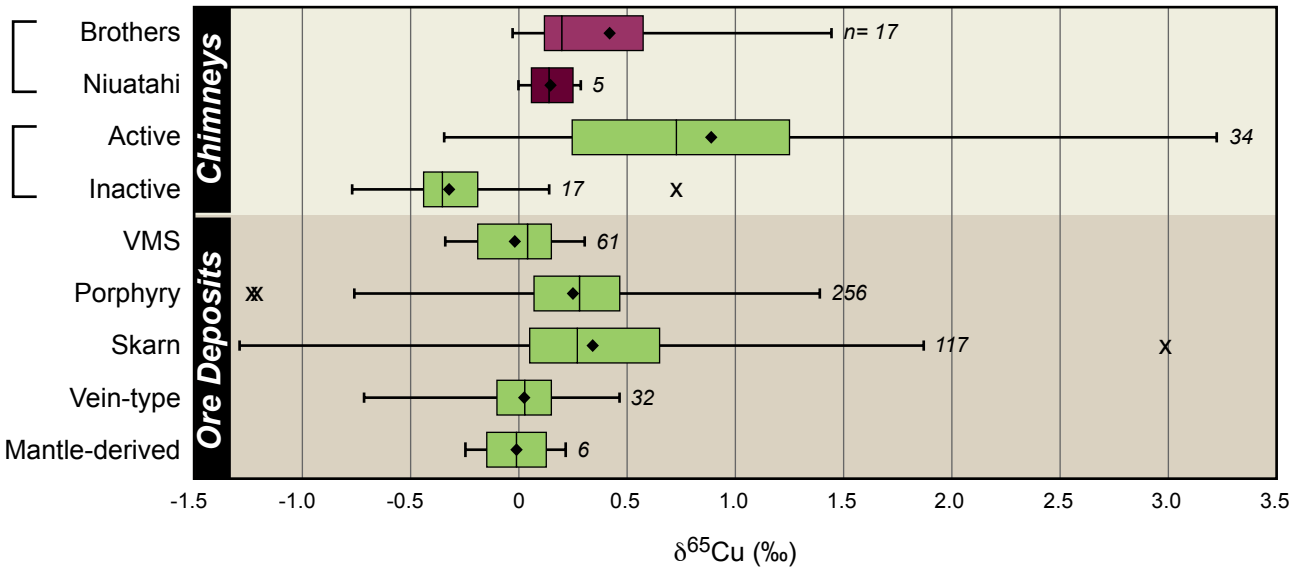

Figure 4.7 Statistical box-and-whisker plots that show the distribution of Cu isotopes in primary chalcopyrite for chimneys from this study (purple) versus those from active and inactive MOR chimneys, and various hydrothermal ore deposit types (green). The vertical line inside each box is the median, while the diamond (♦) shows the mean. Four outliers (x) outside of 3*the Interquartile Range (length of box) are shown and a further six outliers are outside the range of this plot for porphyry and vein-type deposits. Some trends within the dominant peak of Figure 4.6 become apparent by dividing the data this way, as discussed in the text. The mantle-derived range includes seven data points (-0.57 to 0.40‰) from the Sudbury complex, Canada, which may have a meteorite impact origin and/or hydrothermal input and therefore may not reflect pure mantle values. Data sources are the same as listed in the caption to Figure 4.6; BA = backarc; number of data points included in each box-and-whisker is given by the number on the right side of each plot.

The consistency between mantle-associated δ^{65}Cu values and the majority of the intraoceanic arc data presented here suggests that the few higher δ^{65}Cu values found in the Brothers chimneys result from something other than variation in source values. Similarly, Zhu et al. (2000) considered variations in δ^{65}Cu of ~0.3 to 1.2‰ in active chimneys from a MOR site to originate from a process occurring within the hydrothermal system. That is, the observation that chimneys of the Broken Spur hydrothermal field of the mid-Atlantic Ridge were isotopically heavier at their base led these workers to propose a process of selective leaching of ^{65}Cu from the host rock, enriching the initial hydrothermal fluids and thus the first precipitated minerals in the chimneys. By contrast, Rouxel et al. (2004) attributed δ^{65}Cu variations of 3.2‰ measured in active MOR chimneys at the Logatchev hydrothermal field, also of the mid-Atlantic Ridge, to a period of hydrothermal quiescence, whereby sub-seafloor Cu oxidation and reprecipitation occurred, followed by subsequent renewal of hydrothermal activity. Reduced hydrothermal upflow would facilitate oxidized seawater to penetrate below the seafloor, resulting in an alteration halo of oxidized, ^{65}Cu-enriched phases around a body of ^{65}Cu-depleted chalcopyrite, as seen in the supergene environment. Later resumption of hydrothermal activity then passed new vent fluids around the oxidized exterior margins, partially dissolving them, and reprecipitating ^{65}Cu-enriched chalcopyrite at the seafloor. The significance of only the chimneys hosted by ultramafic rocks having δ^{65}Cu values >1.2‰, if any, remains unclear (Rouxel et al., 2004).

The sparse and seemingly random distribution of elevated Cu isotope values within contemporaneous chalcopyrite in Brothers chimneys, however, suggests a more instantaneous fractionation process than those described above. Furthermore, we consider it

unlikely that any late hydrothermal upflow would be restricted to contact with the enriched (δ^{65}Cu >0‰) sub-seafloor halo only and avoid remobilization and reprecipitation of the depleted (δ^{65}Cu <0‰), residual chalcopyrite body as well. Large δ^{65}Cu variations (>1.0‰) are also found within individual chimneys at Rainbow and Logatchev hydrothermal fields, suggesting a relatively rapid Cu isotope fractionation process also occurs there. For example, an active chimney at Rainbow had δ^{65}Cu variations of 1.21‰ in chalcopyrite lining the conduit, while δ^{65}Cu values in another chimney at Logatchev varied by 0.83‰ and 1.08‰ between chalcopyrite filling the conduit, and that within the chimney wall, respectively (Rouxel et al., 2004). Similarly, Maher and Larson (2007) measured relatively large isotopic variations (δ^{65}Cu = -0.02 to 0.66‰) over ~10 m from a single mineralizing event at the Coroccohuayco skarn deposit, Peru, and suggested fractionation occurred during mineralization.

4.6.1 Copper-complexes

We hypothesize that δ^{65}Cu values >0.5‰ in this study reflect isotopic fractionation occurring during transport from deeper sources to the seafloor. Changes in pH, pressure, temperature, salinity, oxygen fugacity and composition of vent fluids are known to affect the stability of Cu-complexes (e.g., Seo et al., 2007; Maher et al., 2011; Rempel et al., 2012; Sherman, 2013). Theoretical studies by Seo et al. (2007) and Sherman (2013) calculated the reduced partition function ratios (RPFR) of several Cu-ligands to demonstrate that isotopic fractionation occurs between complexing species. Assuming the isotopic character of fluids controls that of minerals (i.e., fractionation is not significant during high temperature precipitation, or equilibrium fluid-mineral fractionation is not achieved), then transportation by different complexes will result in a range of mineral δ^{65}Cu values. The major Cu-ligands in high temperature, low pH brines are Cl^- and HS^-, with $CuCl_2^-$ and $Cu(HS)_2^-$ the dominant aqueous species (e.g., Seo et al., 2007; Maher et al., 2011; Sherman, 2013). Similar RPFR of those dominant complexes would cause minimal fractionation at hydrothermal temperatures of 300°C (<0.05‰ and either positive or negative depending on the calculation used; Table 4.3). Even considering increased fractionation at lower temperatures, a maximum difference of only ~0.2‰ exists at the unrealistic temperature of 0°C. If the minor aqueous Cu-complexes $CuCl_3^{2-}$ and $CuHS(H_2O)$ are also considered, the maximum degree of fractionation increases slightly, to ~0.5‰ at 300°C, equal to the spread of values within the lower group at Brothers. Again, an unrealistic chalcopyrite deposition temperature of ~50°C must be obtained before fractionations of ~1.4‰ occur between the minor aqueous complexes.

Copper, however, readily enters the vapor phase in sulfuric magmatic-hydrothermal systems (e.g., Lowenstern et al., 1991; Heinrich et al., 1992; Mavrogenes et al., 2002), with vapor complexes modeled by Seo et al. (2007) having higher RPFR than aqueous ones, permitting greater possible degrees of fractionation. The vaporous, hydrated, Cu-complex $CuCl\cdot(H_2O)$, a major species in hydrothermal systems and degassing volcanoes, could cause fractionations of ~0.6‰ from aqueous complexes at 300°C (Seo et al., 2007; Table 4.3). Furthermore, vaporous Cu_3Cl_3 has been modeled to fractionate by up to ~1.6‰ compared to aqueous species at 300°C. Thus, vapor complexes could be *required* to develop the large δ^{65}Cu fractionations measured at Brothers volcano.

Table 4.3 Reduced partition function ratios, 1000*ln(δ_{65-63}), for select copper-complexes.

Temperature	Aqueous species					Vapour species	
(°C)	$CuCl_3^{2-}$	CuHS	**$CuCl_2^-$**	**$Cu(HS)_2^-$**	$CuHS(H_2O)$	**$CuCl(H_2O)$**	Cu_3Cl_3
0	1.02 (1.26)	1.68	**2.71 (2.79)**	**2.90 (2.72)**	(2.96)	**3.40**	7.85
25	0.85 (1.06)	1.42	**2.29 (2.36)**	**2.46 (2.30)**	(2.50)	**2.89**	6.63
50	0.73 (0.91)	1.22	**1.97 (2.03)**	**2.11 (1.97)**	(2.15)	**2.48**	5.67
100	0.55 (0.68)	0.92	**1.49 (1.53)**	**1.60 (1.49)**	(1.63)	**1.89**	4.29
150	0.43 (0.53)	0.72	**1.17 (1.20)**	**1.25 (1.17)**	(1.28)	**1.48**	3.35
200	0.34 (0.43)	0.58	**0.94 (0.96)**	**1.00 (0.94)**	(1.03)	**1.19**	2.69
300	0.23 (0.29)	0.40	**0.64 (0.66)**	**0.69 (0.64)**	(0.70)	**0.82**	1.84

Dominant complex; data from Seo et al., 2007 and (Sherman, 2013)

Preliminary experimental data, however, contradict the theoretical conclusions of Seo et al. (2007), with two studies suggesting that vapour is ^{65}Cu-depleted compared to fluid. Maher et al. (2011) partially dissolved chalcopyrite with synthetic hydrothermal solutions and measured Cu isotopes in the residual chalcopyrite, leachate, and reprecipitated Cu considered to have deposited from a vapor phase during quenching. For weakly acidic experiments (i.e., pH 4-6), greater amounts of vapor-Cu/fluid-Cu generally corresponded to greater negative fractionation (by up to -1.0‰) compared to the original chalcopyrite, indicating a depleted vapor phase relative to the fluid phase. While Maher et al. (2011) acknowledge continued work with better constraints on pH and fO_2 is needed, they concluded that the major control on fractionation is the degree of Cu-partitioning between liquid and vapor phases, largely controlled by pH and salinity. Similarly, Rempel et al. (2012) measured the δ^{65}Cu of liquid and vapor pairs in the system CuCl-NaCl-H_2O. Although most pairs had equal δ^{65}Cu values within uncertainties, a shift to heavier isotopic values was noticed between measurements at the highest and lowest pressures, particularly in the experiment with the greatest pressure difference (i.e., with the most vapor removed). Thus, Rayleigh fractionation with periodic removal of ^{65}Cu-depleted vapor was invoked to account for the overall enrichment of the system. However, those experiments were performed at a pH of 9.7 and may vary considerably from realistic hydrothermal conditions of pH <4, considering the effect of pH on vapor complex stability (e.g., Mavrogenes et al., 2002; Maher et al., 2011).

Discrepancy between the experimental and theoretical results may also be due to the hydration of Cu-ligands in a hydrothermal system. That is, in steam or a low-density supercritical fluid the Cu_3Cl_3 complex will most likely be hydrated, although the exact solvation number is not known (Maher et al., 2011; Rempel et al., 2012). Likewise, the hydration number of $CuCl\cdot(H_2O)_n$ could range from 2 to 14, depending on the fH_2O at temperatures <400°C (Migdisov et al., 2014). This will affect the energetics of the molecules and therefore could substantially change the calculated RPFRs. For example, Sherman (2013) recognized that the aqueous CuHS complex in hydrothermal systems is actually in two-fold coordination as $CuHS(H_2O)$, and the calculated RPFR for that ligand is significantly different to that of unhydrated CuHS (Table 4.3).

Despite these somewhat inconclusive results, certain field observations are consistent with the theory of ^{65}Cu-enriched vapor transport. For example, Li et al. (2010b) used the concept as a viable explanation for spatial δ^{65}Cu patterns of enrichment and depletion noticed in porphyry deposits at Northparkes, Australia. The outward movement and condensation of an enriched vapor could account for peripheral halo δ^{65}Cu values up to ~0.8‰, while depleted brines may form the low δ^{65}Cu margin (minimum ≈ -0.4‰), when compared to core mineralization (average = 0.19 ±0.14‰). Dilution and dispersion of vapor towards the periphery is also consistent with low Cu-grades present there, while concomitant condensation of acidic volatiles at the margin would correlate with an observed shift from K-feldspar to phyllic alteration. Similarly, Maher and Larson (2007) observed that mineralization proximal to fluid sources tended to be isotopically lighter than distal mineralization in the Coroccohuayco and Tintaya skarn deposits of Peru.

4.6.2 Interpretation of magmatic fluids and copper isotope fractionation

Abundant evidence indicates a substantial magmatic volatile component is included in the hydrothermal systems at Brothers volcano, as detailed by de Ronde et al. (2011). While the Cone site displays the strongest evidence for magmatic contributions, here we limit our discussion to the NW Caldera site because it is the focus of the Cu mineralization analysed in this study. The most sensitive and unequivocal indicator of magmatic gases is ^{3}He sourced from the mantle (Lupton, 1983); highly ^{3}He-enriched plume and vent fluids have been sampled at the NW Caldera site (de Ronde et al., 2005; 2011). Magmatic CO_2 and SO_2 gases would be expected to accompany ^{3}He-enriched discharge at an arc volcano. Concentrations of CO_2 between 17.3 and 42.8 mM/kg (de Ronde et al., 2011) indicate direct injection of magmatic CO_2 when considering concentrations at MOR sites are ≤22 mM/kg (Von Damm, 1995). While direct measurements of SO_2 are not possible due to rapid dissolution and disproportionation in water (e.g., Butterfield et al., 2011), high concentrations of the products of those reactions in NW Caldera fluids (end-member H_2S concentrations of 3.6 to 11.1$_{(liquid+gas)}$ mM/kg and pH values between 2.8 and 3.1) indicate disproportionation of substantial magmatic SO_2 (de Ronde et al., 2011). Isotopic evidence also testifies to a magmatic input; mostly negative δD_{H2O} and δ^{15}N values, along with measured $\delta^{18}O_{H2O}$ values commonly below 0‰ are all consistent with a magmatic fluid source (Giggenbach, 1992; Marty and Dauphas, 2003). Enargite-bearing stockwork veins also attest to a high sulfidation environment in the recent past (de Ronde et al., 2005; 2011). Finally, vent fluid Cl concentrations both less than and greater than seawater are indicative of sub-seafloor phase separation and the subsequent expulsion of condensed gases (de Ronde et al., 2011). Applying hydrological modeling to the NW Caldera site, Gruen et al. (2014) found that the injection of saline magmatic fluids at depth into the hydrothermal system was *required* in order to achieve phase separation. Thus, we consider a process of volatile-transport of Cu, with accompanying isotopic fractionation, a distinct possibility to explain the range of δ^{65}Cu values measured in chimneys sampled from the NW Caldera field.

While Cu isotope analyses were done in this study on a grain-size scale, this technique cannot detect finer-scale mineralogical and/or chemical fluctuations. For example, trace element mapping of

Lena chimney (sample #1) shows visibly laminated chalcopyrite in the interior contains distinct bands of ~30 μm width that host a magmatic suite of elements including Co, Mo, Ag, Te, Au, and Bi (Berkenbosch et al., 2012b). Some of these bands are also considered to include magmatic sulfur as de Ronde et al. (2011) noted a correlation between higher Au contents in Brothers chimney chalcopyrite and more negative $\delta^{34}S$ (i.e., more 'magmatic'). If $\delta^{65}Cu$ variations related to vapour influx also occur on such fine scales, it may soon be resolvable using femtosecond LA-ICPMS with a resolution down to 15 μm (Ikehata et al., 2011). Until then, the *Leg of Lamb* chimney may better provide insight into the variance of $\delta^{65}Cu$ in different bands, as the banding in this particular chimney is much wider. For example, the outer band (~1.5 cm; Fig. 4.3b) of massive chalcopyrite has a generally uniform composition characterized by incorporated Se and Au, while inner bands of later, box-work chalcopyrite contain no Se or Au (Berkenbosch et al., 2012b). Copper isotopes in the outer band were measured as $\delta^{65}Cu$ = 1.44‰, whereas values measured in the inner bands were significantly lower at ~0.15‰. If such large variations in Cu isotopes occurs in other, finer bands, such as those seen in *Lena* chimney, and were randomly sampled during this study, it may explain the large differences in $\delta^{65}Cu$ measured in contemporaneous (<1 yr) chalcopyrite that lines the high temperature, internal conduit of the chimney.

Isotopic analysis of the *Leg of Lamb* chimney also provides insight into the origin of the bornite-chalcocite-covellite assemblage formed at the exterior margin of the massive chalcopyrite conduit in this chimney. Originally, Berkenbosch et al. (2012a) considered the bornite assemblage to be *secondary* in origin, resulting from weathering of the chalcopyrite core due to its proximity with oxidizing ambient seawater. If this were true, current isotopic studies suggest that the remnant chalcopyrite should have lower values than that of primary chalcopyrite (e.g., Ehrlich et al., 2004; Mathur et al., 2005; Kimball et al., 2009). However, the outer ring of chalcopyrite in the *Leg of Lamb* chimney has the highest $\delta^{65}Cu$ value measured in this study. Although it is only one sample, this result is not consistent with the bornite assemblage forming from Cu leached from the inner chalcopyrite. Rather, the external Cu phases may well be *primary* and formed due to vent fluids mixing with seawater as proposed, for example, by Haymon (1983), or through the expulsion of more oxidized vent fluids consistent with the injection of magmatic fluids and/or volatiles (de Ronde et al., 2011).

Niuatahi caldera volcano of the Tonga backarc also displays definitive evidence for metal-bearing magmatic vapors, including a pool of metal-rich, molten sulphur atop the largest, central, resurgent volcanic cone (Kim et al., 2011); however, no detailed studies have been undertaken of the northern caldera wall from which *Pui 'O Tafahi* chimney was collected. The five samples analysed from that chimney all have relatively low $\delta^{65}Cu$ values, between 0.00 and 0.29‰. The lack of any higher $\delta^{65}Cu$ values may be due to insufficient sampling size, or could indicate that magmatic volatiles had less of an influence on the deposition of Cu in this chimney. If the latter, the hydrothermal system along the northern caldera wall may be disconnected from the underlying magmatic source and driven solely by circulating, modified seawater and/or has experienced infrequent injections of magmatic fluids during this chimney's formation.

4.7 Conclusions

In summary, we believe the demonstrable magmatic influence on the Brothers NW Caldera hydrothermal field is reflected in the Cu isotope values of black smoker chimneys at this site. The bulk of the δ^{65}Cu data in this study falls between -0.03 and 0.43‰, indicative of mantle rock source values (e.g., Zhu et al. 2000; Li et al. 2009; Ikehata and Hirata 2012). However, a small subset of the data has higher δ^{65}Cu values, between 0.57 and 1.44‰, which we believe result from relatively rapid fluctuations of vapor content in the vent fluids. It has been suggested that volcanic degassing could lead to significant Cu partitioning between fluid and vapor phases, with heavy ^{65}Cu modelled to concentrate in the vapor phase and light ^{63}Cu into the liquid phase (Seo et al., 2007). Although the exact Cu-ligands involved are uncertain at this time, that ^{65}Cu might concentrate in the vapor phase is consistent with fractionations of ~1.3‰ observed within single chimneys at Brothers volcano, where magmatic contributions are significant, and vapor transport of Cu could be reasonably expected. Repeated, short-lived injections of magmatic volatiles could produce fine-scale bands in chalcopyrite that have varying elemental and isotopic compositions, while relatively longer intervals of vapor injection and/or vapor-favored pathways may result in the formation of wider bands. Such fluctuating hydrothermal activity is congruous with the ongoing cyclic and dynamic nature of expelled lava, fluid, and gas seen at NW Rota-1 volcano, an erupting and degassing submarine volcano of the Mariana arc (Chadwick Jr et al., 2008). The enriched-vapor theory is compatible with models that invoke physicochemical fluctuations to account for Cu isotope fractionation (e.g., Asael et al., 2009), as the stabilities of complexing ligands are sensitive to changes in external conditions. It explains the separation of the isotopically enriched and depleted parts of the system at active seafloor massive sulfide deposits, consistent with the lack of negative δ^{65}Cu values in active chimneys. It is consistent with the suggestion by several authors that Cu transport by vapour is a common mechanism in the formation of porphyry copper deposits (e.g., Heinrich et al., 1992), which are also known to be distinctly magmatic-hydrothermal in origin, and have a similar distribution of positive δ^{65}Cu values as Brothers (Fig. 4.7). Moreover, the ^{65}Cu-enrichment of active chimneys from MOR sites suggests vapor transport of Cu may be more prevalent at those environments than previously recognized, although the very high Cu isotope values (>1.5‰) of chimneys hosted in ultramafic rocks may require some additional fractionation process, such as that described by Rouxel et al. (2004). Finally, considering that the distribution of δ^{65}Cu in primary chalcopyrite from all deposits is concentrated in a relatively narrow band, i.e., between -0.50 and 0.75‰ (Fig. 4.6), the usefulness of Cu isotopes in fingerprinting distinct mantle reservoirs appears limited.

4.8 Acknowledgements

This research was supported by an Australian Research Council Centre of Excellence in Ore Deposits (CODES) research scholarship (University of Tasmania), an AusIMM Bicentennial Gold 88 endowment, and a Society of Economic Geologists Foundation student research grant from the Hugh E. McKinstry Fund, all to H. Berkenbosch. C. de Ronde was supported by public research funding from the Government of New Zealand. We thank S.G. Merle for assistance with Figures 4.1 and 4.2,

and T. Seward for helpful insight into Cu-complexes. This manuscript was also improved by helpful suggestions from R. Mathur and an anonymous reviewer.

Chapter 5
Conclusions

5.1 Summary Remarks

This study employed a three-tier approach at a range of scales to test the hypothesis that *magmatic fluids significnatly affect the composition of mineralization at Brothers NW Caldera vent site*, considering there is significant prior evidence for a magmatic fluid component to the hydrothermal system. This magmatic component is apparent in present-day vent fluid compositions and isotopic characteristics, their composition and concentration of dissolved gases, pH, the $\delta^{34}S$ of sulfides and native sulfur, and the mineralogy of host-rock alteration and veins. This thesis expands on previous work by focusing specifically on the active and inactive Cu- and Zn-rich chimneys of the NW Caldera hydrothermal field.

Firstly, this work has provided more detailed mineralogical descriptions of the various chimney types than previous 'framework' type studies. The chimneys are Cu- or Zn-dominated and have been subdivided into four categories, with paragenetic and morphological growth models presented for each type. Small (generally <5 μm) Bi-(Se) and Au-bearing telluride inclusions are the first Au-bearing phases to be identified in the Cu-rich chimneys at Brothers, formed at temperatures >300°C and which contain up to 91 ppm Au. In the chalcopyrite-bornite chimneys, a suite of Cu-sulfides including bornite, chalcocite and covellite, forms along with specular hematite and crystalline goethite, crystal habits that have not previously been reported from other seafloor deposits. When considered together with the occurrence of rare enargite in the chimneys, this assemblage indicates a more oxidized vent fluid that is consistent with a fluid of magmatic origin.

Secondly, to examine the chimney mineralogy at a smaller scale, trace element distributions across chimney walls were mapped using SXRF, which allowed analyses over a greater area (up to 36.5 x 5 mm^2) at higher resolution (2 μm) than previous studies. The detailed images show previously unrecognized characteristics of the sulfide chimneys at Brothers. For example, the element maps presented in this study clarify the relationship between the two types of Zn-rich chimneys, which share mineralogical and textural similarities. Previously undocumented Cu distributions in the sphalerite-barite chimneys demonstrate the initial stages of chalcopyrite replacement of sphalerite within the chimney interior by low Cu-bearing fluids, which progresses to the visible chalcopyrite-lined channels in the sphalerite-chalcopyrite chimneys. Fine (15 - 40 μm), 'rings' demarcated by specific trace element

enriched suites near the conduit in the chalcopyrite-sulfate chimney include varying combinations and contents of Co, Ni, Zn, As, Se, Mo, Ag, Cd, Sn, Te, Au, Tl, Pb, Bi, and U; the latter clearly signals the penetration of seawater into the interior of even vigorously venting chimneys. These periodic (and relatively short-lived) incursions of seawater are thought to initiate the instantaneous precipitation of metals from the vent fluids. Using the composition of these rings as a proxy for vent fluid compositions, the calculation of enrichment factors distinguish those with a distinct magmatic affiliation, i.e., Au, Te, Bi, Se (cf. the elements that occur in the tellurides) together with Ag and Cu. With the exception of Cu, these are the same suite of elements that are condensed from high-temperature fumaroles at subaerial arc volcanoes, indicative of their magmatic affinity.

Lastly, this research focused on the isotopes of Cu as it represents the dominant, high-temperature ore element at the NW Caldera site at Brothers volcano. Although the bulk of the δ^{65}Cu data in this study lie between -0.03 and 0.43‰, indicative of mantle rock source values, a small subset are higher δ^{65}Cu values between 0.57 and 1.44‰. These higher δ^{65}Cu values are randomly distributed throughout several chimneys (i.e., near the top and bottom, interior and exterior) for chalcopyrite of approximately the same age (<1 yr). This suggests the higher δ^{65}Cu values are not related to oxidation by ambient seawater, an effective process to *decrease* δ^{65}Cu values, and may represent isotopic variation within the vent fluids themselves. Previous research suggests volcanic degassing can lead to significant Cu partitioning between fluid and vapor phases in which, uncommonly, heavy ^{65}Cu may concentrate in the *vapor* phase and light ^{63}Cu into the *liquid* phase (Seo et al., 2007). Thus, the observed Cu isotope fractionation of ~1.3‰ randomly distributed within contemporaneous chalcopyrite of single chimneys at Brothers volcano is consistent with some Cu transport by magmatic volatiles.

Distinguishing any magmatic component in a hydrothermal system from the typically dominant modified seawater hydrothermal fluid is difficult, especially with regards to metals. Within the context of other comprehensive 'framework' studies, this study investigated how magmatic contributions at Brothers volcano are manifest in the sulfide chimneys of the NW Caldera hydrothermal site. This focused work into the composition of Brothers chimneys used techniques that range on a descending scale from microscopy to electron beams to the isotopes of individual atoms, and finds consistent and compelling evidence that some metals contained within the chimneys, namely Au, Te, Bi, Se, Ag and Cu, have a distinct magmatic origin. Repeated, short-lived injections of magmatic volatiles and periods of subseafloor phase separation are believed to occur at the NW Caldera vent field at Brothers, and are considered responsible for the varying elemental and isotopic compositions within the chalcopyrite lining the interior of the chimneys (Dziak et al., 2008; de Ronde et al., 2011; Gruen et al., 2014). Regional, tectonic-scale features related to subduction may account for the particularly Bi- and Au-rich chimneys at Brothers; that is, the subduction of the Hikurangi Plateau and its overlying ~500m of sediment sourced from nearby continental New Zealand. Additions to the sub-arc mantle from the subducted and subsequently melted terrigenous sediment are likely the source of the magmatically-derived Bi, Te, Ag and possibly Se (Timm et al., 2012). Moreover, the local enrichment of Bi in Brothers magma may enhance the Au content of the chimneys

through concentration ("scavenging") of Au by liquid Bi, both of which are efficiently transported to the seafloor, as evidenced by the extreme Bi and high Au contents within Brothers chimneys (maximum >2000 and 91 ppm, respectively; Tooth et al., 2008; de Ronde et al., 2011; Monecke et al., 2016). Furthermore, subduction of the Hikurangi Plateau enhances sub-arc volatile transfer and heat generation, which may ultimately have contributed to the volatile-rich nature of Brothers hydrothermal system and its ability to transport magmatic Cu (e.g., de Ronde et al., 2007). Thus, Brothers unique Cu-Bi-Au-rich chimneys result from a combination of the regional subduction of a large igeneous province containing relatively high amounts of continental sediments, the exsolution of volatile-rich magmatic fluids, and the fluid-focusing effects within a caldera volcano. These findings in an active, undeformed, arc volcano-hosted system further our understanding of the nature and setting of economically important, polymetallic seafloor massive sulfides and their association with subduction environments. In particular, it suggests that ancient Bi-Au-rich VMS deposits such as those in the Urals, Iberian Pyrite Belt, or at Boliden, Sweden (e.g., Marcoux et al., 1996; Wagner and Jonsson, 2001; Maslennikov et al., 2009) may have formed above a convergence zone associated with high amounts of subducted terrigenous sediment and thus occurred in relative proximity to subaerial continental crust.

5.2 Future Research

There are many directions that could be pursued to further research on Brothers sulfide chimneys. With respect to the element mapping component of this thesis, a recent study (Mittelstaedt et al., 2016) suggests fluid flux within chimney walls may be influenced by diurnal effects, such as tides, which may be relevant to the formation of the trace element rings. No comparison was made with results of other chimney mapping studies, either from modern seafloor chimneys (e.g., Butler and Nesbitt, 1999; Li et al., 2010; Yeats et al., 2010; Kristall et al., 2011; Keith et al., 2016) or ancient chimney fragments (Maslennikov et al., 2013; Revan et al., 2014). Likewise, similarities between Brothers' geological setting (i.e., the relationship between mineralization and particular volcanic units within the stratigraphy) and ancient VMS deposits could be examined, in particular for Bi- and Au-rich deposits in the Urals (e.g., Vikentyev, 2006). Regarding Cu isotopes, individual VMS deposits could be investigated regarding the remobilization and homogenization of Cu isotopes during burial, alteration, metamorphism and uplift. Likewise, the relationship between skarn deposit host rocks and the variability of δ65Cu values could be examined further. Secular variations of the compiled, global Cu isotope values presented in this study could be studied to investigate possible variation in mantle source values through time. Finally, the Cu isotope research could be complemented by the analysis of Fe isotopes using Fe separated from the same chalcopyrite as the Cu used in this study. This would test whether both Cu and Fe isotopes show the same enrichment patterns, especially considering that Syverson et al. (2014) have shown experimentally that an isotopically heavy vapour phase results from Fe isotope fractionation during sub-seafloor phase separation of hydrothermal fluids.

References

Arculus, R. J., 1994, Aspects of magma genesisi in arcs: Lithos, v. 33, p. 189-208.

Arculus, R. J., 2005, Arc-backarc systems of northern Kermadec-Tonga, New Zealand Minerals Conference: Realising New Zealand's mineral potential: Auckland, Crown Minerals, Ministry of Economic Development and Australasian Institute of Mining and Metallurgy, New Zealand Branch, p. 45-50.

Arribas, A., 1995, Characteristics of high-sulfidation epithermal deposits, and their relation to magmatic fluid, *in* Thompson, J. F. H., ed., Magmas, fluids, and ore deposits. Short Course Handbook, 23: Ottawa, ON, Canada, Mineralogical Association of Canada. p. 419-454.

Asael, D., Matthews, A., Bar-Matthews, M., and Halicz, L., 2007, Copper isotope fractionation in sedimentary copper mineralization (Timna Valley, Israel): Chemical Geology, v. 243, p. 238-254.

Asael, D., Matthews, A., Oszczepalski, S., Bar-Matthews, M., and Halicz, L., 2009, Fluid speciation controls of low temperature copper isotope fractionation applied to the Kupferschiefer and Timna ore deposits: Chemical Geology, v. 262, p. 147-158.

Auclair, G., and Fouquet, Y., 1987, Distribution of selenium in high-temperature hydrothermal sulfide deposits at 13°N, East Pacific Rise: Canadian Mineralogist, v. 25, p. 577-587.

Baker, E. T., Embley, R. W., de Ronde, C. E. J., and Walker, S. L., 2012, High-resolution hydrothermal mapping of Brothers caldera, Kermadec arc: Economic Geology, v. 107, p. 1583- 1593.

Barton, P. B., Jr., and Bethke, P. M., 1987, Chalcopyrite disease in sphalerite: Pathology and epidemiology: American Mineralogist, v. 72, p. 451-467.

Beaulieu, S. E., 2015, InterRidge Global Database of Active Submarine Hydrothermal Vent Fields: prepared for InterRidge, Version 3.3. World Wide Web electronic publication, Version 3.4 accessed 2017-06-01, http://vents-data-interridge.org.

Berkenbosch, H. A., de Ronde, C. E. J., Gemmell, J. B., McNeill, A. W., and Goemann, K., 2012a, Mineralogy and formation of black smoker chimneys from Brothers submarine volcano, Kermadec arc: Economic Geology, v. 107, p. 1613-1633.

Berkenbosch, H. A., de Ronde, C. E. J., McNeill, A. W., Goemann, K., and Gemmell, J. B., 2012b, Distribution of minor and trace elements in sulfide chimneys from Brothers submarine volcano, Kermadec Arc, 34th International Geological Congress, 34: Brisbane, Australia, International Geological Congress, p. 3176.

Berkenbosch, H. A., de Ronde, C. E. J., Paul, B. T., and Gemmell, J. B., 2015, Characteristics of Cu isotopes from chalcopyrite-rich black smoker chimneys at Brothers volcano, Kermadec arc, and Niuatahi volcano, Lau basin: Mineralium Deposita, v. 50, p. 811-824.

Bischoff, J. L., and Seyfried, W. E., 1978, Hydrothermal chemistry of seawater from 25° to 350°C: American Journal of Science, v. 278, p. 838-860.

Bogdanov, Y. A., Lein, A. Y., Maslennikov, V. V., Syaoli,

L., and Ul'yanov, A. A., 2008, Mineralogical-geochemical features of sulfide ores from the Broken Spur hydrothermal vent field: Oceanology, v. 48, p. 679-700.

Braxton, D., and Mathur, R., 2011, Exploration applications of copper isotopes in the supergene environment: A case study of the Bayugo porphyry copper-gold deposit, Southern Philippines: Economic Geology, v. 106, p. 1447-1463.

Brett, R., Evans Jr, H. T., Gibson Jr, E. K., Hedenquist, J. W., Wandless, M. V., and Sommer, M. A., 1987, Mineralogical studies of sulfide samples and volatile concentrations of basalt glasses from the southern Juan de Fuca Ridge: Journal of Geophysical Research B: Solid Earth, v. 92, p. 11373-11379.

Butler, I. B., and Nesbitt, R. W., 1999, Trace element distributions in the chalcopyrite wall of a black smoker chimney: Insights from laser ablation inductively coupled plasma mass spectrometry (LA-ICP-MS): Earth and Planetary Science Letters, v. 167, p. 335-345.

Butterfield, D. A., Nakamura, K. I., Takano, B., Lilley, M. D., Lupton, J. E., Resing, J. A., and Roe, K. K., 2011, High SO_2 flux, sulfur accumulation, and gas fractionation at an erupting submarine volcano: Geology, v. 39, p. 803-806.

Caratori Tontini, F., Davy, B., de Ronde, C. E. J., Embley, R. W., Leybourne, M. I., and Tivey, M. A., 2012, Crustal magnetization of Brothers volcano, New Zealand, measured by autonomous underwater vehicles: Geophysical expression of a submarine hydrothermal system: Economic Geology, v. 107, p. 1571-1581.

Chadwick Jr, W. W., Cashman, K. V., Embley, R. W., Matsumoto, H., Dziak, R. P., de Ronde, C. E. J., Lau, T. K., Deardorff, N. D., and Merle, S. G., 2008, Direct video and hydrophone observations of submarine explosive eruptions at NW Rota-1 volcano, Mariana arc: Journal of Geophysical Research B: Solid Earth, v. 113, 23 p.

Ciobanu, C. L., Cook, N. J., and Spry, P. G., 2006, Preface – Special Issue: Telluride and selenide minerals in gold deposits – how and why?: Mineralogy and Petrology, v. 87, p. 163-169.

Ciobanu, C. L., Cook, N. J., Pring, A., Brugger, J., Danyushevsky, L. V., and Shimizu, M., 2009, 'Invisible gold' in bismuth chalcogenides: Geochimica et Cosmochimica Acta, v. 73, p. 1970-1999.

Cooke, D. R., and McPhail, A. D. C., 2001, Epithermal Au-Ag-Te mineralization, Acupan, Baguio district, Philippines: Numerical simulations of mineral deposition: Economic Geology, v. 96, p. 109-131.

Corliss, J. B., Dymond, J., Gordon, L. I., Edmond, J. M., von Herzen, R. P., Ballard, R. D., Green, K., Williams, D., Bainbridge, A., Crane, K., and van Andel, T. H., 1979, Submarine thermal springs on the Galápagos rift: Science, v. 203, p. 1073- 1083.

D'Yachkova, I. B., and Khodakovskii, I. L., 1968, Thermodynamic equilibria of sulfur, selenium and tellurium water systems in range of temperatures from 25 to 300°C and their geochemical interpretation: Geokhimiya, v. 11, p. 1358-1375.

Danyushevsky, L., Robinson, P., Gilbert, S., Norman, M., Large, R., McGoldrick, P., and Shelley, M., 2011, Routine quantitative multi-element analysis of sulphide minerals by laser ablation ICP-MS: Standard development and consideration of matrix effects: Geochemistry: Exploration, Environment, Analysis, v. 11, p. 51-60.

De Hoog, J. C. M., Mason, P. R. D., and Van Bergen, M. J., 2001, Sulfur and chalcophile elements in subduction zones: Constraints from a laser ablation ICP-MS study of melt inclusions from Galunggung volcano, Indonesia: Geochimica et Cosmochimica Acta, v. 65, p. 3147-3164.

de Ronde, C. E. J., 1995, Fluid chemistry and isotopic characteristics of seafloor hydrothermal system and associated VMS deposits; potential for magmatic contributions, *in* Thompson, J. F. H., ed., Magmas, fluids, and ore deposits. Short Course Handbook., 23: Ottawa, ON, Canada, Mineralogical Association of Canada, p. 479-509.

de Ronde, C. E. J., Faure, K., Bray, C. J., Chappell, D. A., and Wright, I. C., 2003, Hydrothermal fluids associated with seafloor mineralization at two southern Kermadec arc volcanoes, offshore New

Zealand: Mineralium Deposita, v. 38, p. 217-233.

de Ronde, C. E. J., Hannington, M. D., Stoffers, P., Wright, I. C., Ditchburn, R. G., Reyes, A. G., Baker, E. T., Massoth, G. J., Lupton, J. E., Walker, S. L., Greene, R. R., Soong, C. W. R., Ishibashi, J., Lebon, G. T., Bray, C. J., and Resing, J. A., 2005, Evolution of a submarine magmatic-hydrothermal system: Brothers volcano, southern Kermadec Arc, New Zealand: Economic Geology, v. 100, p. 1097-1133.

de Ronde, C. E. J., Baker, E. T., Massoth, G. J., Lupton, J. E., Wright, I. C., Sparks, R. J., Bannister, S. C., Reyners, M. E., Walker, S. L., Greene, R. R., Ishibashi, J., Faure, K., Resing, J. A., and Lebon, G. T., 2007, Submarine hydrothermal activity along the mid-Kermadec Arc, New Zealand: Large-scale effects on venting: Geochemistry Geophysics Geosystems, v. 8, 27 p.

de Ronde, C. E. J., Massoth, G. J., Butterfield, D. A., Christenson, B. W., Ishibashi, J., Ditchburn, R. G., Hannington, M. D., Brathwaite, R. L., Lupton, J. E., Kamenetsky, V. S., Graham, I. J., Zellmer, G. F., Dziak, R. P., Embley, R. W., Dekov, V. M., Munnik, F., Lahr, J., Evans, L. J., and Takai, K., 2011, Submarine hydrothermal activity and gold-rich mineralization at Brothers Volcano, Kermadec Arc, New Zealand: Mineralium Deposita, v. 46, p. 541-584.

de Ronde, C. E. J., Butterfield, D. A., and Leybourne, M. I., 2012, Metallogenesis and mineralization of intraoceanic arcs I: Kermadec Arc- introduction: Economic Geology, v. 107, p. 1521-1525.

de Ronde, C. E. J., Walker, S. L., Ditchburn, R. G., Caratori Tontini, F., Hannington, M. D., Merle, S. G., Timm, C., Handler, M. R., Wysoczanski, R. J., Dekov, V. M., Kamenov, G. D., Baker, E. T., Embley, R. W., Lupton, J. E., and Stoffers, P., 2014, The anatomy of a buried submarine hydrothermal system, Clark volcano, Kermadec arc, New Zealand: Economic Geology, v. 109, p. 2261-2292.

de Ronde, C. E. J., and Stucker, V. K., 2015, Seafloor hydrothermal venting at volcanic arcs and backarcs, *in* Sigurdsson, H., Houghton, B. F., McNutt, S., Rymer, H., and Stix, J., eds., Encyclopedia of Volcanoes, Academic Press, p. 823-849.

Dekov, V. M., and Savelli, C., 2004, Hydrothermal activity in the SE Tyrrhenian Sea: An overview of 30 years of research: Marine Geology, v. 204, p. 161-185.

Dekov, V. M., Rouxel, O., Kouzmanov, K., Bindi, L., Asael, D., Fouquet, Y., Etoubleau, J., Burgaud, G., and Wälle, M., 2016, Enargite-luzonite hydrothermal vents in Manus Back-Arc Basin: Submarine analogues of high-sulfidation epithermal mineralization: Chemical Geology, v. 438, p. 36-57.

DeMets, C., Gordon, R. G., Argus, D. F., and Stein, S., 1994, Effect of recent revisions to the geomagnetic reversal time scale and estimates of current plate motions: Geophysical Research Letters, v. 21, p. 2191-2194.

Ditchburn, R. G., Bernard, J. B., and de Ronde, C. E. J., 2012, Radiometric dating of volcanogenic massive sulfides and associated iron oxide crusts with an emphasis on ^{226}Ra/Ba and ^{228}Ra/^{226}Ra in volcanic and hydrothermal processes at intraoceanic arcs: Economic Geology, v. 107, p. 1635-1648.

Douglas, N., Mavrogenes, J., Hack, A., and England, R., 2000, The liquid bismuth collector model; an alternative gold deposition mechanism, *in* Silbeck, C. G., and Hubble, T. C. T., eds., Understanding planet Earth; searching for a sustainable future; on the starting blocks of the third millenium, 15th Australian Geological Convention, 59: Sydney, Geological Society of Australia, p. 135.

Dziak, R. P., Haxel, J. H., Matsumoto, H., Lau, T. K., Merle, S. G., de Ronde, C. E. J., Embley, R. W., and Mellinger, D. K., 2008, Observations of regional seismicity and local harmonic tremor at Brothers volcano, south Kermadec arc, using an ocean bottom hydrophone array: Journal of Geophysical Research B: Solid Earth, v. 113, 13 p.

Ehrlich, S., Butler, I., Halicz, L., Rickard, D., Oldroyd, A., and Matthews, A., 2004, Experimental study of the copper isotope fractionation between aqueous Cu(II) and covellite, CuS: Chemical Geology, v. 209, p. 259-269.

Embley, R. W., de Ronde, C. E. J., Merle, S. G., Davy,

B., and Caratori Tontini, F., 2012, Detailed morphology and structure of an active submarine Arc caldera: Brothers volcano, Kermadec Arc: Economic Geology, v. 107, p. 1557-1570.

Embley, R. W., Resing, J., Tebo, B., Baker, E. T., Butterfield, D. A., Chadwick Jr, W. W., Davis, R., de Ronde, C. E. J., Lilley, M. D., Lupton, J. E., Merle, S. G., Rubin, K. H., Shank, T. M., Walker, S. L., Arculus, R. J., Bobbit, A. M., Buck, N., Caratori Tontini, F., Crowhurst, P. V., Mitchell, E., Olson, E. J., Ratmeyer, V., Richards, S., Roe, K., Keener, P., Maritnez-Lyons, A., Sheehan, C., and Brian, R., 2013, Hyperactive hydrothermal activity in the NE Lau basin revealed by ROV dives, 2013 Fall Meeting: San Fransisco, American Geophysical Union, Abstract V21C-2738.

Fisher, L. A., Fougerouse, D., Cleverley, J. S., Ryan, C. G., Micklethwaite, S., Halfpenny, A., Hough, R. M., Gee, M., Paterson, D., Howard, D. L., and Spiers, K., 2015, Quantified, multi-scale X-ray fluorescence element mapping using the Maia detector array: application to mineral deposit studies: Mineralium Deposita, v. 50, p. 665-674.

Fouquet, Y., Auclair, G., Cambon, P., and Etoubleau, J., 1988, Geological setting and mineralogical and geochemical investigations on sulfide deposits near 13°N on the East Pacific Rise: Marine Geology, v. 84, p. 145-178.

Giggenbach, W. F., 1992, Isotopic shifts in waters from geothermal and volcanic systems along convergent plate boundaries and their origin: Earth and Planetary Science Letters, v. 113, p. 495-510.

Goldfarb, M. S., Converse, D. R., Holland, H. D., and Edmond, J. M., 1983, The genesis of hot spring deposits on the East Pacific Rise, 21°N, *in* Ohmoto, H., and Skinner, B. J., eds., Economic Geology Monograph, v. 5: Lancaster, PA, United States, Economic Geology Publishing Company, p. 184-197.

Govindaraju, K., 1994, 1994 compilation of working values and sample description for 383 geostandards, Geostandards Newsletter special issue 18: Paris, Association Nationale de la Recherche Technique, Paris, France, 158 p.

Graham, S., Pearson, N., Jackson, S., Griffin, W., and O'Reilly, S. Y., 2004, Tracing Cu and Fe from source to porphyry: In situ determination of Cu and Fe isotope ratios in sulfides from the Grasberg Cu-Au deposit: Chemical Geology, v. 207, p. 147-169.

Grichuk, D. V., 2012, Thermodynamic model of ore-forming processes in a submarine island-arc hydrothermal system: Geochemistry International, v. 50, p. 1069-1100.

Gruen, G., Weis, P., Driesner, T., de Ronde, C. E. J., and Heinrich, C. A., 2012, Fluid-flow patterns at Brothers volcano, Southern Kermadec Arc: Insights from geologically constrained numerical simulations: Economic Geology, v. 107, p. 1595-1611.

Gruen, G., Weis, P., Driesner, T., Heinrich, C. A., and de Ronde, C. E. J., 2014, Hydrodynamic modeling of magmatic-hydrothermal activity at submarine arc volcanoes, with implications for ore formation: Earth and Planetary Science Letters, v. 404, p. 307-318.

Haase, K. M., Worthington, T. J., Stoffers, P., Garbe-Schoenberg, D., and Wright, I., 2002, Mantle dynamics, element recycling, and magma genesis beneath the Kermadec Arc-Havre Trough: Geochemistry, Geophysics, Geosystems - G3, v. 3, 22 p.

Haest, M., Muchez, P., Petit, J. C. J., and Vanhaecke, F., 2009, Cu isotope ratio variations in the the Dikulushi Cu-Ag deposit, DRC: Of primary origin or induced by supergene reworking?: Economic Geology, v. 104, p. 1055-1064.

Hannington, M., Jamieson, J., Monecke, T., Petersen, S., and Beaulieu, S., 2011, The abundance of seafloor massive sulfide deposits: Geology, v. 39, p. 1155-1158.

Hannington, M. D., de Ronde, C. E. J., and Petersen, S., 2005, Sea-floor tectonics and submarine hydrothermal systems: Economic Geology 100th Anniversary Volume, p. 111-141.

Haymon, R. M., 1983, Growth history of hydrothermal black smoker chimneys: Nature, v. 301, p. 695-698.

Hedenquist, J. W., and Lowenstern, J. B., 1994, The role of magmas in the formation of hydrothermal ore deposits: Nature, v. 370, p. 519-527.

Heinrich, C. A., Ryan, C. G., Mernagh, T. P., and Eadington, P. J., 1992, Segregation of ore metals between magmatic brine and vapor: a fluid inclusion study using PIXE microanalysis: Economic Geology, v. 87, p. 1566-1583.

Heinrich, C. A., 2007, Fluid-fluid interactions in magmatic-hydrothermal ore formation, *in* Liebscher, A., and Heinrich, C., eds., Fluid-Fluid Interactions, 65. Reviews in Mineralogy and Geochemistry, p. 363-387.

Heinrich, C. A., and Candela, P. A., 2013, Fluids and ore formation in the Earth's crust, *in* Scott, S., ed., Geochemistry of Mineral Deposits, 13. Treatise on Geochemistry, Elsevier Ltd., p. 1-28.

Henley, R. W., and Berger, B. R., 2013, Nature's refineries - Metals and metalloids in arc volcanoes: Earth-Science Reviews, v. 125, p. 146-170.

Humphris, S. E., Herzig, P. M., Miller, D. J., Alt, J. C., Becker, K., Brown, D., Brugmann, G., Chiba, H., Fouquet, Y., Gemmell, J. B., Guerln, G., Hannington, M. D., Holm, N. G., Honnorez, J. J., Iturrino, G. J., Knott, R., Ludwig, R., Nakamura, K., Petersen, S., Reysenbach, A. L., Rona, P. A., Smith, S., Sturz, A. A., Tivey, M. K., and Zhao, X., 1995, The internal structure of an active sea-floor massive sulphide deposit: Nature, v. 377, p. 713-716.

Huston, D. L., Relvas, J. M. R. S., Gemmell, J. B., and Drieberg, S., 2011, The role of granites in volcanic-hosted massive sulphide ore-forming systems: An assessment of magmatic-hydrothermal contributions: Mineralium Deposita, v. 46, p. 473-507.

Ikehata, K., Notsu, K., and Hirata, T., 2011, Copper isotope characteristics of copper-rich minerals from besshi-type volcanogenic massive sulfide deposits, Japan, determined using a femtosecond LA-MC-ICP-MS: Economic Geology, v. 106, p. 307-316.

Ikehata, K., and Hirata, T., 2012, Copper isotope characteristics of copper-rich minerals from the Horoman peridotite complex, Hokkaido, Northern Japan: Economic Geology, v. 107, p. 1489-1497.

Jiang, S., Jon, W., Yu, J., Pan, J., Liao, Q., and Wu, N., 2002, A reconnaissance of Cu isotopic compositions of hydrothermal vein-type copper deposit, Jinman, Yunnan, China: Chinese Science Bulletin, v. 47, p. 247-250.

Jones, B., de Ronde, C. E. J., and Renaut, R. W., 2008, Mineralized microbes from Giggenbach submarine volcano: Journal of Geophysical Research B: Solid Earth, v. 113, 13 p.

Kamenetsky, V. S., Binns, R. A., Gemmell, J. B., Crawford, A. J., Mernagh, T. P., Maas, R., and Steele, D., 2001, Parental basaltic melts and fluids in eastern Manus backarc Basin: Implications for hydrothermal mineralisation: Earth and Planetary Science Letters, v. 184, p. 685-702.

Kawada, Y., and Yoshida, S., 2010, Formation of a hydrothermal reservoir due to anhydrite precipitation in an arc volcano hydrothermal system: Journal of Geophysical Research B: Solid Earth, v. 115, 31 p.

Keith, M., Häckel, F., Haase, K. M., Schwarz-Schampera, U., and Klemd, R., 2016, Trace element systematics of pyrite from submarine hydrothermal vents: Ore Geology Reviews, v. 72, p. 728-745.

Kim, J., Son, S. K., Son, J. W., Kim, K. H., Shim, W. J., Kim, C. H., and Lee, K. Y., 2009, Venting sites along the Fonualei and Northeast Lau Spreading Centers and evidence of hydrothermal activity at an off-axis caldera in the northeastern Lau Basin: Geochemical Journal, v. 43, p. 1-13.

Kim, J., Lee, K. Y., and Kim, J. H., 2011, Metal-bearing molten sulfur collected from a submarine volcano: Implications for vapor transport of metals in seafloor hydrothermal systems: Geology, v. 39, p. 351-354.

Kimball, B. E., Mathur, R., Dohnalkova, A. C., Wall, A. J., Runkel, R. L., and Brantley, S. L., 2009, Copper isotope fractionation in acid mine drainage: Geochimica et Cosmochimica Acta, v. 73, p. 1247-1263.

Koski, R. A., Jonasson, I. R., Kadko, D. C., Smith, V. K., and Wong, F. L., 1994, Composition, growth mechanisms, and temporal relations by hydrothermal sulfide-sulfate-silica chimneys at the northern Cleft Segment, Juan de Fuca Ridge: Journal of Geophysical Research B: Solid Earth, v. 99, p. 4813-4832.

Kristall, B., Nielsen, D., Hannington, M. D., Kelley, D. S., and Delaney, J. R., 2011, Chemical microenvironments within sulfide structures from the Mothra Hydrothermal Field: Evidence from high-resolution zoning of trace elements: Chemical Geology, v. 290, p. 12-30.

Large, R. R., 1992, Australian volcanic-hosted massive sulfide deposits: features, styles, and genetic models: Economic Geology, v. 87, p. 471-510.

Large, R. R., Danyushevsky, L., Hollit, C., Maslennikov, V., Meffre, S., Gilbert, S., Bull, S., Scott, R., Emsbo, P., Thomas, H., and Foster, J., 2009, Gold and trace element zonation in pyrite using a laser imaging technique; implications for the timing of gold in orogenic and Carlin-style sediment-hosted deposits: Economic Geology, v. 104, p. 635-668.

Larson, P. B., Maher, K., Ramos, F. C., Chang, Z., Gaspar, M., and Meinert, L. D., 2003, Copper isotope ratios in magmatic and hydrothermal ore-forming environments: Chemical Geology, v. 201, p. 337-350.

Layton-Matthews, D., Leybourne, M. I., Peter, J. M., Scott, S. D., Cousens, B., and Eglington, B. M., 2013, Multiple sources of selenium in ancient seafloor hydrothermal systems: Compositional and Se, S, and Pb isotopic evidence from volcanic-hosted and volcanic-sediment-hosted massive sulfide deposits of the Finlayson Lake District, Yukon, Canada: Geochimica et Cosmochimica Acta, v. 117, p. 313-331.

Lepel, E. A., Stefansson, K. M., and Zoller, W. H., 1978, The enrichment of volatile elements in the atmosphere by volcanic activity: Augustine volcano 1976: Journal of Geophysical Research C: Oceans, v. 83, p. 6213-6220.

Leybourne, M. I., de Ronde, C. E. J., Wysoczanski, R. J., Walker, S. L., Timm, C., Gibson, H. L., Layton-Matthews, D., Baker, E. T., Clark, M. R., Caratori Tontini, F., Faure, K., Lupton, J. E., Fornari, D. J., Soule, S. A., and Massoth, G. J., 2012a, Geology, hydrothermal activity, and sea-floor massive sulfide mineralization at the Rumble II West mafic caldera: Economic Geology, v. 107, p. 1649-1668.

Leybourne, M. I., Schwarz-Schampera, U., de Ronde, C. E. J., Baker, E. T., Faure, K., Walker, S. L., Butterfield, D. A., Resing, J. A., Lupton, J. E., Hannington, M. D., Gibson, H. L., Massoth, G. J., Embley, R. W., Chadwick Jr, W. W., Clark, M. R., Timm, C., Graham, I. J., and Wright, I. C., 2012b, Submarine Magmatic-Hydrothermal Systems at the Monowai Volcanic Center, Kermadec Arc: Economic Geology, v. 107, p. 1669-1694.

Li, S., Lein, A., and Ul'yanov, A. A., 2010a, Trace elements and their distribution in sulfides from black smokers of the Broken Spur hydrothermal vent field (Mid-Atlantic Ridge): Moscow University Geology Bulletin, v. 65, p. 254-258.

Li, W., Jackson, S. E., Pearson, N. J., Alard, O., and Chappell, B. W., 2009, The Cu isotopic signature of granites from the Lachlan Fold Belt, SE Australia: Chemical Geology, v. 258, p. 38-49.

Li, W., Jackson, S. E., Pearson, N. J., and Graham, S., 2010b, Copper isotopic zonation in the Northparkes porphyry Cu-Au deposit, SE Australia: Geochimica et Cosmochimica Acta, v. 74, p. 4078-4096.

Li, X., Maslennikov, V. V., Lein, A. Y., and Ul'yanov, A. A., 2012, Associations of trace elements in the sulfides of black smokers from the broken spur, Menez Gwen, and snake pit hydrothermal fields: Moscow University Geology Bulletin, v. 67, p. 8-17.

Li, Y.-H., and Gregory, S., 1974, Diffusion of ions in sea water and in deep-sea sediments: Geochimica et Cosmochimica Acta, v. 38, p. 703-714.

Lowenstern, J. B., Mahood, G. A., Rivers, M. L., and Sutton, S. R., 1991, Evidence for extreme partitioning of copper into a magmatic vapor phase: Science, v. 252, p. 1405-1409.

Lupton, J. E., 1983, Terrestrial inert gases: isotope tracer studies and clues to primordial components in the mantle: Annual Review of Earth & Planetary Sciences, v. 11, p. 371-414.

Maher, K. C., 2005, Analysis of copper isotope ratios by multi-collector inductively coupled plasma mass spectrometry and interpretation of copper isotope ratios from copper mineralization. Dissertation, Department of Geology, Washington State University, PhD, 249 p.

Maher, K. C., and Larson, P. B., 2007, Variation in copper isotope ratios and controls on fractionation in hypogene skarn mineralization at Coroccohuayco and Tintaya, Peru: Economic Geology, v. 102, p. 225-237.

Maher, K. C., Jackson, S., and Mountain, B., 2011, Experimental evaluation of the fluid-mineral fractionation of Cu isotopes at 250°C and 300°C: Chemical Geology, v. 286, p. 229-239.

Malahoff, A., Feden, R. H., and Fleming, H. S., 1982, Magnetic anomalies and tectonic fabric of marginal basins north of New Zealand: Journal of Geophysical Research B: Solid Earth, v. 87, p. 4109-4125.

Marcoux, E., Moëlo, Y., and Leistel, J. M., 1996, Bismuth and cobalt minerals as indicators of stringer zones to massive sulphide deposits, Iberian Pyrite Belt: Mineralium Deposita, v. 31, p. 1-26.

Maréchal, C. N., Télouk, P., and Albarède, F., 1999, Precise analysis of copper and zinc isotopic compositions by plasma-source mass spectrometry: Chemical Geology, v. 156, p. 251-273.

Markl, G., Lahaye, Y., and Schwinn, G., 2006, Copper isotopes as monitors of redox processes in hydrothermal mineralization: Geochimica et Cosmochimica Acta, v. 70, p. 4215-4228.

Marty, B., and Dauphas, N., 2003, The nitrogen record for crust-mantle interaction and mantle convection from Archean to Present: Earth and Planetary Science Letters, v. 206, p. 397-410.

Maslennikov, V. V., Maslennikova, S. P., Large, R. R., and Danyushevsky, L. V., 2009, Study of trace element zonation in vent chimneys from the Silurian Yaman-Kasy volcanic-hosted massive sulfide deposit (Southern Urals, Russia) using laser ablation-inductively coupled plasma mass spectrometry (LA-ICPMS): Economic Geology, v. 104, p. 1111-1141.

Maslennikov, V. V., Maslennikova, S. P., Large, R. R., Danyushevsky, L. V., Herrington, R. J., and Stanley, C. J., 2013, Tellurium-bearing minerals in zoned sulfide chimneys from Cu-Zn massive sulfide deposits of the Urals, Russia: Mineralogy and Petrology, v. 107, p. 67- 99.

Mason, T. F. D., Weiss, D. J., Chapman, J. B., Wilkinson, J. J., Tessalina, S. G., Spiro, B., Horstwood, M. S. A., Spratt, J., and Coles, B. J., 2005, Zn and Cu isotopic variability in the Alexandrinka volcanic-hosted massive sulphide (VHMS) ore deposit, Urals, Russia: Chemical Geology, v. 221, p. 170-187.

Massoth, G. J., de Ronde, C. E. J., Lupton, J. E., Feely, R. A., Baker, E. T., Lebon, G. T., and Maenner, S. M., 2003, Chemically rich and diverse submarine hydrothermal plumes of the southern Kermadec volcanic arc (New Zealand), *in* Larter, R. D., and Leat, P. T., eds., Intra-Oceanic Subduction Systems: Tectonic and Magmatic Processes, Special Publications, 219: London, Geological Society of London, p. 119-139.

Mathur, R., Ruiz, J., Titley, S., Liermann, L., Buss, H., and Brantley, S., 2005, Cu isotopic fractionation in the supergene environment with and without bacteria: Geochimica et Cosmochimica Acta, v. 69, p. 5233-5246.

Mathur, R., Titley, S., Barra, F., Brantley, S., Wilson, M., Phillips, A., Munizaga, F., Maksaev, V., Vervoort, J., and Hart, G., 2009a, Exploration potential of Cu isotope fractionation in porphyry copper deposits: Journal of Geochemical Exploration, v. 102, p. 1-6.

Mathur, R., Titley, S., Hart, G., Wilson, M., Davignon, M., and Zlatos, C., 2009b, The history of the United States cent revealed through copper isotope fractionation: Journal of Archaeological Science, v. 36, p. 430-433.

Mathur, R., Ruiz, J., Casselman, M. J., Megaw, P., and van Egmond, R., 2012, Use of Cu isotopes

to distinguish primary and secondary Cu mineralization in the Cañariaco Norte porphyry copper deposit, Northern Peru: Mineralium Deposita, v. 47, p. 755-762.

Mathur, R., Munk, L., Nguyen, M., Gregory, M., Annell, H., and Lang, J., 2013, Modern and paleofluid pathways revealed by Cu isotope compositions in surface waters and ores of the Pebble porphyry Cu-Au-Mo deposit, Alaska: Economic Geology, v. 108, p. 529-541.

Mavrogenes, J. A., Berry, A. J., Newville, M., and Sutton, S. R., 2002, Copper speciation in vapor-phase fluid inclusions from the Mole Granite, Australia: American Mineralogist, v. 87, p. 1360-1364.

Metz, S., and Trefry, J. H., 2000, Chemical and mineralogical influences on concentrations of trace metals in hydrothermal fluids: Geochimica et Cosmochimica Acta, v. 64, p. 2267-2279.

Migdisov, A. A., Bychkov, A., Williams-Jones, A. E., and van Hinsberg, V. J., 2014, A predictive model for the transport of copper by HCl-bearing water vapour in ore-forming magmatic-hydrothermal systems: Implications for copper porphyry ore formation: Geochimica et Cosmochimica Acta, v. 129, p. 33-53.

Mirnejad, H., Mathur, R., Einali, M., Dendas, M., and Alirezaei, S., 2010, A comparative copper isotope study of porphyry copper deposits in Iran: Geochemistry: Exploration, Environment, Analysis, v. 10, p. 413-418.

Mittelstaedt, E., Fornari, D. J., Crone, T. J., Kinsey, J., Kelley, D., and Elend, M., 2016, Diffuse venting at the ASHES hydrothermal field: Heat flux and tidally modulated flow variability derived from in situ time-series measurements: Geochemistry, Geophysics, Geosystems, v. 17, p. 1435-1453.

Monecke, T., Petersen, S., Hannington, M., Grant, H., and Samson, I., 2016, The minor element endowment of modern sea-floor massive sulfide deposits and comparison with deposits hosted in ancient volcanic successions, *in* Verplanck, P. L., and Hitzmann, M. W., eds., Rare Earth and Critical Elements in Ore Deposits, 18. Reviews in Economic Geology: Knoxville, Tenn., Society of Economic Geologists, p. 245-306.

Nasdala, L., Witzke, T., Ullrich, B., and Brett, R., 1998, Gordaite [$Zn_4Na(OH)_6(SO_4)Cl{\cdot}6H_2O$]: Second occurrence in the Juan de Fuca Ridge, and new data: American Mineralogist, v. 83, p. 1111-1116.

Ogawa, Y., Shikazono, N., Ishiyama, D., Sato, H., Mizuta, T., and Nakano, T., 2007, Mechanisms for anhydrite and gypsum formation in the Kuroko massive sulfide-sulfate deposits, north Japan: Mineralium Deposita, v. 42, p. 219-233.

Oudin, Ë., 1983, Hydrothermal sulfide deposits of the East Pacific Rise (21°N); Part I, Descriptive mineralogy: Marine Mining, v. 4, p. 39-72.

Palacios, C., Rouxel, O., Reich, M., Cameron, E. M., and Leybourne, M. I., 2011, Pleistocene recycling of copper at a porphyry system, Atacama Desert, Chile: Cu isotope evidence: Mineralium Deposita, v. 46, p. 1-7.

Paterson, D., De Jonge, M. D., Howard, D. L., Lewis, W., McKinlay, J., Starritt, A., Küsel, M., Ryan, C. G., Kirkham, R., Moorhead, G., and Siddons, D. P., 2011, The X-ray fluorescence microscopy beamline at the Australian synchrotron: American Institute of Physics Conference Proceedings, 2011, p. 219-222.

Paton, C., Hellstrom, J., Paul, B., Woodhead, J., and Hergt, J., 2011, Iolite: Freeware for the visualisation and processing of mass spectrometric data: Journal of Analytical Atomic Spectrometry, v. 26, p. 2508-2518.

Ramdohr, P., 1980, The Ore Minerals and their Intergrowths: Berlin, Pergamon, 1205 p.

Rempel, K. U., Liebscher, A., Meixner, A., Romer, R. L., and Heinrich, W., 2012, An experimental study of the elemental and isotopic fractionation of copper between aqueous vapour and liquid to 450°C and 400 bar in the CuCl-NaCl-H_2O and CuCl-NaHS-NaCl-H_2O systems: Geochimica et Cosmochimica Acta, v. 94, p. 199-216.

Revan, M. K., Genç, Y., Maslennikov, V. V., Maslennikova, S. P., Large, R. R., and Danyushevsky, L. V., 2014, Mineralogy and trace-element geochemistry of sulfide minerals

in hydrothermal chimneys from the Upper-Cretaceous VMS deposits of the eastern Pontide orogenic belt (NE Turkey): Ore Geology Reviews, v. 63, p. 129-149.

Reyes, A. G., Grapes, R., and Clemente, V. C., 2003, Fluid-rock interaction at the magmatic-hydrothermal interface of the Mount Cagua geothermal system, Philippines: Special Publication (Society of Economic Geologists (U. S.), v. 10, p. 197-222.

Richards, J. P., 2003, Tectono-magmatic precursors for porphyry Cu-(Mo-Au) deposit formation: Economic Geology, v. 98, p. 1515-1533.

Rona, P. A., and Scott, S. D., 1993, A special issue on sea-floor hydrothermal mineralization; new perspectives; preface: Economic Geology, v. 88, p. 1935-1976.

Rouxel, O., Fouquet, Y., and Ludden, J. N., 2004, Copper isotope systematics of the Lucky Strike, Rainbow, and Logatchev sea-floor hydrothermal fields on the Mid-Atlantic Ridge: Economic Geology, v. 99, p. 585-600.

Rubin, K., 1997, Degassing of metals and metalloids from erupting seamount and mid-ocean ridge volcanoes: Observations and predictions: Geochimica et Cosmochimica Acta, v. 61, p. 3525-3542.

Ryan, C. G., 2001, Developments in dynamic analysis for quantitative PIXE true elemental imaging: Nuclear Instruments and Methods in Physics Research, Section B: Beam Interactions with Materials and Atoms, v. 181, p. 170-179.

Ryan, C. G., Etschmann, B. E., Vogt, S., Maser, J., Harland, C. L., Van Achterbergh, E., and Legnini, D., 2005, Nuclear microprobe - Synchrotron synergy: Towards integrated quantitative real-time elemental imaging using PIXE and SXRF: Nuclear Instruments and Methods in Physics Research, Section B: Beam Interactions with Materials and Atoms, v. 231, p. 183-188.

Ryan, C. G., Kirkham, R., Hougha, R. M., Moorhead, G., Siddons, D. P., De Jonge, M. D., Patersone, D. J., De Geronimod, G., Howarde, D. L., and Cleverley, J. S., 2010a, Elemental X-ray imaging using the Maia detector array: The benefits and challenges of large solid-angle: Nuclear Instruments and Methods in Physics Research, Section A: Accelerators, Spectrometers, Detectors and Associated Equipment, v. 619, p. 37-43.

Ryan, C. G., Kirkham, R., Siddons, D. P., Dunn, P. A., Laird, J. S., Kuczewski, A., Moorhead, G., De Geronimo, G., Davey, P., Jensen, M., Paterson, D. J., de Jonge, M. D., Howard, D. L., and Hough, R. M., 2010b, The Maia 384 detector array in a nuclear microprobe: A platform for high definition PIXE elemental imaging: Nuclear Instruments and Methods in Physics Research, Section B: Beam Interactions with Materials and Atoms, v. 268, p. 1899-1902.

Ryan, C. G., Laird, J. S., Fisher, L. A., Kirkham, R., and Moorhead, G. F., 2015, Improved Dynamic Analysis method for quantitative PIXE and SXRF element imaging of complex materials: Nuclear Instruments and Methods in Physics Research, Section B: Beam Interactions with Materials and Atoms, v. 363, p. 42-47.

Schellart, W. P., and Spakman, W., 2012, Mantle constraints on the plate tectonic evolution of the Tonga-Kermadec-Hikurangi subduction zone and the South Fiji basin region: Australian Journal of Earth Sciences, v. 59, p. 933-952.

Seal II, R. R., Alpers, C. N., and Rye, R. O., 2000, Stable isotope systematics of sulfate minerals, *in* Alpers, C. N., Jambor, J. L., and Nordstrom, D. K., eds., Sulfate Minerals- Crystallography, Geochemistry, and Environmental Significance, 40. Reviews in Mineralogy and Geochemistry, p. 541-602.

Seo, J. H., Lee, S. K., and Lee, I., 2007, Quantum chemical calculations of equilibrium copper (I) isotope fractionations in ore-forming fluids: Chemical Geology, v. 243, p. 225-237.

Sherman, D. M., 2013, Equilibrium isotopic fractionation of copper during oxidation/reduction, aqueous complexation and ore-forming processes: Predictions from hybrid density functional theory: Geochimica et Cosmochimica Acta, v. 118, p. 85-97.

Skirrow, R. G., and Walshe, J., 2002, Reduced and oxidized Au-Cu-Bi iron oxide deposits of the Tennant Creek Inlier, Australia: An integrated geologic and chemical model: Economic Geology, v. 97, p. 1167- 1202.

Smith, I. E. M., and Price, R. C., 2006, The Tonga-Kermadec arc and Havre-Lau back-arc system: Their role in the development of tectonic and magmatic models for the western Pacific: Journal of Volcanology and Geothermal Research, v. 156, p. 315-331.

Spooner, E. T. C., 1993, Magmatic sulphide/volatile interaction as a mechanism for producing chalcophile element enriched, Archean Au-quartz, epithermal AuAg and Au skarn hydrothermal ore fluids: Ore Geology Reviews, v. 7, p. 359-379.

Stefánsson, A., and Seward, T. M., 2003, Experimental determination of the stability and stoichiometry of sulphide complexes of silver(I) in hydrothermal solutions to 400°C: Geochimica et Cosmochimica Acta, v. 67, p. 1395-1413.

Stoffers, P., Wright, I. C., and Party, S. S., 1999, Cruise report Sonne 135, Havre Trough-Taupo Volcanic Zone: Tectonic, magmatic and hydrothermal processes, Suva,Fiji-Wellington, New Zealand, Sept. 9-Oct. 15, 1998, Berichte-Reports, 1, Institut für Geowissenschaften, Universität Kiel, 77 p.

Suzuki, R., Ishibashi, J.-I., Nakaseama, M., Konno, U., Tsunogai, U., Gena, K., and Chiba, H., 2008, Diverse range of mineralization induced by phase separation of hydrothermal fluid: Case study of the Yonaguni Knoll IV hydrothermal field in the Okinawa Trough back-arc basin: Resource Geology, v. 58, p. 267-288.

Symonds, R. B., Rose, W. I., Gerlach, T. M., Briggs, P. H., and Harmon, R. S., 1990, Evaluation of gases, condensates, and SO_2 emissions from Augustine volcano, Alaska: the degassing of a Cl-rich volcanic system: Bulletin of Volcanology, v. 52, p. 355-374.

Symonds, R. B., Reed, M. H., and Rose, W. I., 1992, Origin, speciation, and fluxes of trace-element gases at Augustine volcano, Alaska: Insights into magma degassing and fumarolic processes: Geochimica et Cosmochimica Acta, v. 56, p. 633-657.

Symonds, R. B., Mizutani, Y., and Briggs, P. H., 1996, Long-term geochemical surveillance of fumaroles at Showa-Shinzan dome, Usu volcano, Japan: Journal of Volcanology and Geothermal Research, v. 73, p. 177-211.

Syverson, D. D., Pester, N. J., Craddock, P. R., and Seyfried Jr, W. E., 2014, Fe isotope fractionation during phase separation in the NaCl-H_2O system: An experimental study with implications for seafloor hydrothermal vents: Earth and Planetary Science Letters, v. 406, p. 223-232.

Takai, K., Nunoura, T., Horikoshi, K., Shibuya, T., Nakamura, K., Suzuki, Y., Stott, M., Massoth, G. J., Christenson, B. W., de Ronde, C. E. J., Butterfield, D. A., Ishibashi, J., Lupton, J. E., and Evans, L. J., 2009, Variability in microbial communities in black smoker chimneys at the NW Caldera vent field, Brothers Volcano, Kermadec Arc: Geomicrobiology Journal, v. 26, p. 552 - 569.

Taran, Y. A., Hedenquist, J. W., Korzhinsky, M. A., Tkachenko, S. I., and Shmulovich, K. I., 1995, Geochemistry of magmatic gases from Kudryavy volcano, Iturup, Kuril Islands: Geochimica et Cosmochimica Acta, v. 59, p. 1749-1761.

Terry, R. D., and Chilingar, G. V., 1955, Summary of "Concerning some additional aids in studying sedimentary formations," by M. S. Shvetsov: Journal of Sedimentary Research, v. 25, p. 229-234.

Timm, C., de Ronde, C. E. J., Leybourne, M. I., Layton-Matthews, D., and Graham, I. J., 2012, Sources of chalcophile and siderophile elements in Kermadec Arc lavas: Economic Geology, v. 107, p. 1527-1538.

Timm, C., Leybourne, M., Hoernle, K., Wysoczanski, R., Hauff, F., Handler, M., Caratori Tontini, F., and de Ronde, C. E. J., 2016, Trench-perpendicular geochemical variation between two adjacten Kermadec arc volcanoes Rumble II East and West: the role of the subducted Hikurangi Plateau in element recycling in arc magmas: Journal of Petrology, v. 57, p. 1335-1360.

Tivey, M. K., and McDuff, R. E., 1990, Mineral

precipitation in the walls of black smoker chimneys: a quantitative model of transport and chemical reaction: Journal of Geophysical Research B: Solid Earth, v. 95, p. 12,617-12,637.

Tivey, M. K., Olson, L. O., Miller, V. W., and Light, R. D., 1990, Temperature measurements during initiation and growth of a black smoker chimney: Nature, v. 346, p. 51-54.

Tooth, B., Brugger, J., Ciobanu, C., and Liu, W., 2008, Modeling of gold scavenging by bismuth melts coexisting with hydrothermal fluids: Geology, v. 36, p. 815-818.

Törmänen, T. O., and Koski, R. A., 2005, Gold enrichment and the Bi-Au association in pyrrhotite-rich massive sulfide deposits, Escanaba Trough, Southern Gorda Ridge: Economic Geology, v. 100, p. 1135-1150.

Turner, J. S., and Campbell, I. H., 1987, A laboratory and theoretical study of the growth of "black smoker" chimneys: Earth and Planetary Science Letters, v. 82, p. 36-48.

Vikentyev, I. V., 2006, Precious metal and telluride mineralogy of large volcanic-hosted massive sulfide deposits in the Urals: Mineralogy and Petrology, v. 87, p. 305-326.

Von Damm, K. L., 1990, Seafloor hydrothermal activity: black smoker chemistry and chimneys: Annual Review of Earth & Planetary Sciences, v. 18, p. 173-204.

Von Damm, K. L., 1995, Controls on the chemistry and temporal variability of seafloor hydrothermal fluids, *in* Humphris, S. E., Sierenberg, R. A., Mullineaux, L. S., and Thompson, R. E., eds., Seafloor Hydrothermal Systems: Physical, Chemical, Biological, and Geological Interactions, 91. American Geophysical Union Monographs, American Geophysical Union, p. 222-247.

Wagner, T., and Jonsson, E., 2001, Mineralogy of sulfosalt-rich vein-type ores, Boliden massive sulfide deposit, Skellefte district, Northern Sweden: The Canadian Mineralogist, v. 39, p. 855-872.

Wohlgemuth-Ueberwasser, C. C., Viljoen, F., Petersen, S., and Vorster, C., 2015, Distribution and solubility limits of trace elements in hydrothermal black smoker sulfides: An in-situ LA-ICP-MS study: Geochimica et Cosmochimica Acta, v. 159, p. 16-41.

Wright, I. C., 1994, Nature and tectonic setting of the southern Kermadec submarine arc volcanoes: An overview: Marine Geology, v. 118, p. 217-236.

Wright, I. C., de Ronde, C. E. J., Faure, K., and Gamble, J. A., 1998, Discovery of hydrothermal sulfide mineralization from southern Kermadec arc volcanoes (SW Pacific): Earth and Planetary Science Letters, v. 164, p. 335-343.

Wysoczanski, R. J., Handler, M. R., Schipper, C. I., Leybourne, M. I., Creech, J., Rotella, M. D., Nichols, A. R. I., Wilson, C. J. N., and Stewart, R. B., 2012, The tectonomagmatic source of ore metals and volatile elements in the Southern Kermadec Arc: Economic Geology, v. 107, p. 1539-1556.

Yang, K., and Scott, S. D., 2002, Magmatic degassing of volatiles and ore metals into a hydrothermal system on the modern sea floor of the eastern Manus back-arc basin, western Pacific: Economic Geology, v. 97, p. 1079-1100.

Yeats, C., Belton, D., Laird, J. S., and Ryan, C. G., 2010, Mapping elemental distributions in submarine hydrothermal sulfide smokers using proton induced X-ray emission: Nuclear Instruments and Methods in Physics Research, Section B: Beam Interactions with Materials and Atoms, v. 268, p. 2129-2132.

Zelenski, M., Malik, N., and Taran, Y., 2014, Emissions of trace elements during the 2012-2013 effusive eruption of Tolbachik volcano, Kamchatka: Enrichment factors, partition coefficients and aerosol contribution: Journal of Volcanology and Geothermal Research, v. 285, p. 136-149.

Zelenski, M. E., Fischer, T. P., de Moor, J. M., Marty, B., Zimmermann, L., Ayalew, D., Nekrasov, A. N., and Karandashev, V. K., 2013, Trace elements in the gas emissions from the Erta Ale volcano, Afar, Ethiopia: Chemical Geology, v. 357, p. 95-116.

Zhu, X. K., O'Nions, R. K., Guo, Y., Belshaw, N. S., and Rickard, D., 2000, Determination of natural

Cu-isotope variation by plasma-source mass spectrometry: Implications for use as geochemical tracers: Chemical Geology, v. 163, p. 139-149.

Zoller, W. H., Gladney, E. S., and Duce, R. A., 1974, Atmospheric concentrations and sources of trace metals at the South Pole: Science, v. 183, p. 198-200.

Appendix Location, description and reference(s) for data in Figures 4.5, 4.6 and 4.7.

Reference	***Deposit type*** / Location	Tectonics	Description
	VMS		
22	13°N EPR, Axial Graben	MOR	Chimneys, Sediment barren, Fast-spreading
22	21°N EPR, Axial Graben	MOR	Chimneys, Sediment barren, Fast-spreading
22	86°W Galapagos Rift, Site B	MOR	Chimneys, Sediment barren, Intermediate-spreading
22	Broken Spur, 29°N, MAR, Axial Graben	MOR	Chimneys, Sediment barren, Slow-spreading
21	Logatchev, MAR	MOR	Chimneys, Sediment barren, Slow-spreading, Ultramafic
21	Lucky Strike, MAR	MOR	Chimneys, Sediment barren, Ridge-Hotspot, Basaltic
21	Rainbow, MAR	MOR	Chimneys, Sediment barren, Slow-spreading, Ultramafic
13	Alexandrinka Kuroko-type, Urals, Russia	Island arc	Unmetamorphosed
5	Besshi (Ikadatsu) mine, Japan	MOR	Sediment barren, Metamorphosed
5	Mio Mine, Japan	MOR	Sedimented, Metamorphosed
9	Portugal		
	Porphyry		
9	Ajo, AZ, USA		
2	Bayugo Cu-Au, Philippines		
7, 9	Beaver-Harrison Mine, UT, USA		
9	*Bingham Canyon, UT, USA		
17	Canariaco Norte, Peru	Continental	
19	Chahfiroozeh, Kerman belt, Iran	Continental	
11, 14, 15	Chuquicamata, Chile		
14, 15	Collahuasi, Rosario, Chile		
7, 9, 10	*Coroccohuayco, Peru	Continental	exoskarn
14	El Salvador, Chile		
14	El Teniente, Chile		
14	Escondida, Chile		
2, 7, 9, 14	*Grasberg Cu-Au, Indonesia		Grasberg & Ertsberg intrusions, Kali dykes, Grasberg pyrite shell, Dalum diatreme
14	Mocha, Chile		
9	Montana Tunnels mine, MT, USA		
11, 16	Morenci, AZ, USA		
8	Northparkes (Goonumbla), SE Australia		Orthomagmatic
9	OK mine, UT, USA		
14	Panguna, Papua New Guinea		
18	Pebble, AK, USA	Continental	
7, 9	*Resolution, Superior district, AZ, USA		
15	Silver Bell, AZ, USA		
15	Sisir, Turkey		
20	Spence, Chile	Continental	
1	Steward Mine, Butte, MT, USA		
7, 9, 10	*Tintaya Mine, Peru	Continental	exoskarn
14	Toquepala, Peru		
	Skarn		
9	*Bingham Canyon, UT, USA		
9	Cactus mine, UT, USA		Endoskarn
7, 9	Chalcobamba, Las Bambas, Peru		
9	Christmas mine, AZ, USA		
7, 9, 10	*Coroccohuayco, Peru	Continental	exoskarn
7, 9	Crown Jewel, WA, USA		

REFERENCE

1 Asael et al., 2007
2 Braxton & Mathur, 2011
3 Graham et al., 2004
4 Haest et al., 2009
5 Ikehata et al., 2011
6 Jiang et al., 2002
7 Larson et al., 2003
8 Li et al., 2010
9 Maher, 2005
10 Maher & Larson, 2007
11 Marechal et al., 1999
12 Markl et al., 2006
13 Mason et al., 2005
14 Mathur et al., 2005
15 Mathur et al., 2009a
16 Mathur et al., 2009b
17 Mathur et al., 2012
18 Mathur et al., 2013
19 Mirnejad et al., 2010
20 Palacios et al., 2011
21 Rouxel et al., 2004
22 Zhu et al., 2000

Appendix continued.

Reference	***Deposit type*** / Location	Tectonics	Description
7, 9	Empire Mine, ID, USA		
9	Empire mine, NM, USA		
7, 9	Ferrobamba, Las Bambas, Peru		
3, 7, 9, 14	*Grasberg Cu-Au, Indonesia		Grasberg and Ertsberg skarns, Big Gossan, Kucing Liar
9	Mission mine, AZ, USA		
7, 9	Pine Creek, California, USA		
9	*Resolution, Superior district, AZ, USA		
7, 9, 10	*Tintaya Mine, Peru	Continental	exoskarn
9	Troy prospect, ID, USA		
	Vein- Type		
9	Animas Forks district, Silverton, CO, USA		
12	Artenberg near Steinach, Schwarzwald district, Germany	Continental	
12	Baumhalde near Todtnau, Schwarzwald district, Germany	Continental	
12	Birkenberg near St. Ulrich, Schwarzwald district, Germany	Continental	
12	Brandenberg near Todtnau, Schwarzwald district, Germany	Continental	
12	Dorothea near Freudenstadt, Schwarzwald district, Germany	Continental	
12	Friedrich-August near Horbach, Schwarzwald district, Germany	Continental	
12	Friedrich-Christian near Schapbach, Schwarzwald district, Germany	Continental	
12	Gottesehre near Urberg, Schwarzwald district, Germany	Continental	
12	Haus Baden, Badenweiler, Schwarzwald district, Germany	Continental	
12	Holderpfad near Sulzburg, Schwarzwald district, Germany	Continental	
12	Kafersteige, Pforzheim, Schwarzwald district, Germany	Continental	
12	Mettmatal near Brenden, Schwarzwald district, Germany	Continental	
12	Prosper near Rippoldsau, Schwarzwald district, Germany	Continental	
12	Sophia near Wittichen, Schwarzwald district, Germany	Continental	
12	Wenzel near Wolfach, Schwarzwald district, Germany	Continental	
4	Dikulushi Cu-Ag, Dem Rep of Congo	Continental	
9	Galena mine, ID, USA		
		Contintental	
6	Jinman, Yunnan, China	rift basin	
9	Superior mine, AZ, USA		
	Mantle-derived		
22	Cornwall, England		Mafic- hosted ore deposit
22	Outokumpo Mine, Finland		Mafic- hosted ore deposit
9	Palabora mine, S. Africa		Carbonatite
22	Stavoren Mine, Bushveld complex, S. Africa		Granophyre
9	Stillwater mine, MT, USA		Mafic igneous complex, form as immiscible sulfide melts during petrogenesis
7, 9, 10	*Tintaya Mine, Peru		Mafic dyke

** mine is listed under multiple deposit types, i.e. porphyry and skarn*